

Doctoral Thesis

Decay pion spectroscopy
of electro-produced hypernuclei

(電磁生成したハイパー核の崩壊 π 中間子分光)

Sho Nagao

Department of Physics, Graduate School of Science
Tohoku University
2015 (平成 27 年)

abstract

Investigations of hypernuclei provide information on many-body systems which contains “strangeness”. Therefore, hypernuclei are good tools to understand the baryon-baryon interactions. Λ hypernuclear studies have been performed for a long time, especially, the emulsion experiments contributed greatly to understanding the ΛN interaction. Λ binding energies of the ground states for many kinds of light hypernuclei were measured in the emulsion experiments, the results are used even now in theoretical calculations and energy calibration in experiments. Though they play important roles in the hypernuclear study, the results from the emulsion experiments cannot solve some mysteries such as the ΛN charge symmetry breaking (CSB) effect.

The existence of the large ΛN CSB effect was suggested with the large Λ binding energy difference between $A=4$ iso-doublet hypernuclei ($^4_\Lambda H$ and $^4_\Lambda He$) from the results of the emulsion experiments in 1960’s~1970’s, however, the quantitative understandings have not been obtained even in the latest theoretical frameworks. The recent developments of the theoretical calculation and the new measurements of Λ binding energies made the discussions of the ΛN CSB effect for the other iso-multiplet hypernuclei possible. However, from the comparison between the calculation and the experimental results in the $A=7$ hypernuclear system, small ΛN CSB effect was suggested, while the $A=4$ systems show the large ΛN CSB effect.

It suggests that the theoretical treatments might be too naive or there might be an uncertainty in the experimental measurements. In order to resolve the inconsistency between $A=4$ and $A=7$ system, new determinations of the Λ binding energies with higher accuracy are necessary. Several experiments were proposed or already performed at JLab and J-PARC. In this thesis, a new novel spectroscopic method “decay pion spectroscopy” of electro-produced hypernuclei is proposed. In this method, the masses of hypernuclei are deduced by detecting monochromatic pions from two-body decays of hypernuclei stopped in the target. Simultaneously, kaons are tagged to identify strangeness production events. This method allows us to determine the Λ binding energy of the ground state for light hypernuclei with an accuracy of 100 keV in total.

We aim to clarify the existence of the large ΛN CSB in the $A=4$ hypernuclear system by using this proposed technique. We designed the experiment by using the Monte Carlo simulation tool Geant4 so that the decay pion peak can be observed with good signal-to-noise ratio. In

the simulation, expected peak resolution, hypernuclear yield, and backgrounds were estimated quantitatively. As a result, we estimated that ~ 45 counts decay pion peak from ${}_{\Lambda}^4 H$ can be observed with $150\text{-}\mu\text{m}$ thick ${}^9 \text{Be}$ target and $20\text{-}\mu\text{A}$ beam intensity in 20 days experiment at MAMI-C.

The first pilot experiment was performed at MAMI-C in 2011 to check the feasibility of this new method. The particle rates were measured in each spectrometer, and we confirmed the low counting rate in pion spectrometers. On the other hand, it was found that the detector upgrades were essential in the kaon tagger to take data with better signal-to-noise ratio, especially, a suppression of the large positron background was important.

In order to suppress the large positron background, a novel technique “lead wall” was introduced. In addition, installation of an additional aerogel Cherenkov counter and optimization of the detector’s configurations were performed. Thanks to the improvements of the detector setup, we successfully took data under 30 times lower counting rate even at 10 times higher beam intensity in the physics data taking runs in 2012.

Through the analysis of the physics data, >1000 hyperon or hypernuclear decay events were observed. The first monochromatic peak from the decay pion was observed around $133 \text{ MeV}/c$ with a peak significance of 7.9σ ; it corresponds to the two-body decay of ${}_{\Lambda}^4 H \rightarrow {}^4 \text{He} + \pi^-$. The peak position of the pion peak was $p_{\pi^-} = 132.92 \pm 0.02(\text{stat.}) \pm 0.12(\text{sys.}) \text{ MeV}/c$, after the momentum was calibrated with the elastic scattering peaks of ${}^{181} \text{Ta}(e, e') {}^{181} \text{Ta}$. This momentum was converted to the Λ binding energy of ${}_{\Lambda}^4 H$, and the final result was:

$$B_{\Lambda} = 2.12 \pm 0.01(\text{stat.}) \pm 0.09(\text{sys.}) \text{ MeV}.$$

This binding energy was consistent result with the current world data, that still supports the large ΛN CSB effect in $A=4$ hypernuclear system.

CONTENTS

Chapter.1	Introduction	1
1.1	Hypernucleus	2
1.1.1	Characteristics	5
1.1.2	Methods of hypernuclear formation	5
1.2	Historical overview	9
1.2.1	Emulsion experiments	9
1.2.2	Counter experiments	10
1.3	A new experimental method, “Hypernuclear decay pion spectroscopy” . .	14
1.3.1	Impacts of the hypernuclear decay pion spectroscopy	14
1.4	Goals of present thesis	21
Chapter.2	Principle and Design	23
2.1	Motivation	23
2.1.1	Establishment of the new spectroscopic technique	23
2.1.2	High mass resolution spectroscopy	24
2.1.3	Investigation of the nuclear fragmentation process	25
2.2	Experimental principle	26
2.2.1	Kinematics of the hypernuclear electro-photo production	26
2.2.2	Principle of hypernuclear decay pion spectroscopy	27
2.3	Design	32
2.3.1	target material	32
2.3.2	Yield estimation	33
2.3.3	Resolution	45
2.3.4	Background	50
2.4	Calibration methods	55
2.4.1	Momentum calibration using electron beam	55
2.5	Expected spectrum	57

Chapter.3	Experimental Apparatus	58
3.1	Overview	58
3.2	The Mainz Microtron “MAMI-C”	58
3.3	A1 experimental hall	61
3.3.1	Target system	65
3.3.2	Pion spectrometers (SpekA, SpekC)	66
3.3.3	Kaon tagger (Kaos)	71
3.4	Data acquisition system	90
3.4.1	Kaos logic	90
3.4.2	SpekA and SpekC logic	91
3.4.3	Coincidence logic	91
Chapter.4	Data taking	95
4.1	Pilot experiment	95
4.1.1	Detector setup	96
4.1.2	Data summary	98
4.1.3	Results	98
4.2	Physics run	103
4.2.1	Improvements	103
4.2.2	Data summary	103
Chapter.5	Analysis	112
5.1	Particle tracking	112
5.2	Particle identification	112
5.3	Coincidence time	114
5.4	Momentum calibration of pion spectrometers	116
5.4.1	Data summary of calibration experiments	116
5.4.2	Angular and momentum calibration	118
5.4.3	Linearity	123
5.4.4	Peak shape estimation	129
Chapter.6	Results and discussion	143
6.1	Pion spectrum	143
6.1.1	Coincidence event selection	143
6.1.2	Decay pion momentum distribution	143
6.2	Peak fitting	150

6.3	Systematic error	154
6.4	Discussion	158
6.4.1	Future prospects	159
6.5	Summary	164
Acknowledgment		166
AppendixA	Amplifier in R877-100	168
AppendixB	Reflectance	169
AppendixC	Momentum spectrum in Spek-A	171
AppendixD	Other calibration methods	173
Bibliography		181

Chapter.1

Introduction

“What is the fundamental principle to describe our world” is one of the longtime questions for the nuclear and particle physics. The nuclear and particle physicists have tried to solve the question quantitatively from a microscopic point of view, and found the *laws* which govern our world. The discovery of a nucleus by Rutherford is the starting point of the nuclear physics, and it opened a new point of view for the structure inside the atom. The discovery of the nuclear components (proton and neutron) introduced a new quantum number *isospin* under the flavor SU(2) symmetry in the strong interaction. Nowadays, the elementary particles and their interactions are understood in the framework of the Standard Model. According to this model, several kinds of the elementary particles (fermions, gauge bosons, and the Higgs boson) are advocated, and all particles were experimentally observed. The model explains successfully almost all experimental results, and thus, the Standard Model is the most established theoretical framework in the particle physics. In this framework, Quantum Chromodynamics (QCD) is an established theory for the strong interaction between quarks and gluons.

The nuclear force in the nuclear medium should be described also with QCD, if it is a fundamental theory for the strong interaction. However, *ab initio* calculations of the interaction are difficult because perturbative treatments is impossible due to its large coupling constant in the low energy region, while they work well in high energy region thanks to a property of the asymptotic freedom. Therefore, meson exchange pictures are also important in order to describe the nuclear interaction which is the low energy description of the strong interaction. Though the nuclear interaction at the long range part (~ 2 fm) is well understood by the meson exchange pictures, the interaction at the short range part, especially at the repulsive core (< 1 fm) where nucleons overlap, pictures for constituents of the nucleons (u , d quarks and gluons) and sea-quarks involving s quark may be needed. Expansions of understanding for the Nucleon-Nucleon (NN) interactions to the Baryon-Baryon (BB) interactions are quite important in order to understand the strong interaction in the nuclear medium.

A hypernucleus is a kind of the exotic nucleus which contains hyperons (a baryon which contains “strangeness”), in other words, the hypernucleus is a many-body system consists of hyperons and nucleons. Investigations of the hypernuclei are essential to understand the strong interaction in the low energy region (\lesssim GeV) as the Baryon-Baryon (BB) interaction. In addition, there are subjects which cannot be explained in the current theoretical frameworks such as a charge symmetry breaking. In order to approach these questions, the high resolution spectroscopy of the hypernuclei is one of very important tools.

In this chapter, characteristics and production methods of the hypernucleus (Section 1.1), a historical overview and issues under discussion for light hypernuclei (Section 1.2), a newly designed experiment to solve the issues, and the goal of the present thesis will be explained.

1.1 Hypernucleus

The first observed hadron with s quark is K meson by G. D. Rochester and C. C. Butler in 1947 [Roch47]. Other strange particles were observed later, for example Λ particle and Σ particle. These particles can be classified based on the framework of the flavor SU(3). A quark (u , d , s) and an anti-quark (\bar{u} , \bar{d} , \bar{s}) combine to form light pseudo-scalar meson singlet and octet in this framework (Figure 1.1 (a)). Similarly, combinations of three quarks form the completely symmetric baryon decuplet for spin-flavor state, the mixed symmetric octets, and the completely anti-symmetric singlet. For example, Figure 1.1 (b) shows the baryon octet in $S(\text{spin})=1/2$. The lightest hyperon is Λ ($S=1/2$, $I(\text{isospin})=0$), and $\Sigma^{0,\pm}$ ($S=1/2$, $I=1$) are next. Characteristics of these hyperons are summarized in Table 1.1.

There are still room for study on interactions between baryons to form a nucleus; especially, interactions between Hyperon-Nucleon (YN) and Hyperon-Hyperon (YY) are not well understood because the number of YN and YY scattering data is limited due to the short lifetime and difficulties of hyperon productions. However, hypernuclear states are possible to be observed with narrow widths because their lifetimes are enough long ($>\text{ps}$) to make bound states. Therefore, it is useful method to improve our knowledge of the YN interactions from comparisons of hypernuclear structures such as masses and energy levels between experimental data and theoretical calculations using the well-established method in the studies of non-strange nuclei, because it is difficult to derive the YN interaction only from little number of the YN scattering data. So far, about 40 species of hypernuclei from lightest hypernuclei $^3_{\Lambda}\text{H}$ to heaviest one $^{209}_{\Lambda}\text{Bi}$ have been observed, and their masses have been measured experimentally for most of them. Figure 1.2 shows a chart of hypernuclides from s -shell to p -shell hypernuclei with their Λ binding energies. Most of light hypernuclei were observed by emulsion experiments in 1960's to

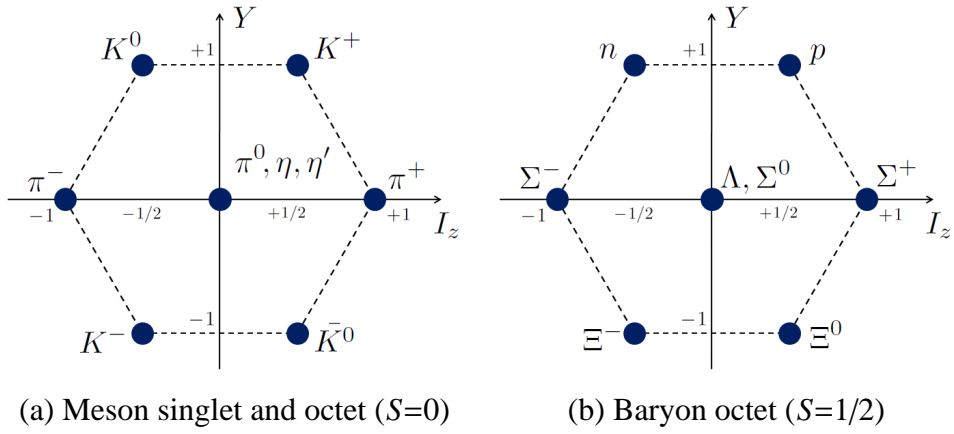


Figure 1.1: Typical examples of hadrons. The hadrons are classified on the hypercharge (Y) and the isospin (I_z).

Table 1.1: Characteristics of light hyperons [PDG12].

Hyperon	Mass (MeV/ c^2)	Lifetime (second)	Decay Mode	Branching ratio (%)
Λ	1115.683(6)	$2.631(20) \times 10^{-10}$	$p + \pi^-$	63.9(5)
			$n + \pi^0$	35.9(5)
Σ^0	1192.642(24)	$7.4(7) \times 10^{-20}$	$\Lambda + \gamma$	100
Σ^+	1189.37(7)	$0.8018(26) \times 10^{-10}$	$p + \pi^0$	51.57(30)
			$n + \pi^-$	48.31(30)
Σ^-	1197.449(30)	$1.479(11) \times 10^{-10}$	$n + \pi^-$	99.848(5)

70s'. Their binding energies were measured with an accuracy of a several tenth keV to a few hundred keV.

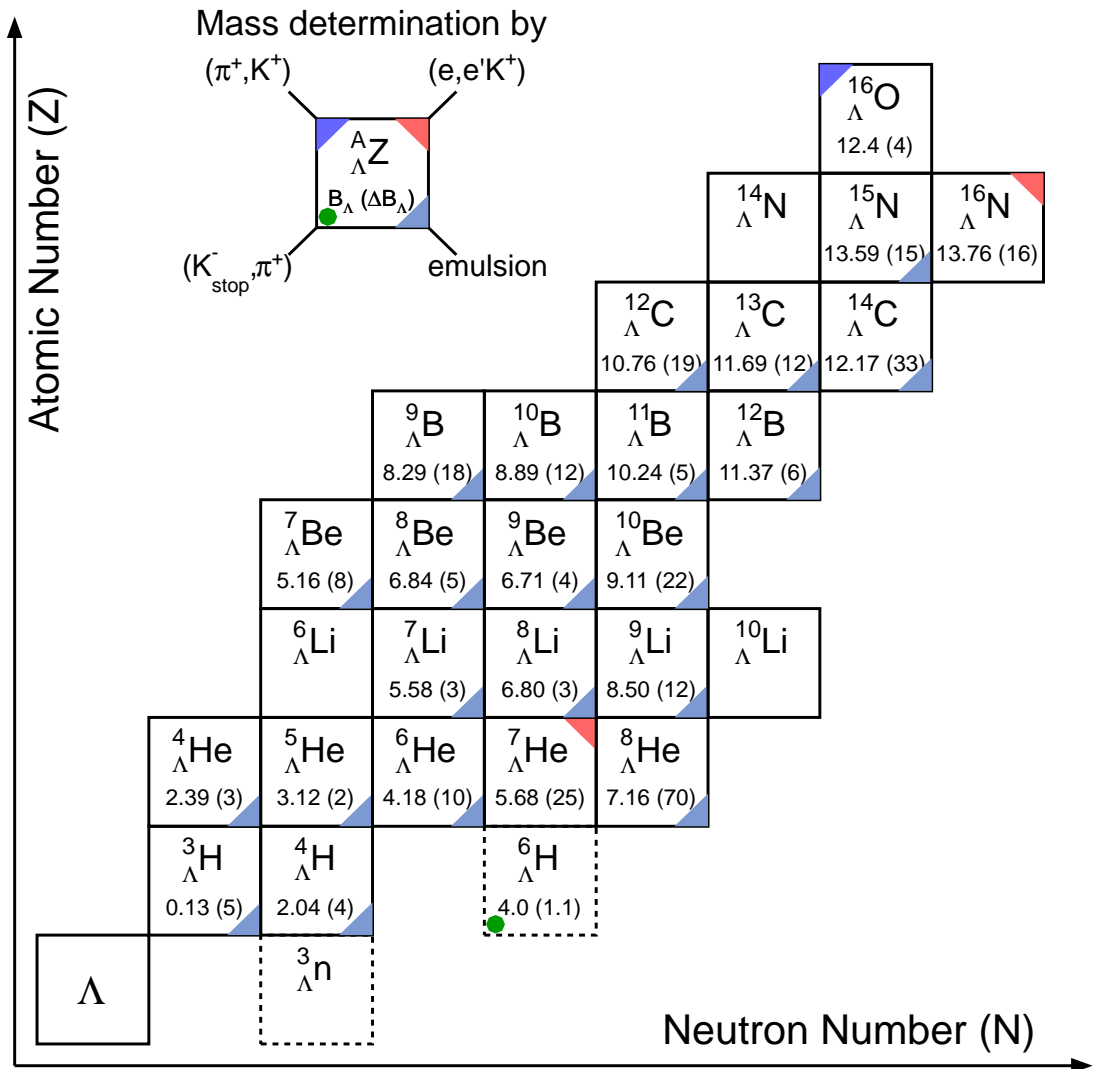


Figure 1.2: A chart of Λ hypernuclei. Species of observed hypernuclei and their measured Λ binding energies (MeV) in the core nuclei are shown. Only statistics errors are given in the emulsion results. Triangles at the edge of boxes mean the methods how the Λ binding energies were determined. Hypernuclei in dashed boxes ($^3_{\Lambda} n$ and $^6_{\Lambda} H$) were reported to be found, while their existences are not well established [Rapp13, Agne12b]

1.1.1 Characteristics

One of unique characters of hypernuclei in comparison with non-strangeness nuclei is their short lives. Typical lifetime for ground states of hypernuclei is about 200 ps from light to medium heavy atomic mass region, which is a bit shorter than that of Λ in free space (Figure 1.3). However, when the lifetimes are compared with a typical time scale of the electro-magnetic interaction such as the gamma transitions from hypernuclear excited states to ground states (< ps), they are about hundred times longer. Therefore, almost all excited hypernuclei decay to normal nuclei through the weak interaction after they de-excite to the ground states through the gamma decays.

Hypernuclei have two weak-decay modes: mesonic weak decay (MWD) in which hypernuclei emit pions and non-mesonic weak decay (NMWD) in which they do not emit pions. MWD is a similar decay mode to the free Λ decay such as $\Lambda \rightarrow p + \pi^-$. NMWD is unique decay mode in hypernuclear medium through interactions between Λ and nucleons such as $\Lambda+N\rightarrow N+N$. In heavy atomic mass hypernuclei, the MWD is suppressed due to the Pauli exclusion principle because the emitted nucleon momentum (~ 100 MeV/c) is much smaller than the nucleon Fermi momentum (~ 250 MeV/c), and thus the NMWD dominates because the emitted momentum is ~ 400 MeV/c in the NMWD. However, light hypernuclei is still able to decay in the MWD mode. Decay width of the MWD in light hypernuclei are summarized in Figure 1.4. MWD is possible even in the p -shell hypernuclei, while the π^- decay widths of light hypernuclei are ~ 3 times smaller than the total decay width of a free Λ .

1.1.2 Methods of hypernuclear formation

Three major reactions have been used to produce hypernuclei: (K^-, π^-) reaction, (π^+, K^+) reaction, and (γ, K^+) or $(e, e' K^+)$ reaction. Feynman diagrams for each reaction are shown in Figure 1.5.

In the (K^-, π^-) reaction, a s quark in a K^- beam is exchanged with a d quark in a neutron, and the neutron is converted to a Λ . Λ production cross sections are large (\sim mb/sr) in comparison with the other reactions. Since the reaction is exothermic and K^- has a negative charge, K^- is absorbed by the target nucleus even at rest and reacts on the surface with a released momentum of ~ 250 MeV/c as shown in Figure 1.6; it has a specific name $(K_{\text{stop}}^-, \pi^-)$ reaction.

In the (π^+, K^+) reaction and the $(e, e' K^+)$ reaction, Λ is produced with a pair production of $s\bar{s}$ quarks. Since these reactions are endothermic, they are needed to bring energies from out of the

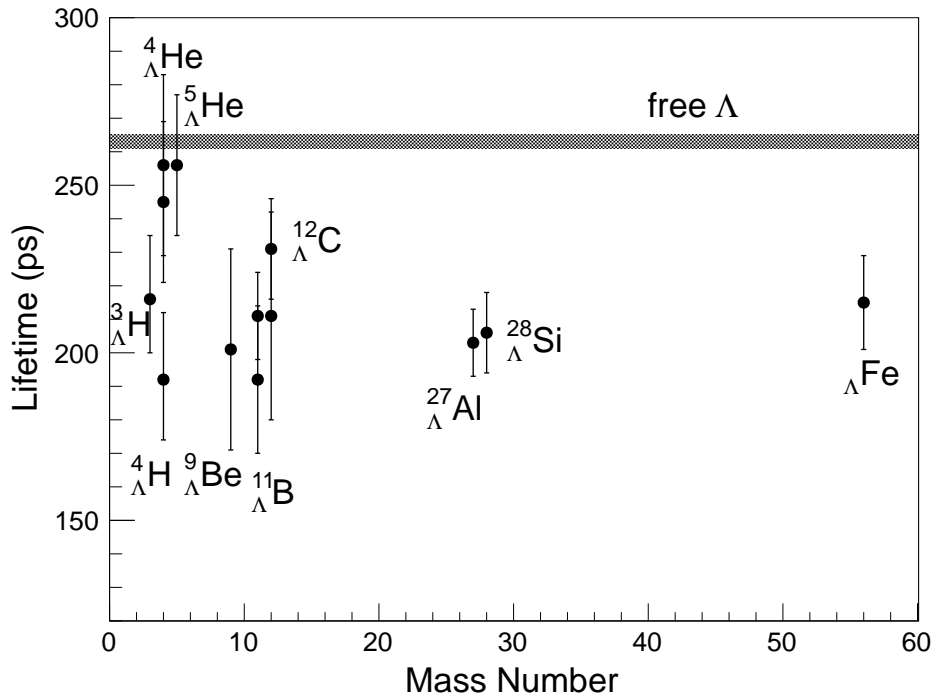


Figure 1.3: Lifetimes of hypernuclei. A lifetime of Λ in free space is shown as a black band with its error. Measured lifetimes are given by references [Rapp14, Park00]. The lifetimes of $^3\Lambda$ H and $^4\Lambda$ H are the statistically combined results from the emulsion experiments and counter experiments, and others are the results of counter experiments. The result of $_{\Lambda}\text{Fe}$ is not identified the isotope.

systems, for example a γ energy threshold of $p(\gamma, K^+)\Lambda$ reaction is 911 MeV. They are useful method to investigate heavy hypernuclei because highly excited or deeply bound hypernuclei can be produced thanks to larger Λ recoil momenta (300~400 MeV/c). On the other hand, Λ production cross section in the (π^+, K^+) reaction is smaller ($\sim 100 \mu\text{b}/\text{sr}$) than the (K^-, π^-) reaction, and the cross section in the (γ, K^+) reaction is much smaller ($\sim 100 \text{ nb}/\text{sr}$).

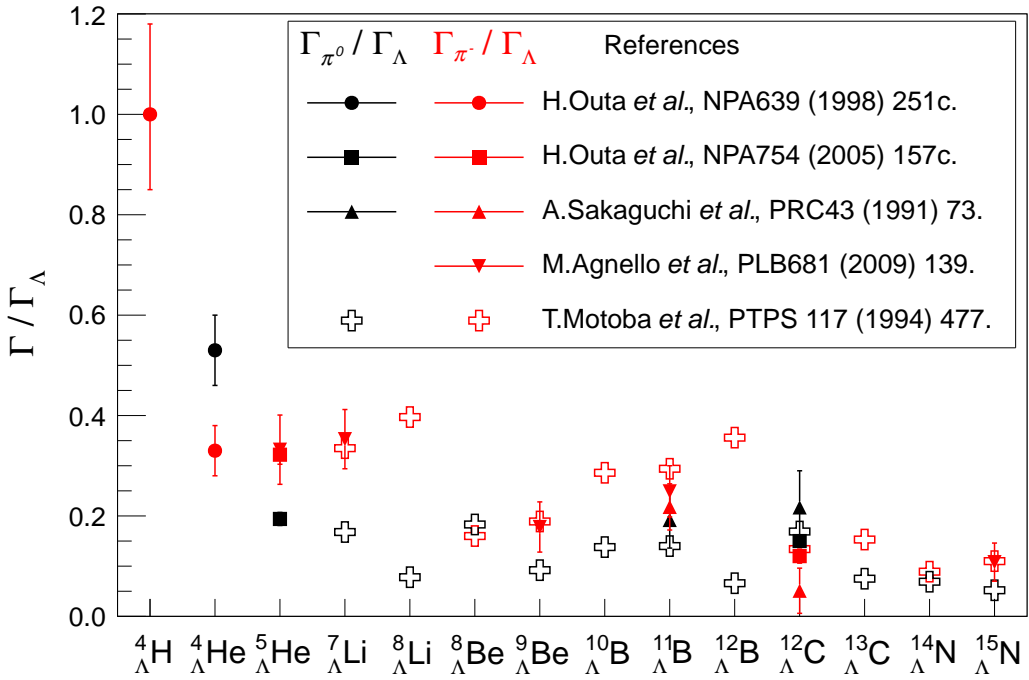


Figure 1.4: Decay widths of light hypernuclear mesonic weak decay. Four experimental results at KEK and DAΦNE [Outa98, Outa05, Saka91, Agne09] and the theoretical calculation by Motoba [Moto94] are summarized. Black points shows the mesonic weak decay widths with π^0 emission normalized with the free Λ decay width, and red points shows with π^- emission.

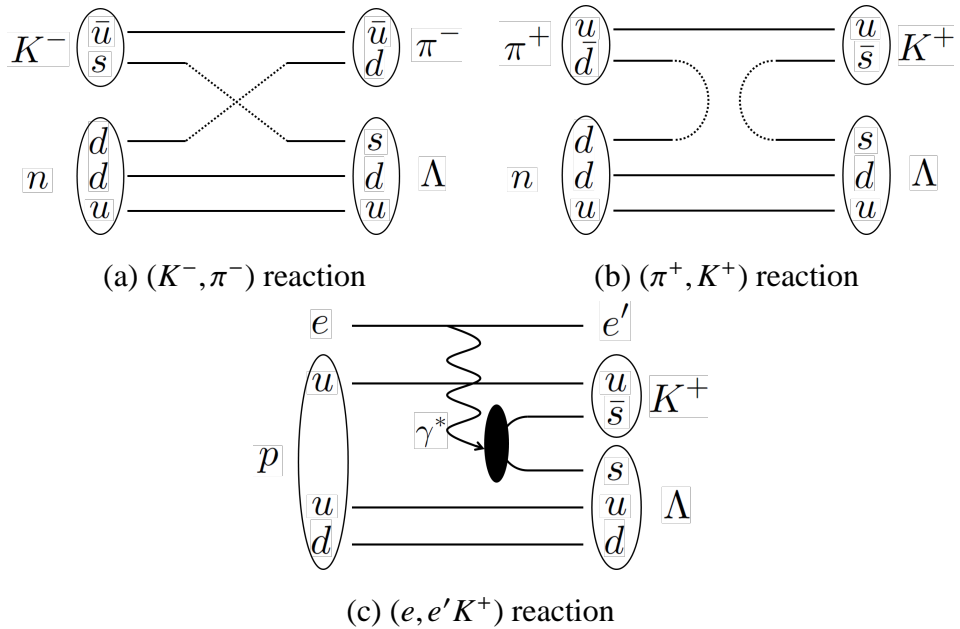


Figure 1.5: Typical methods of hypernuclear formation.

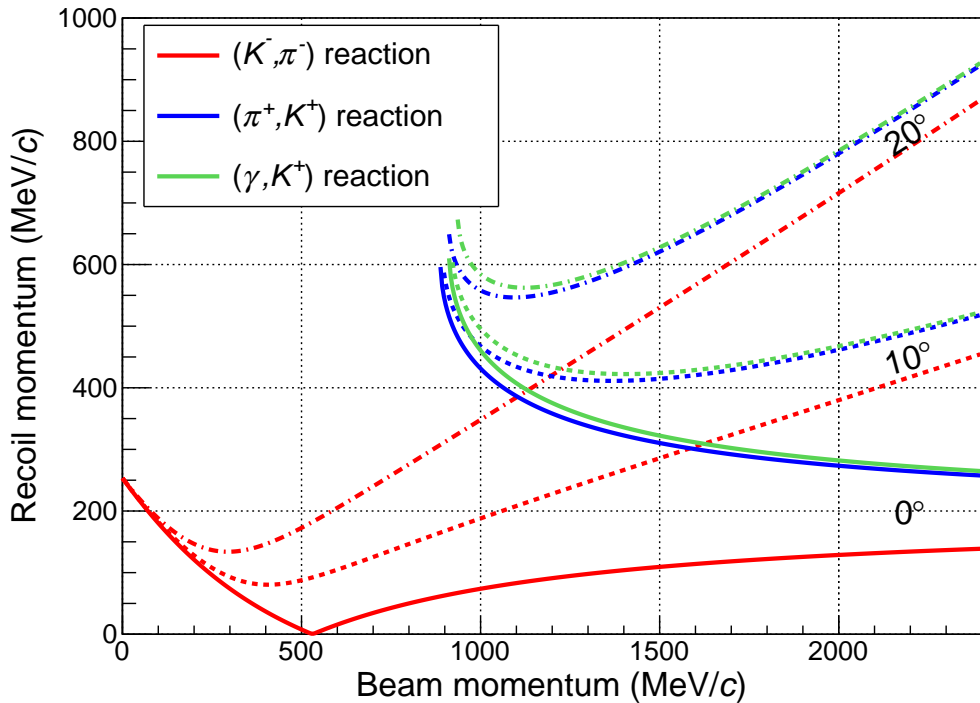


Figure 1.6: Λ recoil momentum dependences on beam momenta in the $n(K^-, \pi^-)\Lambda$, the $n(\pi^+, K^+)\Lambda$, and the $p(\gamma, K^+)\Lambda$ reactions. Three opening angles between the beam particles and the generated mesons (solid lines : 0° , dashed lines : 10° , and chain lines : 20°) are shown. In the $(K_{\text{stop}}^-, \pi^-)$ reaction, a Λ has the recoil momentum ~ 250 MeV/c. Beam momentum thresholds in the (π^+, K^+) and the (γ, K^+) reactions are ~ 900 MeV/c because of endothermic reactions, and typical Λ recoil momenta at the forward angles are ~ 400 MeV/c.

1.2 Historical overview

A lot of technical innovations made investigations of hypernuclei progress. In early days of hypernuclear studies, experiments with the (K^-, π^-) reaction were performed at CERN, BNL, and KEK in 1960's ~ 80's. Absolute Λ binding energies of the ground states for light hypernuclei were measured by emulsion experiments [Davi05]. Excited states for light hypernuclei were measured with the missing mass spectroscopy, and for example, small spin-orbit force of Λ was indicated [Bruc78]. In the second stage of the hypernuclear study, counter experiments with the (π^+, K^+) reaction were begun in the mid 1980's at BNL and KEK. The missing mass spectroscopies of heavy Λ hypernuclei were performed at KEK [Hase96, Hotc01], and the potential depth of Λ particle in the nuclear matter was deduced. In the third stage, counter experiments with the $(e, e' K^+)$ reaction was started at JLab in 2000, and the measurements of the absolute Λ binding energies of hypernuclei were expanded to medium-heavy hypernuclei [Miyo03, Yuan06, Iodi07, Cusa09, Naka13, Tang14, GogaD]. A little bit before, the high resolution spectroscopies of γ -rays from hypernuclear de-excitations using germanium detectors were successfully performed at BNL and KEK [Tamu98, Tamu00, Akik02, Sasa04, Ukai04, Miur05, Tamu05, Ukai06, Ukai08], and the detailed level structures of p -shell hypernuclei were clarified.

In this section, historical overviews of hypernuclear experiments and issues under discussion for light hypernuclei which related to this thesis will be introduced.

1.2.1 Emulsion experiments

Emulsion experiments are prior researches for measurements of absolute Λ binding energies of hypernuclei, and the results of the experiments made issues to be explained in Section 1.3.1. A new determination of absolute Λ binding energy with higher accuracy is one of major motivations of this thesis.

The emulsion experiment is an established method to observed new particles in early days of the particle physics, and it has been performed from the beginning of the hypernuclear studies. In this method, K^- s are absorbed to nuclei in an emulsion stack, and a K^- and a nucleus convert to a hypernucleus and a π^- . Since the emulsion is exposed by an energy deposit of a charged particle, a track is appeared along a particle path. Hypernuclear events can be identified from the unique vertex shapes made by the hypernuclear weak decays. The species and masses of hypernuclei can be determined by analyzing the track information such as the length and the

grain density.

For the investigation of hypernuclei, many emulsion experiments were performed at BNL and CERN in 1960's to 70's [Gaje67, Bohm68, Juri73, Cant74]. Most of light hypernuclei were observed by these experiments. Their masses of the ground states up to $^{15}_{\Lambda}\text{N}$ were determined with an accuracy of a few tenth to a few hundred keV with statistical ambiguities. The results are frequently referred to discuss the potential depth of the ΛN interaction, the ΛNN three-body force due to the $\Lambda\text{-}\Sigma$ coupling [Akai00], and the charge symmetry breaking effect of the ΛN interaction [Bodm85].

The emulsion experiment is still very useful method to search for new species of hypernucleus, because it is possible to observe it even with one event. However, the emulsion is difficult to handle under the high intense beams because it is completely exposed by the beam quickly. Moreover, since it takes a long time to analyze the large number of tracking images in the emulsion, it is difficult to perform the high yield experiments. In addition, progresses of electronics and accelerators brought new apparatuses, and thus, the main experimental techniques for single Λ hypernuclei were changed from the emulsion experiment to the counter experiment. Recently, a combination technique of the emulsion and the counter experiments has been trying to overcome the difficulties as explained above.

1.2.2 Counter experiments

Hypernuclear γ -ray spectroscopy

The hypernuclear γ -ray spectroscopy is one of the most successful experiments in the hypernuclear studies. Energy spacings between hypernuclear states can be measured in this method by measuring γ -ray energies from de-excitations of hypernuclei. In the first stage, energies of γ -rays from *s*-shell hypernuclei produced with the (K^-, π^-) reaction were measured by NaI detectors with a precision of a few tenth keV [Beje76, Beje79, KawaD]. Later, the γ -ray spectroscopy using germanium detector was established at BNL in 1998 [Tamu98], thereafter, detailed level schemes of several *p*-shell hypernuclei have been revealed with an accuracy of a few keV. Because the energy spacings can be determined in the method, Λ binding energies in excited states are able to determined if the binding energy of the ground state is known well. Therefore, the γ -ray spectroscopy is the complementary experiment to the experiment to be discussed in this thesis.

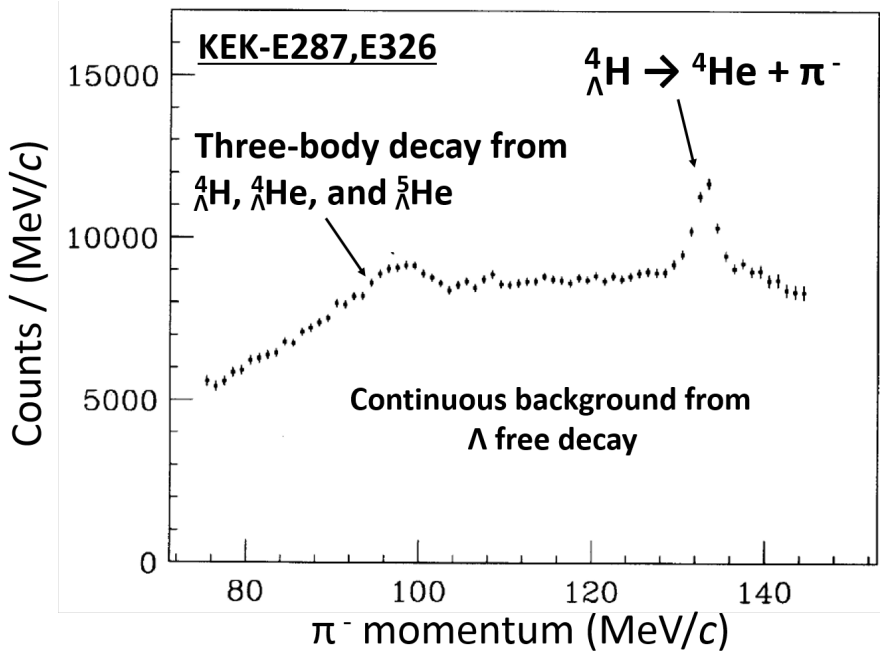


Figure 1.7: A pion momentum distribution tagged with K^- stopped events in a ${}^9\text{Be}$ target [KawaD]. A monochromatic pion peak from two-body mesonic weak decay of ${}^4_{\Lambda}\text{H}$ and continuous distributions from three body decay of ${}^4_{\Lambda}\text{H}$, ${}^4_{\Lambda}\text{He}$, and ${}^5_{\Lambda}\text{He}$ were observed on a large background of π^- from free Λ decay.

Hypernuclear decay pion measurement

Hypernuclear decay pion measurements were performed at KEK in 1980's. Decay pions from hypernuclei produced by the $(K_{\text{stop}}^-, \pi^-)$ reaction was measured with several target materials, and a decay pion peak from ${}^4_{\Lambda}\text{H}$ was observed on a background of free Λ decay as shown in Figure 1.7 [Tamu89a, KawaD]. At the same time, continuous decay pion distributions from three body decays of ${}^4_{\Lambda}\text{H}$, ${}^4_{\Lambda}\text{He}$, and ${}^5_{\Lambda}\text{He}$ were also detected below 100 MeV/c. Hypernuclear fragmentation probabilities which are important data to discuss the fragmentation process were reported. Recently, a similar experiment using the $(K_{\text{stop}}^-, \pi^-)$ reaction was carried from the FINUDA collaboration at DAΦNE. They also confirmed the decay pion peak from ${}^4_{\Lambda}\text{H}$ [Agne12a].

However, high resolution spectroscopies of Λ hypernuclei have not been achieved due to a large momentum spread from an energy deposit in thick targets and a limitation of momentum resolution for π^- .

Electro-photo production of hypernuclei

■ $(e, e' K^+)$ reaction spectroscopy

An electro-photo production of hypernuclei is experimentally difficult because the production cross section is >1000 times smaller in comparison with other production methods. It is necessary to perform experiments under huge backgrounds with high energy and high intense primary electron beam.

The hypernuclear spectroscopy with the $(e, e' K^+)$ reaction was finally established at JLab in this decade [Miyo03, Naka13, Tang14]. In this experiment, two high momentum resolution spectrometers were operated to measure the momenta of scattered electrons and generated K^+ s with a relative momentum resolution of $\Delta p/p = 10^{-4}$, and the masses of hypernuclei were deduced using the missing mass method. Thanks to the high intense primary electron beam, hypernuclear peaks can be observed with high statistics even for thin targets ($\sim 100 \text{ mg/cm}^2$). Because the energy struggling in the target is able to become smaller in comparison with the hypernuclear spectroscopies using the other reactions, hypernuclear mass spectroscopies with sub-MeV resolution are possible. In addition, it is possible to determine the absolute Λ binding energy of hypernuclei with an accuracy of a few hundred keV thanks to the calibration sources of Λ and Σ^0 masses produced with the $p(e, e' K^+)Y$ reactions, that is one of the strong point in comparison with the other reaction spectroscopies.

The establishment of this technique was quite important to design a new experiment in this thesis.

■ Studies of the elementary process for hyperon photo production

Investigations of the elementary processes of the strangeness photo-production is important to understand the reaction mechanism. Reaction cross sections of K^+ production channels were reported in wide kinematics ranges with the SAPHIR detector at ELSA and the CLAS detector at JLab [Glan04, McCr10, Dey10, Pere10], especially, the cross sections of more than 3000 data points were measured for $p(\gamma, K^+)\Lambda$ and $p(\gamma, K^+)\Sigma^0$ channels. Theoretical models such as isobar models [Mart99, Mizu98] and Regge Plus Resonance [Cort06] explain the cross sections reasonably well. Differential cross sections at the invariant energy ($\sqrt{s} \sim 1.84 \text{ GeV}$) are plotted in Figure 1.8. These cross sections are very useful inputs to design the new experiment.

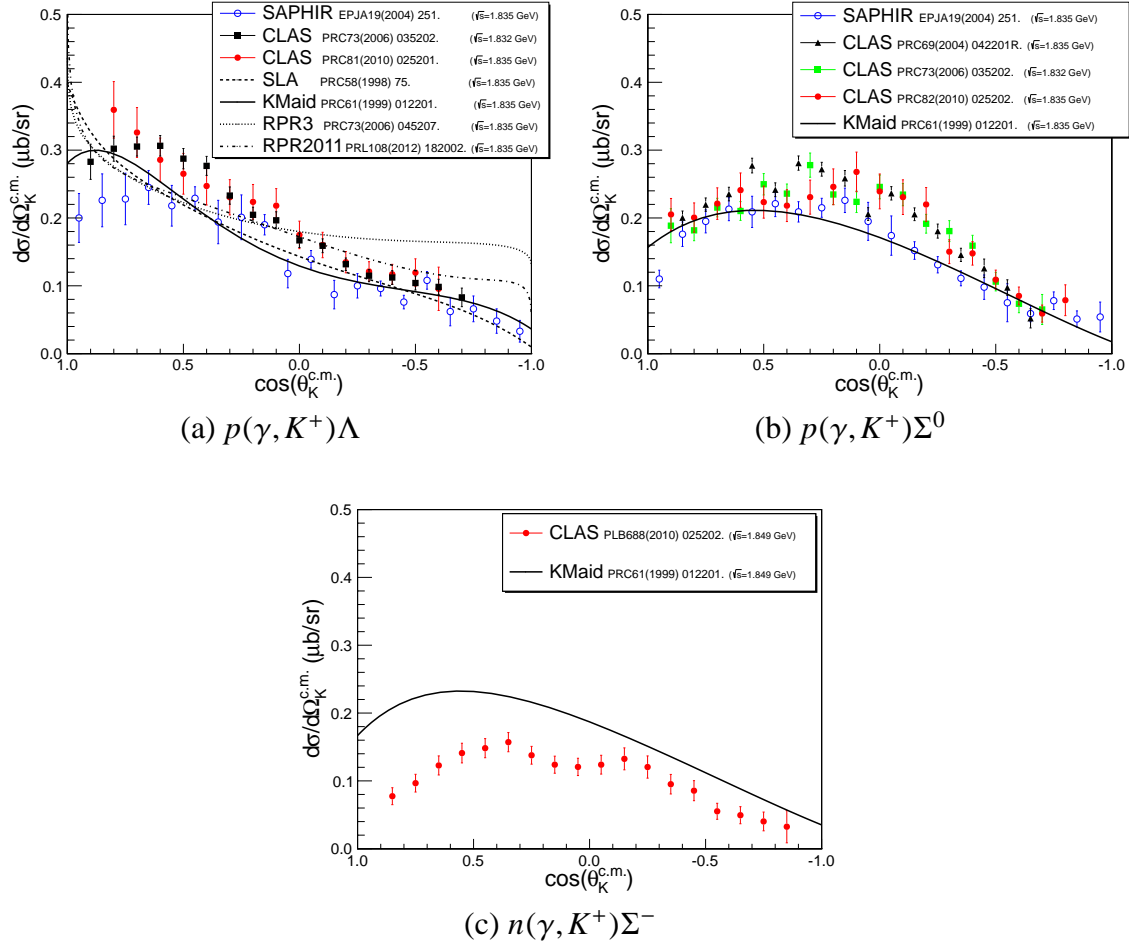


Figure 1.8: Differential cross sections of the hyperon photo productions in each reaction channel. The data points were measured using the photon beam at the electron beam facilities (Bonn ELSA and JLab CEBAF), their invariant energies (\sqrt{s}) are around 1.84 GeV. The theoretical calculations of isobar models and the Regge Plus Resonance are given with lines. The differential cross section of the $p(\gamma, K^+)\Lambda$ reaction is the most investigated reaction on wide angular and energy regions, while the theoretical calculations of the cross section have ambiguities at the very forward angles ($\cos \theta_K^{c.m.} \sim 1$) due to the limited experimental results. There are many data points also for the cross section of the $p(\gamma, K^+)\Sigma^0$ reaction. The calculation of the isobar model (KMAid) is well described the experimental results. The number of the data points for the $n(\gamma, K^+)\Sigma^-$ reaction are less than those for the other reactions because of the experimental difficulties. Therefore, there is a discrepancy by a factor of 2 between the theoretical calculation and the data points at this invariant energy.

1.3 A new experimental method, “Hypernuclear decay pion spectroscopy”

A decay pion from hyperfragments was already measured at KEK [Tamu89a, KawaD]. However, its resolution was poor and spectroscopic study had never performed with this technique. On the other hand, we are able to achieve much higher resolution and less background counts so as to get signals from hypernuclei with better signal-to-noise ratio thanks to the establishment of the hypernuclear studies using the primary electron beam through the $(e, e' K^+)$ spectroscopy. We newly designed a hypernuclear mass spectroscopic technique “hypernuclear decay pion spectroscopy”.

In the new experiment, we design to measure the Λ binding energy with an accuracy of 100 keV in total, which is comparable or better than those in the emulsion experiments. It is noted that the Λ binding energy measurement with realistic systematic error estimations have not been performed. The resolution for the Λ binding energy is designed to achieve at least better than 100 keV: this is highest resolution in the hypernuclear spectroscopies using magnetic spectrometers. Moreover, the Λ binding energies for several hypernuclei are expected to be measured simultaneously because fragmented hypernuclei are also able to be detected. Much more details will be explained in Chapter 2.

Impacts of the new determinations of the absolute Λ binding energy with high accuracy will be explained bellow.

1.3.1 Impacts of the hypernuclear decay pion spectroscopy

The investigations of hypernuclei have revealed the hypernuclear structures. However, some mysteries still remain even for the light hypernuclei, for example, the ΛN charge symmetry breaking and a binding energy shift of $^{12}_{\Lambda} C$. The new measurement of the hypernuclear decay pion spectroscopy is possible to approach these problems as explained bellow.

ΛN Charge Symmetry Breaking (CSB)

The charge symmetry and the charge independence of the nuclear force are basic concepts in the nuclear physics. The symmetry leads a quantum number “*isospin*”. The charge independence is defined with the equalities of interactions under any rotations in *isospin* space, and the charge symmetry is under an *isospin* inversion. These symmetries impose the equalities of the NN

scattering length. In fact, after the electro-magnetic interactions are removed, the forces between nucleons (pp , nn , or np) are almost the same. The latest results of the 1S_0 NN scattering lengths in each channel were summarized by Machleidt [Mach11] as follows:

$$\begin{aligned} a_{pp} &= -17.3 \pm 0.4 \text{ fm} \quad [\text{Mill90}], \\ a_{nn} &= -18.95 \pm 0.40 \text{ fm} \quad [\text{Gonz06, Chen08}], \\ a_{np} &= -23.740 \pm 0.020 \text{ fm} \quad [\text{Houk71, Dumb83, Swar95, Mach01}]. \end{aligned} \quad (1.1)$$

The charge symmetry breaking (CSB) is quite small as the scattering lengths of nn and pp are almost the same. Otherwise, the charge independence breaking (CIB) is large in comparison with the charge symmetry as seen in the larger difference of the scattering length of np . These data suggest that the interaction between nn is about 1% more attractive than pp , and np is approximately 2% more attractive than pp and nn [Henl69].

The larger CIB is explained quantitatively with effects of a pion mass difference in the one-pion-exchange potential and the two-pions-exchange potential [Li98]. In case of the CSB, Coon *et al.* found that the difference of the scattering lengths is reproduced quantitatively with taking the mixing effects of $\rho^0\omega$ into account [Coon87].

The CSB effects in nuclear medium have been investigated in A=3 iso-doublet nuclei (^3H and ^3He), because their masses can be calculated theoretically with high precisions. The measured masses of these nuclei are $M_{^3\text{H}} = 2808.921 \text{ MeV}/c^2$ and $M_{^3\text{He}} = 2808.391 \text{ MeV}/c^2$ which negligibly small errors ($\sim 2 \text{ eV}$) [Audi03]. The nuclear binding energies after subtracting the composed nucleon masses in each nucleus are $B_{^3\text{H}} = 8.482 \text{ MeV}$ and $B_{^3\text{He}} = 7.718 \text{ MeV}$, which means ^3H (neutron rich nucleus) is more deeply bound. The difference of the binding energies is $\Delta B^3 = B(^3\text{H}) - B(^3\text{He}) = 764 \text{ keV}$. There are several studies to estimate the effects from the electro-magnetic interaction [Fria70, Bran78, Mill94] (Table 1.2). These papers report consistent results, namely, $\sim 690 \text{ keV}$ difference appears due to the Coulomb effect, about -40 keV due to the finite size effect, and $\sim 40 \text{ keV}$ from other effects such as the magnetic interaction. As a result, it is found that the sum of the electro-magnetic interaction makes $\sim 690 \text{ keV}$ binding energy difference. A remained difference, that is $\sim 70 \text{ keV}$, is ascribed to the contribution from the strong interaction.

Thereafter, Brandenburg and Wu *et al.* estimated the CSB effect with $\pi^0\eta$ and $\rho^0\omega$ mixing [Bran88, Wu90]. They suggested that the additional binding energy differences due to the $\pi^0\eta$ and $\rho^0\omega$ mixing effect is $\sim 70 \text{ keV}$, and the binding energy difference between ^3H and ^3He can be explained with the contribution of these mixing effects. Thus, the mechanism of the CSB for the NN interaction is almost understood with $\sim \text{keV}$ level.

The strength of the ΛN interaction is much more different from the NN interaction. However,

Table 1.2: The experimental result and the estimations of the charge asymmetric contributions for the binding energy difference between ^3H and ^3He . The observable difference (ΔB^3), the calculated contributions: static Coulomb effects (ΔB_C), finite size effects (ΔB_{size}), other electromagnetic effects (ΔB_{other}), sum of total electro-magnetic effects ($\Delta B_{\text{E.M.}}$), and the CSB effect (ΔB_{CSB}).

	Exp. (keV)	Calc. (keV)				
		[Fria70]	[Bran78]	[Mill94]	[Bran88]	[Wu90]
ΔB_C		$(6.4 \pm 0.1) \times 10^2$	638 ± 17		687	681 ± 3
ΔB_{size}					-39	-33 ± 3
ΔB_{other}			45 ± 23		35	46 ± 3
$\Delta B_{\text{E.M.}}$			683 ± 29	$693 \pm 19 \pm 5$	683	694 ± 5
ΔB_{CSB}					59	78 ± 8
ΔB^3	764				742	772 ± 15

it is qualitatively assumed that the charge symmetry between Λp and Λn interactions is a good symmetry as well as the NN interaction. Unfortunately, the scattering lengths of the Λp and Λn channels are missing due to the difficulties of the scattering experiments. However, the CSB effects between Λp and Λn interactions (ΛN CSB) have been discussed from the Λ binding energy differences in iso-multiplet hypernuclei as for the NN interaction.

The difference of the Λ binding energies of the ground states (0^+ state) between ${}^4_\Lambda\text{H}$ and ${}^4_\Lambda\text{He}$, which is the lightest iso-doublet hypernuclei, is $\Delta B_\Lambda^4 = B_\Lambda({}^4_\Lambda\text{H}) - B_\Lambda({}^4_\Lambda\text{He}) = -350 \pm 40$ keV from the measurement of the emulsion experiments [Davi05]. That of the excited states (1^+ states) is -240 ± 60 keV [Juri73]. The Λ binding energies in ${}^4_\Lambda\text{He}$ are larger in both states, having the opposite sign to the $A=3$ iso-doublet nuclei. In the simplest discussion, there are no additional Coulomb effects when a Λ particle is added in nuclei because Λ particle has no charge. Therefore, the Λ binding energy for the core nuclei, which are ^3H and ^3He in this case, should be the same under the assumption of the ΛN charge symmetry. In fact, compressions of the core nuclei appear also when a Λ particle gets into the central part of hypernuclei. Bodmer *et al.* reported the small effect for the binding energy difference in $A=4$ system ($\Delta B_\Lambda^4 = +50$ keV) [Bodm85]. However, this compression effect is not enough to explain the larger energy difference in the $A=4$ hypernuclei (350 keV).

One of the reasons why the Λ binding energies in the iso-doublet hypernuclei are changed is advocated to be a mixing effect of Σ particle from the $\Lambda\Sigma$ conversion [Gibs72]. The mass

difference of Λ and Σ is about $80 \text{ MeV}/c^2$, that is much smaller than that of $N\Delta$ ($\sim 300 \text{ MeV}/c^2$). Therefore, the admixture probability of a virtual Σ particle is not negligible in a hypernucleus ($\sim 2\%$) [Akai00]. Because each Σ iso-multiplet has a different charge and mass, they populate with different probabilities in hypernuclei. As a result, additional effects due to the Σ mixture appear as the followings: (a) additional electro-magnetic interactions in Σp or pp , (b) a mass shift due to the differences of the admixture probabilities in the iso-multiplet hypernuclei [Nogg01], and (c) a contribution of the one-pion-exchange from $\Lambda\Sigma^0$ mixing effect [Dali64],

Figure 1.9 shows theoretical calculation results with the $\Lambda\Sigma$ conversion effects. The results are $\Delta B_\Lambda^4 = +50 \text{ keV}$ [Hiya01, Nemu02], or -70 [Nogg01], while -350 keV difference is reported from the emulsion experiments. Thus, the CSB puzzle in $A=4$ system is still unsolved.

On the other hand, a systematic uncertainty for the Λ binding energies in the emulsion experiments is one of the unclarified issues, because we cannot find detailed explanation about the systematic uncertainties in a paper about 30-years later [Davi05] after the experimental results are published [Juri73]. Table 1.3 shows a summary of the emulsion experiments which determined the Λ binding energies in $A=4$ system. The latest Λ binding energies are given from only three-body decay events, while there are many two-body decay events of ${}^4_\Lambda H$ in emulsion. In the papers, the authors report that the energy calibration cannot be performed for a pion from a two-body decay of ${}^4_\Lambda H$ because of too long track range. This is a unique case for ${}^4_\Lambda H$. Other two-body decay events, for example ${}^3_\Lambda H \rightarrow {}^3He + \pi^-$, are adopted to determine the Λ binding energy, even though pions from these events also have similar kinetic energies. Nowadays, since the Λ binding energies of hypernuclei for few-body systems can be calculated very precisely, more precise measurements are necessary to progress the discussions about the ΛN CSB effect.

Recently, the investigation for the ΛN CSB was progressed to the other iso-multiplet hypernuclei thanks to well-established cluster model calculations and new measurements of the Λ binding energies. Hiyama *et al.* performed the four-body cluster model calculations for $A=7$ iso-triplet hypernuclei [Hiya09] and $A=10$ iso-doublet hypernuclei [Hiya12] in p -shell hypernuclei. Hiyama *et al.* expanded the few-body calculations to p -shell hypernuclei introducing a phenomenological CSB potential so as to reproduce the experimental results of all the Λ binding energies in $A=4$ hypernuclear system. In addition to the measurements of the emulsion experiments, new data for the Λ excitation energy in ${}^7_\Lambda Li$ ($T=1$ state) and the Λ binding energy of the ground state in ${}^7_\Lambda He$ are reported from the hypernuclear γ -ray spectroscopy [Tamu00] and the $(e, e' K^+)$ reaction spectroscopy [Naka13, GogaD], respectively. Hence, the theoretical predictions and the experimental results are able to be compared as summarized in Figure 1.10. In the experimental results, the Λ binding energy differences in $A=7$ system are $\Delta B_{\Lambda n}^7 = B_\Lambda({}^7_\Lambda He) - B_\Lambda({}^7_\Lambda Li^*) = 420 \pm 280 \text{ keV}$ and

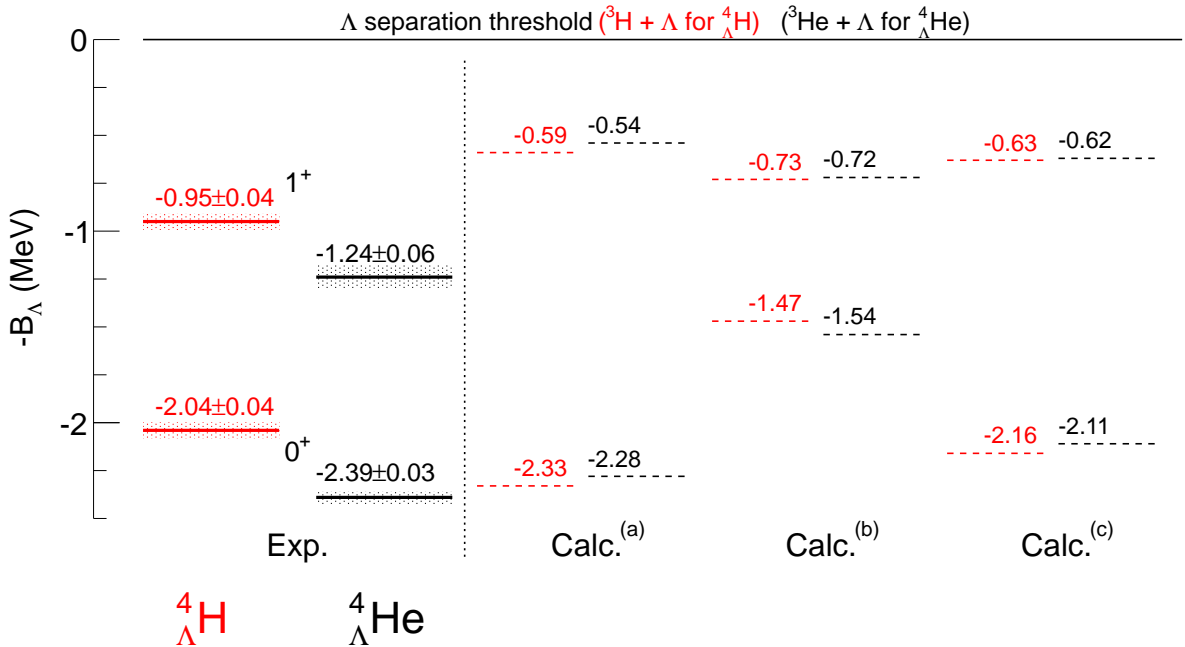


Figure 1.9: A summary of hypernuclear Λ binding energies for 4-body systems. Experimental results [Juri73, Beje76, Beje79, KawaD] and three theoretical calculations including Λ - Σ conversion effect are shown; (a) 4-body calculations using variational method employing Jacobi-coordinate Gaussian-basis functions [Hiya01], (b) Faddeev-Yakubovsky calculations with SC97e potential for YN interaction [Nogg01], and (c) *ab initio* calculations with SC97f potential [Nemu02]

Table 1.3: A summary of measured Λ binding energies in the emulsion experiments for $A=4$ hypernuclei.

${}^4\text{H}$ ($B_\Lambda = 2.04 \pm 0.04$ MeV)			${}^4\text{He}$ ($B_\Lambda = 2.39 \pm 0.03$ MeV)		
decay mode	counts	B_Λ (MeV)	decay mode	counts	B_Λ (MeV)
three body	23	1.86 ± 0.10 *	three body	49	2.20 ± 0.06 *
	70	2.08 ± 0.06 **		130	2.36 ± 0.04 **
${}^1\text{H} + {}^3\text{H} + \pi^-$	56	2.14 ± 0.07 ***	${}^1\text{H} + {}^3\text{He} + \pi^-$	83	2.42 ± 0.05 ***
${}^2\text{H} + {}^2\text{H} + \pi^-$	11	1.92 ± 0.12 ***	${}^1\text{H} + {}^1\text{H} + {}^2\text{H} + \pi^-$	15	2.44 ± 0.09 ***
${}^4\text{He} + \pi^-$	208	2.26 ± 0.07 *			
	552	2.29 ± 0.04 **			

* [Gaje67], ** [Bohm68], *** [Juri73]

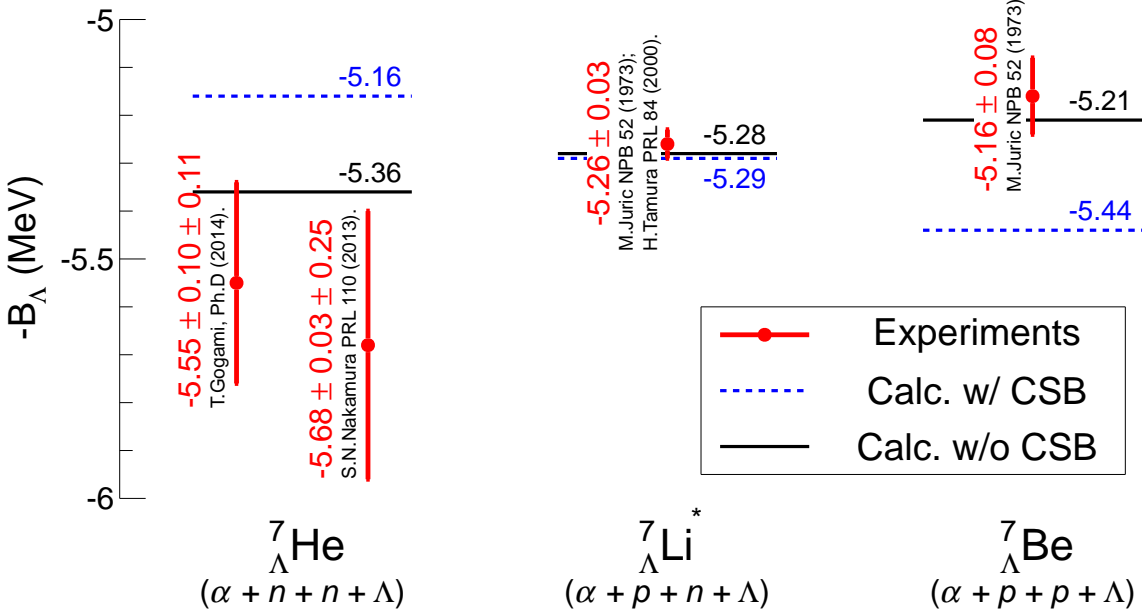


Figure 1.10: A summary of Λ binding energies for $A=7$ iso-triplet hypernuclei. Experimental data is given from the following references [Juri73, Tamu00, Naka13, GogaD]. The results of the four-body cluster mode calculations are shown in both case of with ΛN CSB potential and without ΛN CSB potential [Hiya01].

$\Delta B_{\Lambda p}^7 = B_\Lambda(^7_{\Lambda} \text{Li}^*) - B_\Lambda(^7_{\Lambda} \text{Be}) = 100 \pm 90$ keV. This results mean a Λ particle is deeply bound in the neutron-rich hypernuclei, that is the opposite tendency with $A=4$ system. In the cluster model calculations, when the ΛN CSB potential is not introduced, the calculations well reproduced the experimental data. However, the Λ binding energies in the proton-rich hypernuclei become deeper in the calculation with the ΛN CSB potential. Thus, the results of the experimental measurements support the results of the cluster model calculations without the ΛN CSB effect in $A=7$ system well.

Figure 1.11 shows the energy differences of the ground states in iso-multiplet hypernuclei as a function of the atomic mass number. It must be noted that all observed Λ binding energy differences (ΔB_Λ^A) have zero consistent or positive values except for the $A=4$ system. In addition, recently, -0.54 MeV systematic binding energy shift was indicated [GogaD] from the comparison between the results of the emulsion experiments and the (π^+, K^+) reaction spectroscopies. The large CSB effect is observed only in $A=4$ hypernuclear system even if this binding energy shift is taken into account.

These data and the theoretical calculations suggest the followings: (a) We need to improve calculations and approaches for the ΛN CSB effect, as the effect cannot be explained in the current theoretical frameworks, (b) we need to improve the experimental data which were measured in 40 years ago in order to clarify the Λ binding energy differences. Therefore, high resolution spectroscopy with a cutting-edge technique for the $A=4$ hypernuclear system is quite important to solve the ΛN CSB puzzle.

Because the hypernuclear decay pion spectroscopy can measure the absolute Λ binding energy of these light hypernuclei such as ${}^4_{\Lambda}H$, ${}^7_{\Lambda}He$, and ${}^7_{\Lambda}Li(0^+)$, this method is useful to approach this puzzle.

Binding energy shift of ${}^{12}_{\Lambda}C$

As already mentioned the previous section, the energy calibration in the (π^+, K^+) and the (K^-, π^-) reactions have been performed the Λ binding energy of ${}^{12}_{\Lambda}C$, though -0.54 MeV energy shift is suggested [GogaD]. An absolute Λ binding energy measurement of this ${}^{12}_{\Lambda}C$ is quite important experimentally, because this binding energy relates strongly the Λ binding energy measurements of other hypernuclei. In principle, the Λ binding energy of ${}^{12}_{\Lambda}C$ can be measured from ${}^{12}_{\Lambda}C \rightarrow {}^{12}N + \pi^-$, though this decay branch is not so large ($\Gamma/\Gamma_\Lambda \sim 0.1$). If the decay pion spectroscopy is successfully progressed, this binding energy might be measured.

Spin assignment

The ground state of a hypernucleus can be changed to excited states of the daughter nucleus with the mesonic weak decay process such as ${}^A_{\Lambda}Z \rightarrow {}^A[Z-1]^* + \pi^-$. Because the branching ratio of this process is related to the spins of the parent hypernucleus and the daughter nucleus, the spins of the hypernuclear ground state can be determined using the property of large spin-non-flip weak decay amplitude of Λ [Over67]. Historically, the spins of the ground states of ${}^3_{\Lambda}H$, ${}^4_{\Lambda}H$ and ${}^4_{\Lambda}He$ etc. have been determined with the bubble chamber and the emulsion experiments [Dali59, Bert70]. Recently, other spin assignments of ${}^7_{\Lambda}Li$, ${}^{11}_{\Lambda}B$, and ${}^{15}_{\Lambda}N$ were confirmed by FINUDA collaboration [Agne09]. They successfully assigned the spins from the amplitude of the monochromatic momentum peak from mesonic weak decay π^- s with comparing the theoretical predictions [Moto94, Gal09]. Because the decay pion spectroscopy can measure the monochromatic π^- peaks with much higher resolution, spin assignments of hypernuclei might be performed using similar analysis.

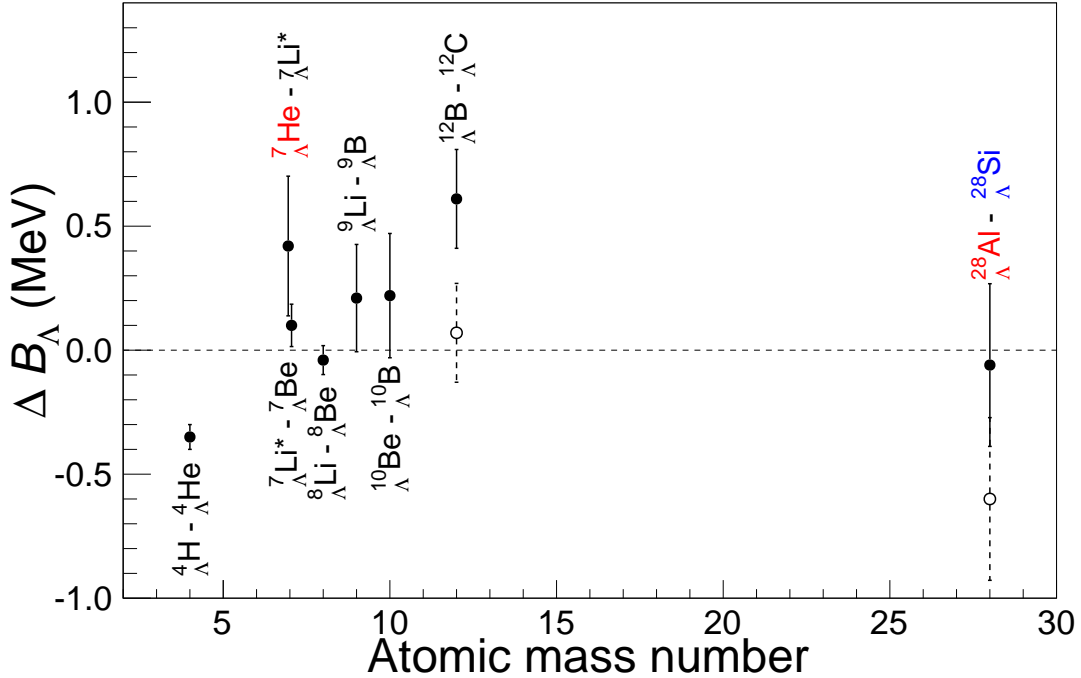


Figure 1.11: Λ binding energy differences for iso-multiplet hypernuclei as a function of the hypernuclear atomic mass number. Hypernuclear species for each data point is also shown. Hypernuclei in red texts (${}^7_{\Lambda}\text{He}$ and ${}^{28}_{\Lambda}\text{Al}$) are reported by the $(e, e'K^+)$ reaction spectroscopy [Naka13, Naka15]. A hypernucleus in a blue text (${}^{28}_{\Lambda}\text{Si}$) is given by the (π^-, K^+) reaction spectroscopy [Hase96], in which the Λ binding energy is calibrated with the result of ${}^{12}_{\Lambda}\text{C}$ in emulsion experiment. A binding energy for ${}^7_{\Lambda}\text{Li}$ is used for T=1 state which is measured with γ -ray spectroscopy [Tamu00]. Other data points are reported by the emulsion experiments [Juri73, Dulz88]. Statistic and systematic errors are given only for the $(e, e'K^+)$ reaction spectroscopy data, and only statistic errors for the other data points. Data of empty circles are after corrections of a -0.54 MeV binding energy shift for ${}^{12}_{\Lambda}\text{C}$ in the emulsion experiment, which suggested by Gogami [GogaD]. A large ΔB_{Λ}^A shift is clearly observed only in A=4 system.

1.4 Goals of present thesis

The goals in this thesis are to establish this new experimental technique and to determine the Λ binding energy for the hypernucleus ${}^4_{\Lambda}\text{H}$. In Chapter 2, the motivation of this paper and details of the design for the new spectroscopy method will be explained. On the basis of the design, we developed the experiments. After apparatuses and experimental setup in the experiments will

be given in Chapter 3, results of a feasibility experiment in 2011 will be shown in Chapter 4, A physics run was performed in 2012 after finishing the data analysis for the feasibility experiment. Details of the analysis in the physics run, for example, particle identifications, detector conditions, and spectrometer calibrations *etc.* will be described in Chapter 5. After that, the analysis and spectrometer calibration will be shown in Chapter 5. Finally, we will discuss the results of the first hypernuclear decay pion spectroscopy and the future prospects.

Chapter.2

Principle and Design

In this chapter, motivation and principle of the new experimental method, the hypernuclear decay pion spectroscopy, will be explained. This experiment was newly designed to determine absolute Λ binding energies of ground states of hypernuclei with an accuracy of ~ 100 keV, that was highest accuracy in the hypernuclear spectroscopic method. To design the experiment, we estimated a hypernuclear yield, peak resolution, and backgrounds. The principle of the experiment and details of the design will be shown in this chapter.

2.1 Motivation

The motivations of the experiment can be summarized as follows.

1. Establishment of the new spectroscopic technique.
2. High mass resolution spectroscopy for light hypernuclei.
3. Investigation of nuclear fragmentation processes.

Each motivation will be explain its details as bellow.

2.1.1 Establishment of the new spectroscopic technique

So far, measurements of momenta of hypernuclear decay pions have been performed using K^- beam [Tamu89a, Outa98, Agne12a]. Hypernuclear studies such as formation probabilities of hypernuclei and decay width of weak decay were reported, however, accurate measurements of absolute Λ binding energies of hypernuclei have not been performed because energy resolution was limited due to a large energy struggling effect in thick targets (\sim a few g/cm²) and momentum resolution of spectrometers ($\Delta p/p \sim 10^{-2}$).

Nowadays, thanks to the construction of the new generation electron beam accelerators such as CEBAF (JLab) and MAMI-C (Mainz), which are able to provide for high energy (>GeV) and

high intense ($>10 \mu\text{A}$) electron beams, it becomes possible to get enough hypernuclear yield to perform the spectroscopy even in thin targets ($<0.1 \text{ g/cm}^2$). Therefore, hypernuclear missing mass spectroscopy using electron beam, namely $(e, e' K^+)$ reaction spectroscopy [Miyo03], succeeded to measure the Λ binding energies of hypernuclei with an energy resolution of better than 1 MeV, that improves the resolution of the spectroscopies using meson beams [Hotc01]. Similarly, measurements of Λ binding energies of ground states of hypernuclei with high resolution and high accuracy can be expected with hypernuclear decay pion measurements using high intense electron beam and thin targets.

However, measurements of decay pions from electro-produced hypernuclei have not been performed, and high resolution spectroscopy of decay pions was unprecedented experiment, because the hypernuclear electro-production technique itself was newly established in the last decade. Hence, it is important to check the feasibility of the experimental method, and establish the new hypernuclear mass spectroscopic technique.

As a first step, we aimed to observe ${}^4_{\Lambda}\text{H}$; high yield was reported in the results of the past experiments using K^- beams [Tamu89a, KawaD, Outa98].

2.1.2 High mass resolution spectroscopy

The difference of Λ binding energies of iso-doublet hypernuclei in $A=4$ system is $350 \pm 50 \text{ keV}$ from the data measured by the emulsion experiments [Juri73]. The error was only statistical error, and the systematic uncertainty (40 keV) in the emulsion experiments was reported by Davis [Davi05], however, the detailed discussions of the uncertainties were not given. Therefore, new measurements of Λ binding energies with a cutting-edge technique are essential.

When we discuss the CSB effect, it is necessary to measure the Λ binding energy of ${}^4_{\Lambda}\text{H}$ with an accuracy of better than 100 keV. Therefore, we aimed to measure monochromatic pions from ${}^4_{\Lambda}\text{H}$ decays with an energy resolution of 100 keV (rms), and determine the Λ binding energy of the ground state with an accuracy of 30 keV in statistics and 100 keV including systematic uncertainties. This energy resolution is several times better than the existing techniques to measure the Λ binding energy of the ground state of hypernuclei, and the accuracies are comparable uncertainties to the errors in the emulsion experiments. It can be improved in future when the uncertainty of the electron beam energy, which dominates the systematic uncertainty, is reduced.

2.1.3 Investigation of the nuclear fragmentation process

Some of produced hypernuclei are broken up and become fragments. Target mass number dependence of the formation probability for ${}^4_{\Lambda}\text{H}$ was measured in (K_{stop}^-, π^-) reaction, and some theoretical discussion was performed [Tamu89b, KawaD, Nara95]. On the other hand, investigations under higher momentum transfer and different production process such as (γ, K^+) and (π^+, K^+) reaction have not been performed. The measurements of hypernuclear formation probability in different conditions lead to clarify fragmentation process, moreover, there could be a possibility to apply the theoretical framework established in hypernuclear studies to calculations of fragmentation process in non-strangeness nuclei. In addition, since the formation probability depends on how a Λ easily sticks to a nucleon, the strength of the interaction between a Λ and a nucleon is expected to be obtained from the measured formation probabilities. As a first step, we aimed to check the feasibility whether the formation probability is able to be measured or not.

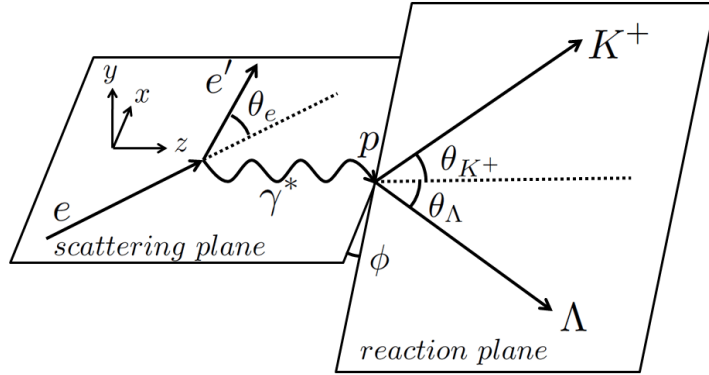


Figure 2.1: A schematic drawing of the hyperon electro-photo production.

2.2 Experimental principle

2.2.1 Kinematics of the hypernuclear electro-photo production

Figure 2.1 shows a schematic drawing of the elementary process for the electro-photo production of Λ particle. The kinematics of this reaction is written by the following,

$$e(p_e) + p(p_p) \rightarrow e'(p_{e'}) + K^+(p_K) + \Lambda(p_\Lambda), \quad (2.1)$$

where the descriptions in the parentheses are four-momenta of each particle ($p_e = (E_e, \vec{p}_e)$). An incoming electron is scattered by a proton with exchanging a virtual photon γ^* . The four-momentum of the virtual photon $q = (\omega, \vec{q})$ is defined by the difference between the incoming electron and the scattered electron. From the definition of the $Q^2 = -q^\mu q_\mu$, the four-momentum transfer can be described as follows,

$$Q^2 = 2(E_e E_{e'} - M_e^2 - |\vec{p}_e| |\vec{p}_{e'}| \cos \theta_e), \quad (2.2)$$

where θ_e is a scattered angle of the electron.

The differential cross section of the $p(e, e' K^+) \Lambda$ reaction is expressed with a flux of the virtual photons (Γ_γ) and the cross section of the K^+ virtual photo-production as follows [Noza90],

$$\frac{d^3\sigma}{dE_{e'} d\Omega_{e'} d\Omega_K} = \Gamma_\gamma \frac{d\sigma_\gamma}{d\Omega_K}. \quad (2.3)$$

The cross section of the K^+ virtual photo-production is described with,

$$\frac{d\sigma_\gamma}{d\Omega_K} = \Gamma_\gamma \left(\frac{d\sigma_T}{d\Omega_K} + \varepsilon_L \frac{d\sigma_L}{d\Omega_K} + \sqrt{2\varepsilon_L(1+\varepsilon)} \frac{d\sigma_{LT}}{d\Omega_K} \cos \phi + \varepsilon \frac{d\sigma_{TT}}{d\Omega_K} \cos 2\phi \right), \quad (2.4)$$

where subscripts T , L , LT , and TT is denoted by transverse, longitudinal, interference, and polarized transverse cross sections, respectively. With taking a mass of an electron into account, the virtual photon polarization ε and ε_L are given as follows [Soto00],

$$\varepsilon = \frac{2\vec{p}_e^2 \vec{p}_e'^2 \sin^2 \theta_e}{Q^2 \vec{q}^2 + 2\vec{p}_e^2 \vec{p}_e'^2 \sin^2 \theta_e}, \quad (2.5)$$

$$\varepsilon_L = \frac{Q^2}{\omega^2} \varepsilon. \quad (2.6)$$

For the limit of $Q^2 \rightarrow 0$, only the transverse term is remained.

The flux of the virtual photon per scattered electron is described with,

$$\Gamma_\gamma = \frac{\alpha}{2\pi^2 Q^2} \frac{E'_e}{E_e} \frac{k_\gamma}{1 - \varepsilon}, \quad (2.7)$$

where k_γ is an equivalent real photon momentum given by,

$$k_\gamma = \frac{s - M_p^2}{2M_p} = \omega - \frac{Q^2}{2M_p}. \quad (2.8)$$

The virtual photon flux is concentrated at very forward angles. In this situation, the virtual photon is almost real photon because the Q^2 is almost zero. The differential cross section of the $p(\gamma, K^+) \Lambda$ reaction is well understood as already shown in Figure 1.8. Therefore, we can apply the photo production cross section to the K^+ electro-photo production cross section. Because the K^+ production cross section is maximized at forward angles, the K^+ yield is also maximized at forward angles with respect to the incoming electron.

2.2.2 Principle of hypernuclear decay pion spectroscopy

■ Determination of Λ binding energies

A schematic drawing of this experiment's principle is shown in Figure 2.2. In this experiment, the masses of hypernuclei are deduced by measuring a monochromatic momentum of pions from two-body decays of hypernuclei stopped in the target as follows,

$$M_{HYP} = \sqrt{M_{nucl}^2 + p_{\pi^-}^2} + \sqrt{M_{\pi^-}^2 + p_{\pi^-}^2}, \quad (2.9)$$

where M_{HYP} is a mass of hypernucleus. M_{nucl} and M_{π^-} are a mass of daughter nucleus and a mass of π^- , respectively, which are well known quantities. For example, the mass of ${}^4_{\Lambda}\text{He}$ and π^- , which are daughter particles of mesonic weak decay in ${}^4_{\Lambda}\text{H}$, are determined with an accuracy

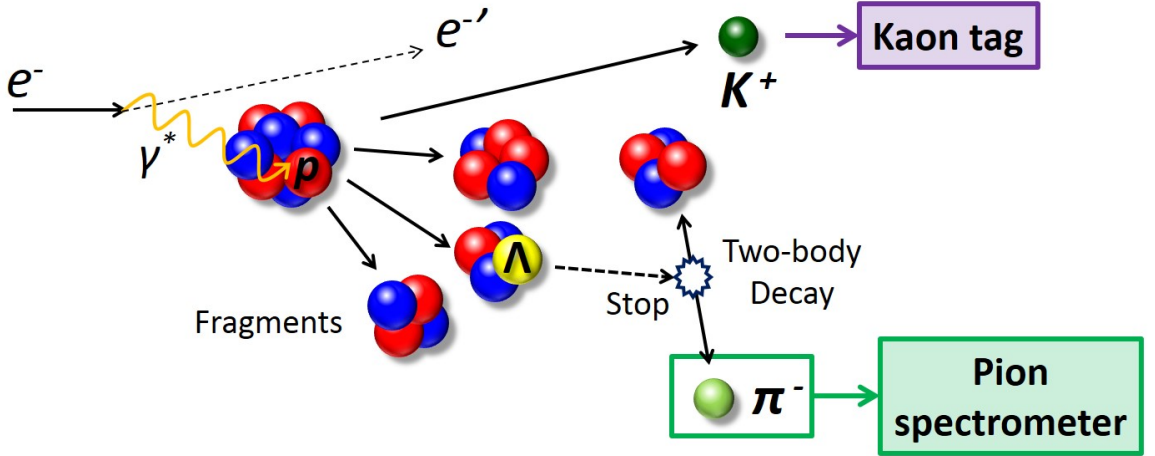


Figure 2.2: A schematic drawing of the hypernuclear decay pion spectroscopy. Hypernuclei or hyperfragments are produced using electron beams via virtual photons. Absolute Λ binding energies of ground states of hypernuclei are deduced by measured momenta of π^- emitted from two-body decays of hypernuclei stopped in the target. K^+ is tagged to suppress backgrounds from non-strangeness production.

of 0.06 eV [Audi03] and 0.35 keV [PDG12], respectively. The momentum of decay pion that we measure is represented as p_{π^-} .

The Λ binding energy of a hypernucleus (B_Λ) can be obtained as;

$$-B_\Lambda = M_{HYP} - (M_{core} + M_\Lambda), \quad (2.10)$$

where M_{core} is a mass of a core nucleus and M_Λ is a mass of Λ . Since these masses are also well known, for example a mass of ${}^3\text{H}$ (core nucleus of ${}^4\text{H}$) is determined with 2808.9210045(23) MeV [Audi03], the Λ binding energy is able to be deduced only by measuring the momentum of hypernuclear decay pion.

In the $(e, e' K^+)$ missing mass spectroscopy, momenta of scattered electrons ($\sim 1 \text{ GeV}/c$) and those of K^+ s ($\sim 1 \text{ GeV}/c$) are measured in two spectrometers with a relative momentum resolution of $\Delta p/p \sim 10^{-4}$. Therefore, the energy resolution of the experiment are limited by the momentum resolution of each particle ($\sim 100 \text{ keV}/c$). On the other hand, in the hypernuclear decay pion spectroscopy, the binding energies of hypernuclei are able to measure with a energy resolution of $\sim 10 \text{ keV}$ because momenta of decay pions ($\sim 100 \text{ MeV}/c$) is ten times smaller, and thus, better absolute momentum resolution can be obtained with the same relative momentum resolution of $\Delta p/p \sim 10^{-4}$. As a result, best mass spectroscopy for the ground state energies of light Λ hypernuclei is possible by this method.

■ Detectable hypernuclei

Hypernuclei are produced using the $p(\gamma, K^+)\Lambda$ reaction from the electron beams. In this method, observable hypernuclei are not only a directly produced hypernucleus (${}^A_\Lambda(Z-1)$) from a target (A_Z) but also hyperfragments; they are fragmented hypernuclei produced with breakups of the nucleus due to recoil momentum transfer in the reaction.

Figure 2.3 shows the hypernuclei which are accessible by the direct or the fragmentation processes from ${}^7\text{Li}$, ${}^9\text{Be}$, and ${}^{12}\text{C}$ targets. These targets have high natural abundance and they are easy to handle because they are solid at the room temperature.

In this spectroscopic method, it is possible to measure the Λ binding energies for light hypernuclei which emit two particles with mesonic weak decay (a π^- and a daughter nucleus). Because the decay mode for medium to heavy hypernuclei is dominated by non-mesonic weak decay, Λ binding energy measurements for these hypernuclei is not suitable. Otherwise, proton rich hypernuclei such as ${}^4_\Lambda\text{He}$ do not decay with two-body decay but decay to more than two-body decay (${}^4_\Lambda\text{He} \rightarrow {}^1\text{H} + {}^3\text{He} + \pi^-$). The hypernuclear decay pion spectroscopy is also not suitable for the Λ binding energy measurements of these proton rich hypernuclei.

Expected momenta of decay pions from two-body decays up to p-shell hypernuclei are listed in Table 2.1. In this experiment, it is difficult to measure the mass of hypernucleus whose daughter nucleus has a short lifetime ($\Gamma_{1/2} < 10^{-21}$ sec), because the decay width cannot be ignored comparing with the spectrometer resolution.

■ Identification of hypernuclei

A species of hypernucleus from observed decay pion peaks are able to estimate with comparing between observed peak momenta and momentum list in Table 2.1. If the monochromatic π^- momentum is isolated such as ${}^4_\Lambda\text{H}$, a species of hypernucleus can be identified uniquely.

On the other hand, if the several decay pion peaks are expected with similar momenta such as ${}^3_\Lambda\text{H}$ ($B_\Lambda = 114.37$ MeV) and ${}^7_\Lambda\text{He}$ ($B_\Lambda = 114.77$ MeV), a kind of hypernucleus can be identified by checking the yield dependence for the different target material. For example, from the ${}^6\text{Li}$ target, ${}^3_\Lambda\text{H}$ is produced, however, ${}^7_\Lambda\text{He}$ is not produced, a kind of hypernucleus is thus able to be identified by changing the target.

■ Inseparable backgrounds

Many π^- s are also produced in non-strangeness production processes. As these π^- s are sources of backgrounds, K^+ s are tagged to identify hyperon production events in a kaon tagger. The kaon tagger is installed at a forward angle with respect to the electron beam direction so that K^+ yield is maximized. The kaon tagger cannot discriminate hypernuclei production from

Table 2.1: A list of expected decay pion momenta. Masses of daughter nuclei were quoted by Reference [Audi03]. Masses of Λ and π^- were obtained from Reference [PDG12]. Λ binding energies were obtained from References [Davi05, Hash06, Cusa09, Naka13]. Half-life ($\Gamma_{1/2}$) and natural width are written for short-lives daughter nuclei in comments. Hypernuclei with blue texts means the Λ binding energy measurements are unrealistic in the hypernuclear decay pion spectroscopy due to too short-lives of their daughter nuclei. Hypernuclei whose cores are not bound (*) or Λ binding energy are not reported (★★) were also added as comments.

Hypernuclei	Decay mode	p_{π^-} (MeV/c)	comments
$^3\Lambda H$	$^3He + \pi^-$	114.37	
$^4\Lambda H$	$^4He + \pi^-$	133.03	
$^4\Lambda He$	$^4Li + \pi^-$	98.17	
$^5\Lambda He$	$^5Li + \pi^-$	99.26	$\Gamma_{1/2} = 3.7 \times 10^{-22}$ s (1.5 MeV)
$^6\Lambda H$	$^6He + \pi^-$	135.27	*
$^6\Lambda He$	$^6Li + \pi^-$	108.48	*
$^6\Lambda Li$	$^6Be + \pi^-$	-	★★
$^7\Lambda He$	$^7Li + \pi^-$	114.77	
$^7\Lambda Li$	$^7Be + \pi^-$	108.11	
$^7\Lambda Be$	$^7C + \pi^-$	95.90	$\Gamma_{1/2} = 3.5 \times 10^{-22}$ s (1.4 MeV) *
$^8\Lambda He$	$^8Li + \pi^-$	116.47	*
$^8\Lambda Li$	$^8Be + \pi^-$	124.20	$\Gamma_{1/2} = 6.7 \times 10^{-17}$ s (6.8 eV)
$^8\Lambda Be$	$^8B + \pi^-$	97.19	
$^9\Lambda Li$	$^9Be + \pi^-$	121.31	
$^9\Lambda Be$	$^9B + \pi^-$	96.98	$\Gamma_{1/2} = 8.0 \times 10^{-19}$ s (0.54 keV)
$^9\Lambda B$	$^9C + \pi^-$	96.82	
$^{10}\Lambda Li$	$^{10}Be + \pi^-$	-	★★
$^{10}\Lambda Be$	$^{10}B + \pi^-$	104.41	
$^{10}\Lambda B$	$^{10}C + \pi^-$	100.49	
$^{11}\Lambda B$	$^{11}C + \pi^-$	86.54	
$^{12}\Lambda B$	$^{12}C + \pi^-$	115.87	
$^{12}\Lambda C$	$^{12}N + \pi^-$	91.48	
$^{13}\Lambda C$	$^{13}N + \pi^-$	92.27	
$^{14}\Lambda C$	$^{14}N + \pi^-$	101.20	
$^{14}\Lambda N$	$^{14}O + \pi^-$	-	★★
$^{15}\Lambda N$	$^{15}O + \pi^-$	98.40	
$^{16}\Lambda N$	$^{16}O + \pi^-$	106.23	
$^{16}\Lambda O$	$^{16}F + \pi^-$	86.54	$\Gamma_{1/2} = 1.1 \times 10^{-20}$ s (40 keV)

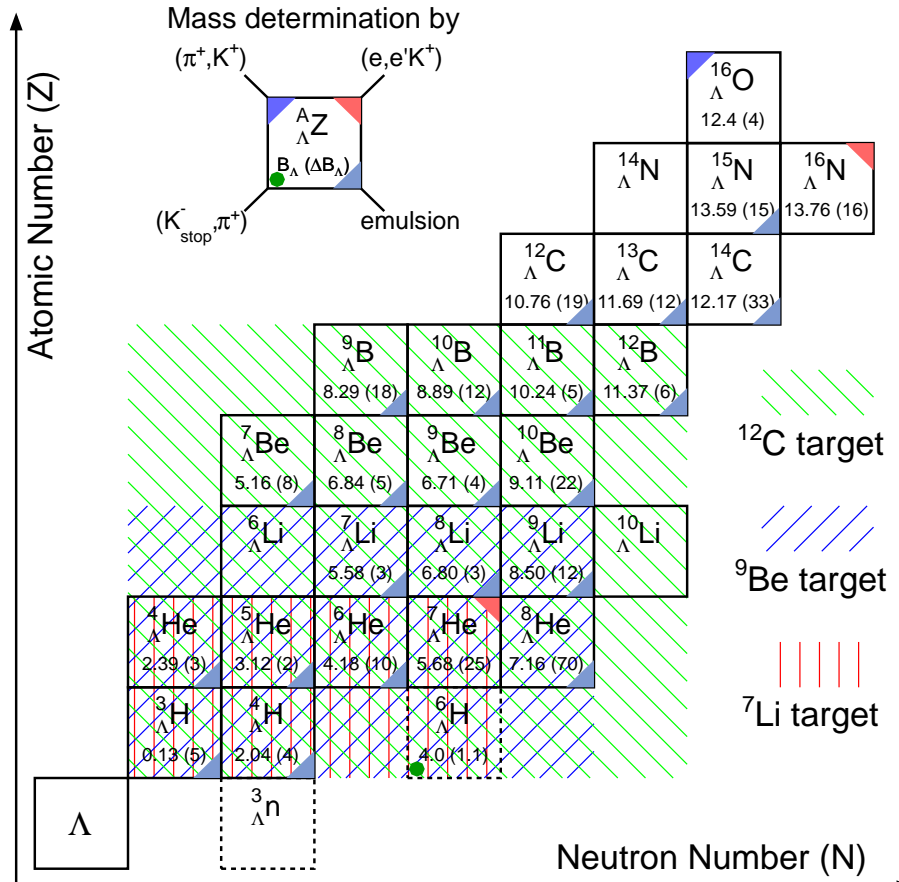


Figure 2.3: Hypernuclear regions covered on the nuclear chart for ^7Li , ^9Be , and ^{12}C targets. They are shown on the hypernuclear chart (Figure 1.2).

hyperon production. However, we are able to optimized the pion spectrometer's configuration so that the signal-to-noise ratio becomes better, because decay pions from hypernuclear decay distribute spherically uniform because the hypernuclei stop in the target, in contrast, decay pions from hyperon decay are boosted to forward angles with respect to the beam direction. Because produced hyperons are boosted and decayed in flight in the laboratory frame. Therefore, the signal-to-noise ratio could be expected to be better at large opening angles with respect to the beam. Details will be explained at experimental designs in Section 2.3.4.

Table 2.2: A list of possible targets. Solid targets that have high natural abundance were listed. The characteristics of materials were obtained from Goodfellow (<http://www.goodfellow.com/>). Though sublimation point of boron nitride is around 2700°C, the highest temperature for the safe continuous use temperature was shown (*).

material	density (g/cm ³)	melting point (°C)	natural abundance (%)	comment
⁷ Li	0.534	180.5	92.5	
⁹ Be	1.848	1278	100	
¹¹ B	2.34-2.37	2180	80.2	
¹² C	2.25	3650	98.89	
B+ ¹⁴ N	1.9-2.2	950-2500*	99.634	boron nitride

2.3 Design

We estimated expected ${}^4_{\Lambda}\text{H}$ yield, momentum resolution of decay pions from hypernuclear decay, and amount of assumed backgrounds to design the experiment. Especially, the optimization of the target thickness is quite important because the momentum resolution of decay pions becomes worse with thicker target, however a rate of the unstopped hypernuclei in the target becomes larger for thinner target. We optimized the target thickness to have the best accuracy of the ${}^4_{\Lambda}\text{H}$ mass. The configuration of the pion spectrometer is also important to obtain data with good signal-to-noise ratio. The details of the estimation for the experimental design will be explained in this section.

2.3.1 target material

Table 2.2 lists possible targets. The identifications of hypernuclei might be difficult for targets with higher mass numbers because there are many candidates of hyperfragments. In addition, since less ${}^4_{\Lambda}\text{H}$ formation probabilities were reported in the higher mass number targets [Tamu89a], ¹²C target might not be the best target to check the proof of the principle.

Higher formation probability was reported for ⁷Li target. However, since lithium rapidly transforms to lithium compounds such as lithium hydroxide and lithium nitride in moist air, ⁷Li target is not very easy to handle. Moreover, a target cooling system is necessary because the

melting temperature is quite low.

As a result, we choose ${}^9\text{Be}$ target in the first experiment.

2.3.2 Yield estimation

The number of Λ hyperons with tagging K^+ mesons (N_Λ) is represented as follows with an assumption that the cross section is in proportion to surface area of a target nucleus ($\propto A^{2/3}$) because the reaction occur at the surface of the nucleus:

$$N_\Lambda = N_{\gamma^*} N_t \frac{d\sigma_\Lambda}{d\Omega} A^{2/3} \Delta\Omega_{K^+} \varepsilon_{K^+}^{\text{decay}} \varepsilon_{K^+}^{\text{det}}, \quad (2.11)$$

where

- N_{γ^*} : number of virtual photons,
- N_t : number of atoms in production target,
- $\frac{d\sigma_\Lambda}{d\Omega}$: differential cross section of $(\gamma^* + \text{p} \rightarrow K^+ + \Lambda)$,
- A : target mass number,
- $\Delta\Omega_{K^+}$: solid angle of K^+ tagger,
- $\varepsilon_{K^+}^{\text{decay}}$: survival ratio of K^+ ,
- $\varepsilon_{K^+}^{\text{det}}$: detection efficiency of K^+ .

The number of virtual photons is obtained as follows with the virtual photon flux shown in Equation 2.7:

$$N_{\gamma^*} = N_e \Gamma_\gamma^{\text{int}}, \quad (2.12)$$

where N_e is the number of introduced electrons, an integrated virtual photon flux ($\Gamma_\gamma^{\text{int}}$) is a virtual photon flux integrated for scattered electrons with a solid angle and an energy above Λ production threshold ($E_{th} = 0.911\text{GeV}$) written as;

$$\Gamma_\gamma^{\text{int}} = \int_0^{4\pi} d\Omega \int_{E_{th}}^{E_{\max}} d\omega \Gamma_\gamma(\theta, \omega). \quad (2.13)$$

An expected yield of ${}^4\text{H}$ in this experimental method is obtained using $\Gamma_\gamma^{\text{int}}$ as,

$$N_{HYP} = N_\Lambda R_{F.P} R_{stop} \frac{\Gamma({}^4\text{H} + \pi^-)}{\Gamma_{all}} \Delta\Omega_{\pi^-} \varepsilon_{\pi^-}^{\text{decay}} \varepsilon_{\pi^-}^{\text{det}}, \quad (2.14)$$

where

$$\begin{aligned}
R_{F,P} &: \text{formation probability of } {}^4_{\Lambda}\text{H from } \Lambda, \\
R_{stop} &: \text{stopping probability of } {}^4_{\Lambda}\text{H in target}, \\
\frac{\Gamma({}^4_{\Lambda}\text{H} + \pi^-)}{\Gamma_{all}} &: \text{branching ratio of } {}^4_{\Lambda}\text{H} \rightarrow \pi^- + {}^4\text{He}, \\
\Delta\Omega_{\pi^-} &: \text{solid angle of } \pi^- \text{ spectrometer}, \\
\varepsilon_{\pi^-}^{decay} &: \text{survival ratio of } \pi^-, \\
\varepsilon_{\pi^-}^{det} &: \text{detection efficiency of } \pi^-.
\end{aligned}$$

In these quantities, the differential cross section of the elementary process ($\gamma + p \rightarrow K^+ + \Lambda$) had been measured in several experiments using real photons [Glan04, McCr10]. The differential cross section is reported also in many theoretical prediction such as isobar models [Mart99, KMaid, Mizu98] and regge-plus-resonance models [Cort06, Cruz12]. The emission ratio ($\Gamma(N + \pi^-)/\Gamma_{all}$) is able to be given from measured variables [Bloc64, Bert70, Outa98] as follows:

$$\begin{aligned}
\frac{\Gamma({}^4_{\Lambda}\text{H} + \pi^-)}{\Gamma_{all}} &= \frac{\Gamma({}^4_{\Lambda}\text{H} + \pi^-)}{\Gamma_{\Lambda}} \times \frac{1}{\Gamma_{all}/\Gamma_{\Lambda}} \\
&= 0.69^{+0.12}_{-0.10} / 1.36^{+0.21}_{-0.15} = 0.51^{+0.10}_{-0.11},
\end{aligned} \tag{2.15}$$

or

$$\begin{aligned}
\frac{\Gamma({}^4_{\Lambda}\text{H} + \pi^-)}{\Gamma_{all}} &= \frac{\Gamma({}^4_{\Lambda}\text{H} + \pi^-)}{\Gamma_{\pi^-}} \times \frac{1}{(\Gamma_{\pi^-} + \Gamma_{\pi^0} + \Gamma_{nm})/\Gamma_{\pi^-}} \\
&= \frac{0.69 \pm 0.02}{1 + 0.1 + (0.26 \pm 0.13)} = 0.51 \pm 0.05,
\end{aligned} \tag{2.16}$$

where Γ is the weak decay width:

$$\begin{aligned}
\Gamma_{\pi^-} &: \text{mesonic weak decay width of } {}^4_{\Lambda}\text{H} \rightarrow X + \pi^-, \\
\Gamma_{\pi^0} &: \text{mesonic weak decay width of } {}^4_{\Lambda}\text{H} \rightarrow X + \pi^0, \\
\Gamma_{nm} &: \text{non-mesonic weak decay width of } {}^4_{\Lambda}\text{H}, \\
\Gamma_{\Lambda} &: \text{weak decay width of } \Lambda.
\end{aligned}$$

The formation probability of ${}^4_{\Lambda}\text{H}$ was assumed to be the same probability as the result of (K_{stop}^-, π^-) reaction [Tamu89a]. We estimated solid angles of spectrometers, survival ratios, and detection efficiencies based on the existing spectrometers at MAMI or JLab. Therefore, we newly estimated the stopping probability of ${}^4_{\Lambda}\text{H}$ as shown in bellow.

Estimation of ${}^4_{\Lambda}\text{H}$ stopping probability

The stopping probability of ${}^4_{\Lambda}\text{H}$ depends on the target thickness and the momentum of ${}^4_{\Lambda}\text{H}$. We estimated the momentum distribution of ${}^4_{\Lambda}\text{H}$ using a Monte Carlo method, and deduced dependences of the target thickness on the stopping probabilities using GEANT4, which is a toolkit for the Monte Carlo simulation with the realistic physics processes distributed by CERN [Agos03, G4].

■ Momentum distribution of ${}^4_{\Lambda}\text{H}$

At first, a procedure to obtain the momentum distribution of ${}^4_{\Lambda}\text{H}$ will be shown as follows with a conceptual drawing (Figure 2.4).

Step1. Random generations of virtual photon and proton.

A distribution of the virtual photons was given as Equation 2.7, while angles of scattering electrons were limited ($0\sim 5^\circ$) to save computer power. A Fermi momentum distribution of protons in a ${}^9\text{Be}$ nucleus was estimated based on the quasi-elastic scattering data in ${}^{12}\text{C}$ target [Bode81] with a scaling factor calculated by the Fermi momentum of each nucleus ($k_F^{\text{Be}}/k_F^{\text{C}} = 200 \text{ (MeV}/c) / 229 \text{ (MeV}/c)$). The energy distribution of the virtual photons and the momentum distribution of the protons are shown in Figure 2.5. Angular distributions of the protons were assumed as spherically uniform. If an invariant energy of the generated event was below a threshold of ($K^+ + \Lambda$) production, a new virtual photon and proton were generated again.

Step2. Lorentz transformation to the center of mass frame for the generated virtual photon and proton.

Step3. Momentum vectors were randomly generated for a produced K^+ .

The angular distribution of K^+ meson was set to reproduce the cross section of the elementary process ($\gamma + p \rightarrow K^+ + \Lambda$) in the isobar model (KMAid) [Mart99]. A 2-dimensional plot of the applied cross section is shown in Figure 2.6. We assumed that the cross section of the ($K^+ + \Lambda$) production from the virtual photon and the proton in the ${}^9\text{Be}$ target have the same cross section of the elementary process for the same invariant energies.

Step4. Calculation of a momentum vector for Λ to conserve the momentum and the energy.

Step5. Lorentz transformation of K^+ and Λ to the laboratory frame.

Step6. Tagging K^+ in a Kaon tagger.

An acceptance table of the Kaos spectrometer at MAMI was used for the kaon tagger.

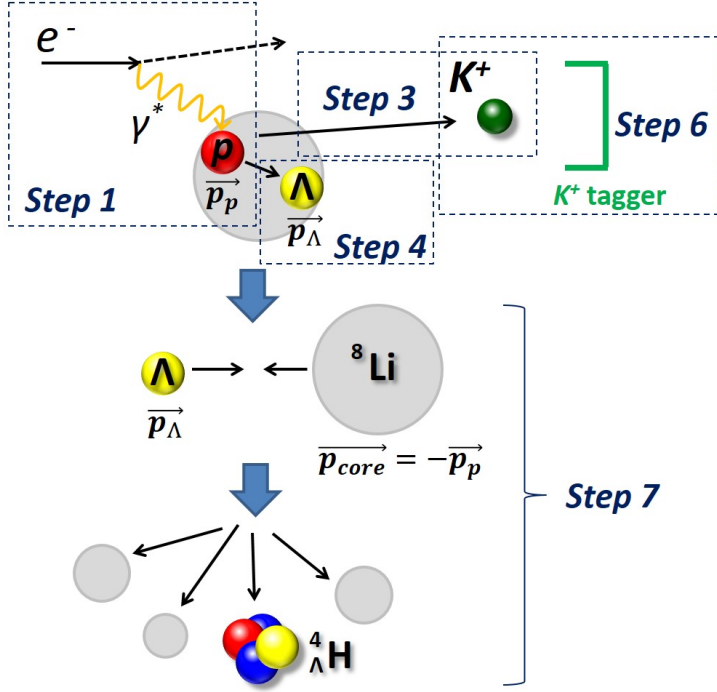


Figure 2.4: A conceptual drawing of a procedure for ${}^4_{\Lambda}\text{H}$ momentum estimation.

The characteristics of the Kaos spectrometer will be described in Section 3. If a K^+ was not detected in the kaon tagger, back to the Step1.

Step7. Producing ${}^4_{\Lambda}\text{H}$ via the reaction of Λ and core nucleus (${}^8\text{Li}$). The momentum of the Λ calculated in Step5 was used. The momentum of the core nucleus was set to the momentum vector for reacted proton with the opposite direction. A decayed channel was assumed as $(\Lambda + {}^8\text{Li} \rightarrow {}^4_{\Lambda}\text{H} + {}^2\text{H} + {}^2\text{H} + n)$. If an invariant energy of $\Lambda + {}^8\text{Li}$ was below a threshold of the decayed channel, back to the Step1.

Step8. Output momentum vector of ${}^4_{\Lambda}\text{H}$.

In this procedure, the momentum and angular distribution of Λ particle can be realistically estimated well because the initial condition (the virtual photon distribution and the Fermi motion) and K^+ formation distribution were confirmed experimentally. On the other hand, because the assumptions in Step7 base on a very naive toy model which dose not include the interactions between Λ and nucleons but only assumed the phase space, the distribution of ${}^4_{\Lambda}\text{H}$ has large uncertainties. If the theoretical calculation including interactions like the AMD calculation is performed, more reliable estimations can be obtained quantitatively.

An expected momentum distribution of ${}^4_{\Lambda}\text{H}$ obtained through the above steps is shown in

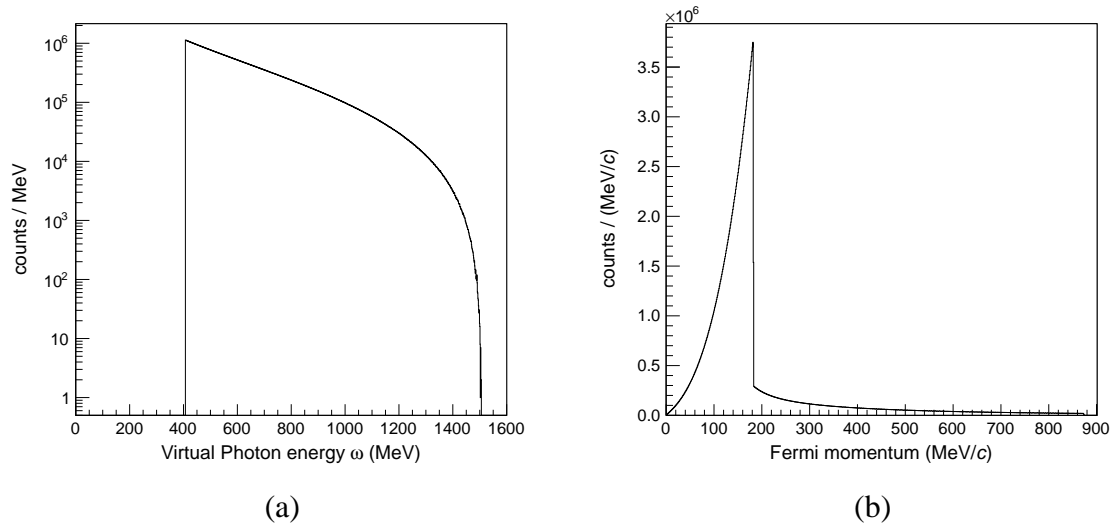


Figure 2.5: (a) An initial energy distribution of virtual photons and (b) a Fermi momentum distribution of protons in ${}^9\text{Be}$ target.

Figure 2.7. It was found that the distribution has a peak around $200 \text{ MeV}/c$, which corresponds to $\sim 5 \text{ MeV}$ with the kinetic energy, and concentrates in forward angles.

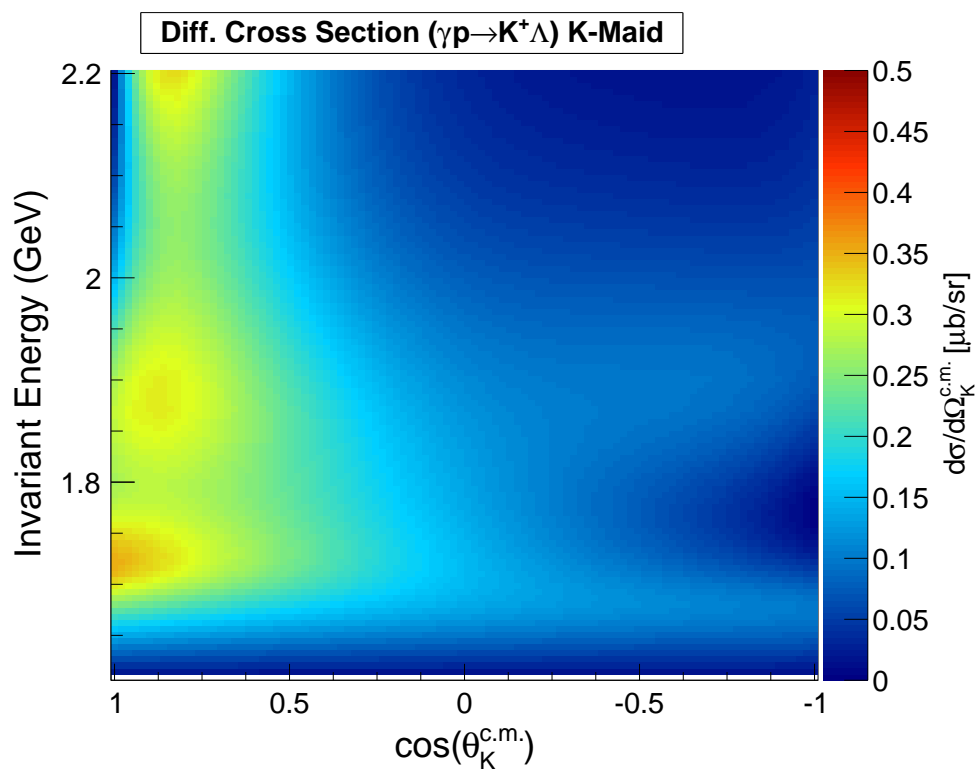


Figure 2.6: A differential cross section distribution of $(\gamma + p \rightarrow K^+ + \Lambda)$ reaction calculated by the isobar model (K-Maid [Mart99]). The cross section and the angle were on center of mass frame.

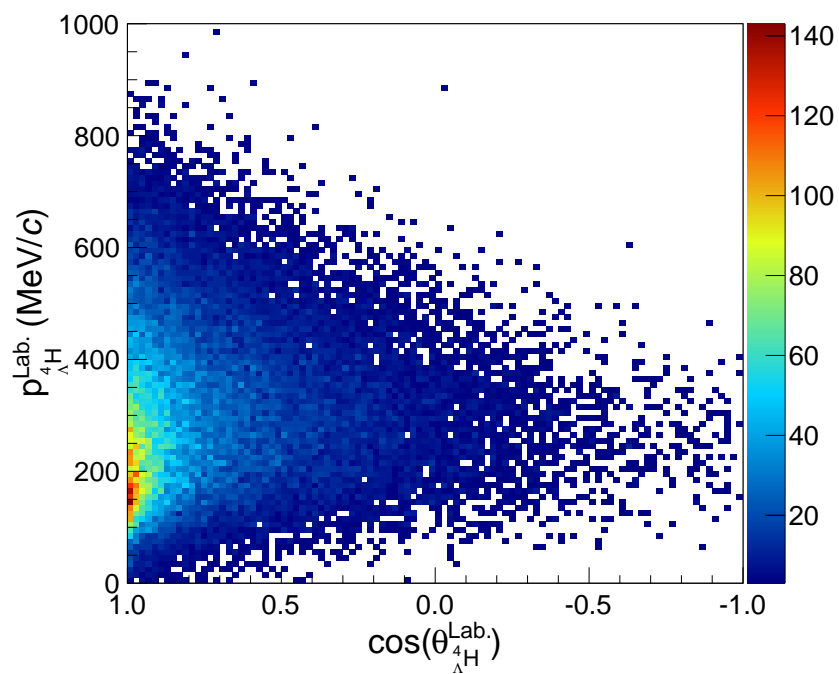


Figure 2.7: A simulated momentum distribution of ${}^4\Lambda\text{H}$ as a function of angles in the laboratory frame.

Stopping range estimation

We estimated the stopping probability of ${}^4_{\Lambda}\text{H}$ from the obtained momentum distribution using GEANT4. Before performing the GEANT4 simulation, we tuned physics processes in the code, because default GEANT4 physics processes (Bethe-Bloch formula [see Section 2.3.3]) are not able to handle energy loss of ions in absorbers in low kinetic energy region well.

In the low energy region, the ions capture electrons from absorber atoms and neutralize the charge, and thus, we have to take this effect into consideration. In this thesis, we tuned the physics process so that the energy loss distribution from GEANT4 agrees with that from *Stopping and Range of Ions in Matter* (SRIM) [Bier80, Zieg85, Zieg10]; that is well-established program which calculates interactions of ions in absorbers. Specifically, the stopping range tables of protons [ICRU49] were used for $Z = 1$ ions, and the range tables of ions [ICRU73] were included for $Z \geq 2$ ions in the code. In addition, masses of hypernuclei were revised using the latest Λ binding energies.

Energy loss distributions as a function of kinetic kinetic energies of ${}^4_{\Lambda}\text{H}$ and ${}^4_{\Lambda}\text{He}$ in ${}^9\text{Be}$ target were shown in Figure 2.8 with reference lines from SRIM outputs. Stopping range distributions of ${}^4_{\Lambda}\text{H}$ and ${}^4_{\Lambda}\text{He}$ were also shown in Figure 2.9. The results of GEANT4 were consistent those of SRIM within 10% accuracy for a kinetic energy of >1 MeV.

Figure 2.10 shows stopped time distribution of ${}^4_{\Lambda}\text{H}$ and ${}^4_{\Lambda}\text{He}$ in ${}^9\text{Be}$ target as a function of initial kinetic energies. Since the stopped times of hypernuclei were 1~2 orders of magnitude shorter than the lifetime of hypernuclei (~ 200 ps) at a kinetic energy of ~ 5 MeV, we found that a ratio of hypernuclear in-flight decay in the target is negligibly small, and in-flight decay out of the target due to not enough thickness is dominated.

Finally, we estimated the stopping probability of ${}^4_{\Lambda}\text{H}$ and ${}^4_{\Lambda}\text{He}$ for several target thicknesses. In the simulated code, ${}^9\text{Be}$ target was installed with a tilt angle of 54° with respect to the electron beam, and hypernuclei were generated in the target with the distribution given in Figure 2.7. Electron beam spot size was not taken into account. Expected stopping probabilities as a function of the target thickness was shown in Figure 2.11. The probabilities increase quickly up to ~ 0.1 -mm thick and saturate at the thick target. The stopping probability of ${}^4_{\Lambda}\text{H}$ in 0.1-mm thick ${}^9\text{Be}$ target with a tilted angle of 54° was estimated as $\sim 40\%$.

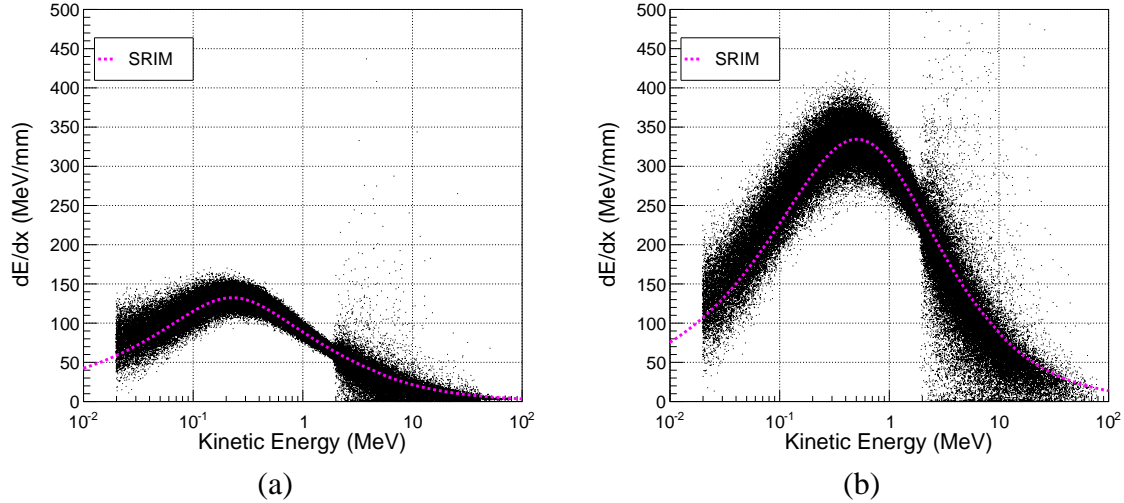


Figure 2.8: Results of calculated energy loss distributions as a function of kinetic energies for (a) ${}^4_{\Lambda}\text{H}$, and (b) ${}^4_{\Lambda}\text{He}$ by GEANT4. Results of SRIM outputs were also plotted as a reference.

Summary of yield estimation

The result of the ${}^4_{\Lambda}\text{H}$ yield estimation is shown in Table 2.3. Conditions of electron beam, kaon tagger, and pion spectrometer were taken from the existing beam lines and spectrometers at MAMI and JLab.

The expected yield of ${}^4_{\Lambda}\text{H}$ at MAMI is 1.5 counts per day at 20 μA . In MAMI, there are the well-established high momentum resolution spectrometers and frequent beam-times. Moreover, the beam-time schedule and experimental settings can be changed flexibly. On the other hand, detectors and a spectrometer for the K^+ tagging are under development.

In JLab, we have performed the hypernuclear spectroscopies using the $(e, e' K^+)$ reaction in several times. From the experiences in these experiments, we already know that the accelerator and detectors are able to be handled at 100 μA . The expected yield at JLab is 1.0 counts per day at 100 μA . There are all tools for the hypernuclear decay pion spectroscopy. However, the beam operation was stopped for the upgrades from 2012, moreover, the beam-time schedule is very crowded even after the upgrades.

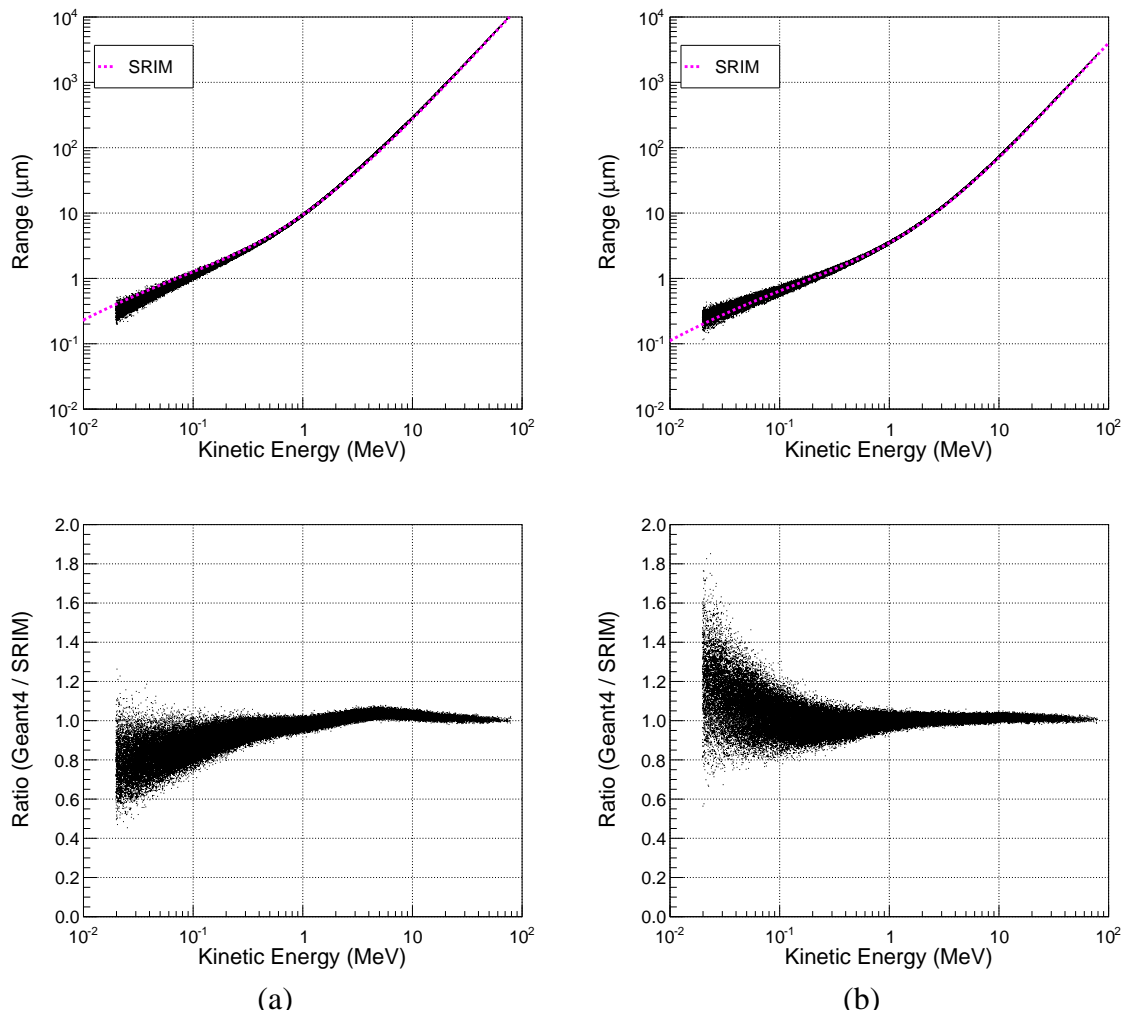


Figure 2.9: Results of stopping range curves for (a) ^4H and (b) ^4He in GEANT4. Results of SRIM outputs were also plotted as a reference. Ratios of GEANT4 results to SRIM outputs were shown below.

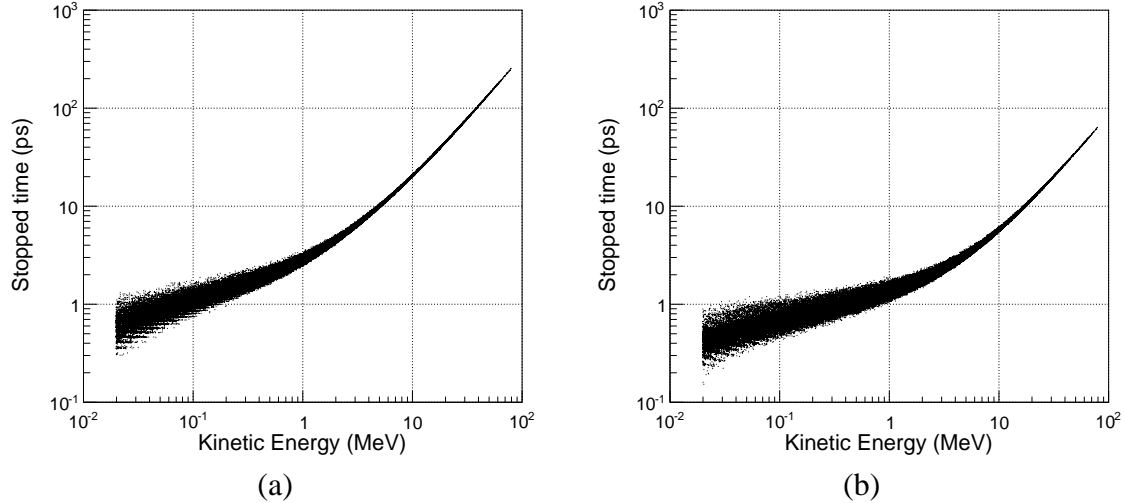


Figure 2.10: Stopped time dependences on kinetic energies of (a) $^4_\Lambda\text{H}$ and (b) $^4_\Lambda\text{He}$ in ^9Be target calculated by GEANT4.

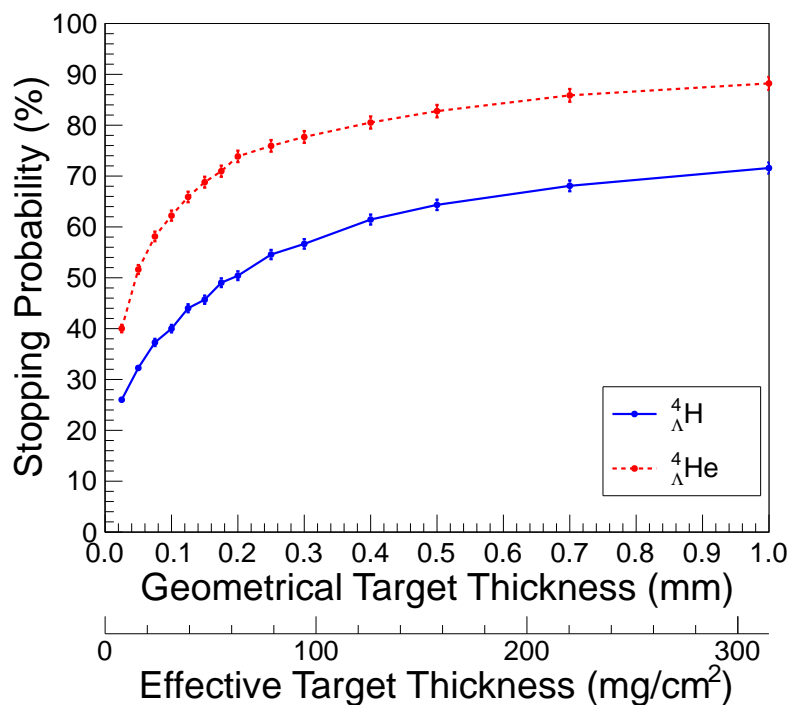


Figure 2.11: Stopping probabilities of $^4_{\Lambda}\text{H}$ and $^4_{\Lambda}\text{He}$ as a function of target thickness. The target was ^{9}Be , and it was tilted 54° with respect to the electron beam. The geometrical target thickness (μm) and the effective target thickness for the beam (mg/cm^2) were shown on the horizontal line.

Table 2.3: A Summary of ${}^4_{\Lambda}\text{H}$ yield estimation with 100- μm thick ${}^9\text{Be}$ target at a tilt angle of 54°. Experimental facilities A1 Hall at MAMI and Hall A at JLab were assumed. Parameters of the Kaos spectrometer and the high-resolution spectrometer SpekC were used for MAMI. Those of the high-resolution kaon spectrometer HKS and an Enge-type split-pole spectrometer were used for JLab.

	MAMI	JLab
electron beam energy	1.5 GeV	3.6 GeV
electron beam current	20 μA	100 μA
integrated virtual photon flux	0.013 /electrons	0.04 /electrons
target thickness		31 mg/cm ²
($\gamma^* + p \rightarrow K^+ + \Lambda$) cross section		0.3 $\mu\text{b}/\text{sr}$
solid angle of K^+ tagger	15 msr	6 msr*
survival ratio of K^+	40 %	18 %*
detection efficiency of K^+		80 %
formation probability of ${}^4_{\Lambda}\text{H}$		1 %
stopping probability of ${}^4_{\Lambda}\text{H}$		40 %
branching ratio of ${}^4_{\Lambda}\text{H} \rightarrow \pi^- + {}^4\text{He}$		51 %
solid angle of π^- spectrometer	28 msr	3.4 msr*
survival ratio of π^-	30 %	56 %*
detection efficiency of π^-		80 %
Yield of ${}^4_{\Lambda}\text{H}$	1.5 counts/day	1.0 counts/day

* parameters in Reference [NagaM] are used.

2.3.3 Resolution

The hypernuclear yield increases with thicker target because the number of targets and the stopping probability increase. However, momentum resolution of measured π^- from hypernuclear decay becomes worse with thicker target due to energy struggling effect in the target. An optimization of the target thickness and expected π^- peak resolution will be shown after explaining details of the energy loss and energy struggling effects in this section.

The energy loss of a charged particle in a absorber is generally obtained with the famous Bethe-Bloch formula [Leo].

The energy loss distribution depends on the ratio (κ) between the mean energy loss ($\bar{\Delta}$) and maximum energy transfer (W_{max}) in a single collision of charged particle with an electron in the absorber:

$$\kappa = \bar{\Delta}/W_{max}. \quad (2.17)$$

$\bar{\Delta}$ is given at non-relativistic region as:

$$\bar{\Delta} \sim \xi = 2\pi N_a r_e^2 m_e c^2 \rho \frac{Z}{A} \frac{z^2}{\beta^2} x, \quad (2.18)$$

with a thickness of absorber x . The parameters are

N_a : Avogadro's number	z : charge of incident particle
r_e : classical electron radius	β : velocity of incident particle
m_e : electron mass	$\gamma = 1/\sqrt{1 + \beta^2}$
ρ : density of absorber	I : mean excitation potential.
Z : atomic number of absorber	A : atomic weight of absorber

If $\kappa > 1$, the distribution approaches to the Gaussian limit. If $\kappa < 1$, the distribution has an asymmetric shape with a long high energy tail. Especially, in case of $\kappa \leq 0.01$, Landau carried out the calculation for the distribution. The distribution is represented as:

$$f(\lambda, \Delta E) = \phi(\lambda)/\xi, \quad (2.19)$$

where

$$\begin{aligned} \phi(\lambda) &= \frac{1}{\pi} \int_0^\infty \exp(-u \ln u - u\lambda) \sin \pi u \, du, \\ \lambda &= \frac{1}{\xi} \left[\Delta E - \xi \left\{ \ln \xi - \left(\ln \frac{(1-\beta^2)I^2}{2m_e c^2 \beta^2} + \beta^2 \right) + 1 - 0.577 \right\} \right], \end{aligned} \quad (2.20)$$

and I is a mean excitation potential.

$\phi(\lambda)$ is so-called Landau distribution. The Landau distribution itself does not have any parameters. The most probable value, which is defined with the λ at $d\phi/d\lambda = 0$, is always given at $\lambda = -0.22278298$ [Kolb84].

The energy loss distribution $f(\lambda, \Delta E)$ has the most probable value at

$$\Delta E_{mp} = \xi \left[\ln \xi - \left(\ln \frac{(1 - \beta^2)I^2}{2m_e c^2 \beta^2} + \beta^2 \right) + 0.198 - \delta \right], \quad (2.21)$$

with a density effect correction term δ :

$$\delta = \begin{cases} 0 & (X < X_0), \\ 4.6052X + C_0 + a(X_1 - X)^m & (X \in [X_0, X_1]), \\ 4.6052X + C_0 & (X > X_1), \end{cases} \quad (2.22)$$

where $X = \log_{10}(\beta\gamma)$. C_0 , a , X_0 , X_1 , and m are parameters depend on the absorbing material. For example, the parameters are $C_0 = 2.785$, $a = 0.804$, $X_0 = 0.059$, $X_1 = 1.692$, and $m = 2.434$ for beryllium [Ster84].

A width of the distribution becomes wider in thicker absorber as shown in Figure 2.12. Because decay pions from hypernuclei are emitted at various depth in a target, the energy deposited distribution is represented with a superposition of Landau distributions in several absorber thicknesses. With a more realistic Monte Carlo simulation, a root mean square (RMS) of the energy loss distribution for π^- ($p = 133$ MeV/c) is estimated as a function of the ${}^9\text{Be}$ target thickness (Figure 2.13). In the simulation, emitted positions of decay pions and the momentum resolution of the pion spectrometer ($\Delta p/p = 10^{-4}$) are introduced. As a result, the RMS is almost proportional to the target thickness, and it is ~ 50 keV/c for a 100- μm thick ${}^9\text{Be}$ target with a tilt angle of 54° to the beam, that is enough resolution to deduce the Λ binding energy with necessary precision.

Expected accuracy of the measured π^- momentum is estimated with

$$\delta = \frac{\sigma}{\sqrt{N}}, \quad (2.23)$$

where σ is a RMS, and N is a yield of a peak. Using the stopping probabilities in Figure 2.11 and the momentum resolution in Figure 2.13, expected momentum accuracies can be estimated (Figure 2.14). Because the stopping probability of hypernuclei becomes small with the too thin target, the momentum accuracy becomes bad. On the other hand, because the momentum resolution of decay pions becomes wide in the thick target, the too thick target also have bad influence for the momentum accuracy. As a result, we design the target thickness with ~ 150 μm so that the accuracy of π^- momentum from ${}^4_\Lambda\text{H}$ becomes best.

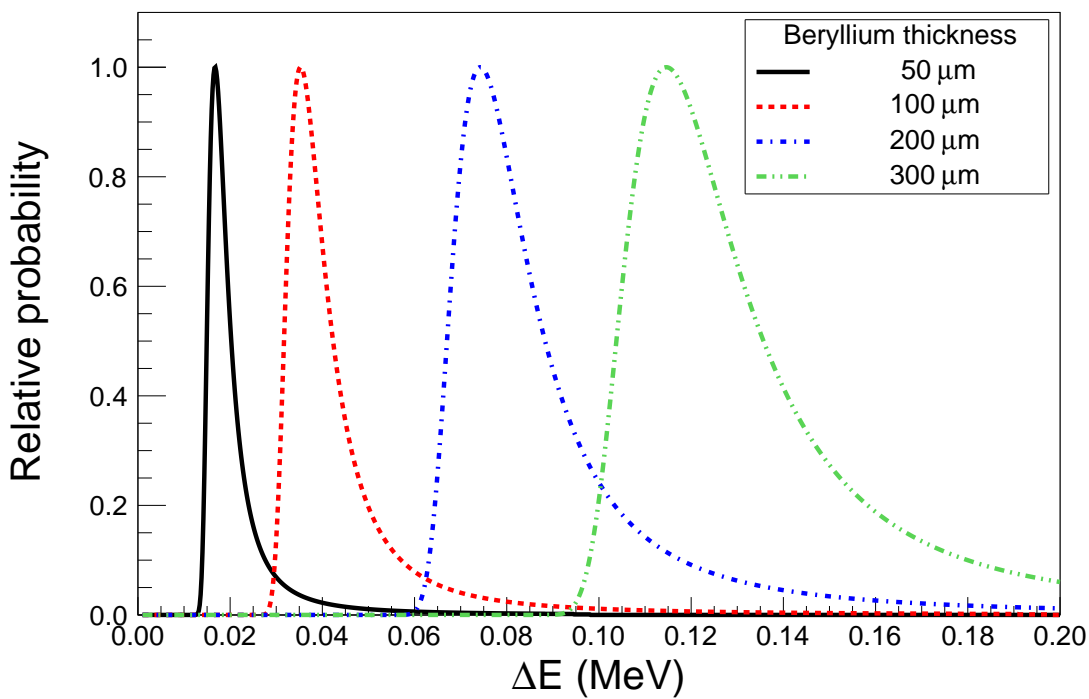


Figure 2.12: Energy loss distributions at several absorber thickness. The distributions were calculated using Equation 2.19 with π^- beams ($p = 133 \text{ MeV}/c$) and ${}^9\text{Be}$ absorbers (50~300- μm thick).

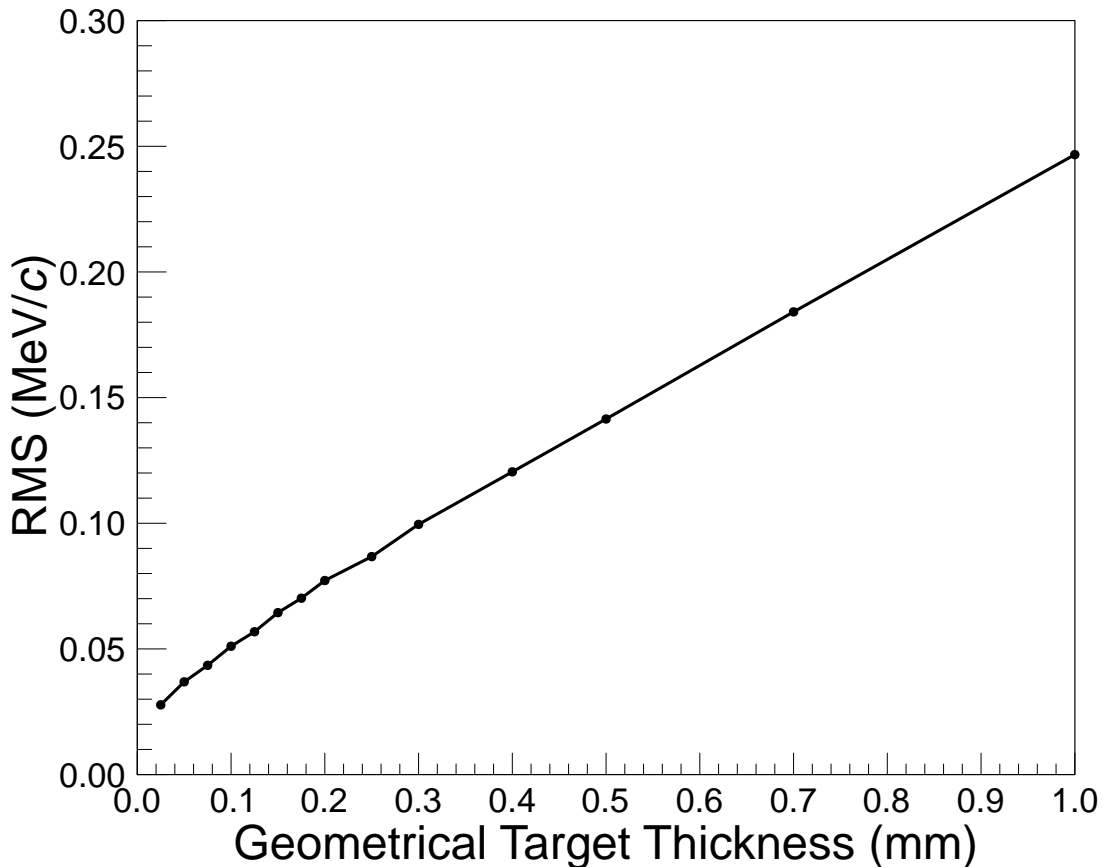


Figure 2.13: Root mean squares of energy loss distributions for π^- s ($p = 133$ MeV/c) as a function of a geometrical ${}^9\text{Be}$ target thickness. The estimated conditions were 54° tilt targets with respect to the electron beam, and a normal direction of the pion spectrometer for the target surface. Uniform position distribution at the target for π^- s and momentum resolution of a pion spectrometer ($\Delta p/p = 10^{-4}$) were assumed.

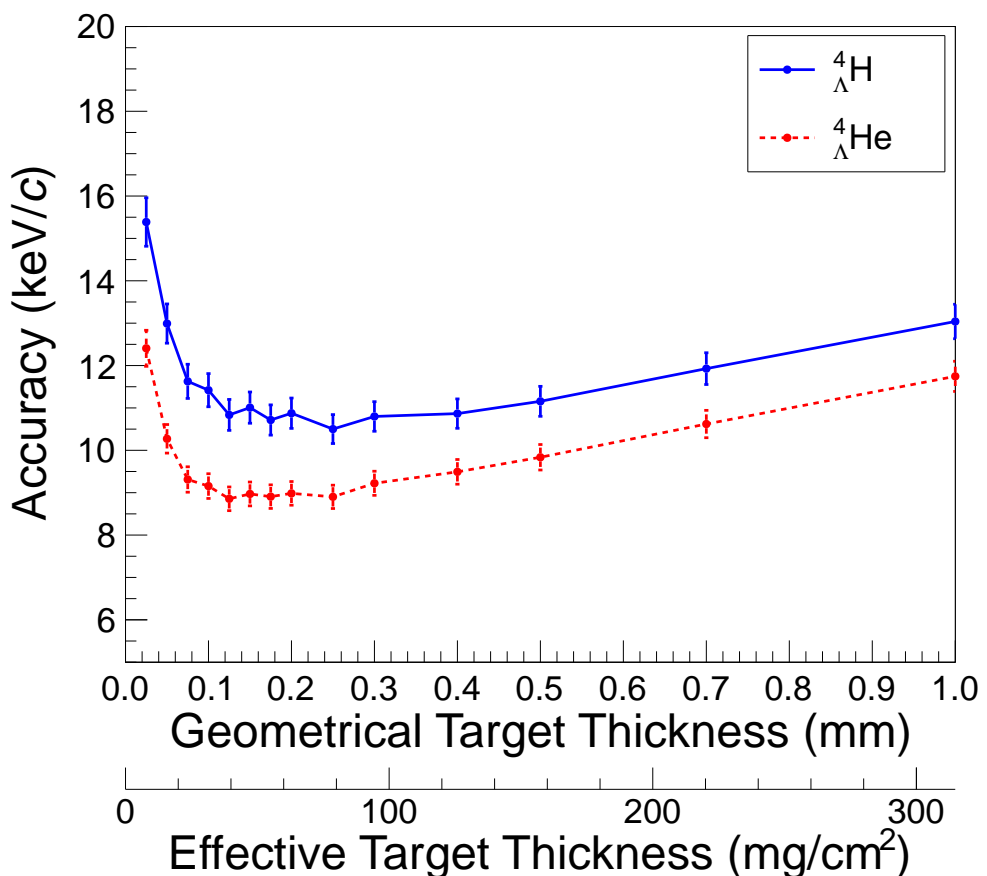


Figure 2.14: An expected accuracy of measured π^- momentum from ${}^4\Lambda H$ decay. The simulated conditions were same as Figure 2.13.

2.3.4 Background

In the hyperon production experiments using electron beam, background rate is generally quite high due to the very high intense electron beam ($> 1 \mu\text{A} \sim 6 \times 10^{12} e^-/\text{s}$). In addition, the cross section of hyperon production using electro-photo production is about three orders of magnitude smaller than that in hadronic production. Therefore, the signal-to-noise ratio is poor. We have to reduce the backgrounds with keeping the hypernuclear yield to take data with a good signal-to-noise ratio. In this section, expected backgrounds and its suppression method will be explained.

Backgrounds in the kaon tagger

In the kaon tagger, positive charged particles from non-strangeness production processes contaminate to backgrounds: namely, e^+ , π^+ and *proton*. The most serious background in the experiment was e^+ , because the kaon tagger was installed at a forward angle.

When high energy electrons introduced in a material, they emit electromagnetic radiations from electric fields of the target nuclei, so call bremsstrahlung. The differential cross section for the solid angle (Ω_k) and the energy (k) of the radiation is represented as [Tsai74]:

$$\begin{aligned} \frac{d^2\sigma_b}{d\Omega_k dk} &= \frac{2\alpha^3 E_e^2}{\pi k m_e^4} \left[b_{b1} (Z^2 + Z) + b_{b2} \{X - 2Z^2 f(\alpha^2 Z^2)\} \right], \\ b_{b1} &= \frac{2y - 2}{(1+l)^2} + \frac{12l(1-y)}{(1+l)^4}, \\ b_{b2} &= \frac{2 - 2y + y^2}{(1+l)^2} - \frac{4l(1-y)}{(1+l)^4}, \end{aligned} \quad (2.24)$$

where

$$\begin{aligned} \alpha &: \text{fine structure constant} \\ E_e &: \text{electron energy} \\ Z &: \text{proton number} \\ m_e &: \text{electron mass} \\ y &= k/E_e, \quad l = E_e^2 \theta_k^2 / m_e^2, \\ X &= Z^2 \left[\ln \frac{a^2 m_e^2 (1+l)^2}{a^2 t'_{min} + 1} - 1 \right] + Z \left[\ln \frac{a'^2 m_e^2 (1+l)^2}{a'^2 t'_{min} + 1} - 1 \right], \\ a &= \frac{111.7}{Z^{1/3} m_e}, \quad a' = \frac{724.2}{Z^{2/3} m_e}, \quad (\text{with } Z \geq 5) \\ t'_{min} &= \left[k m_e^2 (1+l)^2 / 2E_e (E_e - k) \right]^2. \end{aligned} \quad (2.25)$$

The correction term $f(z)$ is represented by [Davi54]:

$$f(z) = z \sum_{n=1}^{\infty} \frac{1}{n(n^2 + z)}. \quad (2.26)$$

The cross section is proportional to Z^2 , and it has the large value in forward angles.

Similarly, the radiations produce e^- and e^+ pairs in the material (pair production). The differential cross section of the pair production is represented by a similar formula to the bremsstrahlung as [Tsai74]:

$$\begin{aligned} \frac{d^2\sigma_p}{d\Omega dp} &= \frac{2\alpha^3 E_e^2}{\pi k m_e^4} \left[b_{p1} (Z^2 + Z) + b_{p2} \{X - 2Z^2 f(\alpha^2 Z^2)\} \right], \\ b_{p1} &= \frac{2x(1-x)}{(1+l)^2} - \frac{12lx(1-x)}{(1+l)^4}, \\ b_{p2} &= \frac{1-2x+2x^2}{(1+l)^2} + \frac{4lx(1-x)}{(1+l)^4}, \end{aligned} \quad (2.27)$$

where

$$x = E_e/k, \quad l = E_e^2 \theta_e^2 / m_e^2. \quad (2.28)$$

The cross section of the pair production also has the large value in forward angles.

The combination of the bremsstrahlung and the pair production produces shower of photons, e^- and e^+ . Since the distribution of the shower concentrate at very forward angles, the kaos tagger which was installed at a forward angle was exposed to the large e^+ backgrounds (>10 MHz).

There are two approaches to suppress the e^+ backgrounds. One is the kaon tagger is set to several degrees off with respect to the electron beam and avoid the very forward angle background such as HKS and HES spectrometers at JLab [Fuji15]. The other is the kaon tagger is installed at a very forward angle with a e^+ background suppressor. We adopted the latter method, and a lead wall was installed as the e^+ suppressor (see Section 3.3.3).

Rates of the other backgrounds, *e.g.* π^+ s and protons, are expected to 100 times higher than that of K^+ s at ~ 1 GeV/c. The K^+ identification methods from these backgrounds have been established in the HKS spectrometer [Fuji15], for example the time-of-flight (TOF) method and the Cherenkov detectors are available. The K^+ identification was also succeeded in the Kaos spectrometer at MAMI in a low momentum region (~ 500 MeV/c)[AcheH]. Therefore, π^+ and proton backgrounds are under control.

Background in π^- spectrometer

Negative charged particles, for example e^- and μ^- , are contaminated as backgrounds. A low background rate (<10 kHz) is expected, because the spectrometer is installed at large angles with respect to the electron beam.

A gas Cherenkov detector is widely used to distinguish π^- s from e^- s. A separation of π^- and μ^- is performed with a range counter and TOF method with a long TOF length (~ 10 m).

However, fundamental data about the background rates and the particle ratios were not known well in the low momentum region (~ 100 MeV/c) using high energy electron beam (> 1 GeV). It was necessary to study the background rates whether the above trigger scheme is feasible or not.

Background from decay pions from hyperon decay

In the experiment, we cannot distinguish hypernuclear production events from hyperon production events. Therefore, quasi-free production events of Λ , Σ^0 and Σ^- are remained on the decay pion spectrum as backgrounds (quasi-free hyperon background). However, we were able to optimize the π^- spectrometer angle so that the quasi-free hyperon background is suppressed with keeping the decay pions from hypernuclei.

The π^- s emitted from two-body decays of hypernuclei stopped in the target have monochromatic momentum and uniform angular distribution. On the other hand, the momenta of π^- s from hyperon decays have angular dependence as follows, because the hyperons are boosted to the beam direction and decay in flight.

$$\begin{aligned} (p_{\pi^-}^{Lab})^2 &= (\beta\gamma E_{\pi^-}^{cm} + \gamma p_{\pi^-}^{cm} \cos\theta^{cm})^2 + (p_{\pi^-}^{cm} \sin\theta^{cm})^2 \\ &= \gamma^2\beta^2(E_{\pi^-}^{cm})^2 + (p_{\pi^-}^{cm})^2 + 2\beta\gamma^2 E_{\pi^-}^{cm} p_{\pi^-}^{cm} \cos\theta^{cm} + (\gamma^2 + 1)p_{\pi^-}^{cm} \cos^2\theta^{cm}, \end{aligned} \quad (2.29)$$

where

$$\begin{aligned} p_{\pi^-}^{Lab} &: \text{pion momentum in the laboratory frame,} \\ \theta^{cm} &: \text{pion emission angle in the center of mass frame,} \\ \beta &: \text{hyperon velocity, } \gamma : 1/\sqrt{1+\beta^2}, \\ E_{\pi^-}^{cm}, p_{\pi^-}^{cm} &: \text{pion energy and momentum in the center of mass frame.} \end{aligned}$$

The momentum of decay pions emitted to backward angles with respect to the hyperon direction becomes small in the laboratory frame due to the Lorentz boost in this way. As the momentum of

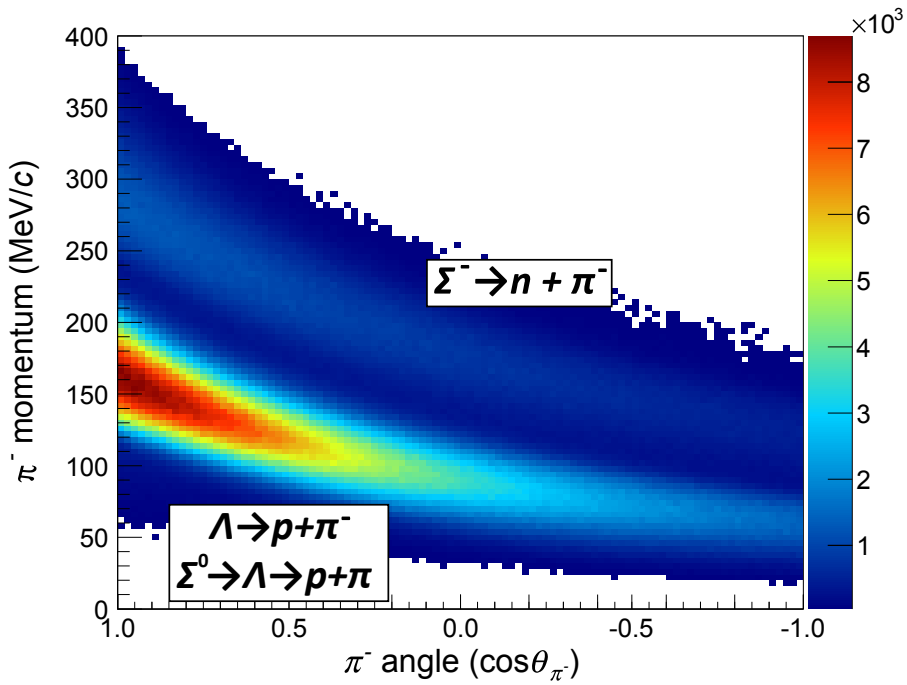


Figure 2.15: An expected momentum and angular distribution of quasi-free hyperon backgrounds. The result was estimated with the Monte Carlo simulation as explained in Section 2.3.2. The pions at lower momentum band corresponds to the decays from Λ s and Σ^0 s, and high momentum band is from Σ^- decays.

the pion from Λ decay at rest is 101 MeV/ c , the momentum distribution overlaps with the pions from hypernuclear decays. However, it is possible to suppress the quasi-free Λ background by installing the pion spectrometer at large angles with respect to the beam.

Figure 2.15 shows an expected correlation of the π^- momentum and emission angle under the assumption of the Fermi motion of nuclei and the cross sections of hyperons; that was applied in the same procedure (Step1.~Step6.) as explained in Section 2.3.2. Two bands in the figure correspond to the pions from Λ decays and Σ^- decays. The number of the quasi-free Λ is ~ 3 times larger than it of quasi-free Σ^- due to the difference of the cross sections. Since most of the quasi-free hyperon background are concentrated at the forward angles, it was found that the background rate can be suppressed at the backward angles. The momentum distribution of decay pions with an angle of $\theta_{\pi^-} = 122 \sim 130^\circ$ is shown in Figure 2.16. Though the quasi-free Σ^- backgrounds are overlapped with the pions from hypernuclear decays (100~130 MeV/ c), the largest background from Λ decays are expected to be suppressed.

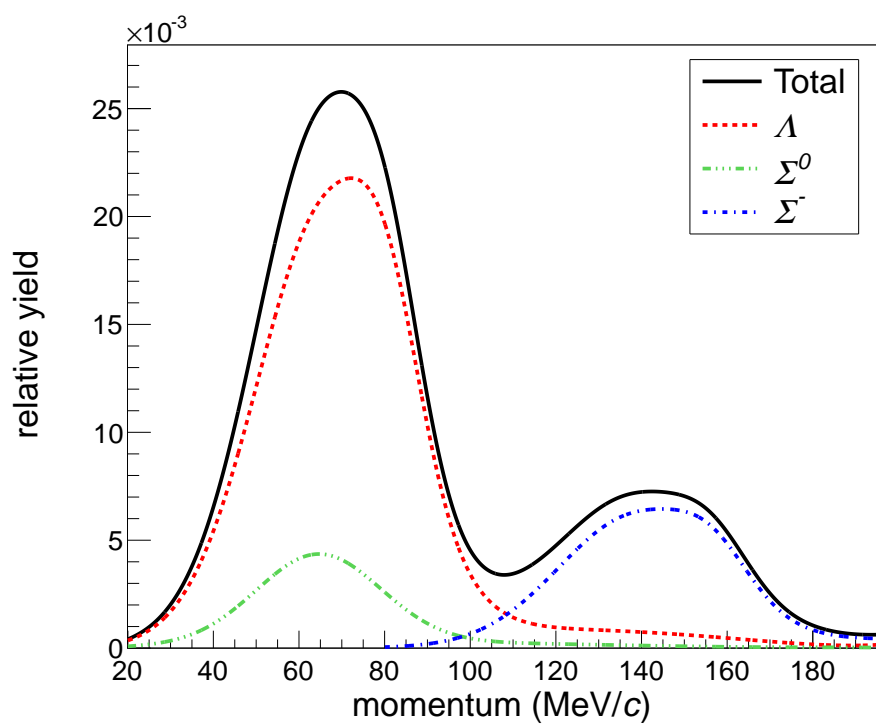


Figure 2.16: An expected momentum distribution of quasi-free hyperon backgrounds at $\theta_{\pi^-} = 122 \sim 130^\circ$. The distribution was normalized with an integration of the pion momentum for the quasi-free Λ ($\int p_{\pi^-} dp_{\pi^-} = 1$).

2.4 Calibration methods

A momentum calibration in the pion spectrometer is essential to deduce the absolute value of the Λ binding energy. To calibrate the momentum, momenta from the well-known sources are needed. In this thesis, the momentum calibration was performed with electrons from the elastic scattering by a target nucleus. The principle of the momentum calibration will be explained below. Calibrations using experimental data will be represented in Section 5.4. In addition, other calibration methods will be listed in Appendix D.

2.4.1 Momentum calibration using electron beam

Since the primary electron beam energy from the accelerator is measured with a high accuracy (~ 100 keV), the primary beam can be used for the calibration. There are two methods: a calibration using the electron beam itself and a calibration using elastic scattering electrons from a nucleus. The first is that the beam is directly introduced to the pion spectrometer, and the calibration is performed with the well-known electron energy. The second is that the beam is introduced to the target, *e.g.* ^{12}C , and a momentum of the elastic scattering electron is measured in the pion spectrometer.

The energy of the elastic scattering electron (E') depends on the scattered angles (θ):

$$E' = \frac{E}{1 + E/M(1 - \cos \theta)}, \quad (2.30)$$

where E is an introduced electron beam energy, and M is a target mass; these parameters are well-known values that we can choose. Figure 2.17 shows calculated energies of scattered electrons as a function of angles for ^{12}C and ^{181}Ta target. We can calibrate the momentum by adjusting the measured electron energy and the angle with calculated values using Equation 2.30.

In addition, the peak's response function can be obtained from the peak shapes of the scattered electron because the elastic scattering peaks can be observed clearly with a good signal-to-noise ratio. On the other hand, because the measured particle in the hypernuclear data is π^- but the particle in the calibration data is e^- . The difference of deposited energy and multiple scattering effect in materials make the absolute momentum change. The amount due to these effects can be estimated with Equation 2.21 and so on. More realistic estimation is also able to be performed using the Monte Carlo method. In this thesis, I estimate the momentum shift from

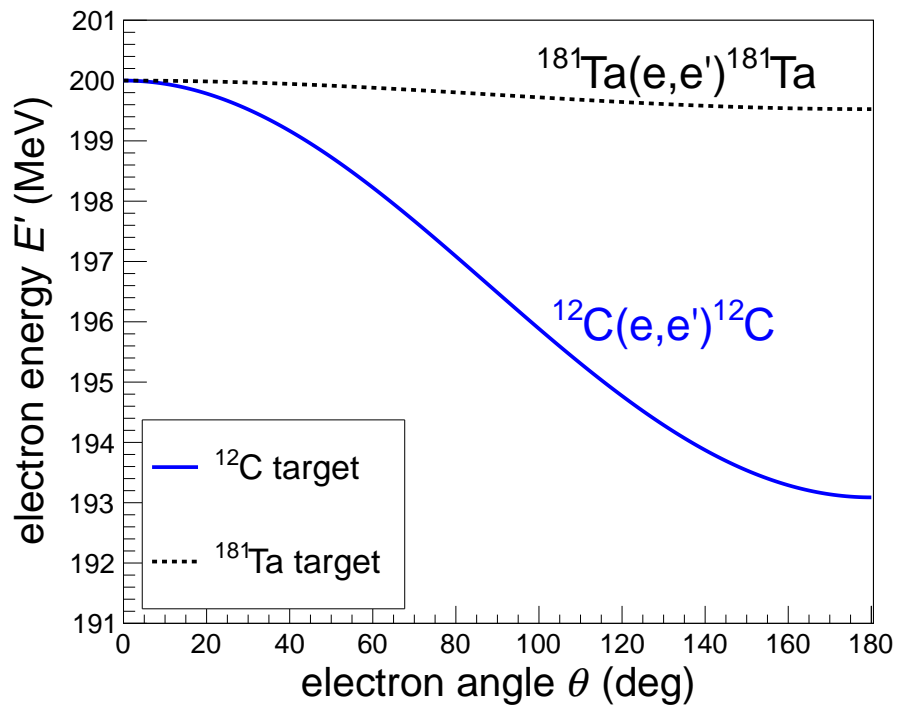


Figure 2.17: Calculated energies of scattered electrons as a function of angles for ^{12}C and ^{181}Ta target. The energy of the introduced electron beam was set to 200 MeV.

quantitative comparisons between the peak shapes from the Monte Carlo estimations and from the calibration data as explained its detail in Section 5.4.4.

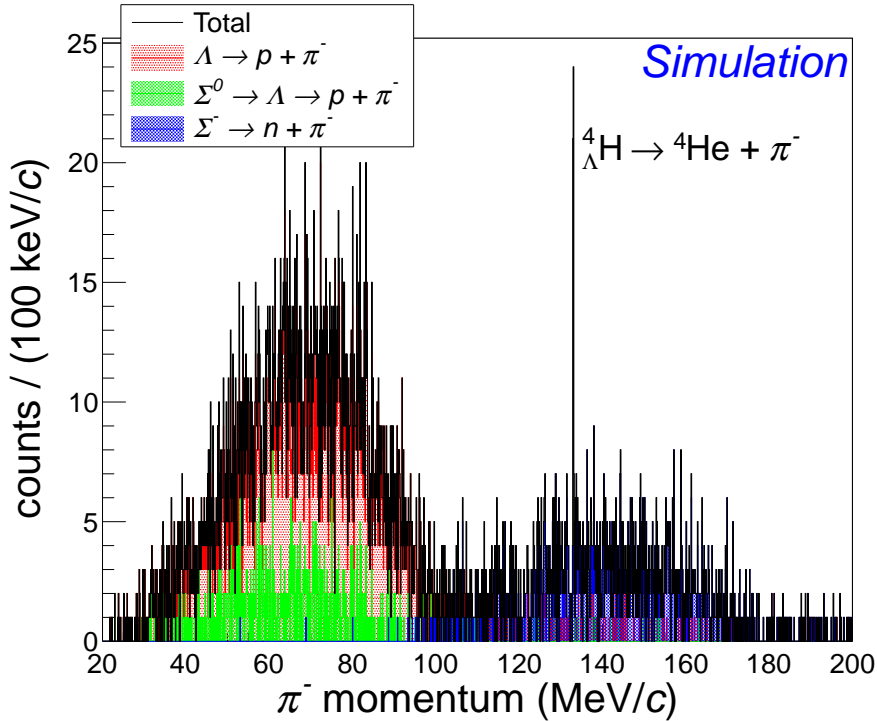


Figure 2.18: An expected spectrum under the condition of 150- μm thick ${}^9\text{Be}$ target, 20 μA beam current, and 20 days beam-time.

2.5 Expected spectrum

The design of the hypernuclear decay pion experiment and the expected yield, resolution, and backgrounds have been explained in this chapter. Figure 2.18 shows an expected spectrum assuming the 150- μm thick ${}^9\text{Be}$ target with tilted angle of 54°. The assumed beam current was 20 μA , and the experimental term was 20 days. The kaon tagger and pion spectrometer were assumed Kaos spectrometer at 0° with respect to the electron beam and SpekC spectrometer at 126°, respectively at MAMI.

Chapter.3

Experimental Apparatus

3.1 Overview

In 2011 and 2012, the hypernuclear decay pion experiments have performed at the A1 experimental hall with the high intense continuous electron beam accelerator “MAMI-C”. The experiments require high hypernuclear yield, high momentum resolution, and low background rate as already mentioned in the previous chapter. MAMI-C satisfies these conditions, and is the only possible accelerator in the world in 2012 because of a long shutdown of CEBAF for beam energy upgrade. Electron beams were introduced 125- μm thick target of ${}^9\text{Be}$ to minimize energy straggling effects. Some produced hypernuclei stopped in a target, and decayed to a pion and a normal nucleus by the weak interaction. Momenta of the decay pions were measured in high momentum resolution spectrometers, “SpekA” and “SpekC”. We tagged K^+ s in spectrometer “Kaos” that has a short orbit to identify the strangeness production events effectively.

Details of these apparatuses and detector setup in the 2012 experiment will be explained in this chapter.

3.2 The Mainz Microtron “MAMI-C”

MAMI-C is a continuous electron accelerator at the Institut für Kernphysik of JOHANNES GUTENBERG UNIVERSITÄT MAINZ in Germany. A floor plan of MAMI is shown in Figure 3.1. MAMI-C consists of 3.5 MeV injector LINAC, three microtrons (RTM1, 2, 3) [Herm76], and Harmonic Double Sided Microtron (HDSM) [Kais08]. The RTM3 consists of two 180° bending magnets with a weight of 450 tons each, and the beam electrons can be accelerated with a maximum energy of up to 855 MeV. The HDSM was newly constructed in 2006, and it consists of four 90° bending magnets (a weight of 250 tons each) and two linacs. The designed maximum electron energy is 1508 MeV with the maximum beam current of 100 μA (unpolar-

Table 3.1: Parameters of MAMI. In order to minimize energy and phase deviations, linacs of HDSM were operated with harmonic frequencies of 2.45 and 4.90 GHz [Kais08].

Stage Name	RTM3 (MAMI-B)	HDSM (MAMI-C)
Maximum output energy	855.1 MeV	1508 MeV
Maximum output current	100 μ A	100 μ A
Number of recirculation	90 turns	43 turns
Frequency	2.45 GHz	2.45/4.90 GHz
Energy spread	13 keV (FWHM)	110 keV (FWHM)
Horizontal Emittance	$13\pi \mu\text{m}\cdot\text{mrad}$ (rms)	$27\pi \mu\text{m}\cdot\text{mrad}$ (rms)
Vertical Emittance	$0.84\pi \mu\text{m}\cdot\text{mrad}$ (rms)	$1.2\pi \mu\text{m}\cdot\text{mrad}$ (rms)

ized beam) and 20 μ A (polarized beam). The strangeness physics research became possible thanks to the increased beam energy and the high beam intensity. The beam energy can be changed from \sim 180 MeV with direct transportation from RTM3 adjusting the number of recirculation. The beam diameter is a few hundred μ m with a beam energy uncertainty of 110 keV in the 1.5 GeV operation. Important parameters of MAMI are shown in Table 3.1. The electron beam was introduced to the A1 experimental hall, where we performed the experiments, A2 hall (experiments using real photons), A4 hall (parity violation experiment), and X1 hall (experiments using X-rays), respectively.

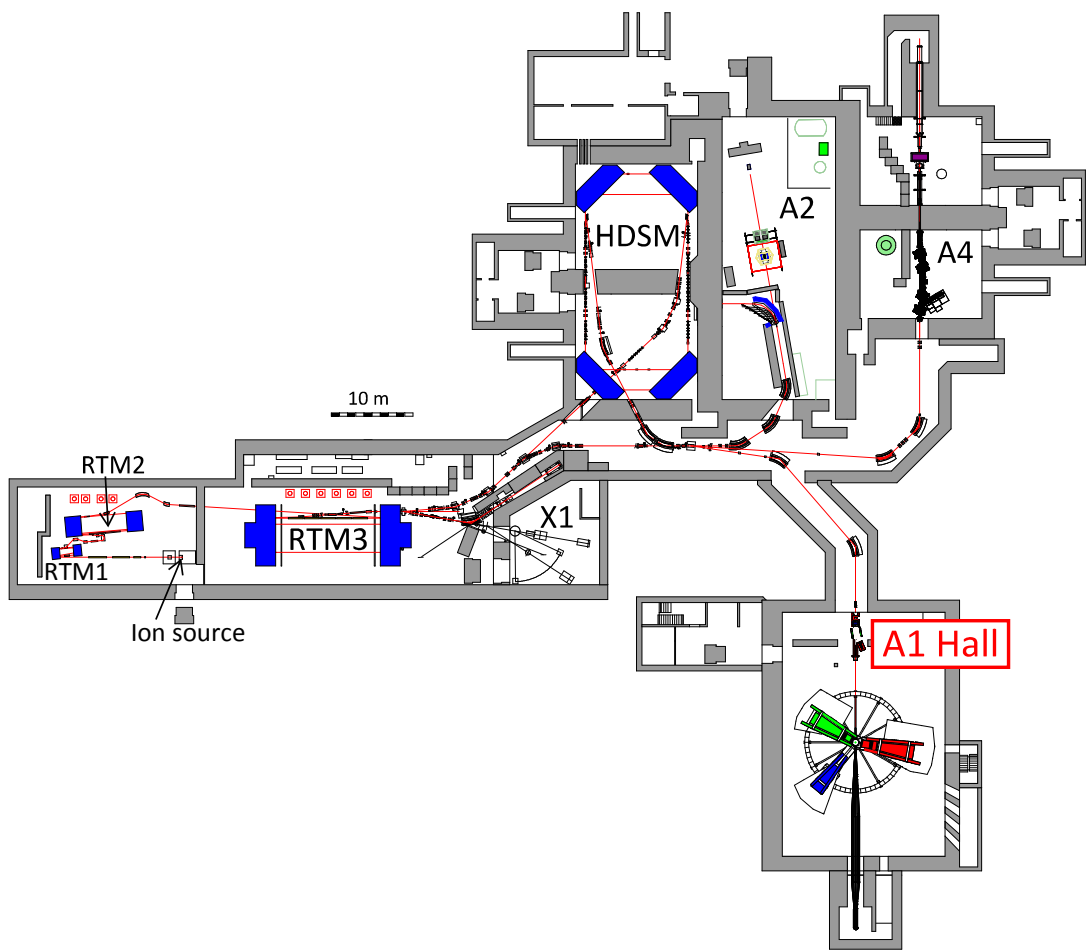


Figure 3.1: MAMI-C floor plan [A1Web]. The electron beam is injected from ion source and is accelerated by LINAC, RTM1, RTM2, RTM3, and HDSM up to 1508 MeV. The accelerated beam is introduced to each experimental hall: A1, A2, A4, and X1. The beam with a energy of 180~855 MeV is also available with a direct transportation from the RTM3. The present research was carried out at the A1 hall.

3.3 A1 experimental hall

The A1 experimental hall (A1 Hall) consists of an electron beam line, liquid or solid-state targets, and surrounding spectrometers (SpekA, SpekB, SpekC, and Kaos). SpekA, SpekB, and SpekC are well established vertically bending magnetic spectrometers which have a good momentum resolution ($\Delta p/p \sim 10^{-4}$) [Blom98]. Kaos with a short orbit spectrometer (~ 6 m) had been originally developed at the SIS heavy ion facility in GSI [Seng93]. Since 2008, Kaos was newly installed at MAMI and started operation with updating the detector system. A photo of the A1 experimental hall from downstream is shown in Figure 3.2. The top view of the experimental setup is also shown in Figure 3.3.

The electron beam was bended at 17° with respect to the incident electron beam line in pre-chicane magnets in order to transfer the beam electrons and associated photons to the dumps under the Kaos magnetic field simultaneously.

Targets were installed in a target frame located between the pre-chicane magnets and the Kaos magnet. A schematic drawing of enlarged view around the target is shown as Figure 3.4. In order to get higher hypernuclear yield with a good momentum resolution of decay pions, the target was tilted by 54° with respect to the incident electron beam. The tilted target was the effectively thinner for the decay pions but thicker for the electron beam. The detail of the target system will be given in Section 3.3.1.

SpekA and SpekC precisely measured the momenta of decay pions. These spectrometers were installed at large angles with the electron beam in order to get better signal-to-noise ratio. SpekC was installed at -126° with respect to the beam which corresponded to a normal direction to the target. SpekA was installed at $+91^\circ$ which was a maximum forward angle without any interference with the Kaos magnet. The details of these spectrometers will be explained in Section 3.3.2.

Generated kaons were tagged in the Kaos spectrometer to identify hyperon formation. Kaos was installed at very forward angles ($\sim 0^\circ$) in order to maximized the kaon yield. The details will be given in Section 3.3.3.

The electrons without interactions in the target were transferred to the electron beam dump. The generated photons were absorbed in a newly designed photon beam dump made of lead stack.

The electron beam line, the target chamber, and a gap in Kaos magnet were connected by vacuum extensions. The gaps in SpekA and SpekC were also evacuated to vacuum, while they were separated by two $120\text{-}\mu\text{m}$ thick Kapton foils with the target chamber.

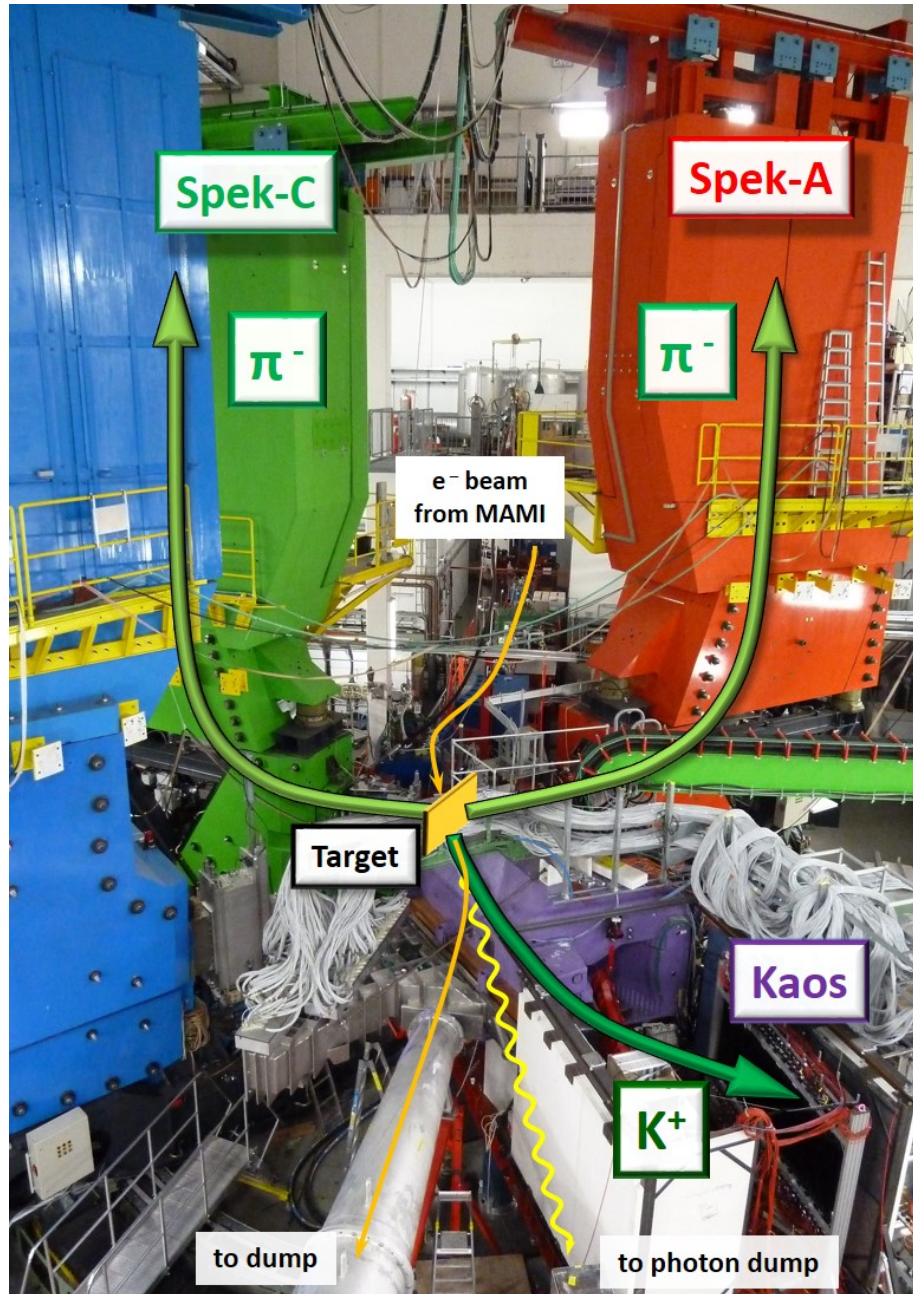


Figure 3.2: A photograph of experimental setup in the A1 hall. The electron beam was injected to the fixed ${}^9\text{Be}$ target after bending at 17° with respect to an incident electron beam line with pre-chicane magnets. A Kaos spectrometer (purple) was installed at a very forward angle as a kaon tagger. A SpekA spectrometer (red) and a SpekC spectrometer (green) were installed as pion spectrometers. Electron beam dumps for electrons and photons were also installed at the downstream (not seen in the photograph).

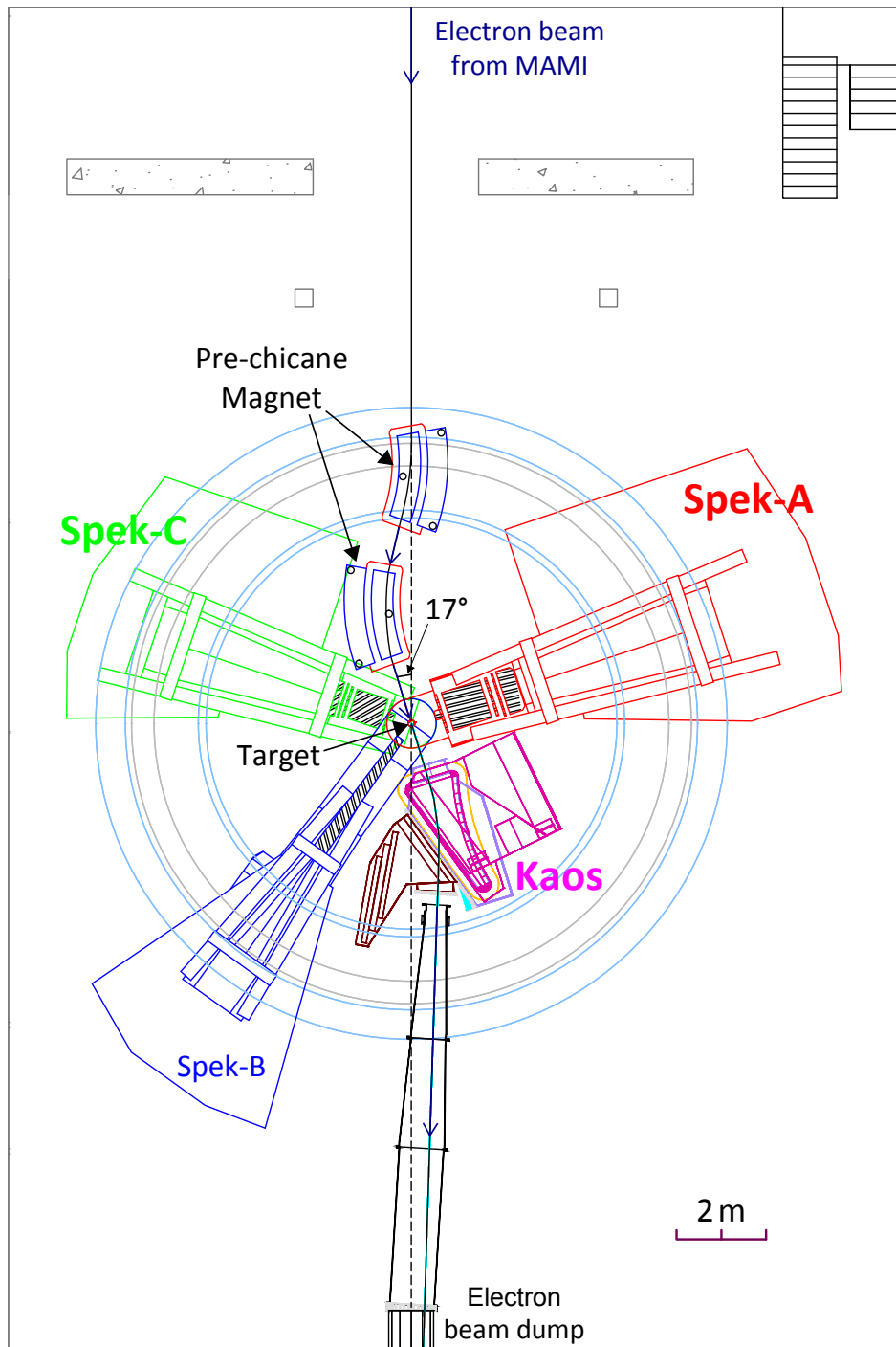


Figure 3.3: A top view of the experimental setup in the A1 hall.

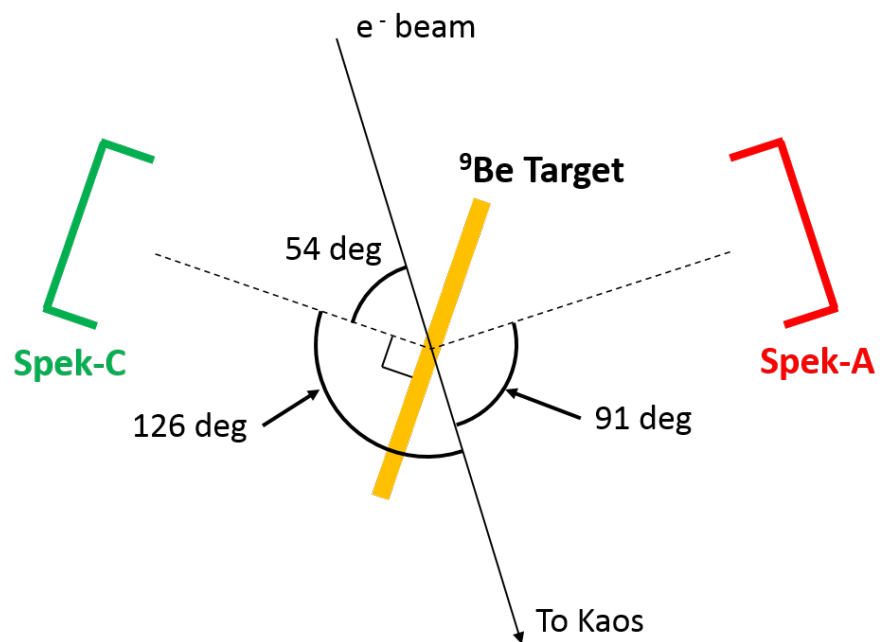


Figure 3.4: A schematic drawing of the target and the spectrometers. The target was tilted by 54° with respect to the electron beam. The SpekA and SpekC were installed at +91° and -126° with respect to the electron beam respectively.

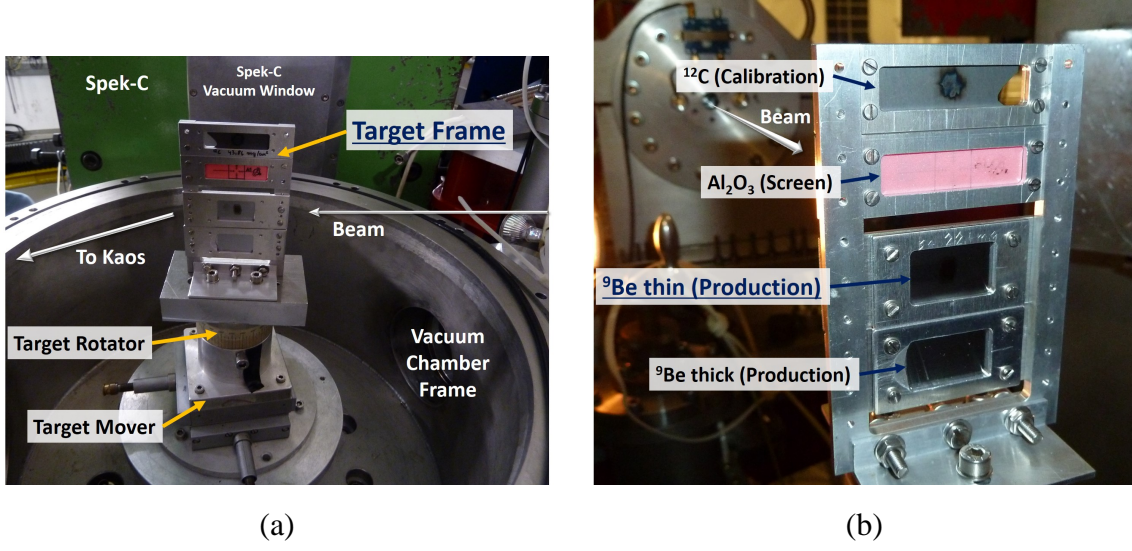


Figure 3.5: Photographs of the target frame. (a) A target mounter from a view of the SpekA entrance. (b) A enlarged view of the target frame. We installed a ^{12}C , a Al_2O_3 , a $125\text{-}\mu\text{m}$ thick ^9Be foil, and a $500\text{-}\mu\text{m}$ thick ^9Be foil from top to bottom in the frame. In order to calibrate momenta in SpekA and SpekC, ^{181}Ta target was installed in calibration runs with a frame of the same structure.

3.3.1 Target system

A main target was a ^9Be foil with a thickness of $125\ \mu\text{m}$ as mentioned before. We also installed a thicker ^9Be foil with a thickness of $500\ \mu\text{m}$ as a backup target. A beam position screen (Al_2O_3) were prepared to check the position, the direction, and the spot size of the electron beam. A ^{12}C foil and a ^{181}Ta foil were used to take elastic scattering data for momentum calibration in SpekA and SpekC. The used targets are summarized in Table 3.2. These targets were installed on a target frame made of aluminum. Photographs of the target frame are shown in Figure 3.5. The target frame was mounted on a target mover which was the well established target control system for adjusting the target position and rotation angle. We adjusted the target position with an accuracy of better than $1\ \text{mm}$ using the theodolite with a guide of the beam line and the equipped markers in the hall before the installation of the vacuum chamber. We also adjusted the target angle using the scale equipped in the target rotator. Since the target mover could safely control the position of the target in Y direction, which was defined as the direction of gravity, from the outside of the hall using a GUI controller, we could exchange the target without accessing to the hall.

Table 3.2: A list of targets. The targets are provided by Goodfellow [GoodWeb].

Target	Thickness	Density	Purity	Comments
⁹ Be	125 μm	1.848 g/cm ³	> 99.8 %	Target
⁹ Be	500 μm	1.848 g/cm ³	> 99.8 %	Backup target
¹² C	200 μm	2.25 g/cm ³	99.8 %	Calibration target
¹⁸¹ Ta	6 μm	16.6 g/cm ³	99.9 %	Calibration target
Al ₂ O ₃	2 mm	-		Beam position monitor

3.3.2 Pion spectrometers (SpekA, SpekC)

The two spectrometers SpekA and SpekC were used as pion spectrometers. Table 3.3 shows main parameters of SpekA and SpekC. These spectrometers are well established vertical bending spectrometers which have large solid angles and high momentum resolutions simultaneously [Blom98]. Each spectrometer can be rotated around the common pivot with an accuracy of 0.01°, therefore the distance between the target and the spectrometer entrance, and the angle between the beam line and the center line of the spectrometer are determined precisely.

Each of SpekA and SpekC consists of four magnets and a detector package. The details will be shown in the following sections. A vacuum chamber ($<1\times10^{-4}$ mbar) was installed from the entrance of the quadrupole magnet to in front of the tracking detector. The entrance window of the vacuum chamber were made of Kapton foil with a thickness of 120 μm . A 12- μm thick mylar foil was installed with Kevlar strings (100 μm ϕ) aligned in every 0.75 mm to reinforce the window.

Magnet

The magnet configuration of each spectrometer is quadrupole - sextupole - dipole - dipole combination from the upstream to the downstream. In order to ensure the stability of the magnetic field, NMR probes are equipped. The first dipole in SpekC has a compensation circuit which controls the magnetic field to keep NMR readouts constant. The magnet configuration in SpekA are shown in Figure 3.6. The beam optics was set to be point-to-point for dispersive plane and by parallel-to-point for non-dispersive plane.

Table 3.3: Main parameters of SpekA and SpekC. [Blom98]

	SpekA	SpekC
Magnet configuration	QSDD	QSDD
Maximum momentum	735 MeV/c	551 MeV/c
Dispersive angular acceptance	± 70 mrad	± 70 mrad
Non-dispersive angular acceptance	± 100 mrad	± 100 mrad
Solid angle	28 msr	28 msr
Momentum acceptance	$\pm 10\%$	$\pm 12.5\%$
Momentum resolution ($\Delta p/p$)	10^{-4}	10^{-4}
Length of central trajectory to focal plane	10.75 m	8.53 m
Angle of focal plane	45°	45°
Dispersion at central momentum	5.77 cm/%	4.52 cm/%
Magnification at central momentum	0.53	0.51
Angular resolution at target (rms)	< 3 mrad	< 3 mrad
Operated central momentum	115 MeV/c	125 MeV/c
Central angle to the beam axis	$+91^\circ$	-126°

Detectors

Figure 3.7 shows a detector setup of SpekA. The detector package consists of two sets of tracking detectors (VDC), two layers of scintillation counters (ToF, dE), and a gas Cherenkov detector (GC).

■ Vertical Drift Chamber (VDC)

Two sets of VDCs, which were planer type drift chambers, were installed just behind the vacuum exit in order to reconstruct tracks at the focal plane. The VDCs covered $222^L \times 40.5^W$ cm² for SpekA and $232^L \times 34^W$ cm² for SpekC. Each VDC consisted of four layers. Two layers which had wires along the non-dispersive plane, called “x layer”, while the other two layers with wires streached to a 40° to the diagonal direction with respect to the x plane, called “s layer”. Each layer had signal wires every 5 mm with ground potential and cathode planes with a negative potential of around -6500 V. The number of readout wires were 400 channels in x layer and 416 channels in x' layer; they were 320 channels in s layer and 336 channels in s' layer. The VDCs were filled a mixture gas of argon and isobuthan (50:50). A typical focal plane resolution

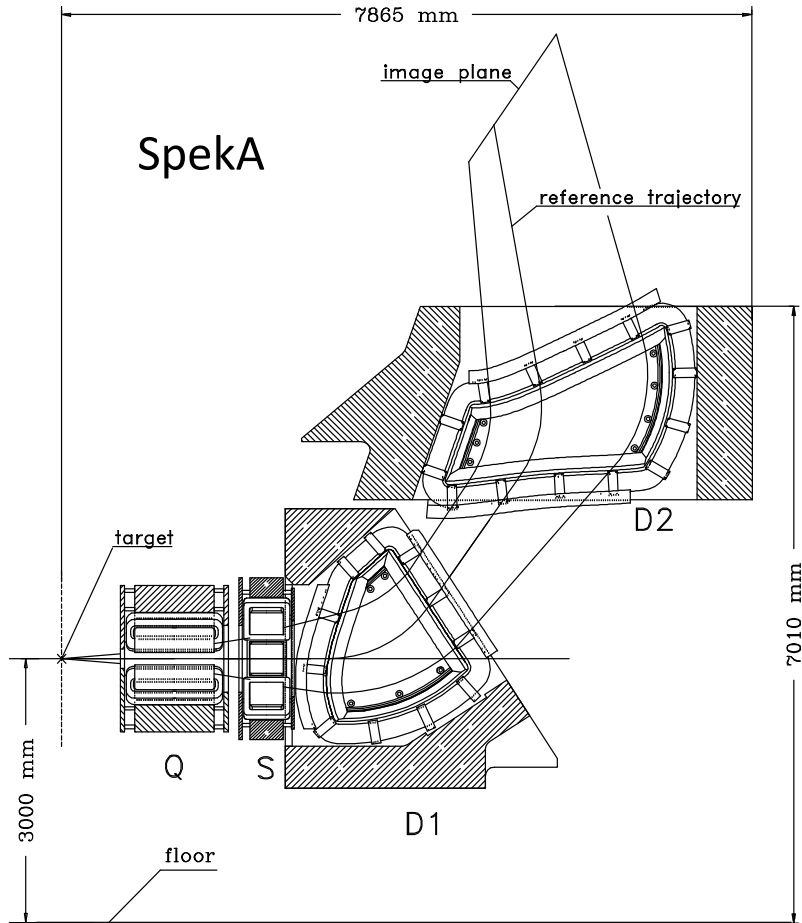


Figure 3.6: A schematic drawing of SpekA with beam optics information [A1Web]. That of SpekC has the similar configuration with SpekA.

was obtained as $100 \mu\text{m}$ (rms) in the dispersive plane and $300 \mu\text{m}$ (rms) in the non-dispersive plane. An angular resolution was 0.25 mrad (rms) in the dispersive angle; it was 1 mrad (rms) in the non-dispersive angle at the focal plane. A typical single layer efficiency was $> 99\%$.

■ Scintillation counter (dE and ToF)

Two layers of segmented plastic scintillation counters were placed in order to make a trigger for the data acquisition and a time reference for the VDCs. Each layer had 15 segments, and each segment covered the area of $45^W \times 16^L \text{ cm}^2$. The first layer “dE” had 3 mm thickness and was used for energy loss measurements. The other layer “ToF” had 10 mm thickness and was used for time of flight measurements. The central position of the segments in “ToF” was shifted by a half segment to the central position of the segments in “dE” to cover the ineffective regions

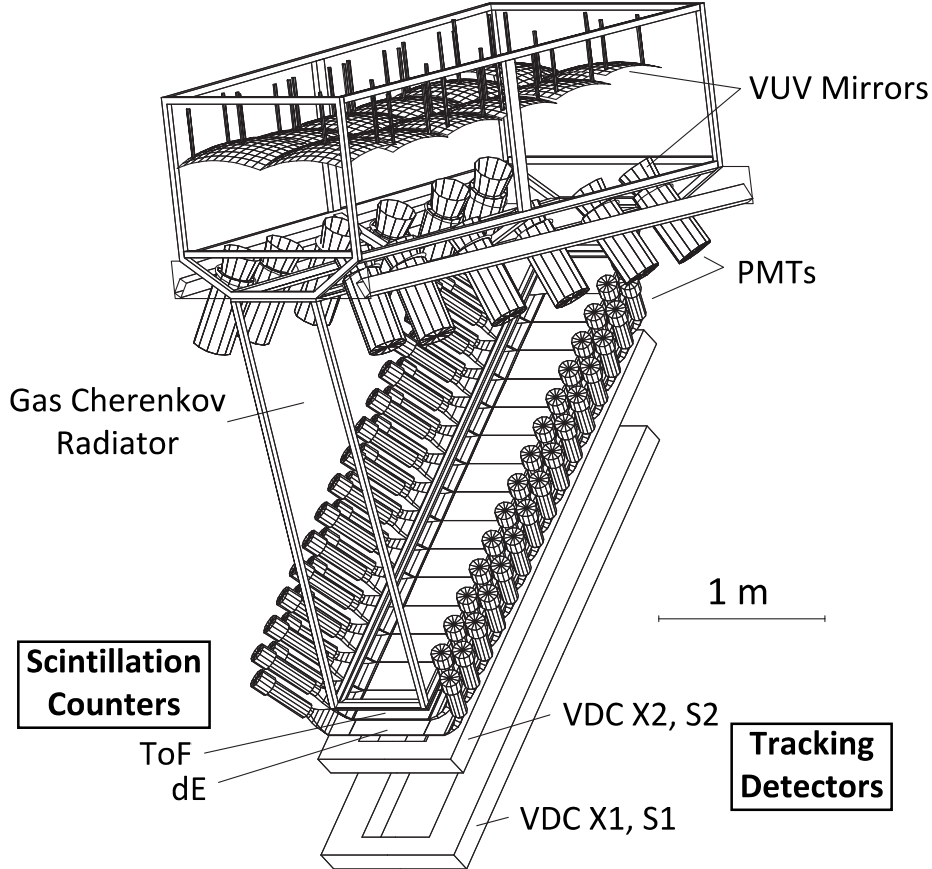


Figure 3.7: A detector setup of SpekA [A1Web]. That of SpekC has the same configuration as SpekA.

between the segments each other. Each segment was read out by two 2" photomultiplier tubes [PMTs] (Philips XP2262B for “dE” and XP4222B for “ToF”) at both ends.

■ Gas Cherenkov detector (GC)

When a charged particle in a material moves faster than the speed of light, Cherenkov radiation is emitted in a material. The threshold of the particle velocity (β) emitting Cherenkov radiation is given as:

$$\beta > 1/n, \quad (3.1)$$

where n is the refractive index of a material. The number of photons (NPEs) per unit wavelength per unit length of the radiator is

$$\frac{d^2N}{d\lambda dx} = \frac{2\pi z^2 \alpha}{\lambda^2} \left(1 - \frac{1}{\beta^2 n^2(\lambda)} \right), \quad (3.2)$$

where

- λ : wavelength of Cherenkov light,
- x : length of radiator,
- z : charge of incident particle,
- α : fine structure constant.

A threshold type Cherenkov detector was used in order to distinguish electrons from pions and muons. Decafluorobutane (C_4F_{10}) gas was used as the radiator. The refractive index was 1.0013 at 400 nm which corresponds to a momentum threshold of $10 \text{ MeV}/c$ for electrons and $2700 \text{ MeV}/c$ for pions. The Cherenkov light was reflected by the vacuum-ultraviolet mirrors (VUV mirrors) and was introduced to 5" PMTs (Philips XP4500B).

Table 3.4: Main parameters of Kaos. The acceptance and solid angle are under the condition of the decay pion experiment in 2012. The relative momentum resolution is estimated by the beam optical calculation [Seng93].

Dispersive angular acceptance	± 185 mrad
Non-dispersive angular acceptance	± 20 mrad
Solid angle	17 msr
Momentum acceptance	$\pm 25\%$
Momentum resolution ($\Delta p/p$)	10^{-3}
Length of central trajectory	6.4 m
Operation central momentum	924 MeV/c
Central angle for the beam axis	0°

3.3.3 Kaon tagger (Kaos)

Kaos spectrometer [Seng93] was used as the K^+ tagger. The Kaos spectrometer was brought from SIS facility at GSI to MAMI for studies of the strangeness physics, and started the operation from 2008. Since the Kaos spectrometer has a short path length (6.4 m) and can accept higher momentum particles than the existing spectrometers: SpekA, B and C, the Kaos spectrometer is suitable for the kaon detection. About 40% of kaons survived at the end of the detector package at 1 GeV/c, while about 10% did for SpekA at 0.7 GeV/c. Furthermore, thanks to the wide momentum acceptance, the Kaos spectrometer achieved large kaon yields. Main parameters are listed up in Table 3.4.

Figure 3.8 shows a setup in Kaos. The Kaos spectrometer consisted of a dipole magnet and a detector package. The details will be shown in the following sections.

Magnet

A Kaos magnet consists of one dipole magnet. Since the dipole magnet was installed at 0° with respect to the electron beam, the magnet had four exits in order to handle simultaneously the electron beam, the photon from the bremsstrahlung, the scattered electrons at the target, and the generated kaon that we tagged. Magnetic field was monitored with a Hall probe .

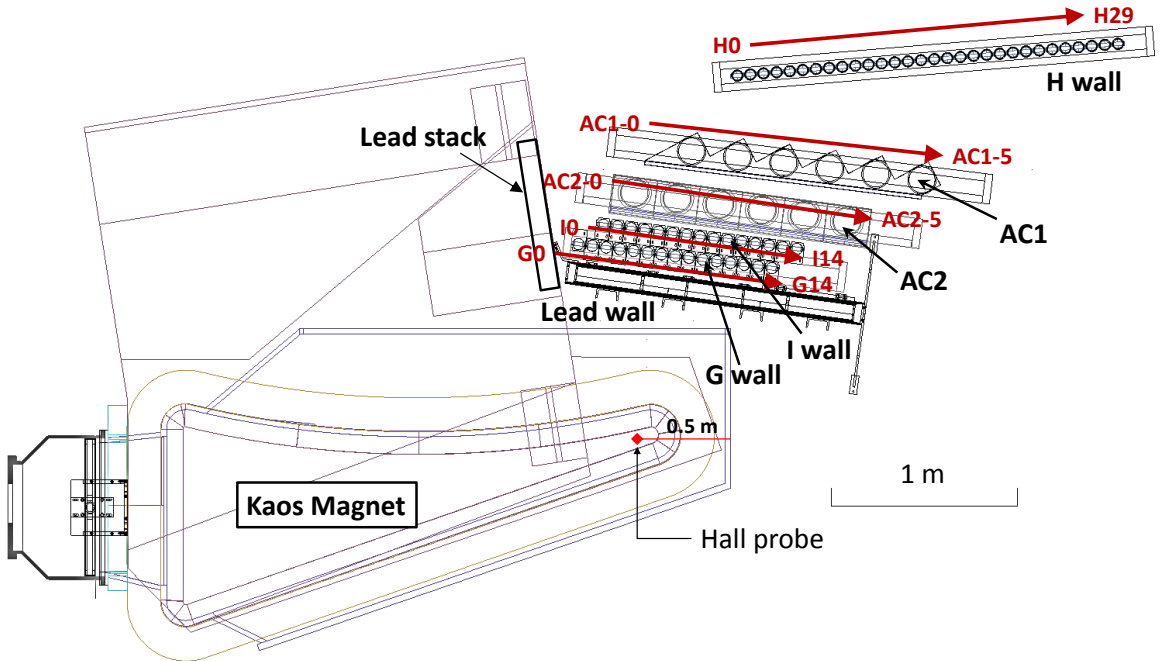


Figure 3.8: A detector setup of Kaos. A detector package of the Kaos spectrometer consists of a lead wall, scintillation counter walls (G and I walls), aerogel Cherenkov counters (AC2 and AC1), and a scintillation counter wall (H wall) from upstream side of particle tracks. Definitions of paddle and segment numbers (red letters) were also shown in each detector. Lead blocks ($5^H \times 10^W \times 20^L$ cm 3 each) were stacked on the edge of the Kaos magnet yoke (Lead stack).

Detector

The Kaos detectors were originally designed in order to identify K^+ for the heavy ion beam experiments at GSI. However, at the very forward angles under the high intensity electron beam, a lot of e^+ , π^+ , and p backgrounds were expected in the Kaos detector plane. The incoming event rates of π^+ , and p were about 100 times more than it of K^+ . The rate of e^+ backgrounds, the most serious background, was at least another 100 times more. The total event rate was expected to more than 40 MHz at 20 μ A. We had to improve the Kaos detector setup in order to distinguish K^+ with these background particles under the high background rate and the poor signal-to-background ratio. We re-designed the detector setup, and newly installed aerogel Cherenkov counters and a lead wall. The details of each detector will be explained below.

■ Time Of Flight (TOF) counter

TOF counters were used for TOF and energy deposited measurements, and made triggers for

data acquisition. The detectors consist of three scintillator walls, named “G”, “I” and “H” from upstream.

Each of G and I wall consisted of 15 plastic scintillator paddles. A material of the plastic scintillator was BC408 (Bicron [BicronWeb]). Volume of one scintillator paddle was $470^H \times 20^T \times 75^W$ mm³. All scintillators were read out from both ends by 2" PMTs (Hamamatsu R1828). Typical high voltages for PMTs were set to about -2000 V by the LeCroy 4032A HV power supply. The walls were installed behind an exit vacuum window of the Kaos magnet. The mounted position of I wall was shifted by a half segment to the central position of G wall in order to cover the ineffective regions between the segments.

The H wall consisted of 30 plastic scintillator paddles. The wall was newly constructed replacing an old wall due to aged depreciation of scintillators in 2011. The volume of one paddle was $580^H \times 20^T \times 70^W$ mm³. The material of the plastic scintillator and used PMTs were the same as G wall. The wall installed approximately on the focal plane position.

In order to achieve a longer flight path length in a high momentum side, the G-I and H walls were tilted respectively by -7.11° and $+4.76^\circ$ to the vacuum exit window.

■ Aerogel Cherenkov counter (AC)

Two layer of threshold type aerogel Cherenkov counters were installed, named “AC2”, “AC1” from upstream. In order to distinguish K^+ from π^+ and e^+ , silica aerogel of the refractive index $n = 1.055$ was chosen as a radiator. The momentum threshold of the Cherenkov radiation was 420 MeV/c for π^+ ; it was 1560 MeV/c for K^+ .

AC1

AC1 was a specular reflection type aerogel Cherenkov detector, which was newly installed in 2011. A drawing of AC1 is shown in Figure 3.9. The frame was made of 1-mm thick aluminum. The effective area of AC1 was $466^H \times 1490^W$ mm².

The radiators of AC1 were used the combination of hydrophobic aerogel tiles (Japan Fine Ceramics Center, Japan) with dimensions of $115 \times 115 \times 10^T$ mm³ and hydrophilic aerogel tiles (Boreskov Institute of Catalysis and Budker Institute of Nuclear Physics, Russia) with dimensions of $50 \times 50 \times 20^T$ mm³. The total thickness of the aerogel tiles was 30 mm, and the effective thickness with incident particles was increased by a factor of ~ 1.4 because the particles were introduced with $\sim 45^\circ$. The transfer space was filled by dry nitrogen in order to prevent the degradation of the hydrophilic aerogel tiles. AC1 consisted of 6 segments.

The segments were separated by the aluminum frame in the transfer space, but not separated in the radiator space. Each of the segment was read out at both ends by 5" PMTs. The PMTs of three segments in the lower momentum side were Hamamatsu R877-100, and another three

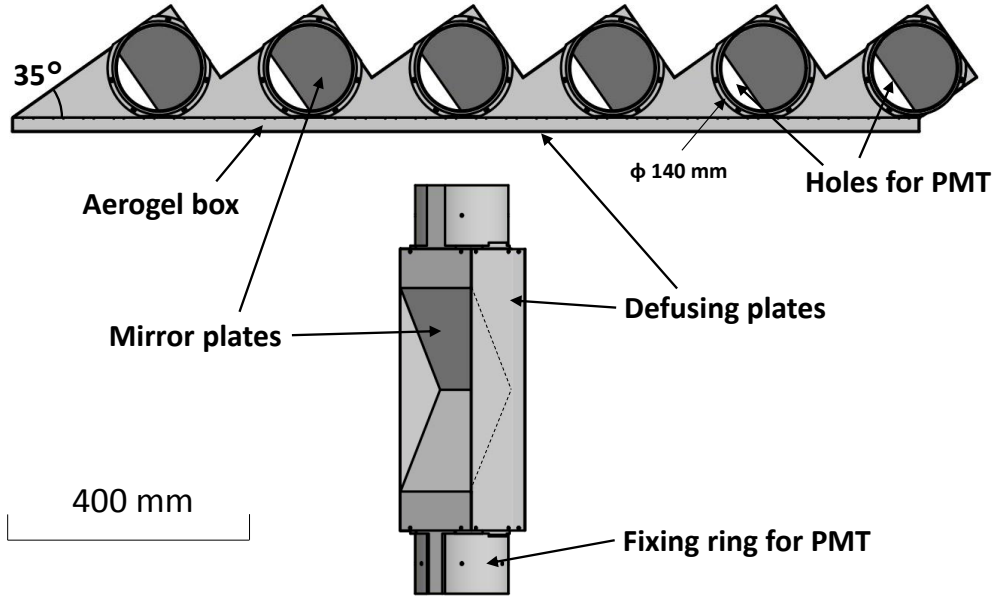


Figure 3.9: A drawing of AC1 [DebeD]. A top view of AC1 and a 3D drawing of one segment were shown.

segments in the higher momentum side were Hamamatsu R1250. R877-100 has the super bi-alkali cathode, which has higher quantum efficiency ($\sim 35\%$ at 400 nm). On the other hand, the gain factor of R877-100 is several tens times smaller than that of R1250. Therefore, R877-100 were installed in the low momentum region where the less number of Cherenkov photons was expected. In addition, in order to get higher gain in R877-100, we installed an additional amplifier in the tube. A circuit diagram of the amplifier will be shown in Appendix A. Cherenkov light was reflected by a aluminum mylar covered on an aluminum plate which was tilted by $\pm 34^\circ$ around the latitude axis. Other plates were coated with a diffused reflector (Labsphere 6080 White Reflectance Coating [LabsphWeb]).

AC2

AC2 was a diffused reflection type aerogel Cherenkov detector. It was newly designed and installed for the experiment in 2012. The performance of the prototype was checked using hadron beams in the J-PARC T44 experiment as shown below.

AC2 was designed to discriminate K^+ from π^+ with less multiple scattering effect of charged particles and less electron-positron shower due to the bremsstrahlung effect compared with AC1. A drawing of the AC2 is shown as Figure 3.10. The effective area was $1384^W \times 456^H$ mm 2 . Frames where the particles passed through were made by carbon-fiber-reinforced plas-

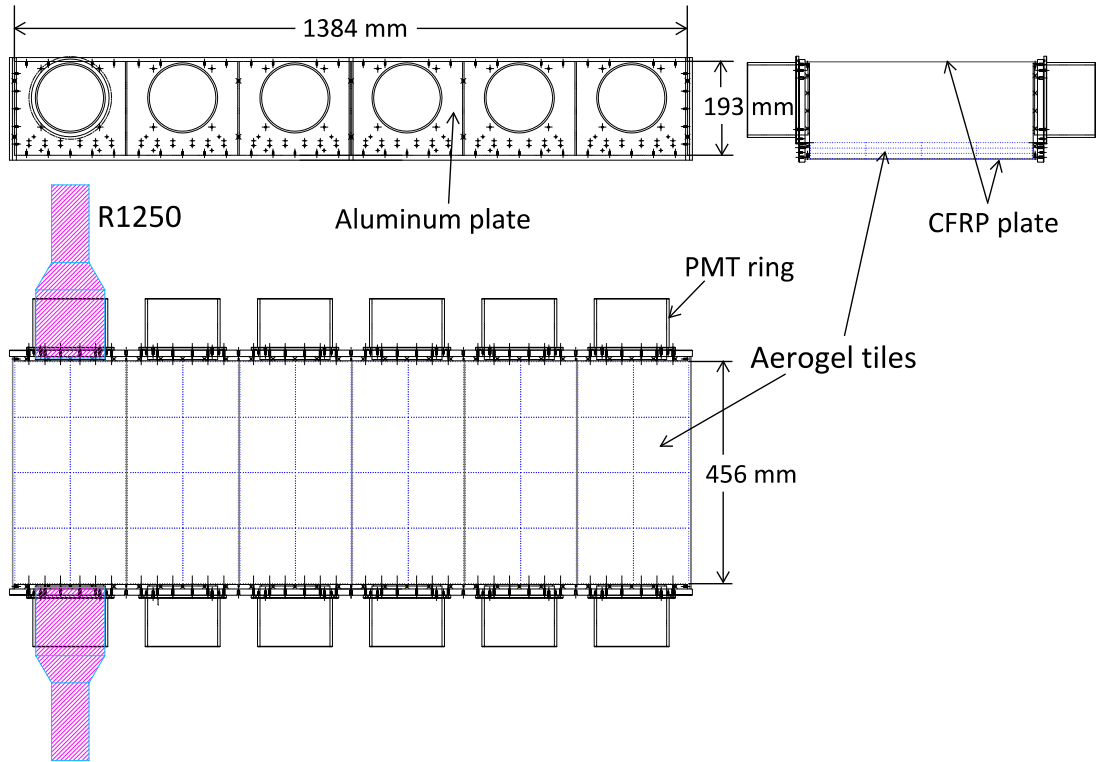


Figure 3.10: A drawing of AC2.

tic (CFRP) with a thickness of 0.4 mm. Top and bottom boards were made by 22-mm thick aluminum. The 3-layers of 0.1-mm thick polytetrafluoroethylene (PTFE) sheets covered on the frames as a diffused reflector of the Cherenkov light. PTFE has good reflectance for light with a wavelength from 300 to 600 nm which corresponds to PMT's sensitive region as shown in Figure 3.11. The PTFEs were attached with low outgas double sided tapes (Nitto LA-50) in order to prevent deterioration of the Cherenkov radiators. Hydrophobic aerogel tiles (Japan Fine Ceramics Center, Japan) were used as a radiator. The geometrical thickness was 30 mm in total, and the effective thickness with incident particles was increased by a factor of 1.4 as with the AC1.

AC2 consists of 6 segments. Each segment was completely separated with the 0.2-mm thick CFRP frame covered by 3-layers of PTFE sheets. 5" PMTs (Hamamatsu R1250) were equipped with both ends of the segment. High voltages for PMTs were supplied from the LeCroy 4032A HV power supply.

Performance test (J-PARC T44 experiment)

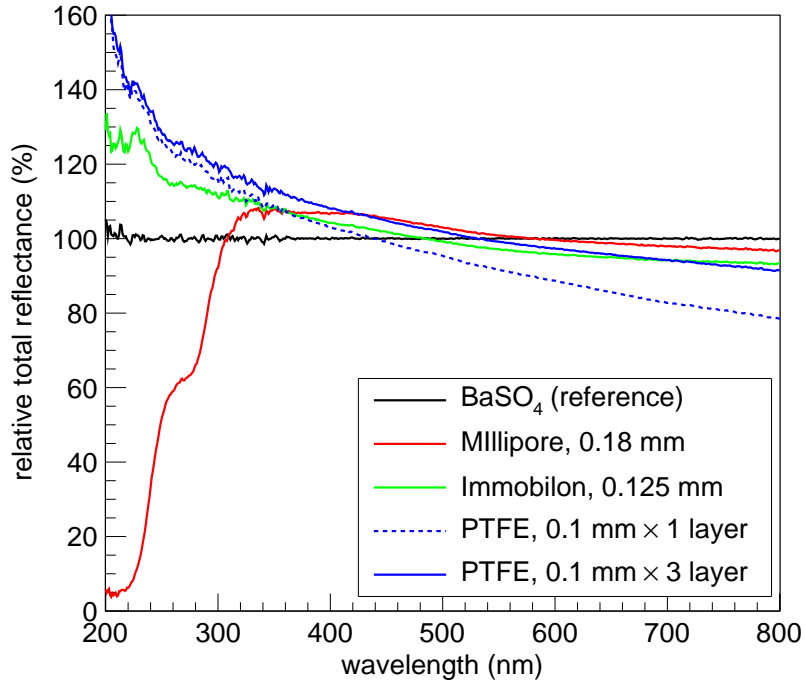


Figure 3.11: Total reflectance curves for several reflectors.

The total reflectances of BaSO₄ (reference), Millipore (GSWP09000, Merck Millipore), Immobilon (IPVH00010, Merck Millipore), and PTFE (PTFE unsintered tape, Chukoh Chemical Industries) were plotted as functions of wave length. The reflectance was measured by a spectrophotometer (UV-2101PC, Shimadzu) and a chamber box (MPC-3100, Shimadzu).

The performance of the prototype was checked using a hadron beam line at J-PARC (K1.1 beam line) in 2012. K1.1 beam line provided π^+ , K^+ and proton beams with a momentum of 0.8 GeV/c. The typical beam rates were $30\sim50\times10^3$ counts per spill for π^+ s and protons; it was 8×10^3 counts per spill for K^+ s (1 spill = 2 seconds).

Experimental setup at J-PARC T44

The experimental setup is shown as Figure 3.12. Two layers of plastic scintillation counters (Trig1 and Trig2) were used as trigger counters for data acquisition.

Two prototype detectors were installed between the two scintillators. One was a specular reflection type detector which had the same configuration as one segment of AC1. Another was a diffused reflection type detector which had the same configuration as one segment of AC2. The frame of each prototype was made by aluminum composite plates covered with 3-layers of PTFE sheets. Radiators were 3-cm thick hydrophobic aerogel tiles (Japan Fine

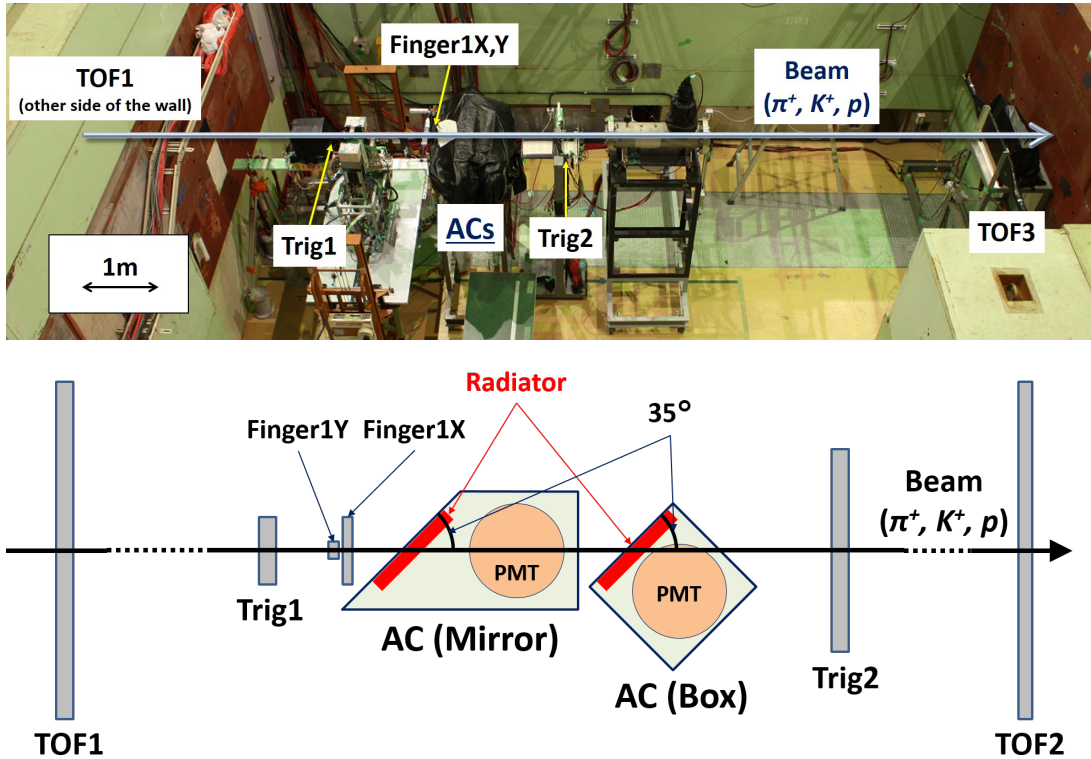


Figure 3.12: A photograph of the experimental setup for J-PARC T44 experiment together with a schematic drawing.

Ceramics Center). Since the radiators were tilted by 35° to the beam, the effective thickness for the incident particles was 52 mm. Each prototype was read out from both ends by 5" PMTs (Hamamatsu R1250).

We installed additional scintillation counters in order to perform particle identifications correctly in the analysis. Two tiny scintillation counters (Finger1Y and Finger1X, $10^W \times 20^H$ mm 2) were installed to ensure that the particles passed in the radiators. Two layers of plastic scintillation counters (TOF1 and TOF2) were also installed for better particle identification under longer flight length (~ 9.4 m).

Results of J-PARC T44

Particle identifications were performed with TOF. A 2-dimensional TOF distribution between the scintillation counters is shown in Figure 3.13. Three clusters which correspond to pions, kaons, and protons were clearly observed. In order to minimize contaminations from accidental backgrounds, we applied TOF cuts between TOF1 and TOF2 and that between Trig1 and Trig2 simultaneously.

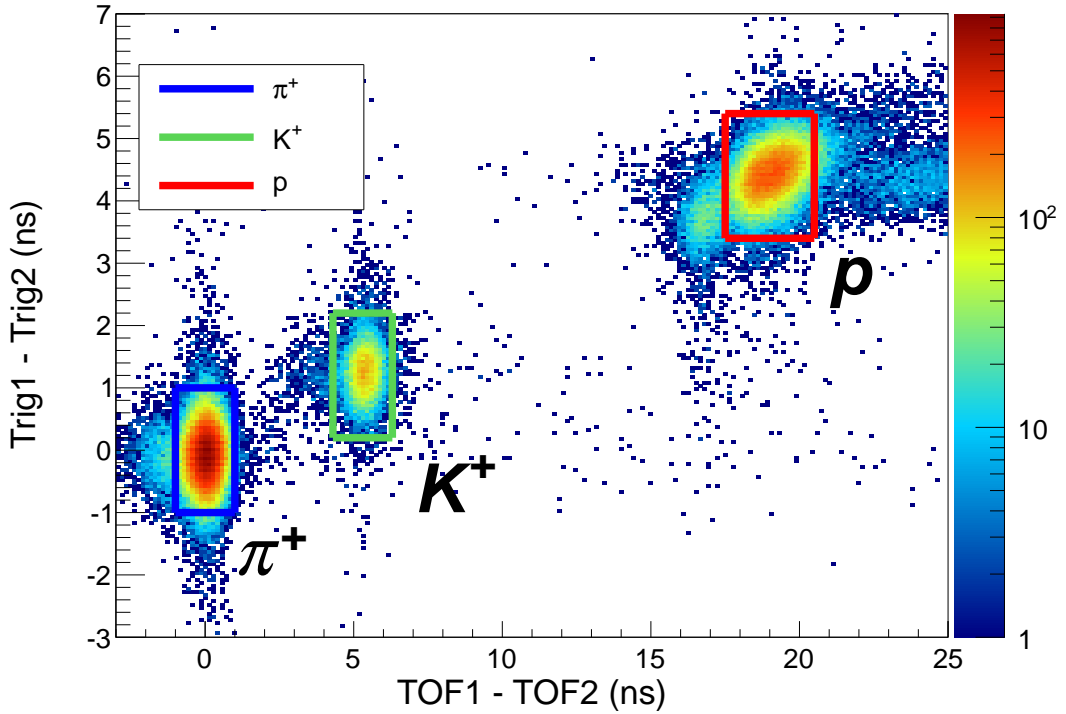


Figure 3.13: A 2-dimensional TOF distribution in the T44 experiment. A correlation between a $\text{TOF}(\text{Trig1-Trig2})$ and a $\text{TOF}(\text{TOF1-TOF2})$ was shown. Data in three runs in which the beam line components were optimized for the transportation of π^+ s, K^+ s and protons were merged. The peaks for pions were set to zero. Events in squares were selected as π^+ s, K^+ s, and protons for the analysis of the aerogel Cherenkov detectors.

Distributions of the number of photo-electrons (NPEs) for each particle are shown in Figure 3.14. The Cherenkov lights were observed only for pions. The distribution for pions was fitted well with Poisson distribution convoluted by the Gaussian distribution, and the average of the NPEs was 12 photo-electrons. Particle survival ratios with cutting thresholds of NPEs are also shown in Figure 3.14. When we applied the threshold of 3 photo-electrons, the rejection ratio of pions was achieved 99.7% under the overkill ratio of 0.6% for kaons in the diffused reflection type detector. We also checked the performances under the other radiators or diffused reflectors, and they are summarized in Appendix B.

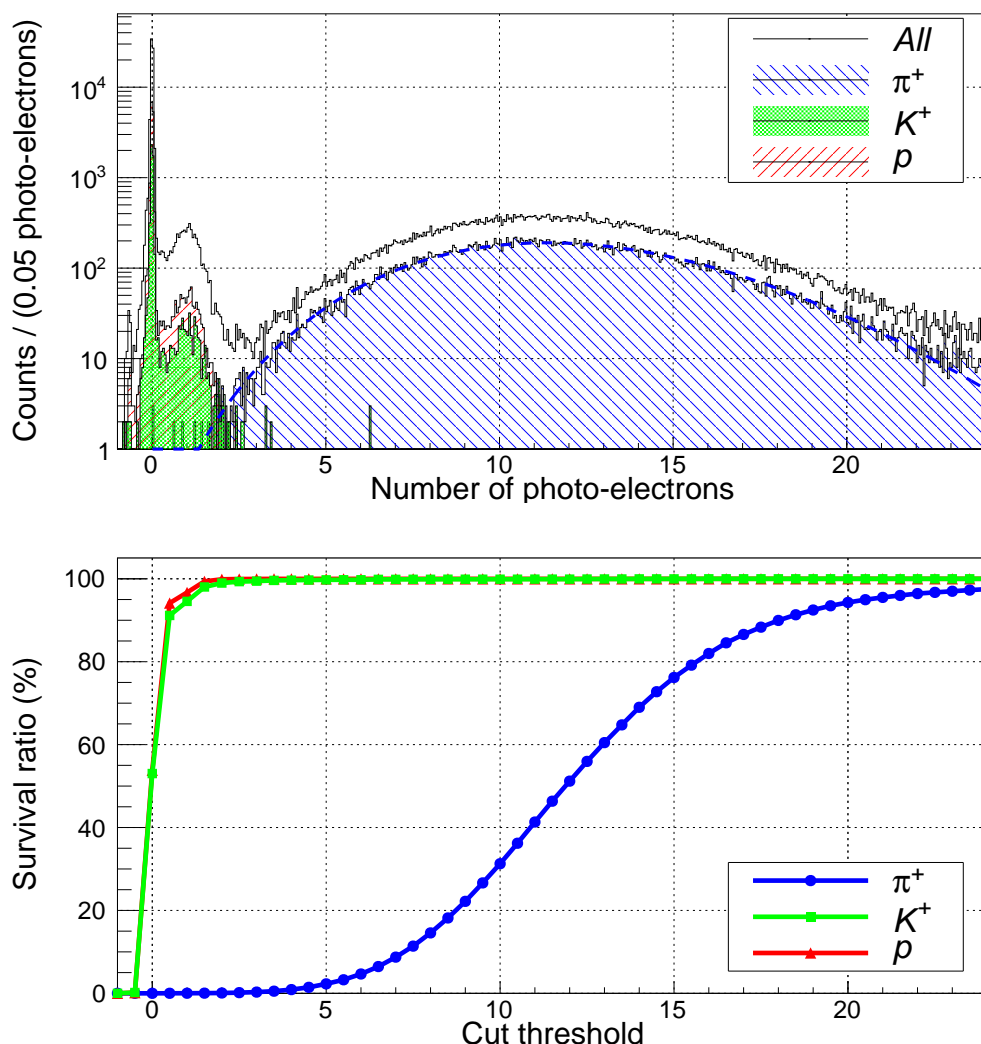


Figure 3.14: Distributions of the number of photo-electrons and particle survival ratios as a function of the cut threshold in a diffused aerogel Cherenkov counter at T44 experiment.

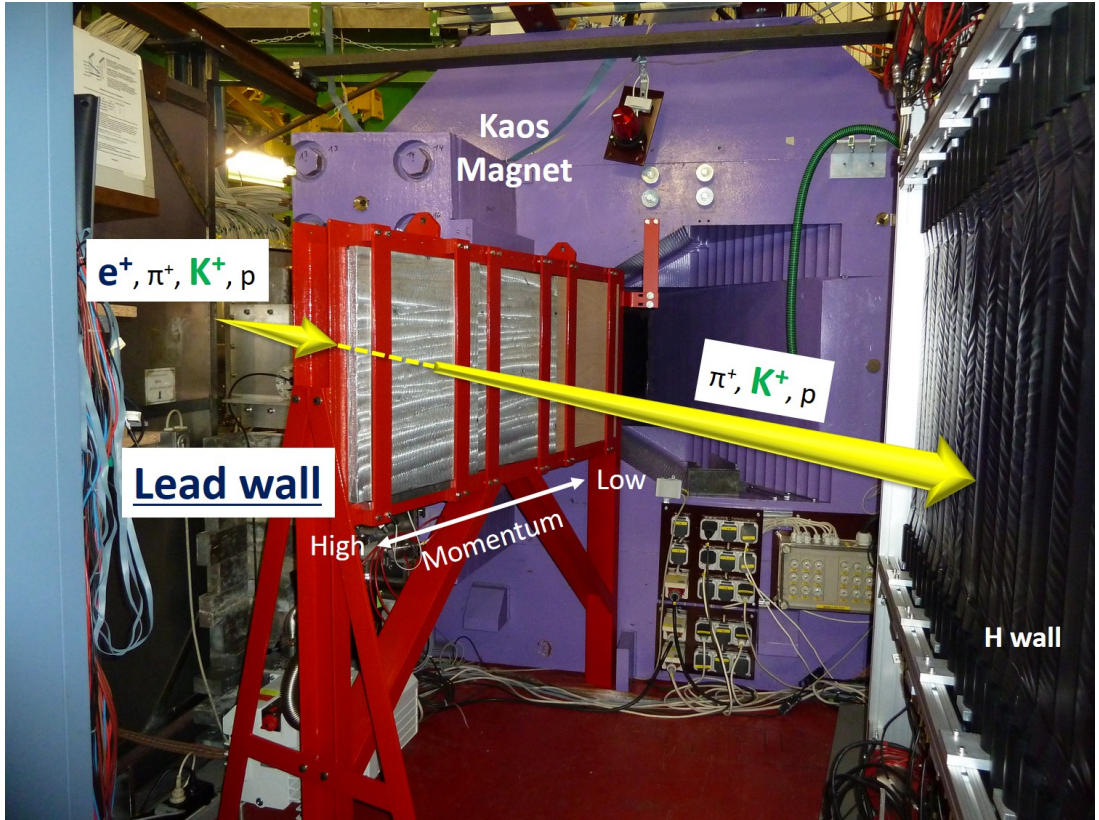


Figure 3.15: A photograph of lead walls. The TOF counters (G and I wall) and aerogel Cherenkov counters were not installed yet in the photograph.

■ Positron suppression technique using lead wall

Purpose

The large positron backgrounds from the electron-positron shower at the target contaminated in the Kaos detectors, because the Kaos spectrometer was installed at 0° with respect to the electron beam. A single rate at the Kaos detector plane was expected to be more than 40 MHz at $20 \mu\text{A}$ of the electron beam current. Data acquisition system cannot handle this high rate. In addition, the signal-to-noise ratio on the decay pion momentum become poor due to the very high accidental background. The suppression of this background was one of the most essential part to get better data quality.

A novel technique to suppress the e^+ background was introduced, namely, a lead wall with a thickness of 10~14 cm was newly designed and installed between the Kaos magnet and the Kaos detector package as a e^+ suppressor in 2012 (Figure 3.15).

Principle

The energy loss of the charged particle is understood as the collisions with atomic electrons of an absorber. However, with an energy above a few hundred MeV (critical energy), the energy loss of the electrons and positrons is dominated by bremsstrahlung. The energy loss due to the radiation is represented by [Leo],

$$-\frac{dE}{dx} = 4r_e^2 \alpha N E_0 Z^2 \left[\ln(183 Z^{-1/3}) + \frac{1}{18} - f((\alpha Z)^2) \right], \quad (3.3)$$

where

- r_e : classical electron radius,
- α : fine structure constant,
- N : number of atoms per cm³,
- E_0 : initial total energy of electron or positron,
- Z : atomic number of absorber,
- $f(z)$: correction factor (see Equation 2.26).

The energy loss of hadrons is proportional to $\rho Z/A$. On the other hand, since the energy loss of electrons and positrons is proportional to Z^2 , high Z materials, for example lead, effectively stop only electrons and positrons.

A quantity *radiation length* (X_0) is defined as a distance where electrons or positrons lose the energy to be $\exp(-1)$ due to radiation loss, and it is represented by,

$$\frac{1}{X_0} \simeq 4r_e^2 \alpha N Z (Z + 1) \left[\ln(183 Z^{-1/3}) - f((\alpha Z)^2) \right], \quad (3.4)$$

The radiation length of lead is 5.6 mm. A lead wall with a thickness of 14 cm, which was a typical effective thickness in the experiment, corresponded to $25X_0$.

In addition, since a total cross section of $K^+ p$ collision is ~ 2 times smaller than those of $\pi^+ p$ and $p p$ collisions [PDG12], π^+ and proton rates are more suppressed comparing with a K^+ rate.

The momentum resolution of Kaos spectrometer was expected to be worse due to the multiple scattering effect in the lead wall. However, the purpose of the Kaos spectrometer was kaon tagging, therefore, the momentum resolution of kaons was independent on the energy resolution of hypernuclei.

Feasibility check

We confirmed a feasibility of this method using scattering electrons in SpekB.

SpekB was the single-dipole spectrometer, which had a high momentum resolution ($\Delta p/p \simeq 10^{-4}$). The spectrometer equipped with VDCs, scintillation counters, and gas Cherenkov detector, those were similar configuration with SpekA and SpekC. We installed the spectrometer at

26.5° with respect to the electron beam. The beam energy was set at 1034 MeV, and ^{12}C target was used.

A photograph of the test experiment setup is shown in Figure 3.16. We installed lead blocks between the VDC and the scintillation counters. A thickness of the lead blocks was changed from 5 to 40 mm. Since the incoming scattered electrons were tilted by about 45°, the effective thickness was increased by a factor of ~ 1.4 . We took data with several central momenta of SpekB from 100 to 738 MeV/c. Data acquisitions were performed with a single trigger of the scintillation counter (ToF) in SpekB.

Figure 3.17 (a) shows a particle position distribution at 40-mm thick lead block with the central momentum of 738 MeV/c. We clearly separated e^+, e^- from other particles using the gas Cherenkov counter. Since most of incident particles fired in the Cherenkov detector, incident particles were dominated by high momentum electrons. The high momentum electrons were drastically decreased after the lead block as shown at 1100~1200 mm in Figure 3.17 (a). However, we found that particles which did not fire in the Cherenkov detector were increased.

In order to explain the distributions, we performed a Monte Carlo simulation using GEANT4. In the simulation code, we installed a 40-mm thick lead block, 3-mm and 10-mm thick scintillation counters, and a gas Cherenkov counter, which modeled the setup of the test experiment. Electrons with momenta of 738 MeV/c were generated in front of the lead block with uniform angular distribution ($-5 \sim +5^\circ$). A energy threshold in the 10-mm scintillation counter was set to be 0.5 MeV, and a momentum threshold of e^- and e^+ in the Cherenkov detector was applied to 30 MeV/c. The simulated distribution reproduced well the experimental one as shown in Figure 3.17 (b). We found that gamma rays and very low momentum electrons made the not-fired events in Cherenkov detector.

The consistency between experimental data and simulation results was checked by quantities of a penetration efficiency of electrons (ε_e) and a γ conversion ratio (ε_γ), defined as:

$$\varepsilon_e = \frac{N_{\text{GC Lead}}}{N_{\text{GC noLead}}}, \quad (3.5)$$

$$\varepsilon_\gamma = \frac{N_{\text{noGC Lead}}}{N_{\text{GC noLead}}}. \quad (3.6)$$

The parameters “ $N_{\text{GC Lead}}$ ”, “ $N_{\text{GC noLead}}$ ”, and “ $N_{\text{noGC Lead}}$ ” are the number of events with GC hits at lead block, with GC hits out of lead block, and without GC hits at lead block, respectively. The simulated results reproduced well with the experimental data as shown in Figure 3.18, and thus we confirmed that a lead wall design using GEANT4 was possible to be trusted.

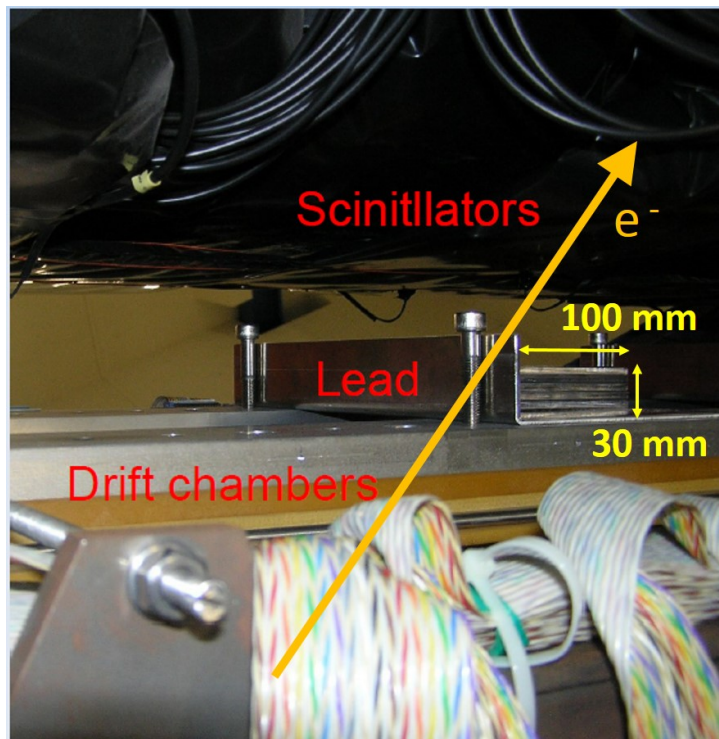


Figure 3.16: A photograph of the test experiment setup for lead wall. The photograph shows a side view of the detector package in SpekB. A scattered electron from the target was bended with the magnet, and was measured its position in drift chambers (VDCs). Lead blocks with a thickness of 5~40 mm were partially installed on the momentum dispersion plane behind the VDCs. Two layers of scintillation counters were also installed and detected charged particles. Particle identifications were performed in a gas Cherenkov detector behind the scintillation counters (out of the photograph). A gas Cherenkov detector was

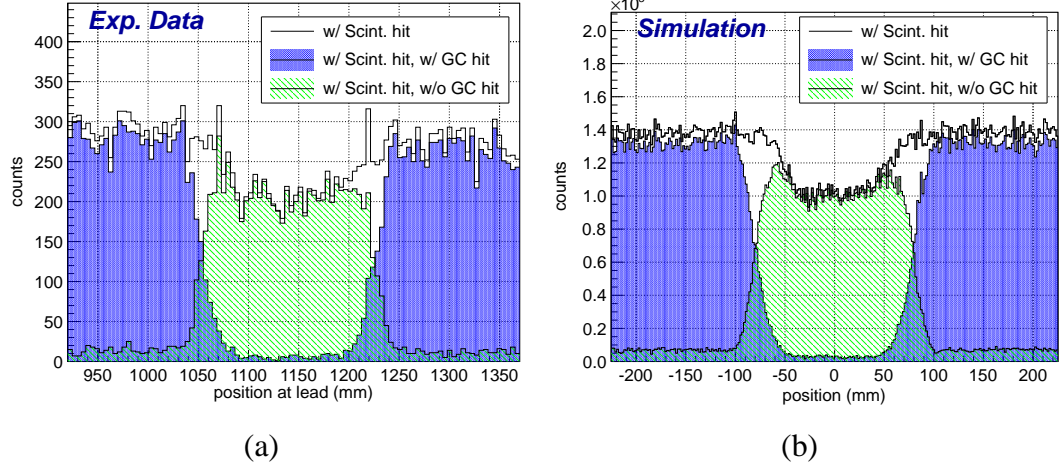


Figure 3.17: Particle distribution at lead block position in (a) an experimental data and (b) a simulation. In the simulation, electrons and pions were generated with a ratio of 20 to 1.

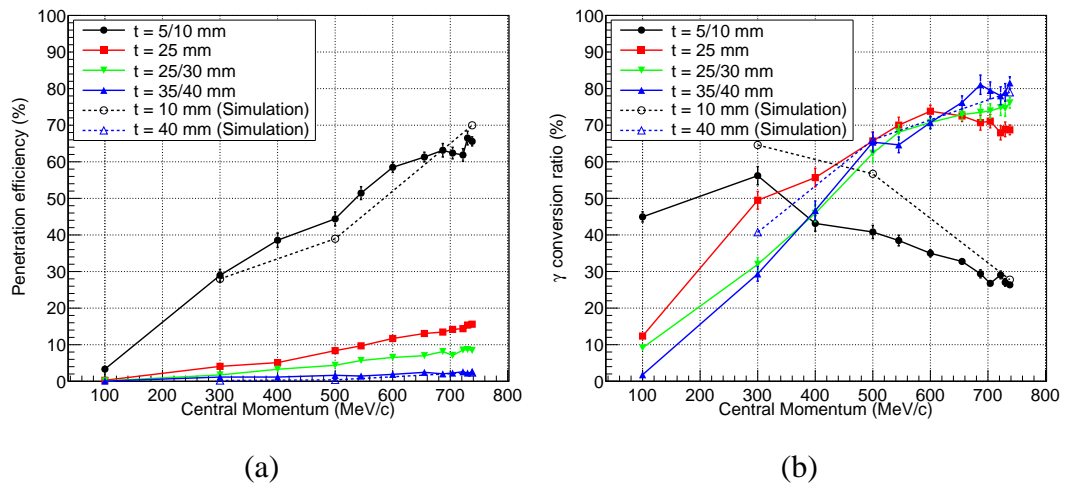


Figure 3.18: Comparisons of lead block effect between experimental data and simulated results. (a) Penetration efficiencies of electrons and (b) γ conversion ratios. The experimental data at all setup (solid lines) and the simulated results (dashed lines) were shown. In the simulation, generated angles and energy thresholds in each detector were under same conditions (see text).

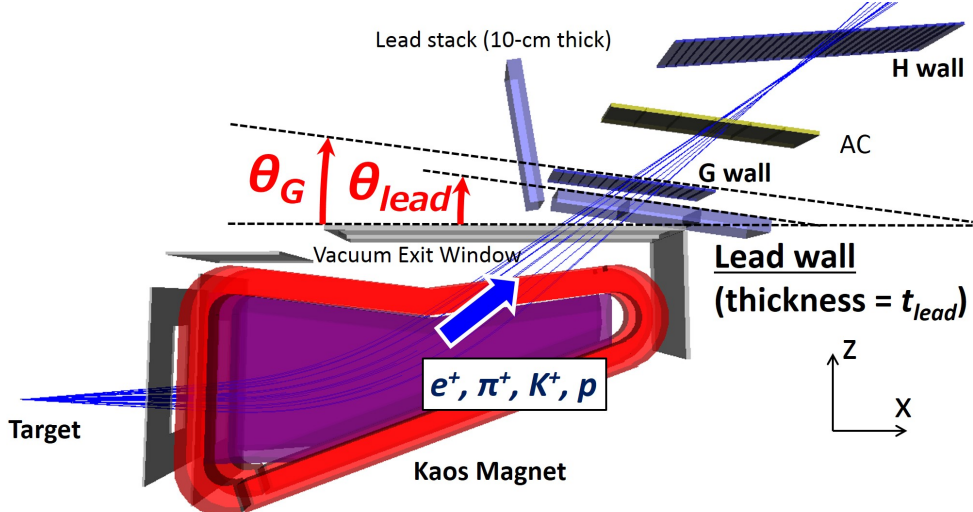


Figure 3.19: Configurations of Kaos spectrometer in GEANT4 code for the lead wall simulation. An example of a GEANT4 implementation was shown as a VRML. Definitions of parameters (θ_{lead} , θ_G , and t_{lead}) were also shown in the figure. We optimized these parameters to design the lead wall.

Design

Since the experiment and the simulation results were consistent, we proceeded the simulation to be more realistic condition, which corresponds to the Kaos setup. Figure 3.19 shows configurations of the Kaos magnet and the detectors in GEANT4 code in order to estimate the lead wall effect in the Kaos spectrometer. In the model, electrons, pions, kaons, and protons were generated at the target position uniform distributions in momenta (400~1500 MeV/c) and in an azimuthal angle ($-10 \sim +10^\circ$). The lead wall with a geometrical thickness of t_{lead} was installed behind the vacuum exit window with an opening angle of θ_{lead} . Since the particles were introduced with $\sim 45^\circ$, the effective thickness for the particles was increased by a factor of ~ 1.4 . The scintillation counter (G wall) was also installed behind the lead wall with an opening angle of θ_G for the vacuum exit window. The multiple scattering, the ionizations, the bremsstrahlung, and positron annihilations were taken into account as physics processes of e^+ . In addition, well-known GHEISHA code [Fese85], which were parametrized models to implement elastic and inelastic hadron scattering from nuclei in low energy region ($<\sim 20$ GeV), was also included to be calculate hadron-nucleon interactions.

Dependences of particle detection ratios on the lead wall thickness were estimated for each

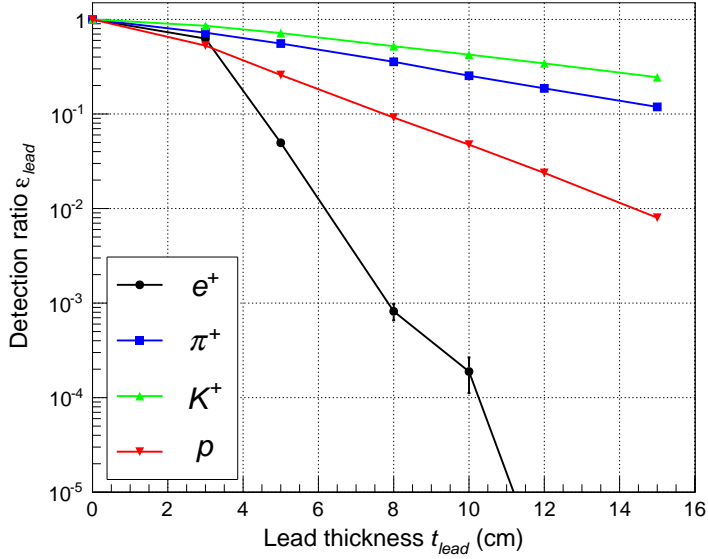


Figure 3.20: Dependences of trigger coincidence ratio on the lead wall thickness estimated by GEANT4 simulation. The triggers required that the same particle hit in G and H wall as the generated particle for the hadron generations. By contrast, the energy threshold of 0.1 MeV in G and H wall was required for the positron generation in order to take electron or γ -ray backgrounds into account.

particle as shown in Figure 3.20. The ratio was defined as:

$$\epsilon_{lead}^i = \frac{N_{w/lead}}{N_{w/o\ lead}}, \text{ (with } i = e^+, \pi^+, K^+, \text{ and } p\text{)}, \quad (3.7)$$

where $N_{w/lead}$ is the number of particles i detected in G and H walls with the lead wall; and $N_{w/o\ lead}$ is without the lead wall. The ratio for kaons ($\epsilon_{lead}^{K^+}$) was $\sim 40\%$ decreased due to the multiple scattering effect and the hadronic interactions at 10-cm-thick. However, the ratio for positrons ($\epsilon_{lead}^{e^+}$) was expected to be much more decreased by a factor of $\sim 10^{-4}$ at the same thickness.

Besides, the ratios for pions ($\epsilon_{lead}^{\pi^+}$) and protons (ϵ_{lead}^p) were 30% and 6% respectively. These results were well described with the differences of the total cross sections for each collision. Furthermore, in the low momentum region, protons stopped in the lead wall due to the larger energy loss by atomic collisions.

In order to optimized the lead wall thickness and position, we estimated hyperon yields and background rates.

The background rate on the coincidence between Kaos and SpekC was obtained with trigger

rates in each spectrometer and its time window as follow. It was assumed that the rate was dominated by the accidental backgrounds.

$$N_{b,g} = N_{SpekC} \times \sum_{i=e,\pi,K,p} (N_{Kaos}^i \times \varepsilon_{\text{lead}}^i) \times 100 \text{ ns}, \quad (3.8)$$

where N_{SpekC} was SpekC trigger rate, and N_{Kaos}^i was Kaos trigger rate for each particle without the lead wall. The measured rates in 2011 experiment was used as some trigger rates: $N_{SpekC} = 1 \text{ kHz}/\mu\text{A}$, and $\sum(N_{Kaos}^i \times \varepsilon_{\text{lead}}^i) = 1 \text{ MHz}/\mu\text{A}$. An accidental coincidence between G wall and H wall was also taken into account under 2 MHz/ μA in G wall, 2.5 MHz/ μA in H wall, and 30-ns coincidence window. Incoming particle rates without the lead wall in Kaos were assumed as $e^+ : \pi^+ : K^+ : p = 10000 : 100 : 1 : 100$.

Since the hyperon production rate is proportional to the beam current and the detection ratio of K^+ , the relative hyperon rate was simply defined as:

$$N_Y = N_e \times \varepsilon_{\text{lead}}^K. \quad (3.9)$$

where N_e is the number of the electrons normalized with 1 μA . However, a corrected hyperon rate ($N_Y^{coll.}$) is limited with the accepted rate of the data acquisition system (ε_{DAQ}) as follow:

$$N_Y^{coll.} = N_e \times \varepsilon_{\text{lead}}^K \times \varepsilon_{DAQ}. \quad (3.10)$$

where we assumed the ε_{DAQ} based on the result of the experiment in 2011.

$$\varepsilon_{DAQ} = \begin{cases} 1 & (N_{b,g} < 400 \text{ Hz}), \\ 400 \text{ Hz}/N_{b,g} & (N_{b,g} > 400 \text{ Hz}) \end{cases} \quad (3.11)$$

We estimated the hyperon yields with several settings by changing the beam current (N_e), the thickness (t_{lead}), and angles (θ_{lead} or θ_G). Figure 3.22 shows the estimated collected hyperon rates ($N_Y^{coll.}$) as a function of the geometrical lead thickness (t_{lead}). We found that the hyperon yield was maximized at 14~16-cm thick lead with a tilted angle of 10°.

When the lead thickness increases, as the reconstructed time resolution at target becomes worse due to the multiple scattering effect, the contaminations of the backgrounds are increased. In addition, since the particle identification was performed by TOF measurements between the scintillation counters, the installed position of G wall is directly related with the goodness of the particle identification. We assumed a contaminated rate in the particle identification process as,

$$N_{\text{PIDmiss}} \propto F_{\text{Recon}} \times F_{\text{TOF}}, \quad (3.12)$$

where F_{Recon} is a factor due to the multiple scattering effect, and F_{TOF} is due to the TOF measurement. F_{TOF} was obtained by the π^+ contamination ratio on the TOF distribution of K^+ in

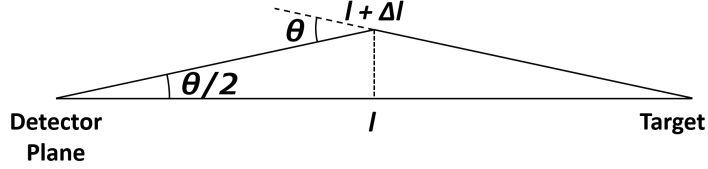


Figure 3.21: A simple drawing for an assumption of F_{Recon} . A reconstructed flight pass length from the detector plane to the target (l) was changed into Δl due to a multiple scattering in the lead wall. The scattering angle was defined as θ .

the GEANT4 simulation. F_{Recon} was simply assumed to be proportional to the scattered angle in the lead wall with a first-order approximation, because the reconstructed time resolution at the target is obtained with an error propagation as follows:

$$\Delta t = \sqrt{(l\Delta\beta)^2 + (\beta\Delta l)^2} \underset{\text{at } \beta \sim 1}{\sim} \Delta l, \quad (3.13)$$

where β is a particle velocity and l is a flight pass length from the detector plane to the target (see Figure 3.21). We assumed that this equation is written as follows at a small multiple scattering angle due to the lead wall (θ):

$$\begin{aligned} \left(\frac{l + \Delta l}{2}\right)^2 &= \left(\frac{l}{2}\right)^2 + \left(\frac{l}{2} \tan \frac{\theta}{2}\right)^2, \\ 2l\Delta l &\sim l^2 \tan^2 \theta \quad (\text{with } \Delta l^2 \sim 0), \\ \Delta l &\propto \theta \quad (\text{with } l = \text{const.}). \end{aligned} \quad (3.14)$$

Since the root-mean-square of the angular distribution of θ is proportional to the square root of the absorber thickness [Lync91], F_{Recon} is proportional to the lead wall thickness. Therefore, Equation 3.12 can be written with:

$$N_{\text{PIDmiss}} \propto t_{\text{lead}} \times F_{\text{TOF}}. \quad (3.15)$$

Using these quantities, we defined a figure of merit as follow,

$$\text{F.O.M} = N_Y^{\text{coll.}} / N_{\text{PIDmiss}}. \quad (3.16)$$

The estimated result of F.O.M is shown in Figure 3.23. As a result, we got the maximum F.O.M with the 12-cm thick lead wall at $\theta_{\text{lead}} = 10^\circ$ and $\theta_G = 10^\circ$. In the experiment, θ_{lead} was set at 8° due to an interference with projections of the Kaos magnetic yoke. The thicknesses were 10 cm, 12 cm, and 14 cm in the low, middle, and high momentum regions respectively in order to reduce the multiple scattering effect in the low momentum region.

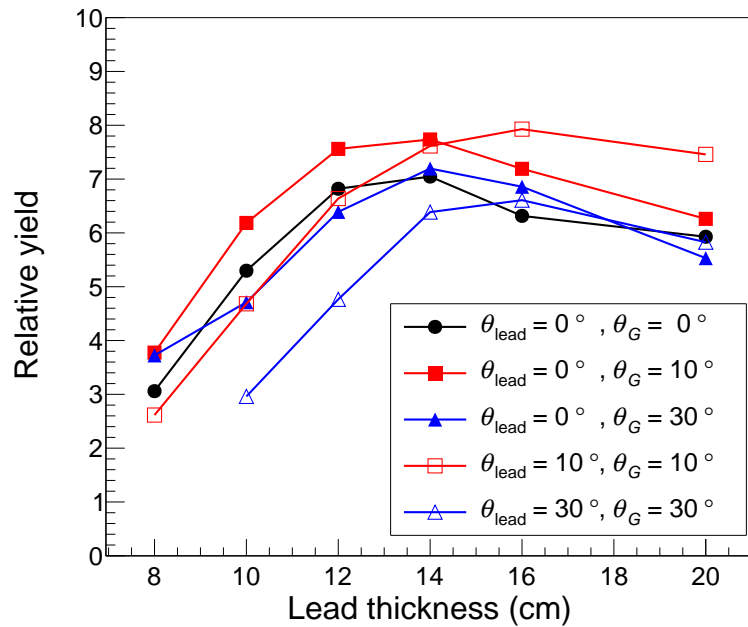


Figure 3.22: Collected hyperon yield ($N_Y^{coll.}$) dependences on lead wall thickness.

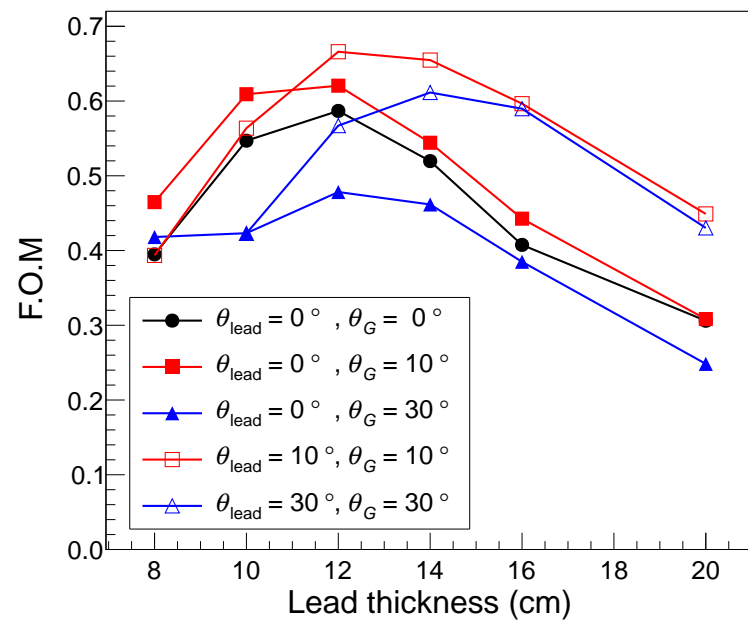


Figure 3.23: Figure of merits (F.O.M.) dependences on lead wall thickness.

3.4 Data acquisition system

A diagram of the trigger logic for data acquisition was shown in Figure 3.24. Analog signals from PMTs were integrated to the charge information during Gate signal on, and digitized in Analog-to-Digital-Converter (ADC). Discriminated signals were also digitized in Time-to-Digital-Converter (TDC) in order to get the timing information. Front-end PCs, which were installed on each spectrometer platform, controlling the data structures of each module. The accumulated data in the hall were sent through the Ethernet to a main data acquisition computer in the counting room. The detail will be explain in the following sections.

3.4.1 Kaos logic

A triple coincidence between three layers of scintillation counter (G, I, and H walls) made a trigger logic of Kaos. An output signal from PMT was split to an ADC line and a TDC line with a splitter module (GSI SU 1601). The signal of the ADC line was fed to a ADC module (LeCroy 1885F) after 250 ns logic delay module (GSI DP 1620). The signal of the TDC line was converted to digital signal with a Constant-Fraction-Discriminator (CFD) (GSI CF 8105), and fed to a TDC module (LeCroy 1875) after 500 ns logic delay module (GSI DL 1610). The splitter module outputs a sum of the signals from the top PMT and from bottom PMT in each paddle. The sum signal was also converted with the CFD, and fed to a logic module (VUPROM2), which equipped a Xilinx VIRTEX-4 FPGA chip and 256 I/O channels, for the trigger generation. A schematic drawing of the logic circuit in VUPROM2 is shown in Figure 3.25. VUPROM2 output a Kaos trigger signal, which was filtered with geometrically possible G, I, and H paddle combinations in straight line. The detail of the combination matrix is shown in Table 3.5.

AC1 and AC2 were not included in the trigger. The signal from PMT was divided to the ADC and TDC line. The signal of the ADC line was delayed with a ~400 ns analog cable decay, attenuated with two dividers, and fed to a ADC module (CAEN V792). The signal of the TDC line was digitized with a Leading-Edge-Discriminator (LeCroy 4413), and fed to a TDC module (CAEN V775) after the delay module GSI DL 1610. The voltage thresholds of each discriminator were set below one photo-electron excepting for the signals from PMT R877-100. The thresholds were set to minimum values (-15 mV) for the signal from R877-100 due to the low signal hight.

3.4.2 SpekA and SpekC logic

Trigger logics in SpekA and SpekC were made by single layer hit in scintillation counter ToF. Analog signal of the PMT from ToF was divided to ADC line and TDC line. ADC module LeCroy 2249A and TDC module LeCroy 2228A were used in order to measure the signal height and timing. A Leading-Edge-Discriminator (LeCroy 4413) was used to digitize the signal. The digitized signals from the both ends of ToF counter produced logical AND, and a trigger for each pion spectrometer were produced by a logical SUM of the all ToF paddles. A logic for scintillation counter dE had a similar circuit, while it did not join the trigger because the low detection efficiency for charged particles was concerned.

A signal from the gas Cherenkov detector was not included in the trigger. The signal was fed to an ADC module (LeCroy 2249A). A digitized signal from the VDCs was fed to a TDC module (LeCroy 4291B).

3.4.3 Coincidence logic

The trigger signals of SpekA and SpekC were sent to a Kaos platform, and the coincided with the trigger signal of Kaos. The logic was $(\text{SpekA} \vee \text{SpekC}) \wedge \text{Kaos}$. The trigger was interrupted with a busy signal from the data acquisition PC. The outgoing coincidence signal was fed to the event builder module, which merged the information from each module and labeled the event number each other. The ADC gate signals, TDC stop signals, and arming signals for TDC LeCroy 1875 were also made from the coincidence signal.

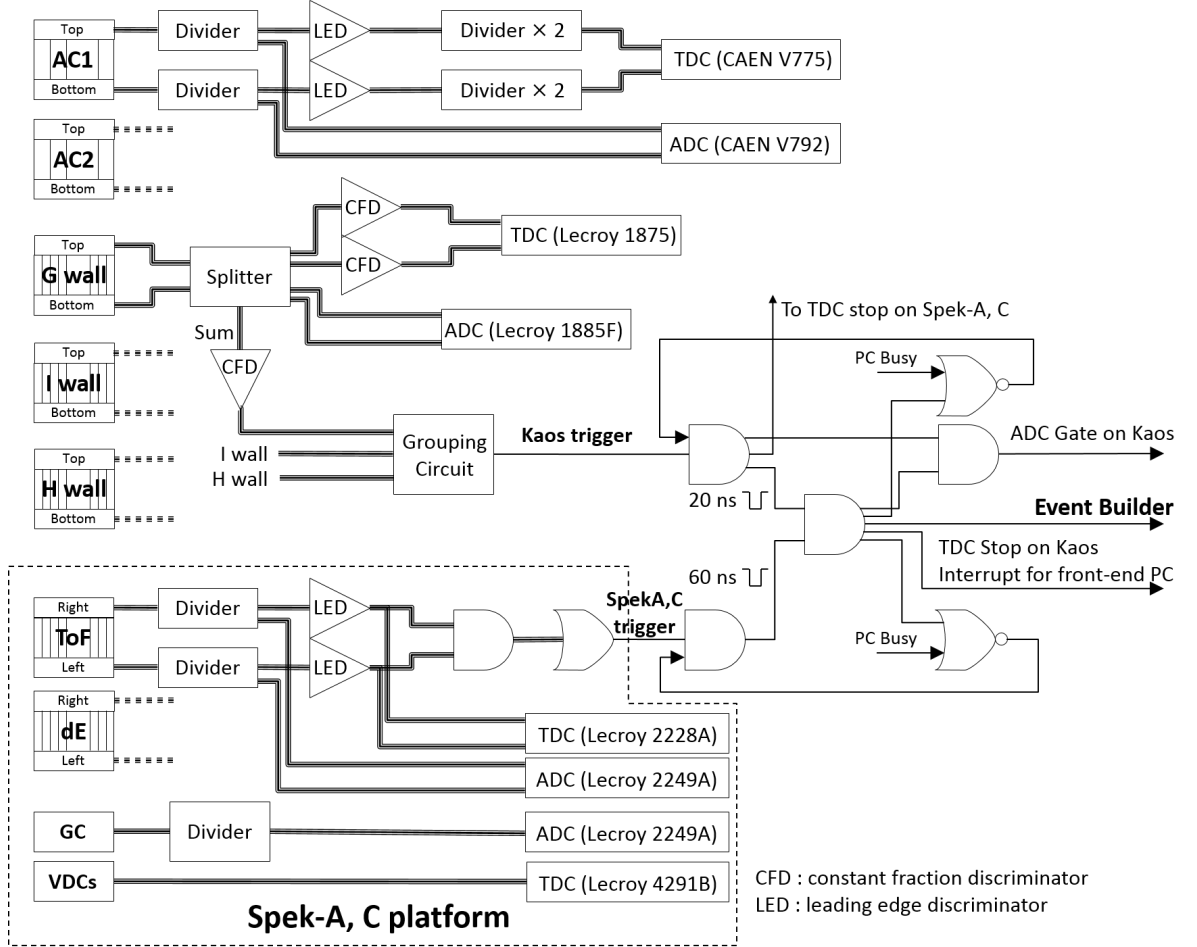


Figure 3.24: An overview of the trigger logic. Signals from PMTs in the scintillation counters, G, I, and H walls produced the Kaos trigger in a grouping circuit on FPGA module after digitizing the sum signals of top and bottom PMTs in CFD module. SpekA and SpekC triggers were produced by a logic SUM of all paddles after making a logic AND of right and left PMTs in the scintillation counter, ToF. A trigger of data acquisition was produced by a logic $(\text{SpekA} \vee \text{SpekC}) \wedge \text{Kaos}$ with a busy signal from a PC for the data acquisition. The trigger provided gate signals for ADC modules, and stop signals for TDC modules. Time and charge information were recorded in the data acquisition PC with their event number.

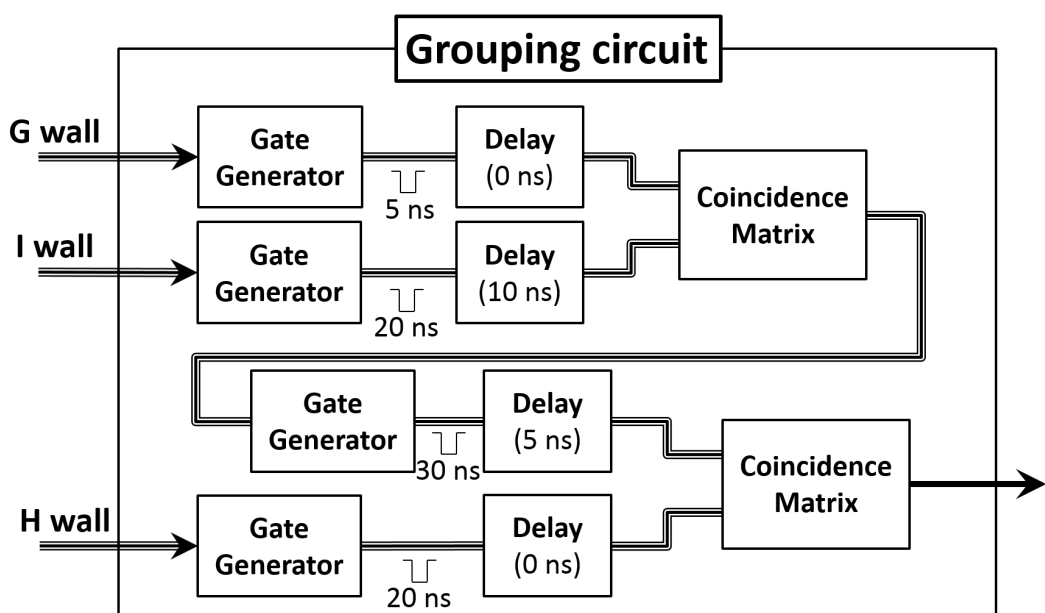


Figure 3.25: A schematic drawing of the grouping circuit. (Revised from Ph.D thesis by A. Esser [EsseD].) Timing was adjusted to maximize the Kaos trigger rate. Details of coincidence matrix are shown in Table 3.5

Paddle No.	I0	I1	I2	I3	I4	I5	I6	I7	I8	I9	I10	I11	I12	I13	I14
G0	H0~19	H6~29	H21~29												
G1	H0~6	H0~21	H7~29	H23~29											
G2		H0~7	H0~23	H8~29	H24~29										
G3		H0~8	H0~24	H10~29	H26~29										
G4			H0~10	H0~26	H11~29	H28~29									
G5				H0~11	H1~28	H13~29	H29								
G6				H0~1	H0~13	H2~29	H14~29								
G7					H0~2	H0~14	H3~29	H15~29							
G8						H0~3	H0~15	H4~29	H17~29						
G9							H0~4	H0~17	H6~29	H18~29					
G10								H0~6	H0~18	H7~29	H20~29				
G11									H0~7	H0~20	H8~29	H21~29			
G12										H0~8	H0~21	H9~29	H22~29		
G13										H0	H0~9	H0~22	H10~29	H24~29	
G14											H0	H0~10	H1~24	H12~29	

Table 3.5: Coincidence matrix elements in VUPROM2. Each element showed accepted paddle numbers of H wall for each paddle number of G (Column) and paddle number of I (Row). For example, the Kaos trigger was output from VUPROM2 with H6~29 hits when G0 and I0 fired.

Chapter.4

Data taking

We performed the experiments of the hypernuclear decay pion spectroscopy in twice. The first experiment was carried out from 25th May to 14th June and from 19th July to 1st August in 2011 as a pilot experiment. The purpose of this pilot run was to check the feasibility whether this experimental method works or not. The experimental setup was a bit different from the setup as explained in Chapter 3. The second experiment was from 24th October to 12th November in 2012 after improving the detector setup. This term corresponds to the first physics run of the hypernuclear decay pion spectroscopy.

In this chapter, details of the data acquisition and the results in the pilot experiment will be shown. Later, I will explain improvements towards the physics run and a summary of the data acquisition.

4.1 Pilot experiment

When the hypernuclear decay pion spectroscopy was proposed, nobody had checked the experimental feasibilities. Angular and momentum distributions of a K^+ meson was already known well thanks to the experiments using the electron beams [Glan04, McCr10, Dey10, Pere10]. The counting rate for the background particles was able to be estimated from the results of the $(e, e' K^+)$ reaction spectroscopy at JLab, in addition, techniques of the K^+ identification were already established there. However, the particle rate around 100 MeV/c, which is similar momentum to it of pions from hypernuclear decay, had not been studies when the 1 GeV electron beam is introduced. If the rate is significantly large, this hypernuclear decay pion spectroscopy does not work because peaks of decay pion will be hidden by backgrounds. Therefore, it is essential to check the conditions in each spectrometer. In this section, differences of the detector setup with the physics run, a summary of the data acquisition, and some results will be shown.

4.1.1 Detector setup

In the pilot experiment, the target, the positions of the spectrometers, and the beam line components are the same as explained already in Chapter 3. However, detector setups in the Kaos spectrometer and the Spek-C spectrometer are different.

Figure 4.1 shows differences of the detector setups of Kaos spectrometer between the pilot and the physics experiments. The setup in this pilot experiment followed the previous experiments which was the elementary cross section measurement of the $p(e, e' K^+) \Lambda, \Sigma^0$ reactions [Ache10, AcheH]. In the pilot experiment, a lead wall and the second layer of the aerogel Cherenkov counter were not installed. Multi-wire proportional chambers (MWPCs) were installed in front of the scintillation detector G wall. However, we did not use the MWPCs in the analysis because they did not work well under the high counting rate. The G wall consisted of 30 scintillator paddles, however, the paddles of the high momentum side (No.23~29) did not operate because they are out of the acceptance. TOF lengths were 0.8 m at the low momentum side and 1.2 m at the high momentum side. This length is shorter than that in the physics run (1.2~2.2 m), because the G wall was installed more downstream position.

During the pilot experiment, tagger counters were installed to reduce a large positron background in mid-plane due to the e^-e^+ shower from the target. Figure 4.2 shows a photograph of the tagger counters. As the positrons were generated with very forward angles with respect to the beam direction, the distribution of the positrons concentrated on the mid-plane of the spectrometer. The signal-to-noise ratio in the mid-plane is expected to be poor because the counting rate of the positron background is quite high in comparison with K^+ mesons. Therefore, the tagger counters were installed with a off space in the mid-plane. They consisted of two large horizontal scintillation counters read from both ends by PMTs (Philips XP2262B). The gap width between two counters was 80 mm. The size of each counter was $1800^W \times 200^H \times 10^T$ mm³.

The gas Cherenkov detector in Spek-C did not work well because the gas leakage was under repair.

The trigger for the data acquisition system was $(\text{SpekA} \vee \text{SpekC}) \wedge \text{Kaos}$, it was same as the physics run. The Kaos trigger was made with a coincidence of the scintillation counters ($G \wedge H$). After the tagger counters were installed, the Kaos trigger was updated to a triple coincidence ($G \wedge H \wedge \text{Tagger}$).

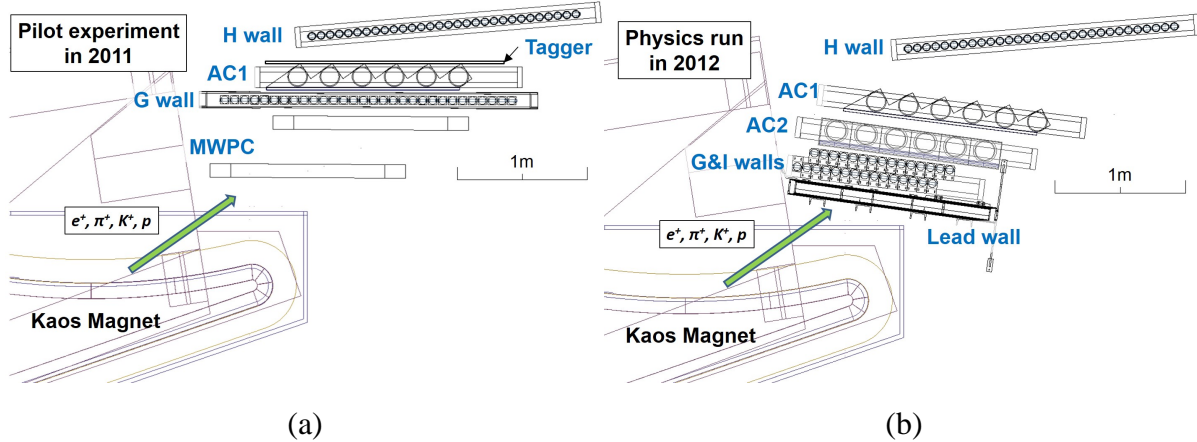


Figure 4.1: Differences of detector setup in the Kaos spectrometer. (a) Setup of the pilot experiment in 2011. (b) Setup of the physics run in 2012. In the pilot experiment, the lead wall, I wall, and AC2 were not installed. MWPCs, were installed, while they were not used in the analysis. During the experiment, tagger counters were installed just behind AC1.

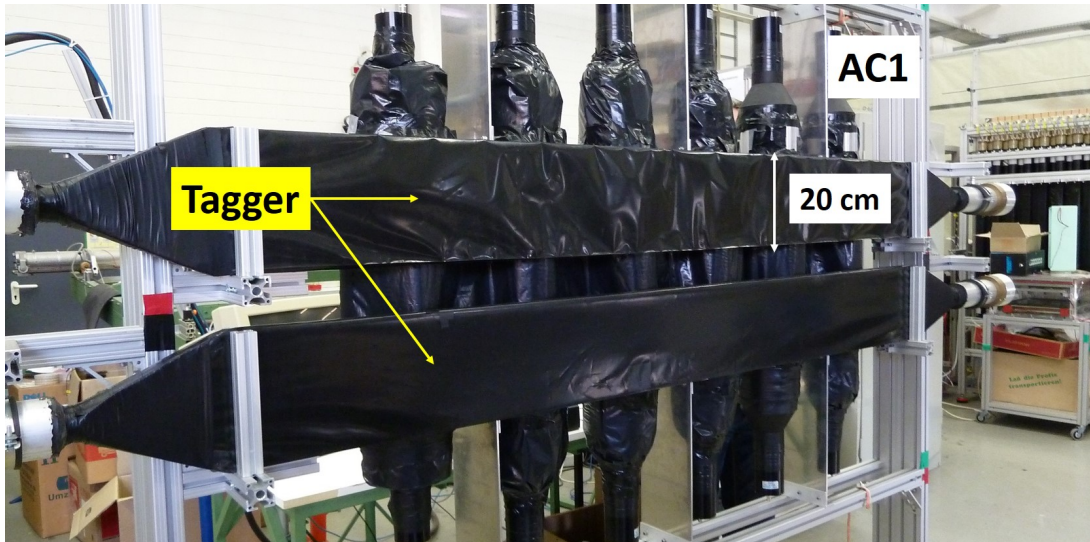


Figure 4.2: A photograph of tagger counters. Two scintillation counters (tagger top and tagger bottom) were installed just downstream of AC1. There was a 80 mm gap between the two counters not to detect particle in the mid-plane, in which the large positron background is expected.

4.1.2 Data summary

In the pilot experiment, the typical beam current was $0.3\sim2.0\mu\text{A}$. Amount of the introduced beam was 0.68 C in the first three weeks (25th May to 14th June); and it was 0.74 C in the next two weeks (19th July to 1st August).

Counting rates in each spectrometer were measured, because we had to know whether we can take data with the designed setup or not.

Figure 4.3 shows a trigger rate of Spek-C. The counting rate was increased in proportion to the beam current with a gradient of $1\text{ kHz}/\mu\text{A}$. Because the designed beam current was $\sim20\mu\text{A}$, the expected counting rate is 20 kHz. This expected rate is enough low to handle the signals in the current trigger system, and so we found that we do not need to update the detectors and the logic circuits in the pion spectrometers.

Figure 4.4 shows trigger rates of the scintillation walls in the Kaos spectrometer. The counting rates of G and H walls are proportional to the beam current in the low beam current, however, they start to get out of the linear line about $\sim0.7\mu\text{A}$, then, they saturate their rate at 3000 kHz. The coincidence rate between G and H walls also have similar curve. Therefore, the beam current was limited with $0.5\mu\text{A}$ in the G and H coincidence trigger.

After the tagger counters were installed, the saturation of the trigger rate was suppressed. The triple coincidence rate between G, H, and Tagger was $\sim0.4\text{ MHz}/\mu\text{A}$. However, because the base lines of the PMT outputs of the tagger counters shifted above $2.5\mu\text{A}$ due to the too high counting rate, the beam current was limited with $2.0\mu\text{A}$.

As the expected particle rates per current are $\sim2.5\text{ MHz}/\mu\text{A}$, the expected particle rate at designed beam current ($20\mu\text{A}$) will be 50 MHz. The Kaos trigger system cannot handle this high rate. In addition, a counting rate of the PMT is expected to $>4\text{ MHz}$ at $20\mu\text{A}$, this rate is a few times higher rate than the operation limit of the PMT. For this reason, the improvement of the detector system for the Kaos spectrometer is important to run under the higher beam current.

4.1.3 Results

Figure 4.5 shows a 2-dimensional distribution between the energy deposit in the scintillation counters and the mass square calculated from the velocity and momentum in Kaos. In the light mass square region, there were many events which correspond to π^+ s and e^+ s. Protons were also observed at $\text{Mass}^2 \sim 1(\text{GeV}/c^2)^2$. K^+ s should be $dE/dx \sim 2\text{ MeV}$ and $\text{Mass}^2 \sim 0.25(\text{GeV}/c^2)^2$, however, we could not observe clear K^+ signal there due to the large background tail from π^+

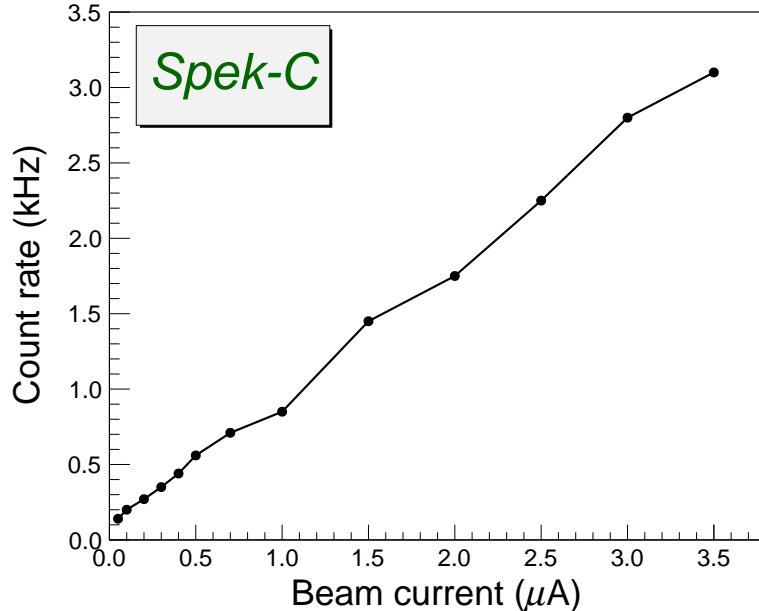


Figure 4.3: Counting rates of Spek-C in the pilot experiment. The counting rate is increased in proportion to the beam current. The rate have an offset (~ 100 Hz) from the cosmic ray.

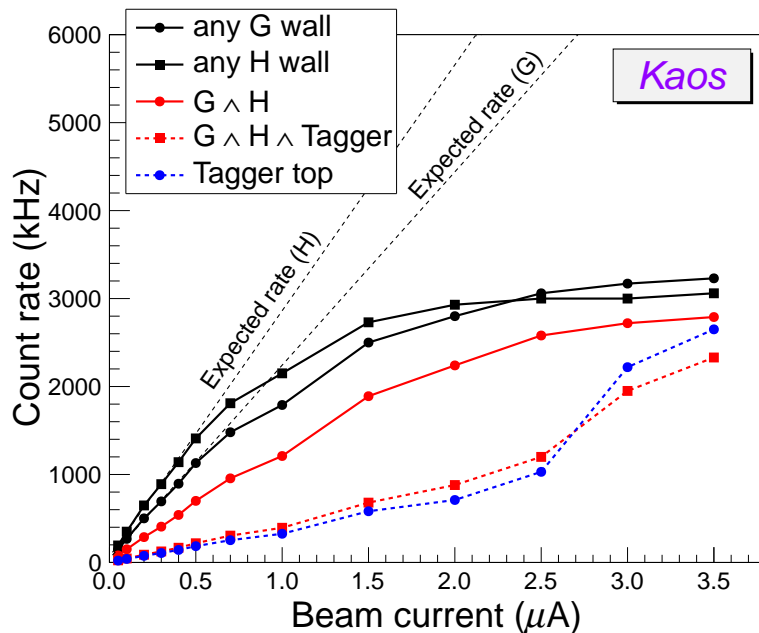


Figure 4.4: Trigger counting rates of Kaos in the pilot experiment. The rates for five kinds of triggers (any G wall hit, any H wall hit, G&H coincidence, G&H&tagger coincidence, and top scintillator of the tagger counter) were shown. The expected rates in each wall are the extrapolation of 0~0.3 μA . The rates are saturated around 3 MHz.

and e^+ events.

After squared regions were selected as π^+ , K^+ , and proton events, coincidence time spectra between Spek-C and the Kaos spectrometer was obtained as shown in Figure 4.6. Clear “ π^-, p ”, “ μ^-, p ”, and “ e^-, p ” coincidence peaks were observed on the spectrum with the proton selection in Kaos. With the π^+ selection, “ π^-, π^+ ” coincidence peak was confirmed, however, other peaks such as “ μ^-, π^+ ” coincidence peak were not obtained due to the large accidental background events. “ π^-, K^+ ” coincidence events in which the hypernuclear decay pion events are contained should exist between “ π^-, π^+ ” and “ π^-, p ” coincidence peaks, however, there are no visible peaks after K^+ region was selected in Kaos.

Though the “ π^-, K^+ ” coincidence events were not observed, events in the expected timing window were selected. Figure 4.7 shows a momentum spectra in Spek-C at expected “ π^-, K^+ ” position. Simultaneously, events out of the expected time window are selected in order to estimate background which originates from the accidental coincidence between Spek-C and Kaos in the trigger (accidental background).

Though there are possible peak candidates, any clear peaks were not observed in the momentum spectrum. However, in this pilot experiment, introduced beam charge was ~ 10 times less than the requirement, in addition, the performance of K^+ identification was poor in Kaos. As a result, from the result of the pilot experiment, we found that the counting rate in Spek-C was enough low to measure the pion momentum, and improvements to suppress the backgrounds is necessary in Kaos.

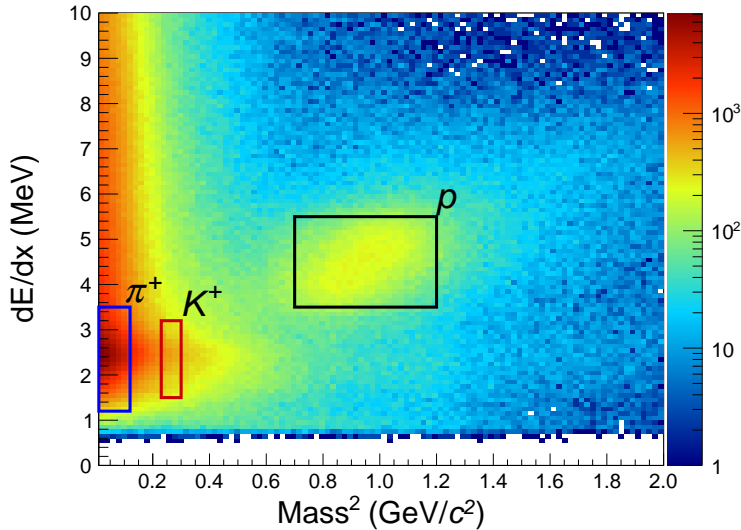


Figure 4.5: A particle distribution on a particle energy deposited in the scintillation counter and a reconstructed mass square in the Kaos spectrometer. Squared regions are selected as π^+ s, K^+ s, and protons.

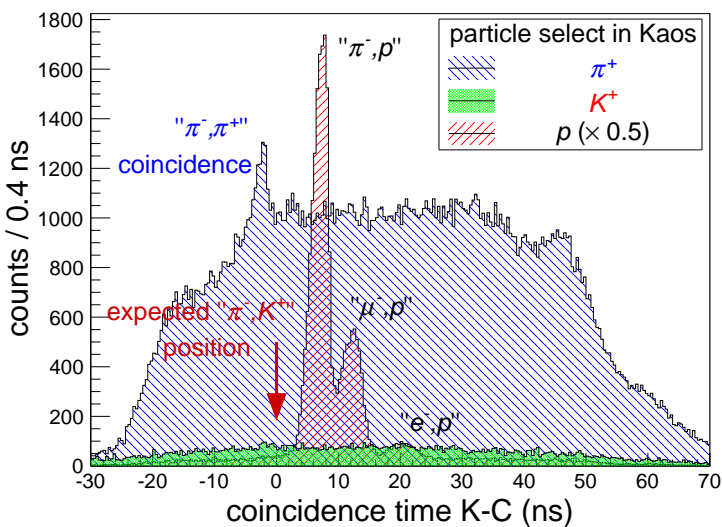


Figure 4.6: Coincidence time spectra between Kaos and Spek-C in the pilot experiment after particle selections in Kaos. Expected peak position of the “ π^-, K^+ ” coincidence is set to zero. With a proton identification in Kaos, three peaks which corresponds to π^- , μ^- , and e^- were found. A coincidence peak between π^- and π^+ is also found, however, other coincidence peaks such as “ μ^-, π^+ ” cannot be observed. The accidental background between Kaos and Spek-C is dominated because of a large e^+ background in the Kaos spectrometer. No peak structure is found around expected peak position of the “ π^-, K^+ ” coincidence after K^+ is selected.

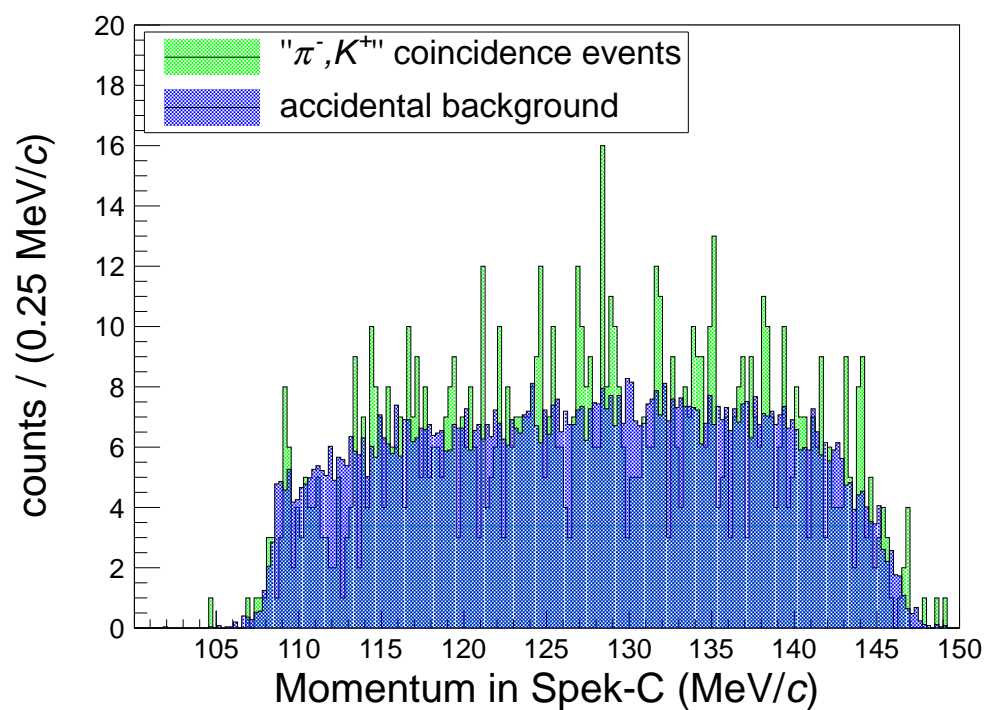


Figure 4.7: A momentum distribution in Spek-C on the pilot experiment in 2011. Expected hyperon or hypernuclear decay events are selected at ± 1.5 ns on the coincidence time spectrum between Kaos and Spek-C after K^+ events are selected. Events out of the time window are selected to estimate an accidental background distribution, that is scaled by a ratio of the entries (the number of events in the " π^-, K^+ " coincidence / the number of events in the accidental background).

4.2 Physics run

From the results of the pilot experiment, we clarified that the particle rate in the pion spectrometers was enough low to be handled by our the data acquisition system. On the other hand, we also found that detector updates are necessary in Kaos to take data with much higher beam intensity. After the analysis of the pilot experiment was summarized, I will describe improvements of the experimental setup so as to approach the designed beam intensity ($\sim 20 \mu\text{A}$).

4.2.1 Improvements

The differences of the Kaos detector setup are already shown in Figure 4.1. The different points are represented by the followings:

- The MWPCs and tagger counters were uninstalled.
- The lead wall and AC2 were newly installed.
- The scintillator paddles of G wall were re-aligned, half of paddles were used for the I wall.
- The detector positions were optimized so as to get longer TOF length.

The details of each detector were already explained in Section 3.3.3.

Figure 4.8 shows rates of each PMT in H wall normalized by the beam current. Thanks to the lead wall, the large e^+ background was suppressed. A typical counting rate of a PMT was 200 kHz at $20 \mu\text{A}$, that was about 20 times less than the rate in the pilot experiment. The Kaos trigger rate was about 30 kHz at $20 \mu\text{A}$. Since the Kaos trigger rate in the pilot experiment was about 1000 kHz at $2 \mu\text{A}$, the rate was reduced by a factor of 30 even in 10 times higher beam intensity. This rate was able to be handle in the current Kaos logic circuit, we succeeded to suppress most of e^+ background.

On the other hand, because many background particles were leaked from a geometrical gap between the lead wall and the lead stack, the PMT-HV for the nearest paddles in G and I wall (G0 and I0) were turned off to take data with better signal-to-noise ratio.

4.2.2 Data summary

Table 4.1 shows a summary of data in the physics run. Thanks to the improvements, in the physics run, we succeeded to take data with the 10 times higher beam intensity than the pilot

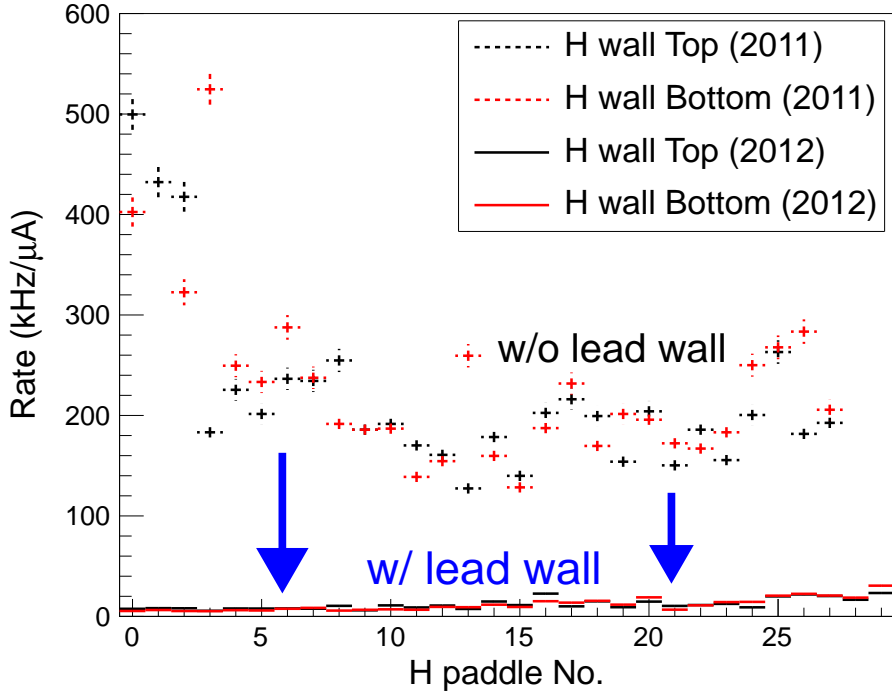


Figure 4.8: Comparisons of counting rates for each paddle in H wall between the pilot experiment in 2011 and the physics run in 2012. After the lead walls were installed, we succeeded to decrease the counting rate by a factor of ~ 20 .

experiment. Introduced electron beam was 20.8 C, that is 15 times larger. From this data, we selected good data (16.6 C) in which the data acquisition and the detector conditions did not have any problems. Performances of the detectors in the physics run will be explained in the following.

The scintillation counters in Kaos

In order to distinguish K^+ s from π^+ s and protons, resolutions and stabilities for the TOF and the energy deposited are important.

However, due to the initialization trouble in the CFD module for the scintillation walls in Kaos, the TOFs had large dependences with the signal height from 17 o'clock 4th to 17 o'clock 6th Nov. The TOF resolutions between G and H walls were $\sigma > 0.4$ ns, that was not enough time resolutions to separate K^+ from π^+ . Figure 4.9 (a) shows an example of a TOF distribution for the signal height during the CFD trouble. We applied 7th polynomial correction functions for all PMTs in the scintillator walls (time-walk correction) so that these curved distributions become straight such as Figure 4.9 (b). The TOF resolutions were improved to $\sigma \sim 200$ ps after

Table 4.1: Run conditions of the physics run.

Experimental term	24 Oct. – 12 Nov.
Beam current	20 μA
Total charge	20.8 C
Analyzed charge	16.6 C
Kaos trigger rate	30 kHz
Spek-A trigger rate	30 kHz
Spek-C trigger rate	28 kHz
DAQ rate	110~120 Hz
DAQ efficiency	87.3%

the correction, it achieved $\sim 3\sigma$ separation between K^+ s with π^+ s. These kinds of the time-walk corrections were applied for all runs to improve the time resolutions.

Figure 4.10 shows the time resolutions and the energy resolutions of each paddle for π^+ s, respectively. The time resolutions of each paddle in G and I walls were $\sigma \sim 100$ ps; and those in H wall were $\sigma \sim 150$ ps. The time resolutions of some paddles, for example G07, were worse than the other paddles because the correction functions were impossible to compensate the extremely bended ADC-TDC distributions. The energy resolutions of the low number paddles in G and I walls were not good. This is because multiple hits, which cannot be separated in the analysis, in a paddle made second or third peaks on the energy deposited distribution. These paddles were exposed the high counting rates due to the background particles contaminated from the gap between the lead wall and the lead stack.

Stabilities of the TOF and the energy deposited were also checked for π^+ s. Figure 4.11 shows the energy deposited in G and H walls, and the particle velocity ($\beta = v/c$) measured between G and H walls for π^+ s in whole runs. The performances of the scintillation counters were enough stable to select K^+ s.

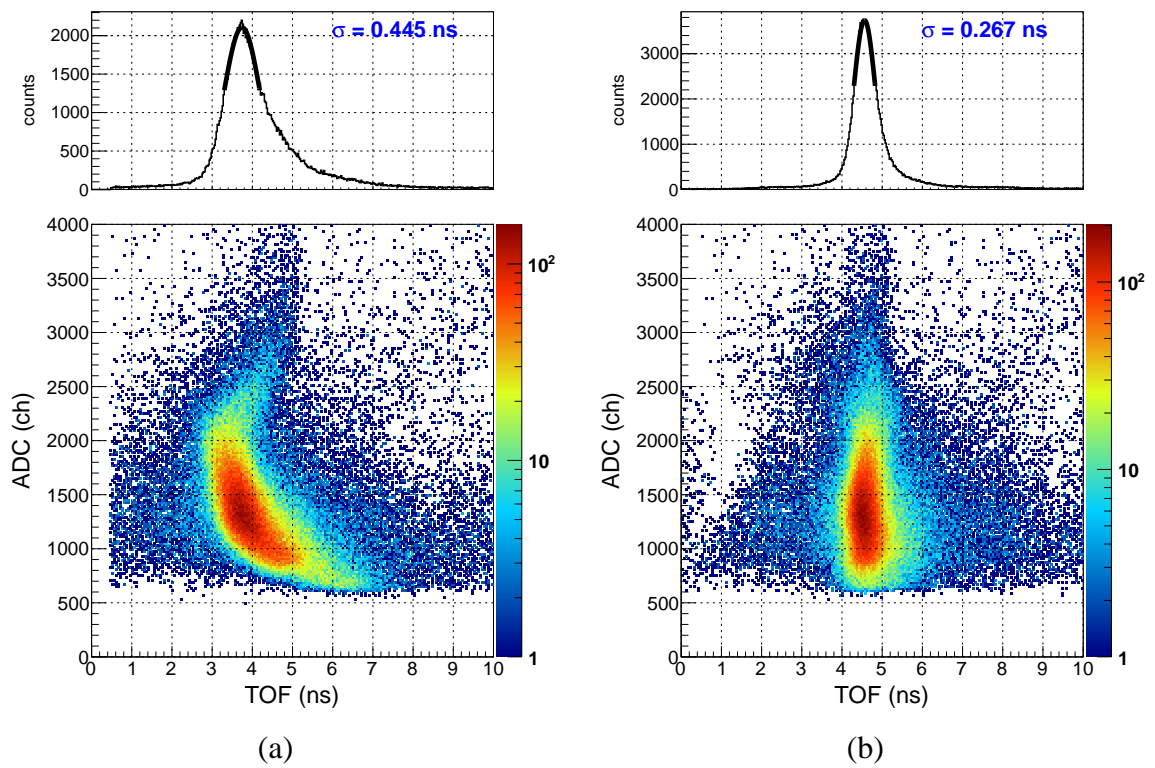


Figure 4.9: ADC-TOF distributions (a) before and (b) after the time-walk correction.

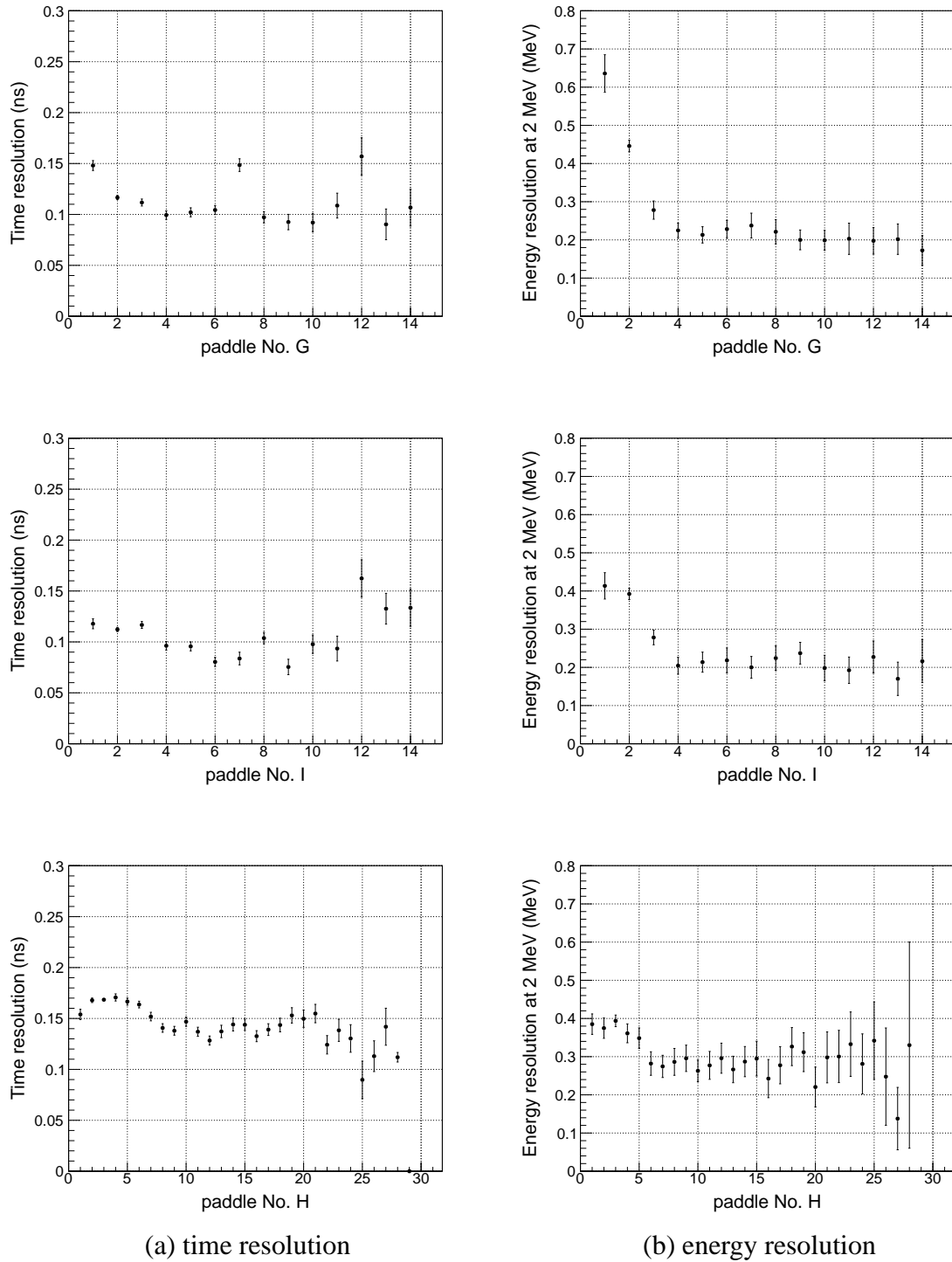


Figure 4.10: Time and energy resolutions of each paddle for π^+ s in Kaos. The resolutions for the high number paddles have large errors due to the poor statistics.

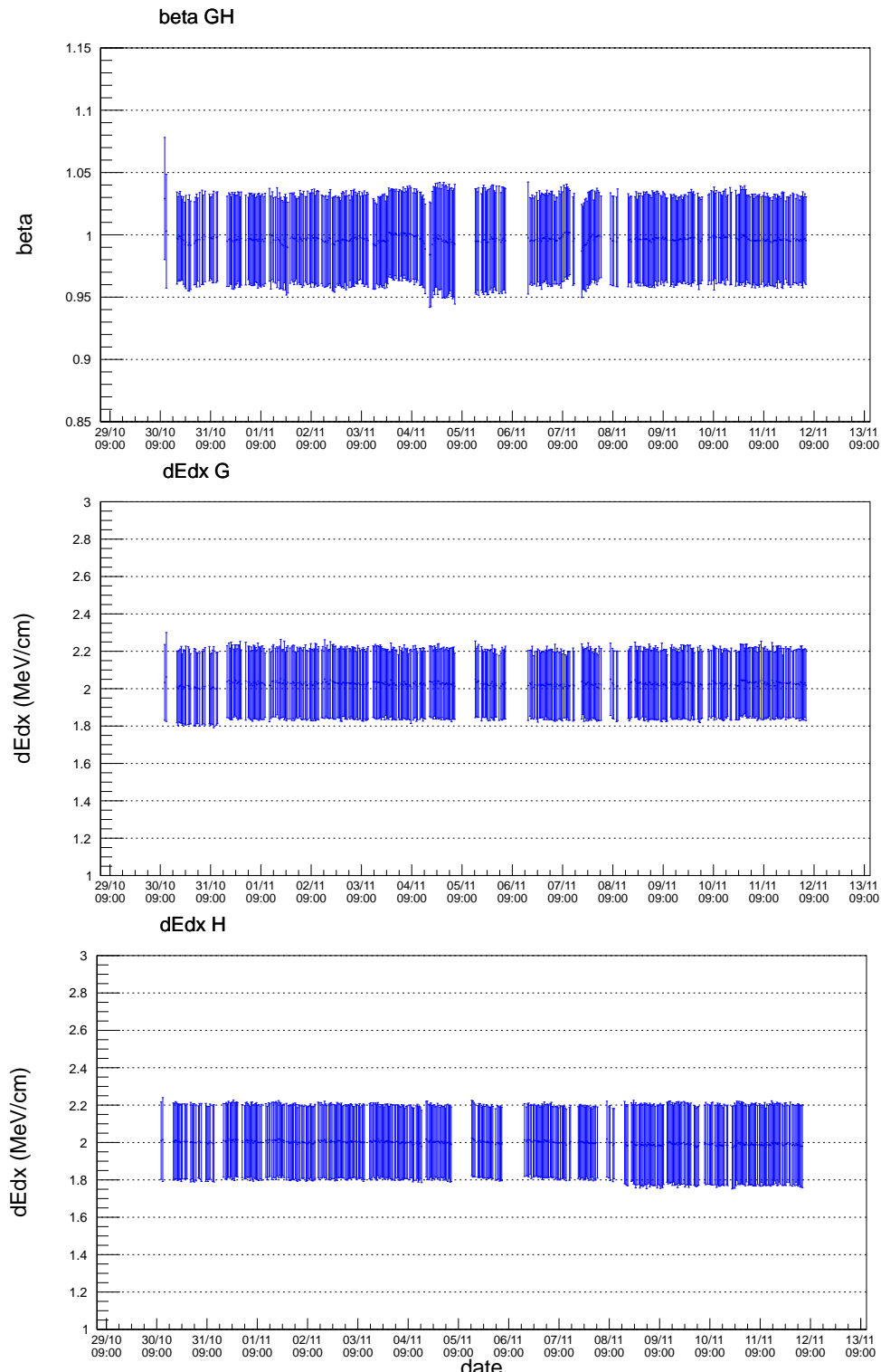


Figure 4.11: Run dependences of the particle velocity ($\beta = v/c$) and the energy deposited from 29th Oct. to 13th Nov.. The error bars correspond to the widths (rms) of the π^+ peak.

Table 4.2: Means of NPE distributions for π^+ in each AC segment. Means in AC1-5 and AC2-5 were not analyzed because they are out of acceptance.

Segment No.	Mean NPEs in AC1	Mean NPEs in AC2
0	7.6	1.2
1	7.1	0.9
2	7.7	5.0
3	8.3	7.1
4	9.1	8.9

The AC detectors in Kaos

The performances of ACs were checked for each particle. Figure 4.12 shows the number of photo-electron (NPE) distributions for π^+ s, K^+ s, and protons in AC2-0 and AC2-4. The particle identification for each particle will be explained in Section 5.2. The NPE distribution for π^+ s in AC2-4 had a peak ~ 9 PEs, that was the consistent with the designed value. However, the peak position in AC2-0 was ~ 1 PEs due to the magnetic field effect from the Kaos magnet. Under the magnetic field (>5 Gauss), as photo-electrons converted from the photo-cathode cannot reach to the first dynode in the PMT, the efficiency for the light input is decreased. Because the installed position of low number segments in AC2 were close from the Kaos dipole magnet, the PMTs could not work well.

Means of NPE distribution taken from the fitting results with the Poisson function convoluted by the Gaussian function were summarized in Table 4.2. The NPEs were clearly decreased in the low number segments in AC2.

Dependences of particle survival ratios with NPE cut thresholds were obtained as shown in Figure 4.13. In AC1, the survival ratios were 15.0% for π^+ s, 73.8(2)% for K^+ s, and 86.2% for protons with NPE cut < 4 PEs. In AC2, those were 59.9% for π^+ s, 93.2(2)% for K^+ s, and 95.1% for protons with the same cut condition.

As a result, the performance of ACs was decreased in comparison with the performance in J-PARC T44 experiment due to the magnetic field effect, however, the $\pi^+ - K^+$ separations using the NPE cuts were confirmed.

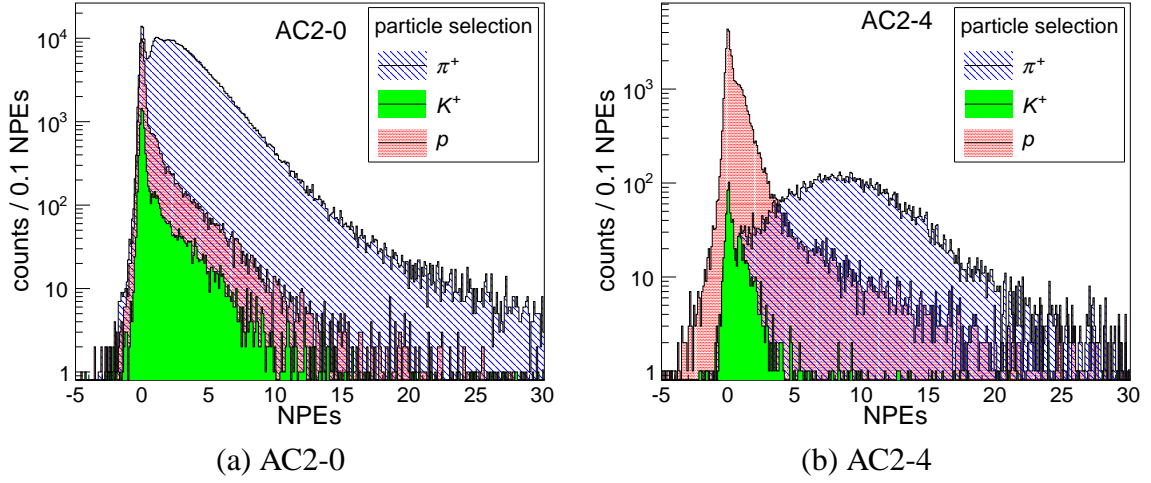


Figure 4.12: Number of photo-electrons (NPEs) distributions for π^+ s, K^+ s, and protons in AC2-0 and AC2-4. The NPEs distribution for π^- s in AC2-0 was reduced due to the magnetic field leakage from the Kaos magnet.

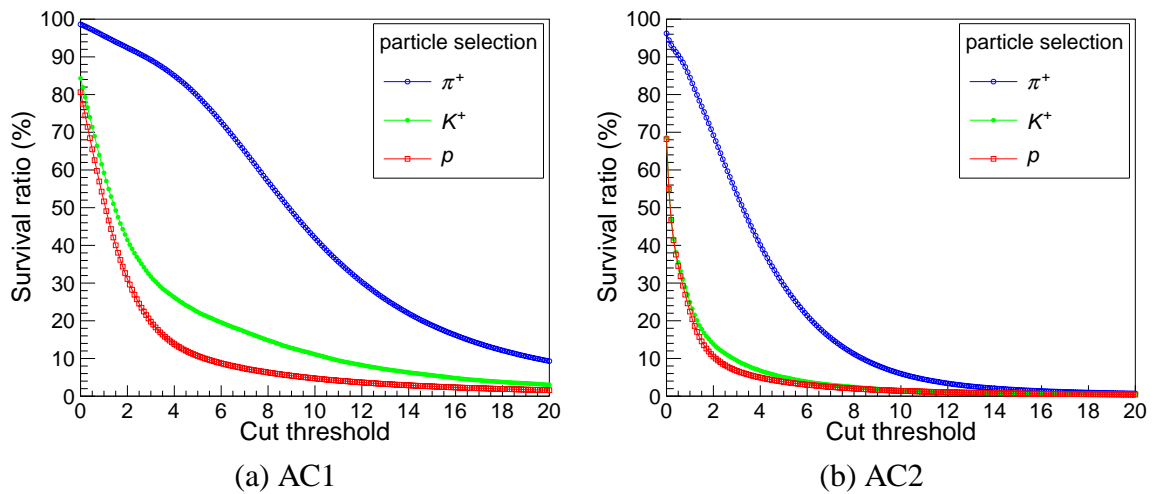


Figure 4.13: Particle survival ratios for NPE cut thresholds in AC1 and AC2 for π^+ s, K^+ s and protons.

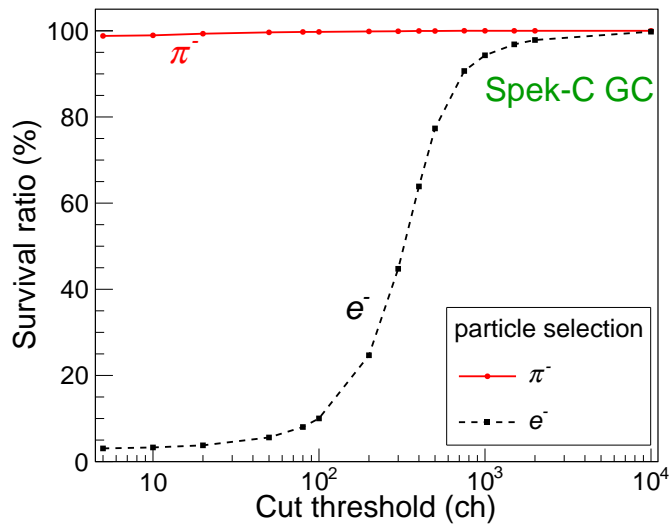


Figure 4.14: Particle survival ratios for NPE cut thresholds in GC for e^- s and π^- s. The unit of cut threshold in the horizontal axis corresponds to the ADC channels.

The GC detector in pion spectrometers

Figure 4.14 shows particle survival ratios for π^- and e^- in Spek-C. The number of particles to calculate the survival ratio were obtained from the number of events in the “ π^-, π^+ ” and “ e^-, π^+ ” coincidence peaks on the coincidence time spectra between Spek-C and the Kaos, which will be explained in Section 5.3.

In Spek-C, the survival ratios were 3.3% for e^- s and 98.9% for π^- s with NPE cut<10 ch. In Spek-A, those were 0.1% for e^- s and 97.9% for π^- s with the same cut condition. Thus, the GC detectors had the good performance for π^- - e^- separation.

Chapter.5

Analysis

In this section, analysis to obtain a distribution of a decay pion momentum from strangeness production events. Particle identifications in Kaos and Spek-C, and a coincidence spectrum between the two spectrometers will be explained. A momentum calibration, which is most important part in the analysis, also will be described.

5.1 Particle tracking

In the Kaos detector, there are no tracking chambers such as the drift chamber to measure a particle position and angle. The particle position and angle are obtained from a hit information in the scintillation walls (G, I, and H walls). After hit combinations in each wall are selected with brute force, the particle path is calculated from a fitting with the linear function for each combination. A goodness of the fit was evaluated by chi-square calculated from hit positions in each scintillation paddle.

5.2 Particle identification

Figure 5.1 shows a 2-dimensional distribution between the velocity (β) and the energy deposit in the scintillator (dE/dx). π^+ and proton events are clearly selected from this distribution. In addition, NPE cuts of ACs are also applied with >4 PEs for π^+ selection and <4 PEs for proton selection.

On the other hand, K^+ s are selected with more complex cut conditions as explained below.

■ K^+ selection

The condition in the Kaos detector plane is significantly different between low momentum region and high momentum region, namely, the counting rates at the low paddle number in the

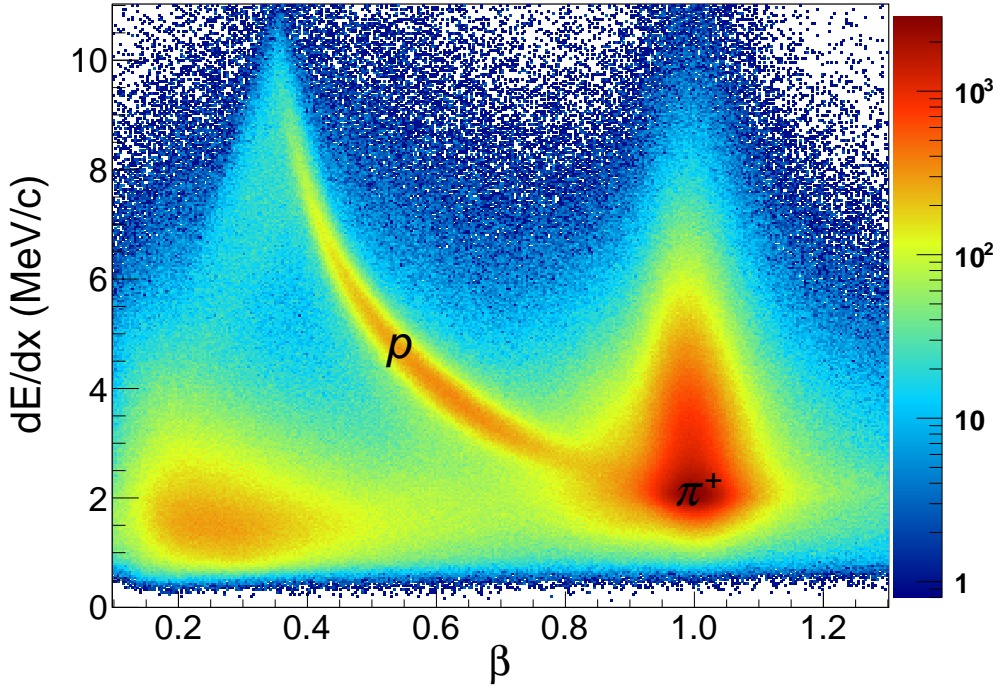


Figure 5.1: A 2-dimensional distribution between the velocity and the energy deposit in the scintillator. A cluster at $\beta \sim 1$ and $dE/dx \sim 2$ MeV/c are selected as π^+ events. Another cluster around $\beta \sim 0.6$ and $dE/dx \sim 4$ MeV/c are selected as proton events.

scintillation walls are much higher than those at the high paddle number, and the performance of AC2 was not good at lower momentum side. Therefore, we performed K^+ selection with two approaches: a threshold K^+ selection and a likelihood K^+ selection.

In the threshold selection, K^+ 's are selected using measured quantities (velocity [β], energy deposit [dE/dx], and NPEs of ACs) independently as follows:

$$\left(\frac{\beta - \bar{\beta}}{\sigma_\beta} \right) < 1 \otimes \left(\frac{dE/dx - \bar{dE/dx}}{\sigma_{dE/dx}} \right) < 1 \otimes \left(\frac{NPE - \bar{NPE}}{\sigma_{NPE}} \right) < 1, \quad (5.1)$$

This selection is worked well when the K^+ events are clearly observed. However, if the other particles exist similar position, it is difficult to reject these background events. Therefore, these K^+ selection is applied when the particles hit at G3-G13 and H3-H26 where the scintillation detectors have good performances.

On the other hand, in the likelihood selection, a likelihood selection of K^+ are defined as follows:

$$\left[\left(\frac{\beta - \bar{\beta}}{\sigma_\beta} \right)^2 + \left(\frac{dE/dx - \bar{dE/dx}}{\sigma_{dE/dx}} \right)^2 + \left(\frac{NPE - \bar{NPE}}{\sigma_{NPE}} \right)^2 \right] < 1, \quad (5.2)$$

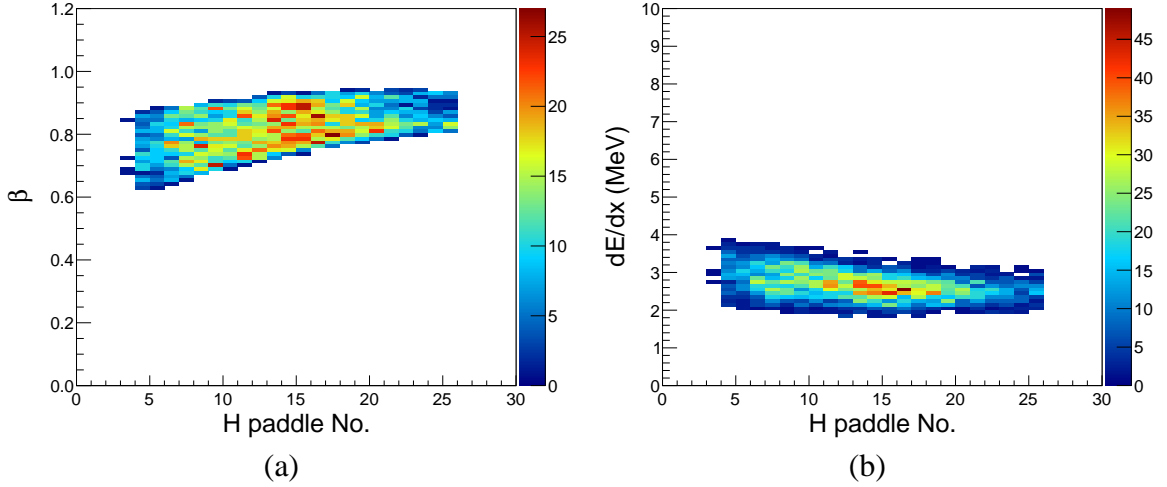


Figure 5.2: K^+ selections with threshold selection. (a) the velocity (β) and (b) the energy deposit (dE/dx) distributions as a function of H paddle number are described.

where β is a measured quantity, $\bar{\beta}$ is a expected velocity of K^+ , and σ_β is a width of expected K^+ distribution. The definitions for the energy deposit (dE/dx) and the NPEs in AC (NPE) are same as those for β . The expected values are estimated from the Monte Carlo simulation using Geant4. This selection can select K^+ s under the duty conditions effectively in comparison with the threshold cut, while it is tighter cut.

Finally, we obtained the K^+ selection with a sum of the threshold selection and the likelihood selection.

5.3 Coincidence time

Figure 5.4 shows coincidence time spectra between Kaos and Spek-C obtained with the particle selection in Kaos. Three coincidence peaks for π^- , μ^- , and e^- are observed with each particle identification in Kaos. The timing of these peaks are consistent with the expected time.

As a result, we successfully observed “ π^-, K^+ ” coincidence peak on the coincidence time spectrum.

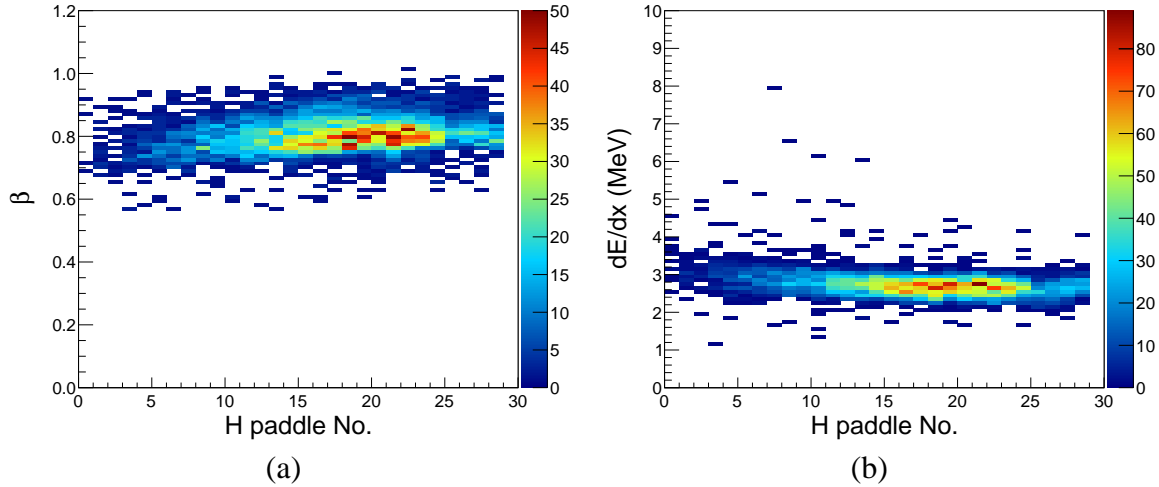


Figure 5.3: K^+ selections with likelihood selection. (a) the velocity (β) and (b) the energy deposit (dE/dx) distributions as a function of H paddle number are described.

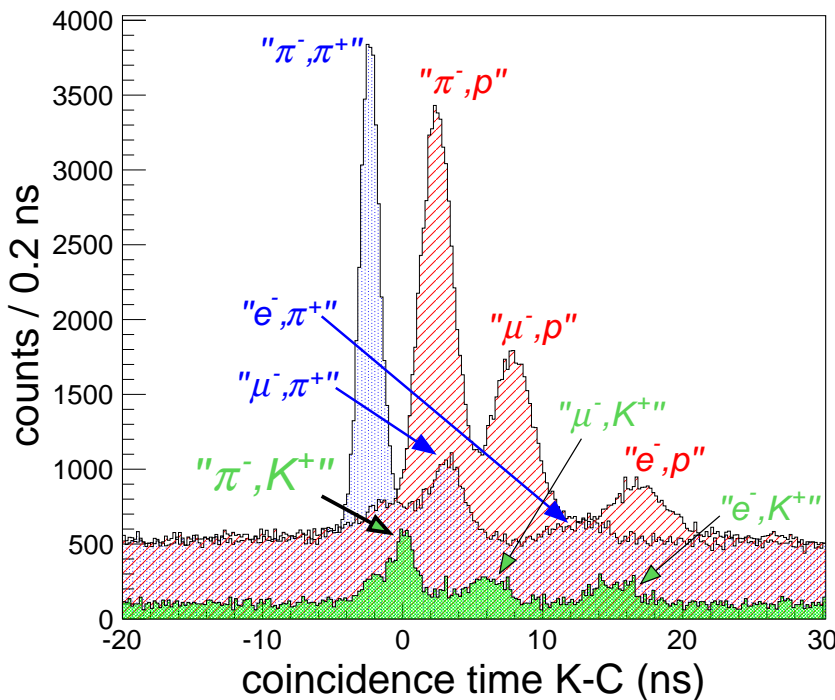


Figure 5.4: Coincidence time spectra between Kaos and Spek-C obtained with π^+ selection (blue), K^+ selection (green), and proton selection (red) in Kaos. Any cuts of GC detector do not apply to these spectra.

5.4 Momentum calibration of pion spectrometers

In order to determine the absolute momentum for the decay pion, the momentum calibration was most important part of the analysis. The candidates of the calibration method was already listed up in Section 2.4. In the 2012's experiment, the electron elastic scattering was performed as a calibration method, because the method could be work without changing the detector setups from the decay pion spectroscopy. The electron beam with an energy of ~ 200 MeV directory transferred from RTM3 was irradiated to Carbon and Tantalum targets. As the momentum of scattering electron depends on the scattering angle as already written by Equation 2.30, scattering electrons were measured the angle and the momentum in Spek-A and Spek-C with the data acquisition trigger for any hits of scintillation counters “ToF” in each spectrometer.

The purposes of the calibration experiment were

- Calibration of angle and absolute momentum for pion spectrometers.
- Confirmation of linearity for the relative momentum.
- Estimation for the peak shape of decay pions.

The details of the calibration experiments and the results are explained in this section.

5.4.1 Data summary of calibration experiments

We performed the calibration experiments twice in 2014 with several conditions as shown in Table 5.1. First three data (“Ta1”, “Ta2”, and “C1”), which had high statistics, were used for the momentum calibration and liniarity check. In these runs, the target vacuum chamber was separated with vacuum chamber in each spectrometers by two sets of $125\text{-}\mu\text{m}$ thick Kapton foils as well as the production experiments. Other two data (“Ta3” and “C2”) were obtained as additional information to discuss the peak shape and expected resolution, though the statistics were limited due to the larger scattering angle. In these runs, the target vacuum chamber was connected with the vacuum chamber in each spectrometer by a vacuum extensions. A schematic drawings of two data sets are shown in Figure 5.5.

A $6\text{-}\mu\text{m}$ thick tantalum target was adopted to calibrate the absolute momentum, because the momentum has the small dependence with the angular ambiguity due to large mass number. Furthermore, as the natural abundance of ^{181}Ta is 99.988%, the impurity effect from other isotopes was minimized.

A $200\text{-}\mu\text{m}$ thick carbon target was adopted to check the momentum linearity, because well

Table 5.1: A summary table of calibration runs. Run names, electron beam energies, target materials, initial central momenta, spectrometer angle, and installation of vacuum extensions between target and spectrometers are summarized.

Name	Beam Energy [MeV]	Target	Central Momentum		Angle		Vacuum Extension
			A	C	A	C	
“Ta1”	195.17±0.16	^{181}Ta	194.996	194.994	52.00	52.00	×
“Ta2”		^{181}Ta	204.365	208.294			
“C1”		^{12}C	181.764	181.681			
“Ta3”	210.10±0.16	^{181}Ta	224.858	226.739	93.50	126.00	○
“C2”		^{12}C	187.324	185.512			

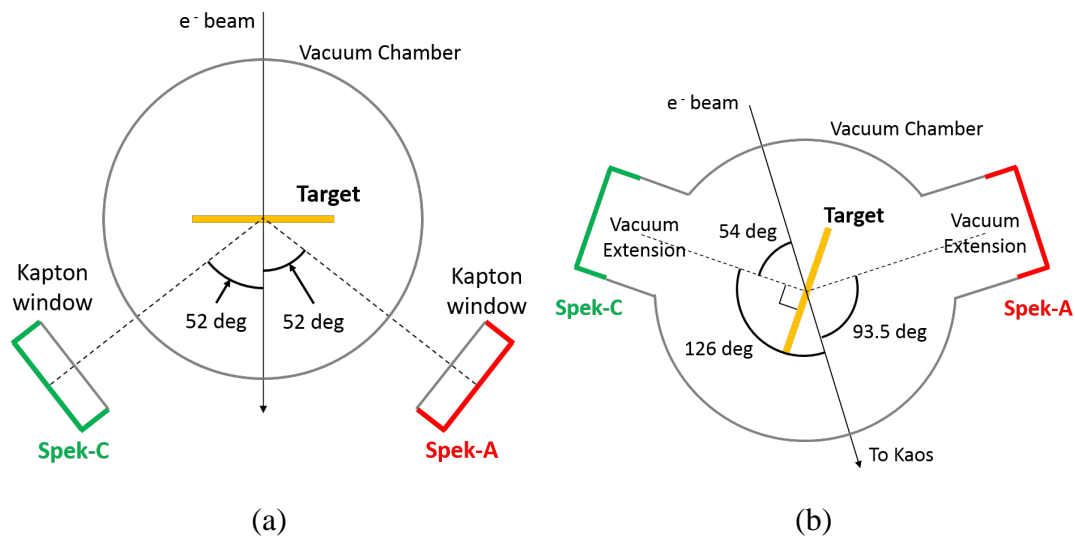


Figure 5.5: Schematic drawings of calibration runs. (a) A setup at “Ta1”, “Ta2”, and “C1”. (b) A setup at “Ta3” and “C2”.

known and well separated excited state can be observed.

The main parameters of these targets were summarized in Table 3.2.

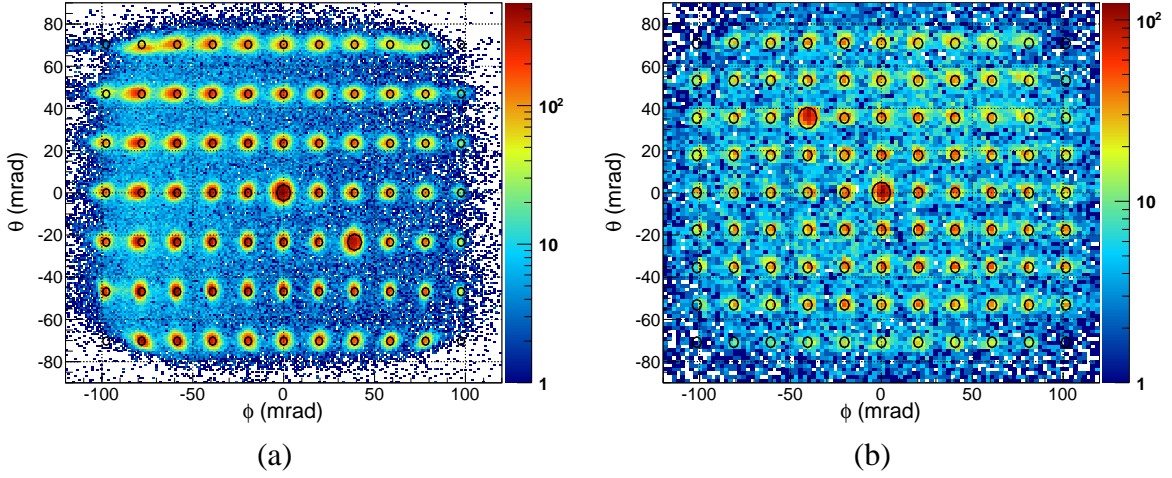


Figure 5.6: Scattered electron angular distribution at target with sieve collimator. (a) The distribution in Spek-A at run “C1”. (b) The distribution in Spek-C at run “C2”. The dispersive angle is θ , and the non-dispersive angle is ϕ .

5.4.2 Angular and momentum calibration

Angular calibration

Scattered angle was checked using consistency of the hole position in sieve collimator. Figure 5.6 showed dispersive and non-dispersive angular distribution at the target with simultaneous drawings of the designed hole position in sieve collimator. The sieve collimator pattern not for run “C1” but for “C2” was shown for Spek-C. The sieve collimator pattern was also measured in Spek-C at run “C1”, while the hole pattern was consistently shifted with -11 mrad for non-dispersive angle due to a miss alignment of Quadrupol in Spek-C. The scattered electron distribution was well reproduced the hole pattern with an accuracy of $\sim 3\text{ mrad}$, which corresponds to $1\text{ keV}/c$ accuracy calculated in 2.30 for ^{181}Ta target. The width of each peak was 1.8 mrad for dispersive angle and 2.0 mrad for non-dispersive angle in Spek-A, and was 2.1 mrad for dispersive angle and 3.4 mrad for non-dispersive angle in Spek-C. As a result, the accuracy and the resolution had much enough resolution to calibrate the momentum.

Momentum calibration

The momentum calibration was performed using tantalum target. The procedure of the momentum calibration was the followings.

1. Energy loss correction in materials for measured electron energy.
2. Fitting a distribution of differences between measured momentum and calculated one.
3. Determination of calibration factor to correct first term of momentum so that the weighted average of two tantalum peaks evaluated to 0.

■ Energy loss correction

The energy loss in absorbers can be obtained as the Bethe-Bloch formula, and the most probable value of the distribution is represented with Equation 2.21. The thickness of absorbers was enough thin to regard the energy loss distribution as the Landau distribution in the experiment, because κ , which is the ratio between the mean energy loss and the maximum energy transfer in a single collision, was smaller than 0.01. The amount of energy loss in each absorber were summarized in Table 5.2 with assumed parameters.

In order to take the energy loss in incident electrons and scattered electrons into consideration, the target thickness was calculated as the following equation.

$$x = \frac{x}{2} \times (1 + \arccos \theta), \quad (5.3)$$

where θ is scattered angle. For the tantalum target, the most probable value of the energy loss was expected with 73 keV at $\theta = 52$ degree. In the analysis, as θ could be measured, path length was calculated in every event.

The shell correction and density correction term has uncertainty parameters in the bethe-bloch fomura. In addition, as the reaction position distribute uniformly in the target thickness, the electron path length cannot be described by simple equation like 5.3. The uncertainty as above was confirmed using the difference with Geant4 simulation, and the amount of the uncertainty was 5 keV, that was included in the systematic error.

Table 5.2: Energy loss in each material at calibration experiment. The experimental setup was considered by Figure 5.5 (a). The target thickness for incident electrons and scattered electrons was taken into account.

	Tantalum	Carbon	Kapton	Air	Sum(Ta)
Z	73	6	5.026	7.220	
A	180.948	12.011	9.803	14.440	
ρ [g/cm ³]	16.585	2.250	1.420	1.205×10^{-3}	
ρx [g/cm ²]	1.306×10^{-2}	5.905×10^{-2}	3.550×10^{-2}	1.205×10^{-2}	
W_{max} [MeV]			199.5		
κ	4.052×10^{-6}	2.269×10^{-5}	1.400×10^{-5}	4.634×10^{-6}	
dE [keV]	18.9	114.2	71.3	29.6	119.8
dE_{MP} [keV]	9.8	71.2	43.5	19.3	72.6

■ Fitting momentum difference distribution

As a next step, the momentum difference was checked to calibrate the absolute momentum. The momentum difference was defined as the following equation.

$$\begin{aligned}\Delta p &= p_{\text{calc}} - p_m \\ &= \sqrt{\left(\frac{E_b}{1 + E_b/M_t(1 - \cos\theta_m)}\right)^2 - m_e^2} - p_m.\end{aligned}\quad (5.4)$$

The scattered electron angle θ_m and momentum p_m are measured quantities in each spectrometer, and the beam energy E_b and the target mass M_t are setting parameters in the experiment.

The momentum difference distribution in each spectrometer on the run “Ta1” were shown in Figure 5.7 with fitting result of Landau-Gauss distribution. Peaks of elastic scattering electrons from the ground state in ^{181}Ta were clearly observed. The width of peaks was about 110 keV/c for Spek-A and 200 keV/c for Spek-C with FWHM. The width was important to discuss the intrinsic resolution of the spectrometers, and that will be discussed in Section 5.4.4.

In order to calibrate the momentum in the pion spectrometers with high accuracy, we had to determine the peak position very carefully. Because the Landau-Gauss function has asymmetric distribution, there are several definition for the peak position; a mean position of the distribution, a location at the highest yield and so on. Therefore, we have to define of the peak position.

The Landau-Gauss distribution has four parameters; a width of Landau function, a location of Landau function, a width of Gaussian function, and a magnification. The most probable value of Landau-Gauss distribution depends on not only the location parameter but also width of Landau and Gaussian distribution. Therefore, we used the re-parametrized Landau-Gauss function as a fitting function to minimize the systematic error of the absolute momentum as explained the more detail below.

The definition of Landau function is given by:

$$\phi(x) = \frac{1}{\pi} \int_0^\infty \exp(-u \ln u - ux) \sin \pi u \, du,\quad (5.5)$$

as already shown in Equation 2.20. This function is not defined with any parameters for the location and the width, and the most probable value of the function is not zero but $MPV_L \sim -0.22278$. Because this function is difficult to handle, the parametrized function is often used as fitting function for the computation with introducing the location parameter MPV and the width parameter σ [Scho84]. In the parametrized Landau function, the most probable value of the Landau function in Equation 5.5 is represented as follows:

$$MPV_L = \frac{x - MPV}{\sigma}.\quad (5.6)$$

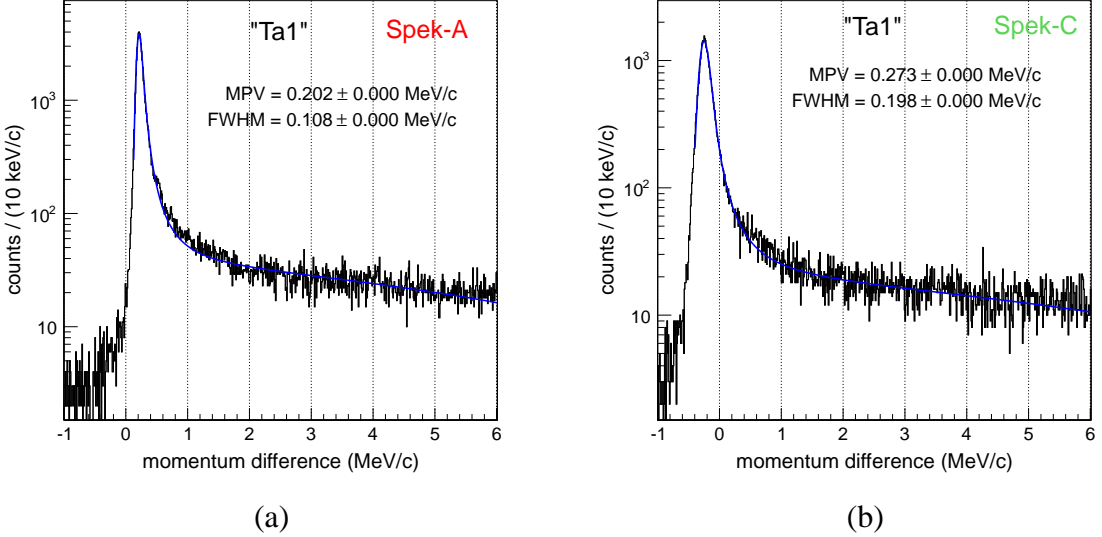


Figure 5.7: Momentum differences in the calibration run “Ta1” for (a) Spek-A, and (b) Spek-C.

Therefore, the most probable value of the parametrized Landau function is in proportion to $MPV_L \times \sigma$. As a result, the location parameter of the fitting Landau function MPV depend on the width parameter σ .

If the following re-parametrization is applied to Equation 5.6, the dependence with the width parameter can be canceled:

$$MPV' = MPV + 0.22278 \times \sigma. \quad (5.7)$$

Thus, this re-parametrized MPV' is independent on the width of Landau function σ , and it is always same location as the most probable value of the Landau distribution even if the Gaussian function is convoluted, while it should be note that the most probable value of this Landau-Gauss function is shifted with the width of Gaussian function. Because the energy losses in absorbers are always corrected with the most probable value of the Landau distribution as already given in Equation 2.21, this re-parametrization helps to determine the peak position simply.

The MPV 's were summarized in Table 5.3. We defined the calibration factor as,

$$\text{Calibration Factor} = 1 + \left(\frac{\Delta p^{Ta1}}{p_c^{Ta1}} + \frac{\Delta p^{Ta2}}{p_c^{Ta2}} \right) / 2. \quad (5.8)$$

where, p_c is the initial central momentum shown in Table 5.1. As a result, we applied 1.000958 in Spek-A and 0.998657 in Spek-C as the calibration factor.

Table 5.3: Results of location parameters with re-parametrized Landau-Gauss function and momentum calibration factors.

Run Name	MPV' in Spek-A	MPV' in Spek-C
“Ta1”	202.2 ± 0.3 (keV/c)	-272.7 ± 0.7 (keV/c)
“Ta2”	179.6 ± 0.2 (keV/c)	-268.2 ± 0.6 (keV/c)
Calibration Factor	1.000958 (2)	0.998657 (5)

5.4.3 Linearity

After multiplying the correction factor to the initial central momentum, momentum linearities were checked using the missing mass distribution in each spectrometer. Figure 5.8 was the excitation energy distribution of ^{12}C target with fitting results as Landau-Gauss function. The excitation energies (E_x) were calculated with subtraction carbon nuclear mass ($M_{^{12}\text{C}}$) from missing mass (M_{miss}) as follows,

$$E_x = M_{miss} - M_{^{12}\text{C}} = \sqrt{(E_e + M_{^{12}\text{C}} - E_{e'})^2 + (\vec{p}_e - \vec{p}_{e'})^2} - M_{^{12}\text{C}}. \quad (5.9)$$

The peak of ground state and three excited state were clearly observed in both spectrometer. Furthermore, a peak was also observed around $+16$ MeV/ c^2 . All peaks were identified from the literature value shown in Figure 5.9 (a).

The linearity of the momentum was checked by the shifts of excitation energies with the relative momentum as shown in Figure 5.10. It was found the excitation energy from the carbon target consistently shift to the higher excitation direction than that from the tantalum target in both spectrometers. The tendency could be explained with the drift of the beam energy as shown in Figure 5.11, that was excitation energy dependences with a -50 -keV shift of the incident electron beam energy only for ^{12}C target. The shifted energy was within the error of the incident electron beam (± 160 keV).

As the same beam energy was ensured for the five peaks in carbon target, the excitation energies shift dependences were fitted as first polynomial function in order to estimate the linearity. The slopes from the fitting results were -0.6 ± 0.3 keV/% for Spek-A and -0.6 ± 0.4 keV/% for Spek-C, which were corresponds to 12 ± 8 keV and 15 ± 10 keV in the full momentum acceptance.

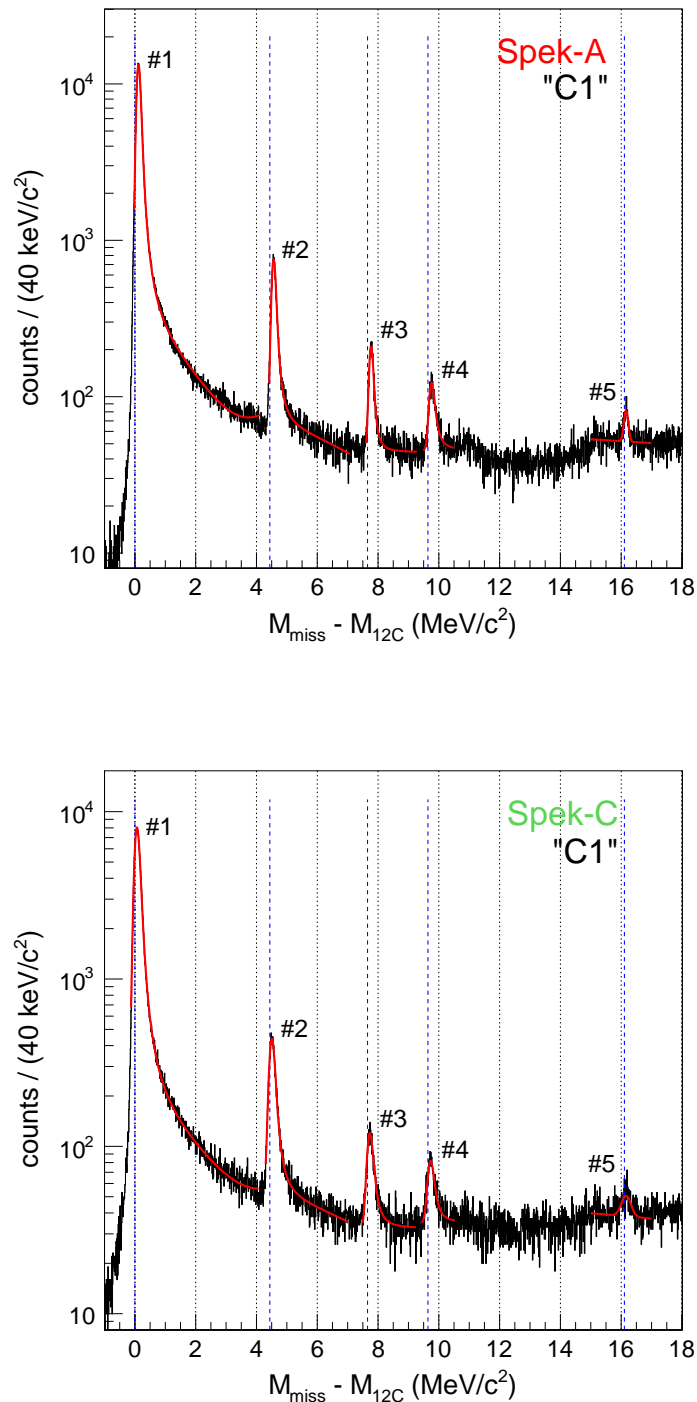


Figure 5.8: A missing mass distribution for run “C1” in each spectrometers. Landau-Gauss functions were used as the probability density function for fitting. First polynomial function were assumed as a background. The excited energies from the literature were also plotted as dotted blue lines.

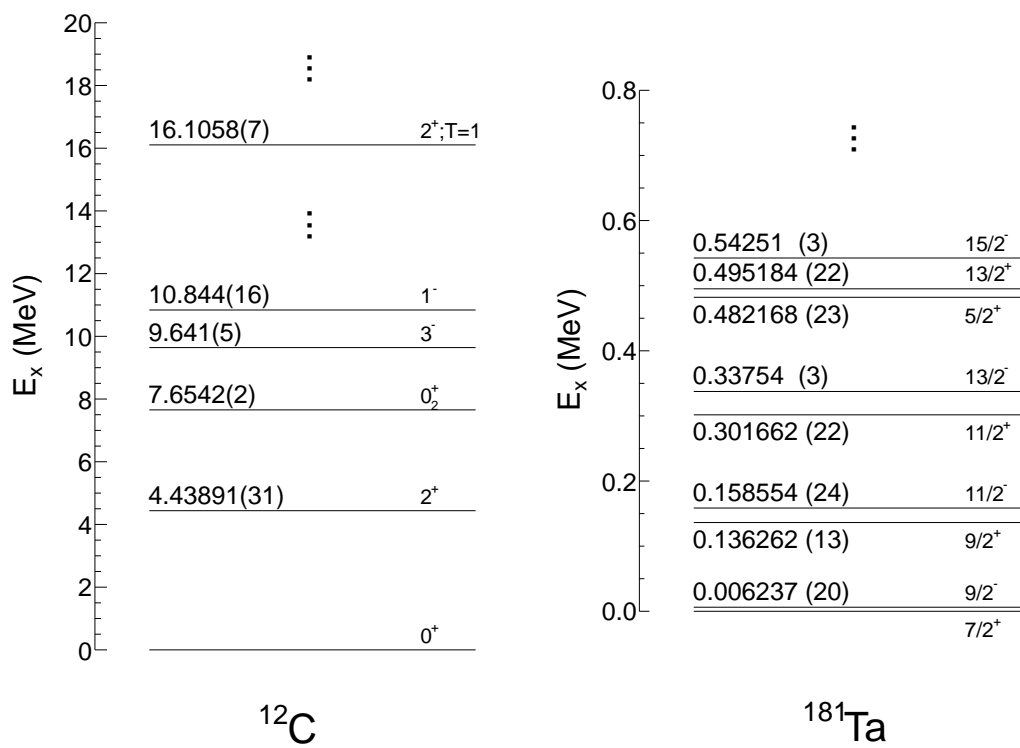


Figure 5.9: Nuclear level structures for ^{12}C [Ajze90] and for ^{181}Ta [Wu05].

Table 5.4: A summary table of the excitation energies. The literature values [Ajze90] and most probable values of Landau component with fitted by Landau-Gauss function were shown.

Peak	literature		Spek-A	Spek-C
	E_x (MeV)	$\Gamma_{c.m.}$	MPV (MeV)	MPV (MeV)
“C1” #1	0.000	-	0.096(0)	0.041(0)
“C1” #2	4.439(0)	<1	4.542(1)	4.477(2)
“C1” #3	7.654(0)	<1	7.749(3)	7.702(4)
“C1” #4	9.641(5)	34(5)	9.737(4)	9.700(6)
“C1” #5	16.106(1)	5(0)	16.160(8)	16.162(23)
“Ta1”	0.000	-	0.016(0)	-0.010(1)
“Ta2”	0.000	-	-0.007(0)	-0.032(1)

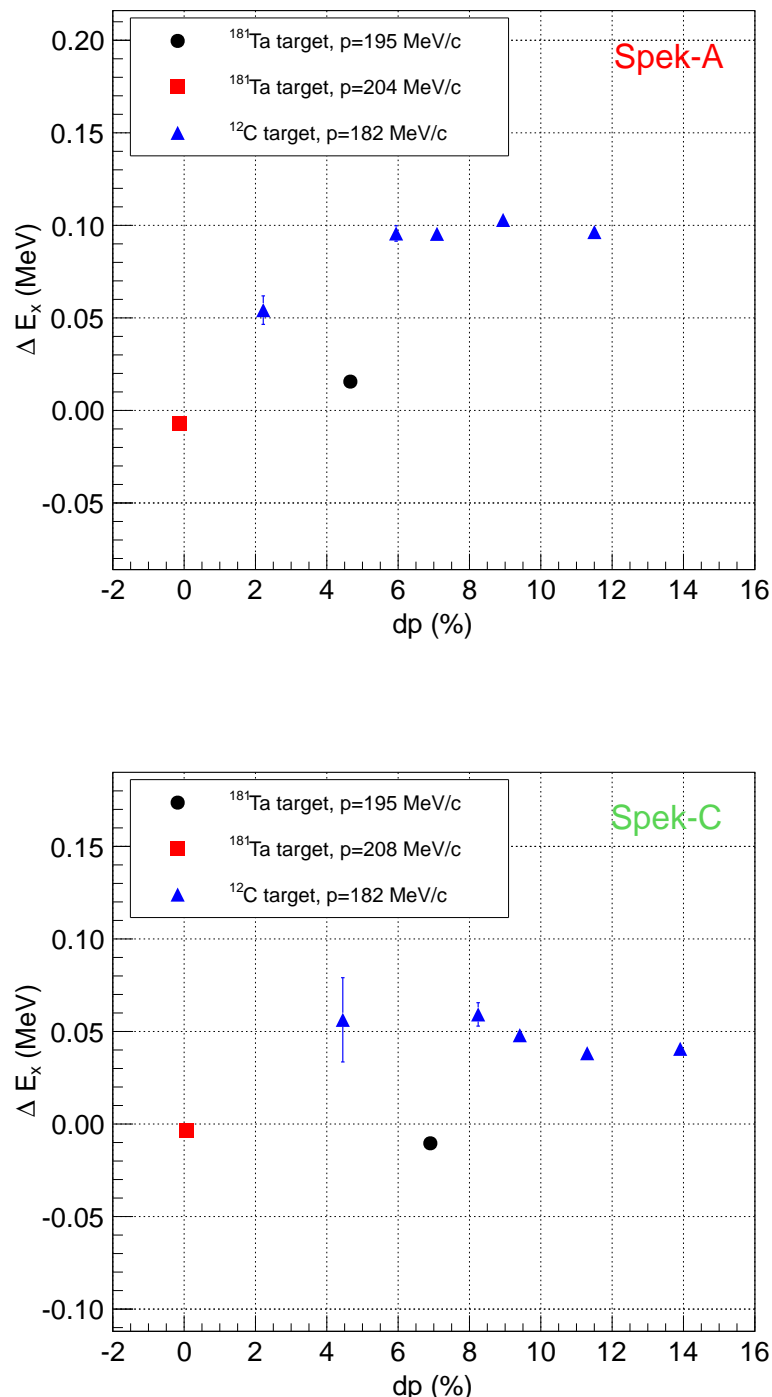


Figure 5.10: A missing mass dependence with a relative momentum in each spectrometer.

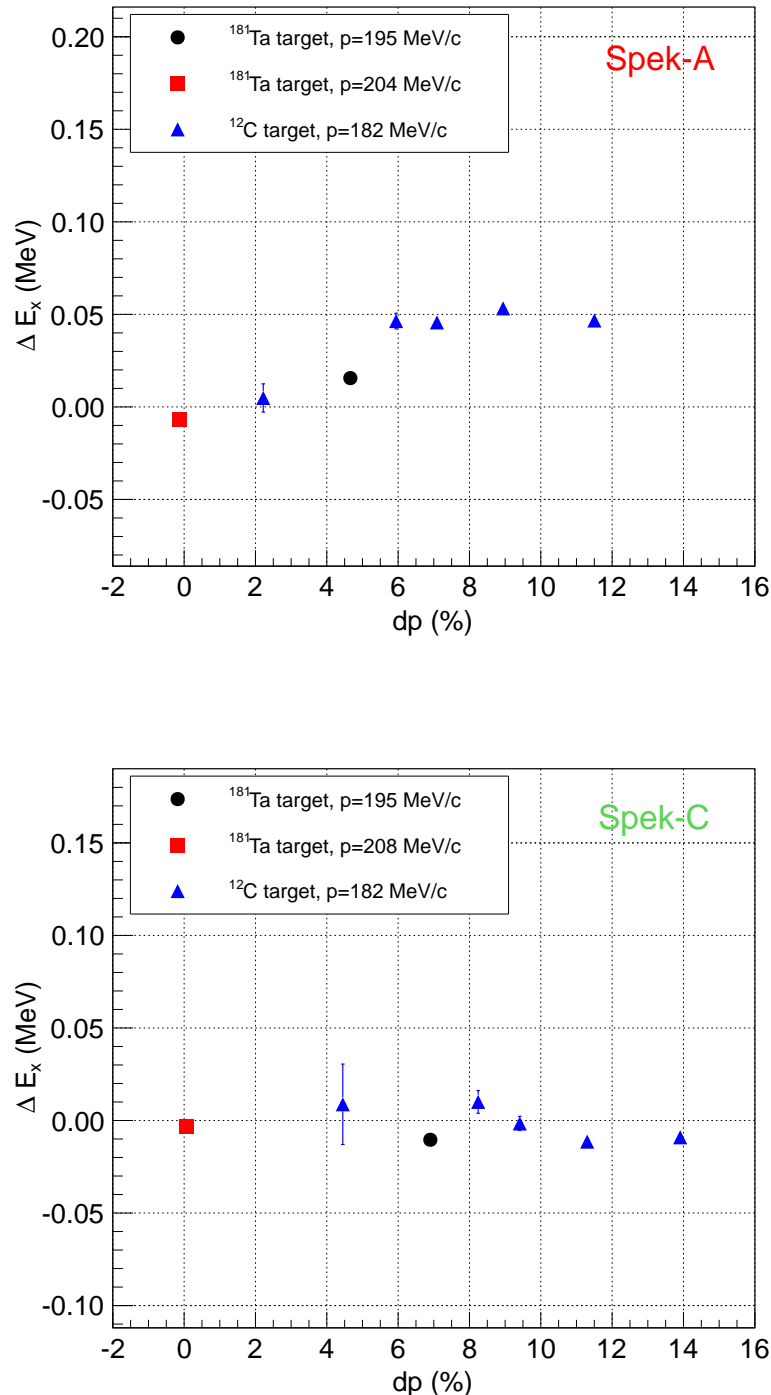


Figure 5.11: A missing mass dependence on a relative momentum with -50 keV beam energy offset only for carbon target.

5.4.4 Peak shape estimation

We already obtained the peak shape from the electron elastic scattering experiments. However, the peak shape of decay pion was expected different shape with that of scattering electrons, because the energy loss and multiple scattering effect depend on a species of particle or its momentum. Therefore, we evaluated the peak shape of scattering electron data quantitatively, and estimated the expected peak shape on decay pion momentum using the evaluation.

All scattered electron peaks could be fitted with Landau function ($F_{e'}^L$) convoluted with Gaussian function ($F_{e'}^G$):

$$F_{e'}(\sigma_{e'}) = F_{e'}^L(\sigma_{e'}^L) * F_{e'}^G(\sigma_{e'}^G), \quad (5.10)$$

with a width of Landau function ($\sigma_{e'}^L$) and Gaussian function ($\sigma_{e'}^G$).

It was assumed that this peak shape consists of the following components.

1. An energy loss distribution in absorbers between the target and the spectrometer (F_1).
2. A multiple scattering effect in absorbers (F_2).
3. An effect from position and angular resolution of VDCs (F_3).
4. An effect from angular resolution at target (F_4).
5. An effect from an ambiguity of transfer matrix for a momentum reconstruction (F_5).

In this paper, the functions of each component were assumed as Landau-Gauss distribution so as to be simplify. Consequently, equation 5.10 could be converted to

$$\begin{aligned} F_{e'}(\sigma_{e'}) &= F_1(\sigma_1) * F_2(\sigma_2) \dots \dots \\ &= F_1^L(\sigma_1^L) * F_1^G(\sigma_1^G) * F_2^L(\sigma_2^L) * F_2^G(\sigma_2^G) \dots \dots \\ &= F_{e'}^L\left(\sum_i \sigma_i^L\right) * F_{e'}^G\left(\sqrt{\sum_i \sigma_i^G 2}\right). \end{aligned} \quad (5.11)$$

We evaluated the function in each component using the elastic scattering data and the simulated results as follows.

Energy loss effect in absorbers (F_1)

The energy loss distribution in absorbers can be explained with 2.19, while the distribution was approximated by ignoring the logarithmic term. More precise estimations of the energy loss distribution was performed in Geant4 in which the same parameters were applied as Table 5.2. The procedure of the simulation was as follows.

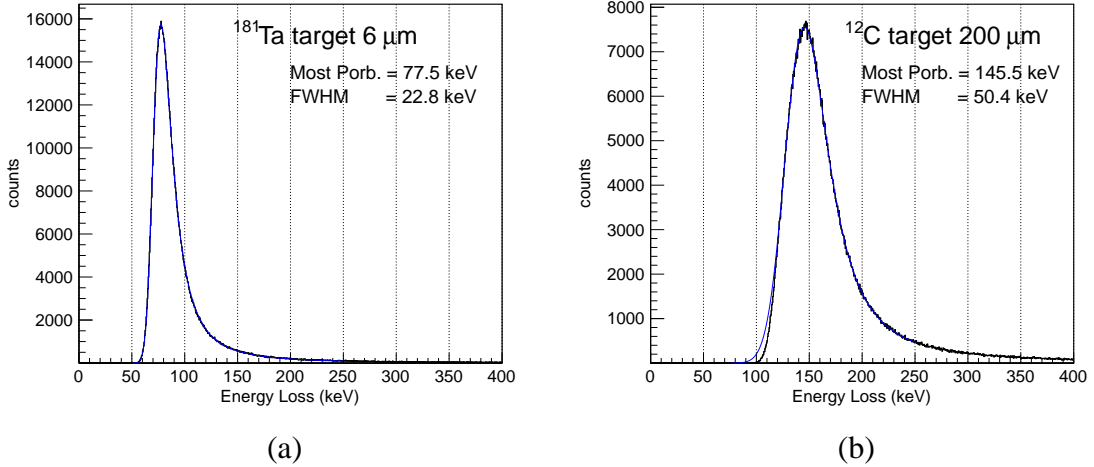


Figure 5.12: Expected energy loss distribution simulated by Geant4. (a) ^{12}C target. (b) ^{181}Ta target. The experimental setup was considered by Figure 5.5 (a). Each distribution was fitted with Landau-Gauss distribution (Blue line).

At first, in order to take the energy loss of the electron beam into account, electrons with a energy of 195.17 MeV were generated to the opposite direction with the beam direction in the target uniformly, and the generated positions and the energies after the energy loss in the target were stored as a seed file. Second, the scattered electron energies were calculated by Equation 2.30 using electron energies in seed file and scattered angle distributed $52 \pm 5^\circ$ with respect to the beam direction uniformly. Third, the energies of scattered electrons, that were generated along the calculated energies, assumed angle, and stored positions, were simulated after the energy loss in the target, the vacuum windows, and air. Finally, the energy loss effect in absorbers was estimated from Equation 2.21 on the same condition as the analysis, namely, the 195.17-MeV beam energy and the simulated results of scattered electron energy and angle.

The results were shown in Figure 5.12. The width was 50 keV for ^{12}C target and 23 keV for ^{181}Ta target with FWHM respectively. The Landau and Gaussian components were $\sigma^L = 9$ MeV and $\sigma^G = 13$ MeV for ^{12}C target and $\sigma^L = 5$ MeV and $\sigma^G = 4$ MeV for ^{181}Ta target.

Multiple scattering effect in absorbers (F_2)

The position and angle at detector position are spread due to the multiple scattering effect in absorbers. Figure 5.13 shows a simple example of the multiple scattering effect in the pion spectrometer. A particle emitted from the target passes along an original path (black dotted

line) and reaches to a focal plane position ①, if there are not any absorbers from the target to the focal plane. However, in the experimental setup, there are the vacuum windows at the entrance and the exit of the pion spectrometers. Therefore, the particle scatters with θ_1 at the entrance vacuum window, passes along a scattered path (red solid line) in the spectrometer magnet, scatters with θ_2 at the exit window, and reaches to ③. Because we do not know the scattering angle at the windows, we reconstruct the particle track from the focal plane to the target along a reconstructed path (blue solid line). As a result, a reconstructed momentum becomes different with the *true* momentum due to the difference of the tracking pass between the black dotted line and the blue solid line. The multiple scattering effect to the reconstructed momentum was estimated using Monte Carlo simulations as follows.

At first, after generated particles (e^- or π^-) at the target transferred to the entrance vacuum window (①) with a transfer matrix $\mathcal{M}_{t \rightarrow w}$, their flight angles were deformed so as to reproduce the multiple scattering effect:

$$\mathcal{M}_{t \rightarrow w} \begin{pmatrix} x_t = 0 \\ \theta_t \\ y_t \\ \phi_t \\ dp \end{pmatrix} = \begin{pmatrix} 1 & L & 0 & 0 & 0 \\ 0 & 1 & 0 & 0 & 0 \\ 0 & 0 & 1 & L & 0 \\ 0 & 0 & 0 & 1 & 0 \\ 0 & 0 & 0 & 0 & 1 \end{pmatrix} \begin{pmatrix} x_t \\ \theta_t \\ y_t \\ \phi_t \\ dp \end{pmatrix} = \begin{pmatrix} x_w \\ \theta_w \\ y_w \\ \phi_w \\ dp \end{pmatrix} \xrightarrow{\text{deform}} \begin{pmatrix} x'_w \\ \theta'_w \\ y'_w \\ \phi'_w \\ dp \end{pmatrix}, \quad (5.12)$$

where L is a distance between the target and the entrance vacuum window (40 cm).

Second, the particles were re-transferred from the entrance vacuum window to the target (②) with a matrix $\mathcal{M}_{w \rightarrow t}$, which is an inverse matrix of $\mathcal{M}_{t \rightarrow w}$. After the particles transferred from the target to the focal plane with a matrix $\mathcal{M}_{t \rightarrow f}$, the particle distribution was deformed so as to reproduce the multiple scattering effect at the exit vacuum window (③):

$$\mathcal{M}_{t \rightarrow f} \mathcal{M}_{w \rightarrow t} \begin{pmatrix} x'_w \\ \theta'_w \\ y'_w \\ \phi'_w \\ dp \end{pmatrix} = \begin{pmatrix} x'_f \\ \theta'_f \\ y'_f \\ \phi'_f \\ \vdots \end{pmatrix} \xrightarrow{\text{deform}} \begin{pmatrix} x''_f \\ \theta''_f \\ y''_f \\ \phi''_f \\ \vdots \end{pmatrix}, \quad (5.13)$$

where the transfer matrix $\mathcal{M}_{t \rightarrow f}$ was calculated from the backward matrix (focal plane to target transfer matrix in the analysis) with the singular value decomposition (SVD).

Finally, the particles were transferred from the focal plane to the target with the backward matrix (④):

$$\mathcal{M}_{f \rightarrow t} \begin{pmatrix} x_f'' \\ \theta_f'' \\ y_f'' \\ \phi_f' \\ \vdots \end{pmatrix} = \begin{pmatrix} \theta_t'' \\ y_t'' \\ \phi_t'' \\ dp'' \end{pmatrix}, \quad (5.14)$$

where $\mathcal{M}_{f \rightarrow t}$ is the backward matrix. The momentum spread due to the multiple scattering effect was thus evaluated with the difference between the generated momentum p and the deformed momentum p'' .

The scattering angles at the vacuum windows were estimated using the Geant4 simulation. In the simulation code, two kapton windows with a thickness of 125 μm and an air gap with a thickness of 10 cm were taken into consideration as the absorbers at the entrance of the pion spectrometer. A kapton window with a thickness of 51.4 μm , an air gap with a thickness of 20 cm, and aluminum mylar and gas in VDC1 were taken into consideration as absorbers at the exit of the pion spectrometer. Electrons with the energy of 200 MeV were introduced to these absorbers, and the scattered angular distributions after the absorbers were simulated. These angular distributions were fitted with Gaussian functions, and the width of the scattered angles were obtained with $\sigma = 2.0$ mrad and 1.9 mrad for the entrance and the exit, respectively.

Figure 5.14 shows p'' distributions in Spek-C when $p = 191.36 \text{ MeV}/c$ electrons were generated. In order to understand the scattering effect at the entrance and the exit separately, only the absorbers (a) at the entrance and (b) at the exit in Spek-C were installed in the estimation. Thus, the the multiple scattering effect in Spek-C was $\sigma^G = 26 \text{ keV}/c$ for the entrance absorbers and $\sigma^G = 13 \text{ keV}/c$ for the exit absorbers. Similarly, the effect in Spek-A was $\sigma^G = 21 \text{ keV}/c$ for the entrance absorbers and $\sigma^G = 9 \text{ keV}/c$ for the exit absorbers.

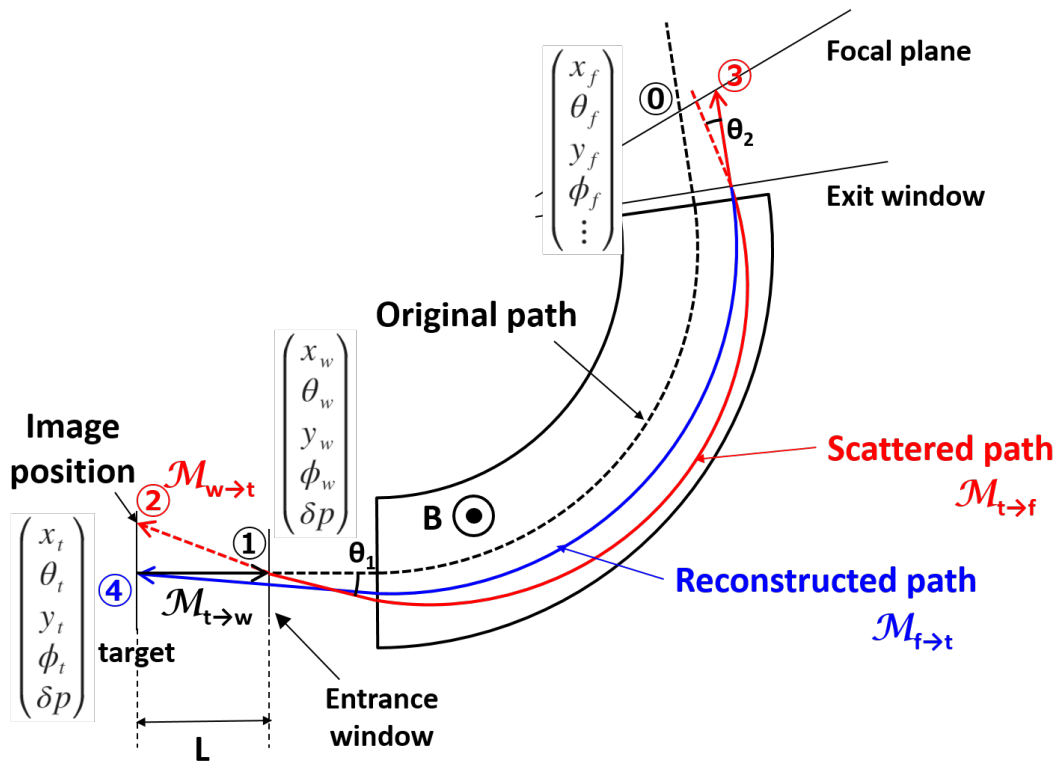


Figure 5.13: A simple drawing of multiple scattering effect. In order to estimate the particle momentum differences between the *true* momentum and the reconstructed momentum due to the multiple scattering effect, particles were generated and transferred in the Monte Carlo simulation.

- ① : The particles transferred from the target to the entrance vacuum window.
- ② : After the scattering angles at the window were taken into account, the particles re-transferred to the image position at the target.
- ③ : The particles transferred from the target to the focal plane.
- ④ : After the scattering angles at the exit vacuum window were taken into consideration, the particles were transferred to the target.

The momentum difference between the generated momentum and the momentum at ④ corresponds to the multiple scattering effect in the absorbers.

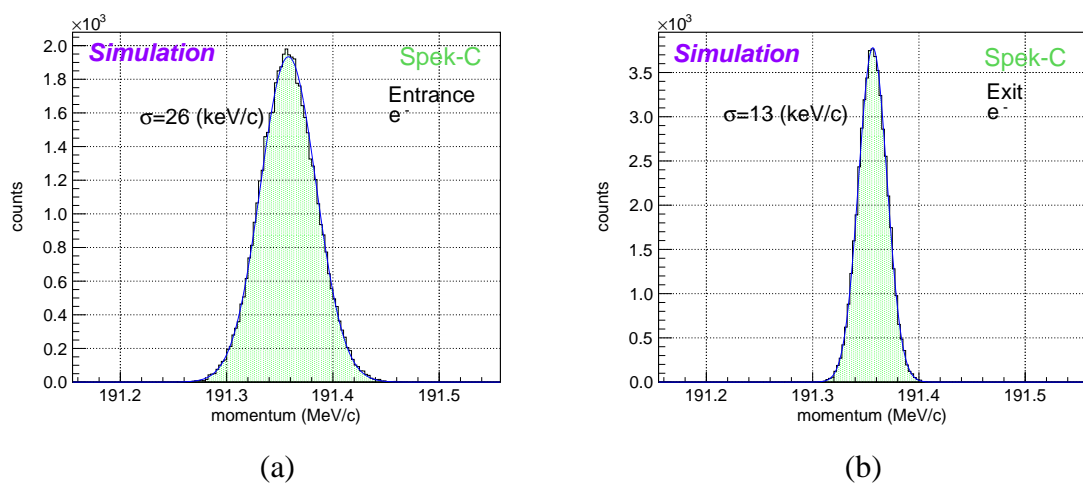


Figure 5.14: An expected momentum spread with multiple scattering effect in Spek-C. The each component were estimated separately. (a) A momentum spread due to the spectrometer entrance absorbers. (b) A momentum spread due to the spectrometer exit absorbers.

Effect from detector resolution (F_3)

The momentum spread due to the detector position and angular resolution were estimated using the Monte Carlo simulation. The difference of the reconstructed momentum calculated by Equation 5.14 between with VDC resolutions and without VDC resolutions were calculated. The the VDC resolutions were given from the data in the calibration runs. As a result, the effect from the VDC resolution was $\sigma^G \sim 1 \text{ keV}/c$ for both spectrometers; that was negligibly small.

Effect from angular resolution at target (F_4)

The angular resolution at each hole of the sieve collimator was ~ 2 mrad, which corresponds to less than 1 keV for tantalum target and 5 keV for carbon target according to the scattering electron energy calculation in Equation 2.30. In addition, the deviation of the hole pattern, which was 3 mrad as mentioned in Section 5.4.2, must to be consideration. The uncertainty of detection angle in the full acceptance was taken as square root of the sum of the squares, that is, 4 mrad with rms. This corresponds to 1 keV for tantalum target and 11 keV for carbon target.

Effect from transfer matrix ambiguity (F_5)

The reconstructed momentum from detected position and angle is spread due to the ambiguity of the transfer matrix. The scattered events from one hole which has larger diameter at central position in the sieve collimator were selected so as to minimized this ambiguity. Figure 5.15 shows Δp distributions at run “C1”. Peaks of the ground state and the first excited state were fitted with Landau-Gauss functions to get peak shapes. Similarly, the elastic scattering peak for ^{181}Ta was also fitted.

Table 5.5 shows a summary of the peak shapes with all acceptance (σ_{all}^L for Landau width and σ_{all}^G for Gaussian width) and one hole selection (σ_{cut}^L for Landau and σ_{cut}^G for Gaussian). Expected peak shapes estimated from $F_1 \sim F_4$ were also given in the table. It was found that the peak shapes σ_{cut}^G were well consistent with the expected shapes excepting for “C1” in Spek-A, it means that the peak shapes in the limited acceptance were well understood with the estimation $F_1 \sim F_4$. Therefore, we considered the peak shape differences between all acceptance and one hole selection were caused by the ambiguity of the transfer matrix. The momentum spread due to the matrix ambiguity was estimated with $(\sigma_{all}^L - \sigma_{cut}^L)$ for Landau component and $\sqrt{(\sigma_{all}^G)^2 - (\sigma_{cut}^G)^2}$ for Gaussian component. A summary of this estimation was summarized in Table 5.6.

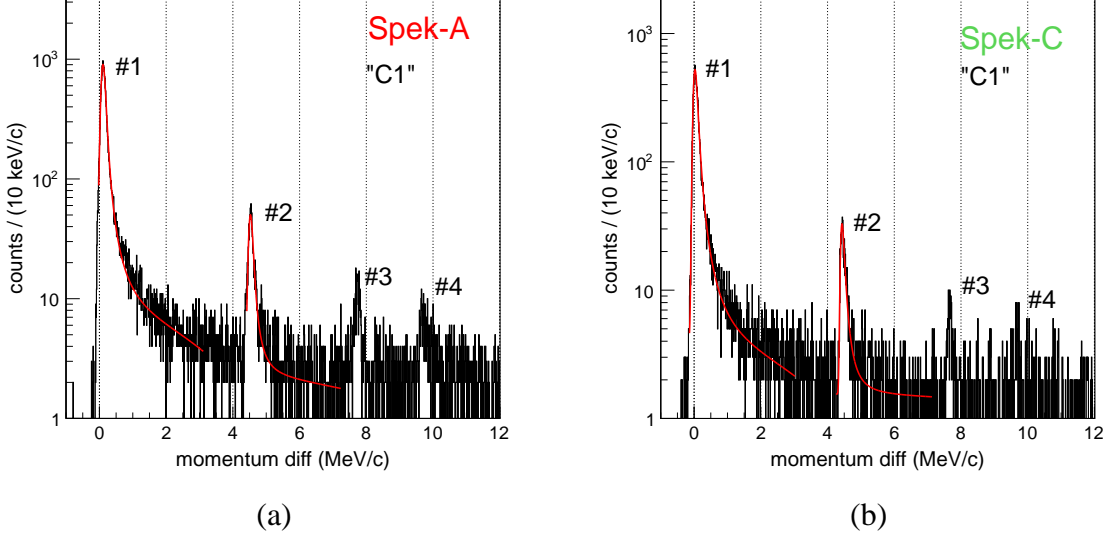


Figure 5.15: Momentum differences with angular acceptance cut at run “C1”.

Table 5.5: A summary of peak shapes in elastic scattering experiments. Results of first four rows were obtained from the fitting for all acceptance data (σ_{all}^L and σ_{all}^G). Next four rows were for one hole selection (σ_{cut}^L and σ_{cut}^G).

Run	width in Spek-A		width in Spek-C	
	Landau σ^L (keV/c)	Gauss σ^G (keV/c)	Landau σ^L (keV/c)	Gauss σ^G (keV/c)
“Ta1”	18±0	29±0	27±1	61±1
“Ta2”	19±0	28±0	26±1	55±1
“C1” g.s.	23±0	53±0	30±0	68±1
“C1” 1st 2 ⁺	23±1	54±2	31±2	75±3
“Ta1” w/ cut	15±1	22±1	18±1	23±2
“Ta2” w/ cut	16±1	24±1	19±1	26±3
“C1” g.s. w/ cut	20±1	48±1	27±1	34±1
“C1” 1st 2 ⁺ w/ cut	23±3	42±5	25±4	28±7
Expected (¹⁸¹ Ta) w/ cut	5	23	5	28
Expected (¹² C) w/ cut	9	27	9	32

Table 5.6: A summary of expected momentum spread due to the matrix ambiguity. We took weighted averages of two peaks in Table 5.5 for each target.

Run	Spek-A		Spek-C	
	Landau	Gauss	Landau	Gauss
	σ^L (keV/c)	σ^G (keV/c)	σ^L (keV/c)	σ^G (keV/c)
¹⁸¹ Ta	3±1	17±1	6±1	52±3
¹² C	2±1	25±1	3±1	59±2

Summary of the peak shape for electron elastic scattering data

So far, the effects of the momentum spread were estimated for each component $F_1 \sim F_5$ to reproduce the peak shapes in the calibration runs. The results are summarized in Table 5.7.

Through these estimations, we succeeded to explain the peak shapes of the Gaussian component for ^{12}C and ^{181}Ta calibration runs in Spek-C. For Spek-A, the expected peak shape of the Gaussian component for ^{181}Ta target reproduced the peak shape in the data, while it was ~ 15 keV/c narrower than the data for ^{12}C run. In addition, the peak shapes of the Landau component in the calibration data were about two times or ten and several keV wider than the expected width. We considered these inconsistency as a systematic uncertainty for the peak shape estimation of decay pions.

Table 5.7: Summary of peak shape assumption

Spek-A	¹⁸ Ta			¹² C		
	Landau width σ^L (keV/c)	Gaussian rms σ^G (keV/c)	Landau width σ^L (keV/c)	Gaussian width σ^G (keV/c)	Landau width σ^L (keV/c)	Gaussian rms σ^G (keV/c)
Energy loss (F_1)	5	4	9	9	13	13
Multiple scattering effect (F_2)	-	23	-	-	23	23
Detector resolution (F_3)	-	<1	-	-	<1	<1
Angular res. at target at one hole (F_4)	-	<1	-	-	5	5
Angular res. at target in full acceptance (F_4)	-	1	-	-	11	11
Matrix (F_5)	3±1	17±1	2±1	25±1	25±1	25±1
Expected resolution	8±1	29±3	11±1	38±2	38±2	38±2
Experimental data	19±0	28±0	23±0	53±0	53±0	53±0
Landau width σ^L (keV/c)	Gaussian rms σ^G (keV/c)	Landau width σ^L (keV/c)	Gaussian width σ^G (keV/c)	Landau width σ^L (keV/c)	Gaussian rms σ^G (keV/c)	
Energy loss (F_1)	5	4	9	9	13	13
Multiple scattering effect (F_2)	-	29	-	-	29	29
Detector resolution (F_3)	-	<1	-	-	<1	<1
Angular res. at target at one hole (F_4)	-	<1	-	-	5	5
Angular res. at target in full acceptance (F_4)	-	1	-	-	11	11
Matrix (F_5)	6±1	52±3	3±1	59±2	59±2	59±2
Expected resolution	11±1	60±3	12±1	68±2	68±2	68±2
Experimental data	25±1	58±1	30±0	68±1	68±1	68±1

Expected peak shape for decay pion momentum

In order to estimate the peak shape for decay pions, we expanded the peak shape estimation for electrons to pions.

Table 5.8 shows a summary of the peak shape estimation for pions. The fitting parameters for a decay pion peak are limited within the range of the expected resolution.

The estimations of F_1 , F_2 , and F_3 were performed with the same procedure as those for scattered electrons, while the generated particle was not electron but $133 \text{ MeV}/c \pi^-$. The component F_4 was set to 0, because the momenta of decay pions from hypernuclei dose not depend on their emitted angles, while the scattered electrons have the dependence according to the Equation 5.14. The component F_5 is in proportion to the central momentum because the momentum reconstruction with the transfer matrix is calculated with a relative momentum dp .

As already mentioned in the previous section, there are a systematic uncertainty for the peak shape estimation. We assumed this uncertainty in the best case and the worst case. For example, in Spek-C, the expected Landau width for ^{181}Ta was $11 \text{ keV}/c$ and that for ^{12}C was $12 \text{ keV}/c$, while the Landau width was $25 \text{ keV}/c$ and $30 \text{ keV}/c$ for calibration runs of ^{181}Ta and ^{12}C , respectively. If an additional Landau width is needed to explain the calibration data, the additional width should be $25 - 11 = 14 \text{ keV}/c$ or $30 - 12 = 18 \text{ keV}/c$. On the other hand, if a multiplication factor for the expected Landau width is needed, the factor should be $25/11 = 2.25$ or $30/12 = 2.5$; the worst case is factor 2.5. Because the expected Landau width for the pion peak was $13 + 4 = 17 \text{ keV}/c$, the additional Landau width should be $(17 \times 2.5) - 17 = 26 \text{ keV}/c$. From three kinds of the additional Landau width 14, 18, and $26 \text{ keV}/c$, we chose the best case and the worst case, namely, the systematic uncertainty for the Landau width was obtained with $14\sim26 \text{ keV}/c$. Thus, the expected peak shape of decay pion from $^4\Lambda\text{H}$ in Spek-C was estimated as shown in Figure 5.16.

Table 5.8: Summary of expected peak shapes on momentum.

	${}^9\text{Be}$			
	Spek-A		Spek-C	
	Landau width σ^L (keV/c)	Gaussian rms σ^G (keV/c)	Landau width σ^L (keV/c)	Gaussian rms σ^G (keV/c)
Energy loss (F_1)	13	32	13	24
Multiple scattering effect (F_2)	-	45	-	58
Detector resolution (F_3)	-	<1	-	<1
Angular res. at target (F_4)	-	0	-	0
Matrix (F_5)	2±1	12±1	4±1	35±2
Additional component	+10~21	+12~15	+14~26	0
Expected resolution	25~36 ±1	64~67 ±1	31~43 ±1	70±2

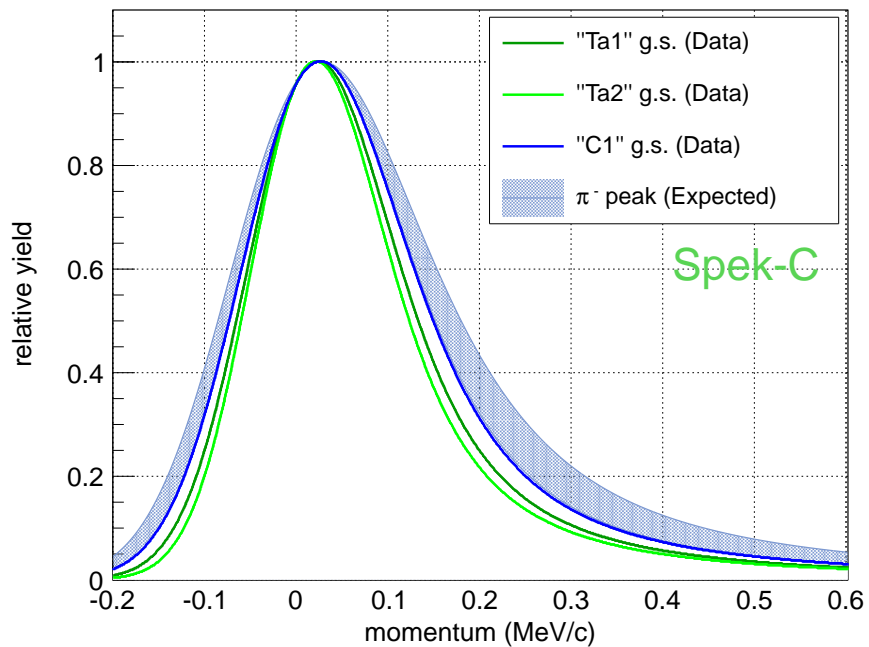


Figure 5.16: Peak shapes in the calibration runs and expected shapes on pion momentum in Spek-C. A location parameter of the Landau distribution was set to zero. Expected parameter limits for the peak shape of decay pion was summarized in Table 5.8. The peak shapes on the calibration runs were also given as solid lines.

Chapter.6

Results and discussion

In this chapter, the first observation of a decay pion peak from ${}^4_{\Lambda}\text{H}$ on the momentum distribution in Spek-C will be introduced. A evaluation of the robustness and the peak position will be described. Though a pion momentum was measured also in Spek-A, the momentum acceptance was set out of the decay pion peak from ${}^4_{\Lambda}\text{H}$. A momentum spectrum in Spek-A will be introduced in Appendix C

6.1 Pion spectrum

6.1.1 Coincidence event selection

Figure 6.1 shows the coincidence time spectrum between Spek-C and the Kaos spectrometers after K^+ events were tagged. The “ π^-, K^+ ” coincidence peaks on the coincidence time spectrum with a time window of ± 1.25 ns were selected as the decay pion events from the hyperons or hypernuclei. The number of the selected “ π^-, K^+ ” coincidence events are 1168 events (461 events for the threshold K^+ selection and 815 events for the likelihood K^+ selection with overlap of 108 events). Simultaneously, events out of the coincidence peaks are selected in order to estimate the distribution of the accidental background. The selected time windows for the accidental background are 15 ns for the left and the right side of the “ π^-, K^+ ” coincidence peak each. The number of the accidental background events are 3138 events.

6.1.2 Decay pion momentum distribution

Figure 6.2 shows decay pion momentum distributions in Spek-C with different K^+ selections: the threshold K^+ selection, the likelihood K^+ selection. The decay pion momentum distribution with the combined K^+ selection is also shown in the bottom side of Figure 6.3. The momentum distributions of the accidental background are simultaneously plotted on the true coincidence

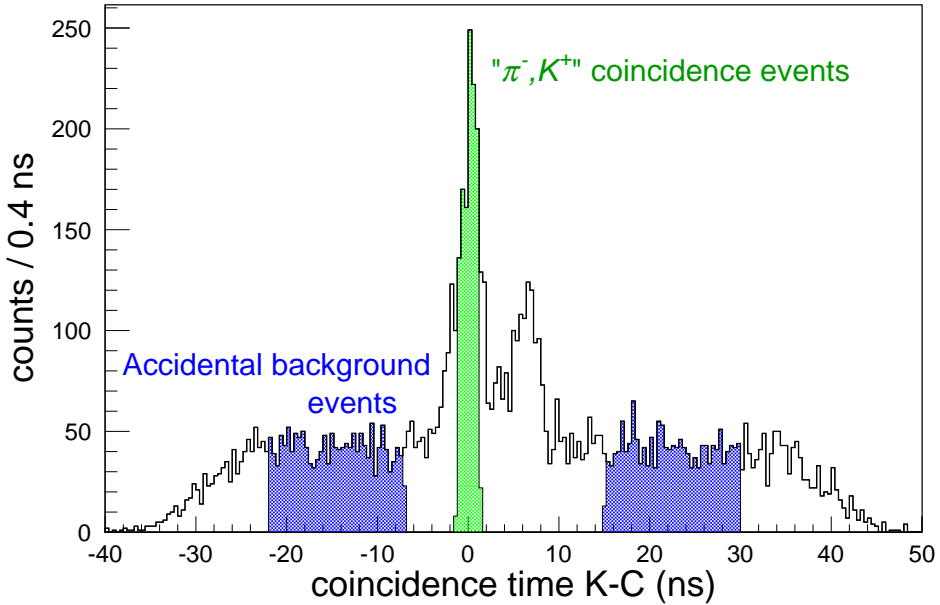


Figure 6.1: Coincidence time spectrum with K^+ tag. Selected “ π^- , K^+ ” coincidence time windows are filled with a green color for the Spek-C and Kaos coincidence. The width of the time windows are ± 1.25 ns for each coincidence peak. Blue regions are selected to estimate accidental background distribution. The total width of the selected windows are 30 ns for each coincidence spectrum.

events after collection of the width of selected time windows (1.25 ns / 15 ns).

This accidental background distributions correspond to the distributions of the momentum acceptance in pion spectrometers. We confirm the accidental backgrounds have flat distributions from 110~140 MeV/c in Spek-C. The distributions above the accidental backgrounds are attributed to the decay pion events from hyperon or hypernuclear decays. Maximum likelihood fits with the linear functions are performed to these pion momentum distributions excepting for 132~134 MeV/c in Spek-C.

In these momentum distributions and fitting results, a significant excess is found around 133 MeV/c in Spek-C. From the table of the expected momentum (Table 2.1), the peak is uniquely identified with the monochromatic pions from ${}_{\Lambda}^4\text{H} \rightarrow {}^4\text{He} + \pi^-$. Some other enhancement was recognized at 113, 126, and 131 MeV/c. In order to check the significance quantitatively, p -values of the peak counts are calculated every 20 keV/c with the Poisson distribution, which are defined as follows:

$$\Pr(X \geq N_p \mid N_b), \quad (6.1)$$

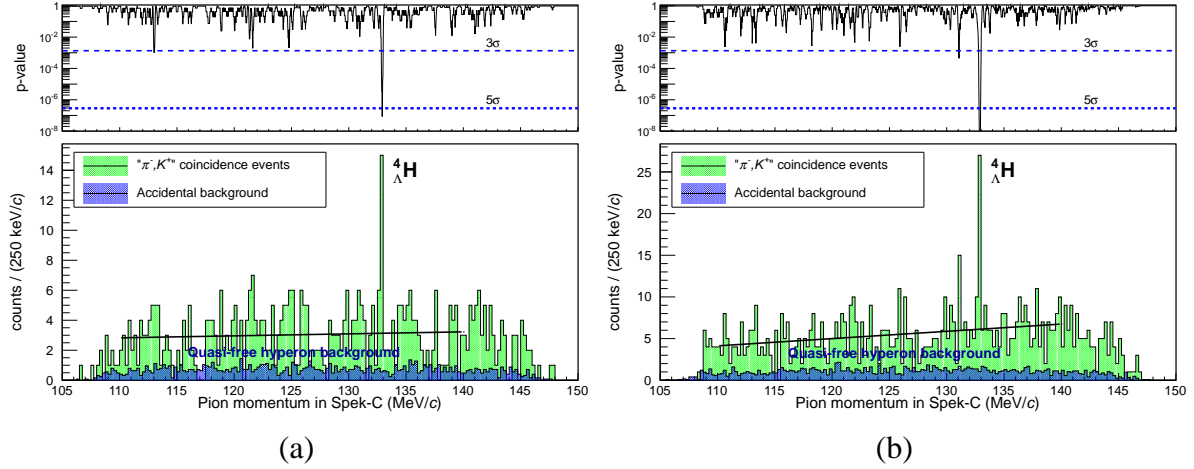


Figure 6.2: Pion momentum distributions in Spek-C with (a) the threshold K^+ selection and (b) the likelihood K^+ selection with p -values of the peak counts. The momentum distributions in “ π^-, K^+ ” coincidence peaks and those out of peaks (accidental backgrounds) are shown. A solid line on the momentum distribution shows the background obtained by the fitting with the linear and the Gaussian functions for background and ${}^4\Lambda$ peak, respectively (only the linear component was drawn). In the top panels, p -values of the peak counts for the background counts are given with lines of the 3σ and 5σ confidence level.

where, N_p is the number of peak counts within $\pm 1\sigma$ of the expected momentum resolution ($\sigma = 80 \text{ keV}/c$), and N_b is the number of expected background counts within the same momentum range. The background height are estimated by the simultaneous fitting with the linear (background) and the Gaussian (peak) functions using the maximum likelihood method.

The results of the p -value calculations are shown in the top panels of each pion momentum distribution (Figure 6.2 and Figure 6.3) with lines of 3σ and 5σ confidence levels.

From the confidence level distribution, we observe a peak around $133 \text{ MeV}/c$. The significance of the peak is 6.7σ ($p\text{-value} = 1.3 \times 10^{-11}$) at $132.92 \text{ MeV}/c$ on the distribution in Figure 6.3. The peak structure is also observed at the similar momenta with the K^+ threshold selection ($p\text{-value} = 1.2 \times 10^{-8}$ at $132.94 \text{ MeV}/c$) and the K^+ likelihood selection ($p\text{-value} = 1.4 \times 10^{-11}$ at $132.92 \text{ MeV}/c$). Since the peak significance of all other excesses are less than 5σ , statistically these peaks do not allow us to discuss about them.

Thus, we concluded that one decay pion peak from ${}^4\Lambda$ was observed with statistically good significance at $133 \text{ MeV}/c$ in Spek-C.

A bottom panel of Figure 6.4 shows the distribution of the Λ binding energy in ${}^4\Lambda$ calculated

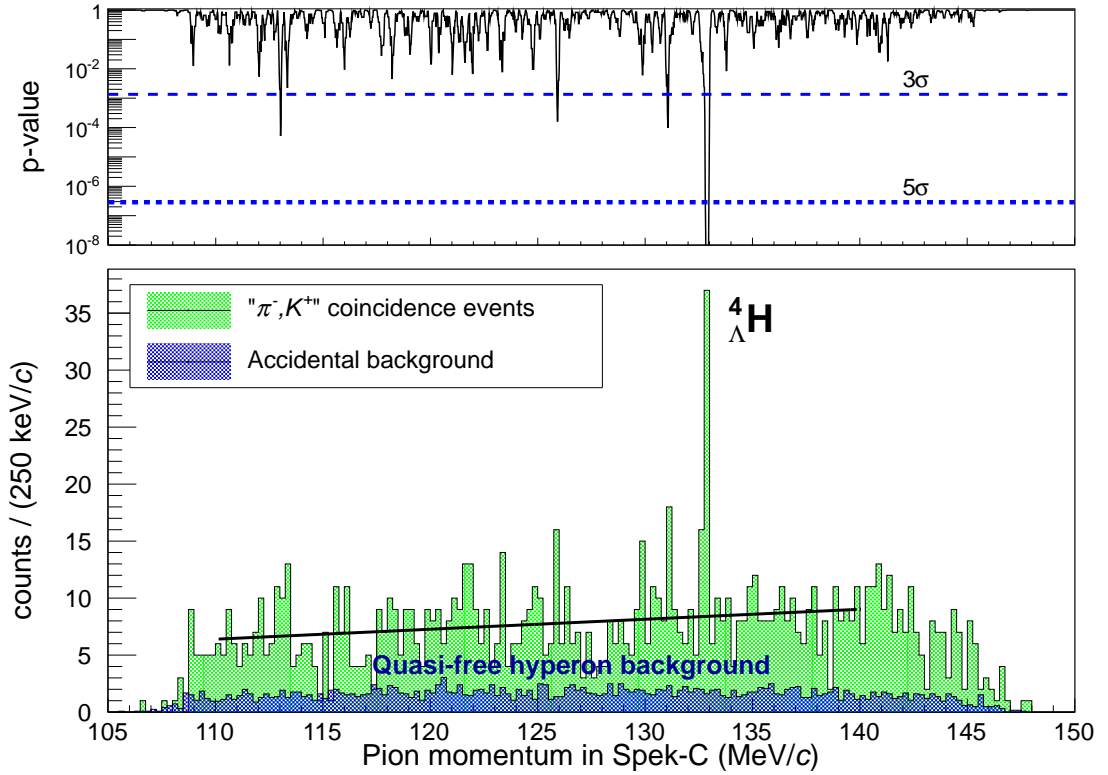


Figure 6.3: A pion momentum distribution in Spek-C with the combination K^+ selection with p -values of the peak counts. Configurations of the figure were same (see the caption in Figure 6.2).

from the pion momentum distribution in Figure 6.3. The conversion from the pion momentum to the Λ binding energy was performed in Equation 2.10. The used masses of particles and nuclei used in the calculation of the Λ binding energy of ${}^4\Lambda H$ are listed in Table 6.1.

The top panel of Figure 6.4 shows the Λ binding energy distributions of ${}^4\Lambda H$ from the available data of the emulsion experiments [Gaje67, Bohm68, Juri73]. The latest Λ binding energy of ${}^4\Lambda H$ is derived from the average of these emulsion data. The precision of our data is much better than it of emulsion data.

In order to confirm whether the peak structure exists only from the " π^-, K^+ " coincidence events, the pion momentum distributions are checked with other coincidence combinations, namely π^+ or proton tag. Figure 6.5 (a) shows the coincidence time distributions in Spek-C-Kaos with π^+ selection in Kaos. The coincidence peaks between π^- and π^+ are selected with time windows of ± 1.2 ns, and the accidental background events are also selected in 15 ns for left and right side of the peaks as with the " π^-, K^+ " coincidence event selections. Figure

Table 6.1: A List of the particle masses in the Λ binding energy calculation of ${}^4_{\Lambda}\text{H}$ [PDG12, Audi03].

Particle	π^-	${}^4\text{He}$ (daughter nucleus)	${}^3\text{H}$ (core nucleus)	Λ
Mass (MeV/c^2)	139.570	3727.379	2808.921	1115.683

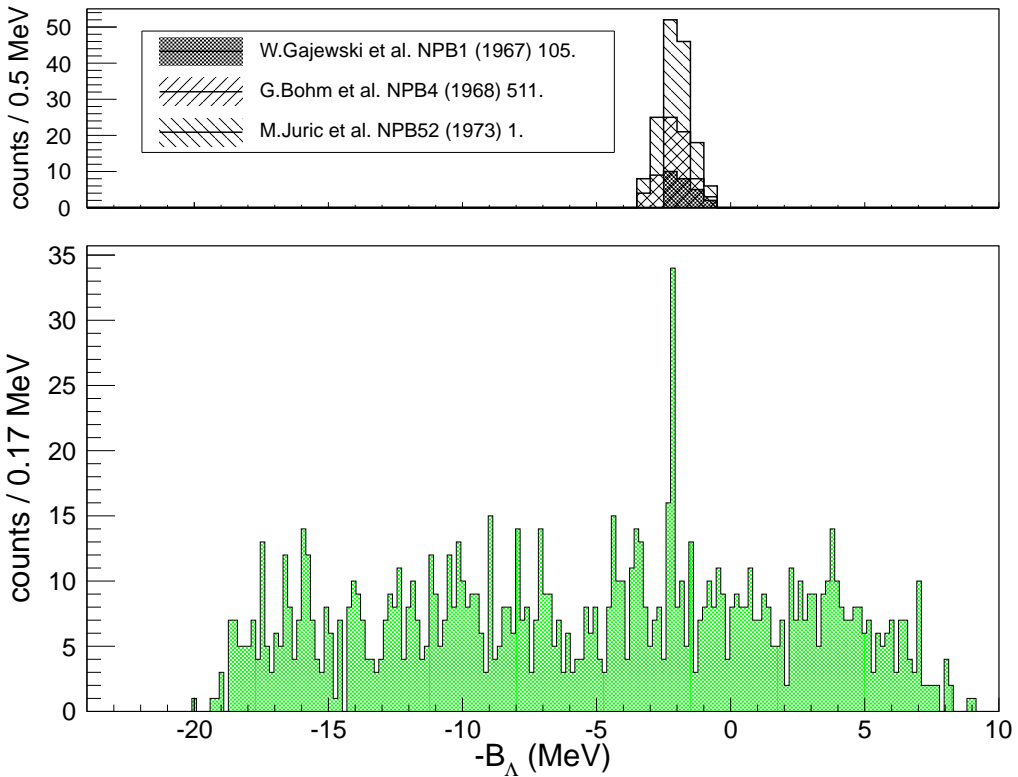


Figure 6.4: Λ binding energies of ${}^4_{\Lambda}\text{H}$. The top panel of the figure shows the available data in the emulsion experiments [Gaje67, Bohm68, Juri73]. The colored distribution in the bottom panel is the observed data in Spek-C with same scale for the binding energy. The observed peak position of ${}^4_{\Lambda}\text{H}$ is consistent with those in the emulsion experiments. The full width at half maximum of the peaks are 1.4 MeV and 0.13 MeV for the emulsion experiments and the observed data, respectively from the fitting results with the Gaussian function.

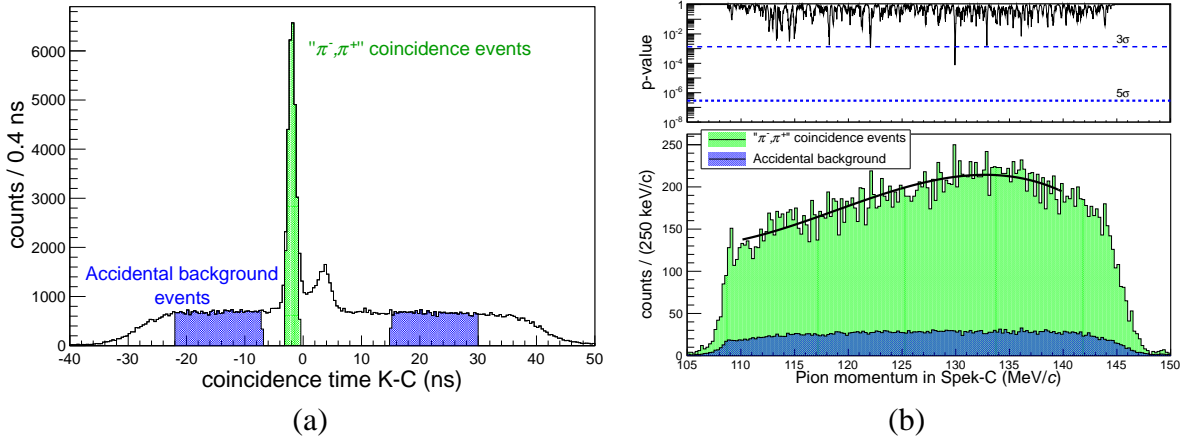


Figure 6.5: Coincidence time spectra in π^+ selection in Kaos, and momentum distribution in Spek-C. (a) The coincidence time distribution between Spek-C and Kaos. (b) The pion momentum distribution of the selected coincidence events in Spek-C with a simultaneous plot of p -value of the peak counts. The green colored regions correspond to the “ π^-,π^+ ” coincidence events with Spek-C. The blue colored regions are selected accidental backgrounds to estimate the shape of the momentum acceptances. Lines on the pion momentum distributions are the fitting curve with the third order polynomial function. Any significant peak structures are not found on the momentum spectra.

6.5 (b) shows the momentum distributions in the pion spectrometers in the selected coincidence times. We fit the momentum distributions with third order polynomial functions, and calculate the p -values following the same procedure for the peak search for “ π^-,K^+ ” coincidence events. Peak structures with $> 5\sigma$ cannot be observed in the “ π^-, π^+ ” coincidence spectrometers.

Similarly, the pion momentum distributions in “ π^-, p ” coincidence events are checked. The selected coincidence time windows are ± 2.0 ns for true coincidence events, and 15 ns time windows are set for accidental background events. The selected events and their momentum distributions are shown in Figure 6.6. No peak structures were observed.

Thus, the clear peak structure is observed at 133 MeV/c in Spek-C only for “ π^-, K^+ ” coincidence events. This peak corresponds to the decay pion from ${}^4_{\Lambda}\text{H} \rightarrow {}^4\text{He} + \pi^-$, and we conclude that this is the first observation through this decay pion spectroscopy using electro-photo production method.

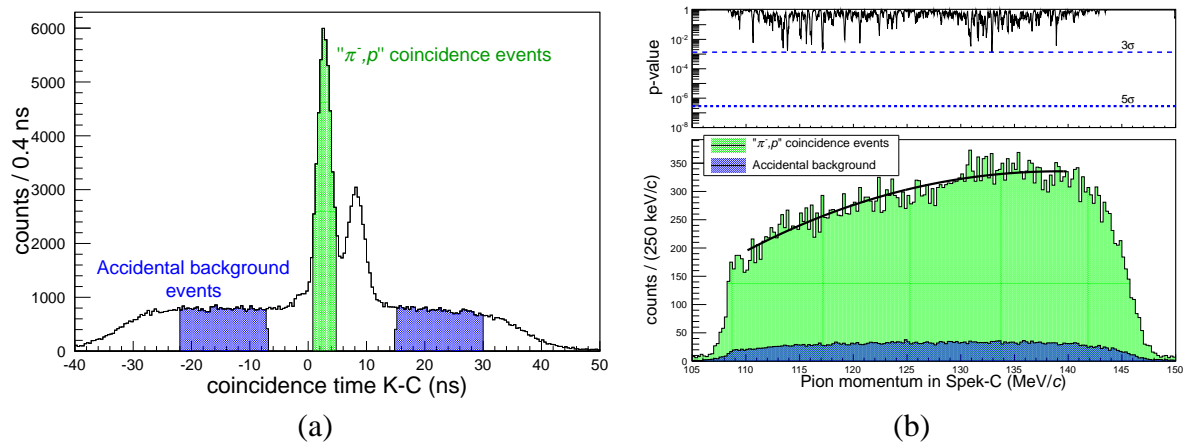


Figure 6.6: Coincidence time spectra in proton selection in Kaos, and momentum distribution in Spek-C. The same figures as Figure 6.5 are shown, but the selected events are not π^+ s but protons in Kaos. Any significant peak structures are not find also in the " π^- , p " coincidence events.

6.2 Peak fitting

In this section, the details of the peak fitting procedures for decay pion momentum distribution will be explained.

The peak is fitted by the Landau-Gauss distribution, which has three parameters; a most probable value (*MPV*) of Landau function (p_{π^-}), a width of Landau function (σ_L), and a width of Gaussian function (σ_G). The expected peak shape has been discussed in Section 5.4.4. From that study, we set limits of the allowed regions for the fit parameters. The width of Landau function was limited as $\sigma_L = 0.030 \sim 0.044$ keV/c and the width of Gaussian function was done as $\sigma_G = 0.068 \sim 0.072$ keV/c. The most probable value of Landau distribution was defined as a free parameter.

Since the number of events were limited, *un-binned maximum likelihood fit* was performed treating our dataset obeyed to the Poisson statistics. In case of the Landau-Gauss distribution, a probability density function $F(m; p_{\pi^-}, \sigma_L, \sigma_G)$ can be described by observable momentum m , and fit parameters $\vec{p} = (p_{\pi^-}, \sigma_L, \sigma_G)$. The parameter fit was carried out by a minimization of a negative logarithm of the likelihood (NLL) for every event;

$$-\ln L(\vec{p}) = - \sum_i \ln F(m_i; \vec{p}), \quad (6.2)$$

using MIGRAD in the MINUIT package. An error of each parameter was defined as +0.5 above a minimum value of NLL , which corresponds to standard deviation errors at the large statistics limit.

Peak fitting with parameter limitations (Landau-Gauss + linear function)

Figure 6.7 shows a simultaneous fitting result of the pion momentum distribution in Spek-C with the Landau-Gauss function as a peak structure and the linear function as a background. Only the linear part is picked out at the view of the full momentum acceptance. An enlarged view of the ${}^4_\Lambda H$ peak region is given in the window. The pion momentum distribution with 100 keV/c bins and their errors under the Poisson distribution are simultaneously plotted, while the fitting are performed for the un-binned data.

Figure 6.8 shows the distribution of the NLL . From this distribution, we determined the momentum of the peak position as $p_{\pi^-} = 132.92 \pm 0.02$ MeV/c. It should be noted that we do not use the *MPV* of the Landau-Gauss distribution as the peak position but the *MPV* of the Landau component is adopted as the peak position. Because the definition of the peak position must be same as the definition in the momentum calibration as explained in Section 5.4.2. The

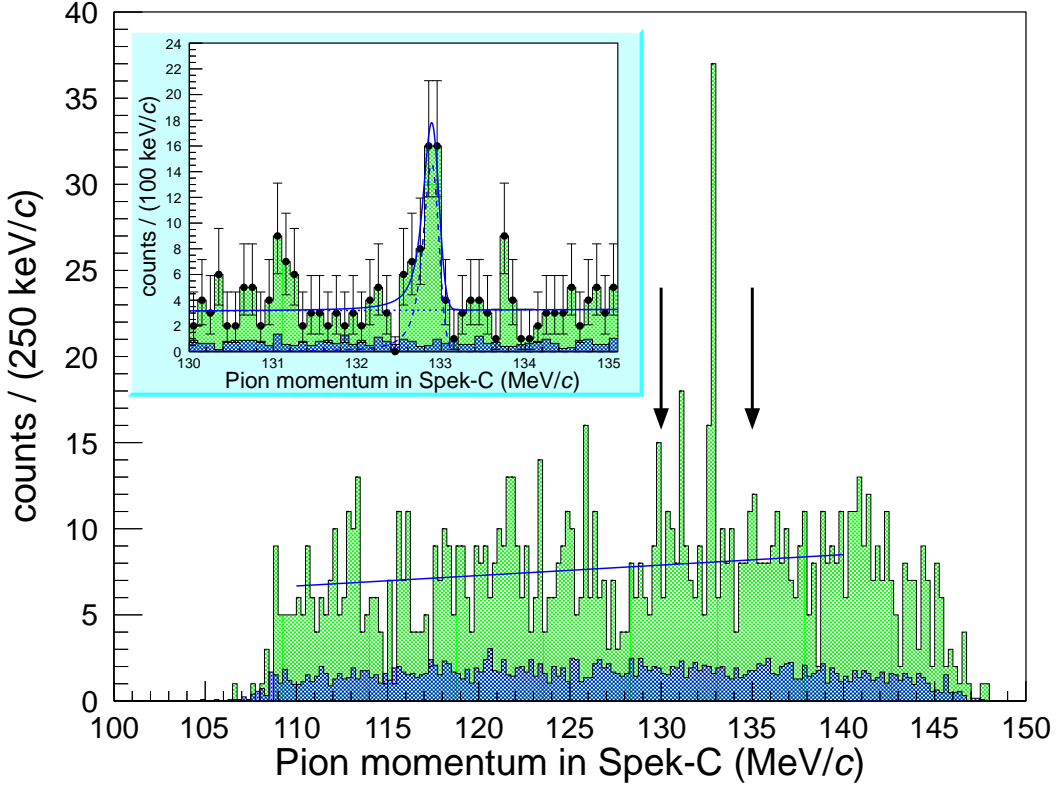


Figure 6.7: The pion momentum distribution with a fitted line in Spek-C. The Landau-Gauss function and the linear function are assumed with the peak distribution and the background distribution, respectively. Only the linear part is plotted in the wide view. The fitting is performed under the *un-binned maximum likelihood fit* (see text). The enlarged view of the interested region within the arrows is shown as inset.

MPV of the Landau-Gauss distribution is obtained as $132.89 \text{ MeV}/c$, and this $-0.03 \text{ MeV}/c$ shift can be explained with the convolution of the Gaussian distribution.

The width of the the Gaussian part (σ_G) is $0.07 \pm 0.01 \text{ MeV}/c$ with the root mean square, and that of Landau part (σ_L) is $0.03 \pm 0.01 \text{ MeV}/c$. The peak width is $0.22 \pm 0.02 \text{ MeV}/c$ with the full width at half maximum.

Peak fitting without parameter limitations (Landau-Gauss + linear function)

In order to find the minimum convergence points, the pion momentum distribution is almost freely without parameter limits from the expected peak shape. The used probability density function is exactly the same function as the previous fitting (the Landau-Gauss function + the linear function). Figure 6.9 shows the fitting result and the *NLL* distributions. Through this fitting, it was found that the fitting converges at $p_{\pi^-} = 132.92 \pm 0.02 \text{ MeV}/c$, $\sigma_G = 0.04 \pm 0.02$

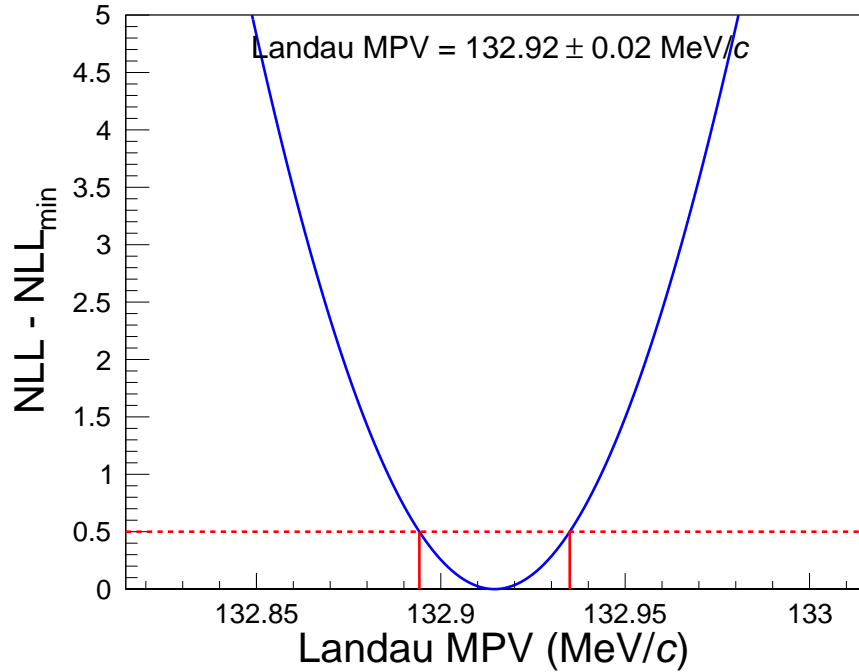


Figure 6.8: A distribution of the negative log likelihood (NLL) as a function of a most provable value (MPV) of the Landau function. The minimum value of the NLL is set to zero. Cross points of the NLL curve and a dashed line indicates the standard deviation errors of the parameter MPV.

MeV/c , and $\sigma_L = 0.02 \pm 0.01 \text{ MeV}/c$. The peak position was obtained at the same position with the previous result with limits. The peak width was $0.15 \pm 0.04 \text{ MeV}/c$, which is $\sim 70\%$ narrower width than the fitting result with parameter limitations, thought the difference dose not affect the Λ binding energy.

There is an another convergence point at $\sigma_G = 0.00 \text{ MeV}/c$ and $\sigma_L = 0.02 \text{ MeV}/c$. However, this point is rejected because the width becomes un-physically narrow.

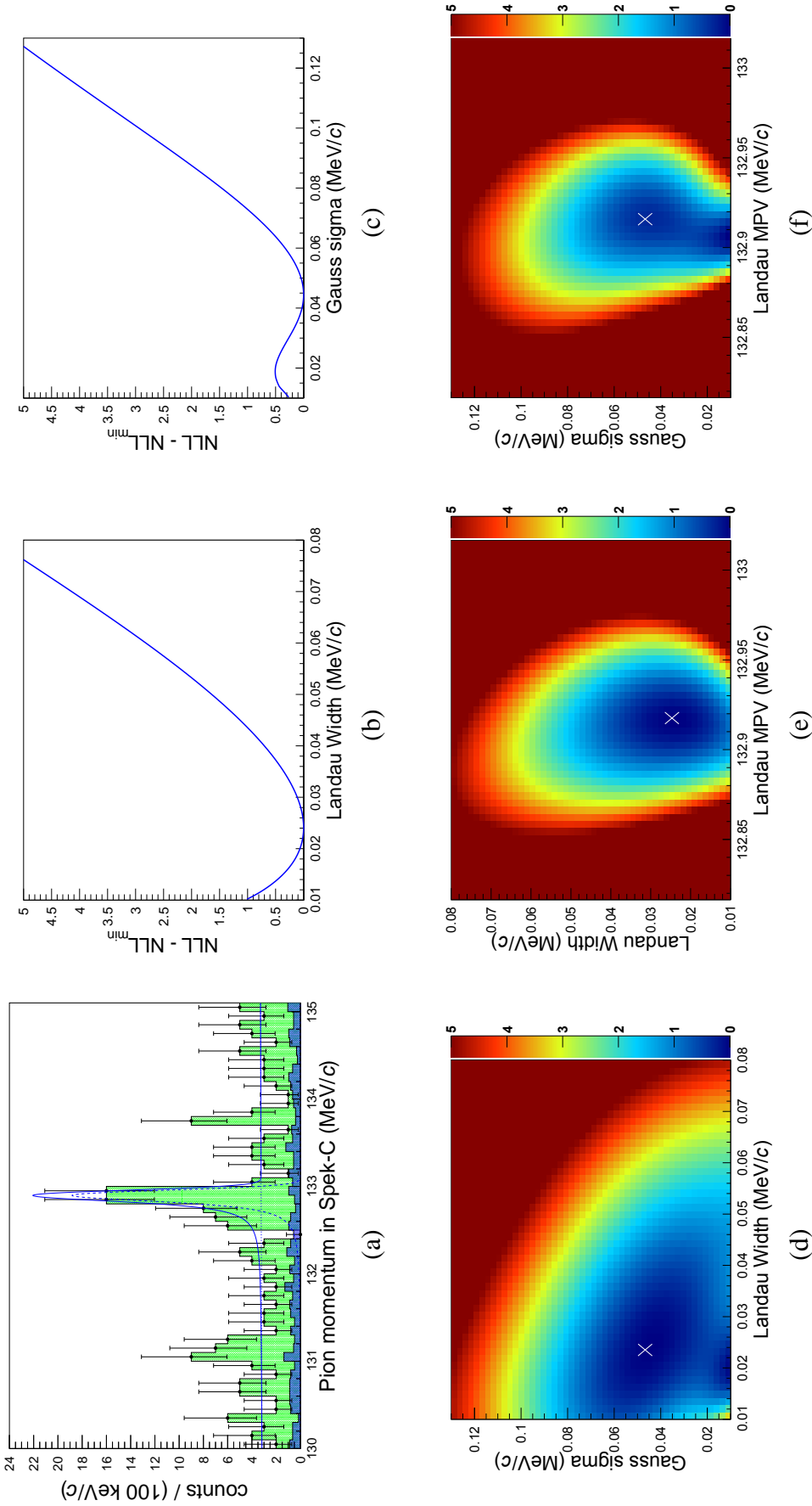


Figure 6.9: Results of a peak fitting without parameter limitations. (a) A histogram of pion momentum in Spek-C. A 2-dimensional NLL distribution as a function of (b) the parameter σ_L and (c) the parameter σ_G . (d-f) A 2-dimensional NLL distributions

Table 6.2: A summary of the fitting result for the pion momentum distribution.

PDFs		Limitations		Results			
Peak	B.G.	σ_G	σ_L	σ_G	σ_L	p_{π^-}	NLL
Landau	1 st pol	0.068-0.072	0.030-0.044	0.07(1)	0.03(1)	132.92(2)	3198.15
	1 st pol	0.010-0.200	0.010-0.200	0.04(2)	0.02(1)	132.92(2)	3197.21
	3 rd pol	0.010-0.200	0.010-0.200	0.04(2)	0.02(1)	132.92(2)	3196.84
	QF Hyp*	0.010-0.200	0.010-0.200	0.03(2)	0.02(1)	132.92(2)	3203.73
Non	1 st pol	-	-	-	-	-	3229.96

* The simulated quasi-free hyperon background shape is assumed (see text).

Peak fitting in several background shapes

In order to study effects of dependences on fitting functions of the background, fitting results are checked by assuming various background functions. The assumed functions are the third order polynomial function and the expected quasi-free hyperon distribution by the Monte Carlo simulation, which was already shown in Figure 2.16. In the simulation, the elementary cross sections of the $p(\gamma, K^+) \Lambda$ reaction, the $p(\gamma, K^+) \Sigma^0$ reaction, and the $n(\gamma, K^+) \Sigma^-$ reaction from the K-Maid model [Mart99] were taken into account. The details of the simulation was explained in Section 2.3.4.

Peak fitting summary

The results of the fitting results are summarized in Table 6.2. The peak positions in all background functions are obtained at the same momentum. Therefore, we confirm the robustness of the peak position at $p_{\pi^-} = 132.92 \pm 0.02$ MeV/c.

A fitting result with a background-only probability density function (linear function) is also given in order to discuss the goodness of the fitting. The significance of the signal (S_L) calculated under the likelihood ratio in the Reference [Cous08] is the following;

$$S_L = \sqrt{-2 \ln(L(bg)/L(s + bg))} = 7.9 , \quad (6.3)$$

where $L(bg)$ is a minimized likelihood with a background-only function, and $L(s + bg)$ is that with a signal and background functions.

6.3 Systematic error

The measured pion momentum contains ambiguities due to the following uncertainties:

1. A beam energy in the momentum calibration,

2. angles of the pion spectrometer with respect to the target,
3. a beam position at the target,
4. energy loss corrections in the materials,
5. a Stability of the magnetic field in the pion spectrometer,
6. a momentum linearity of the pion spectrometer.

The first two uncertainties (1. and 2.) are related to the accuracy of the momentum calibration data, the last two (5. and 6.) are to the reliability of the measured momentum for the decay pion, and the remained two are to the both data. The detail discussions are given in bellow.

■ Effects for the beam energy uncertainty

An uncertainty of the beam energy was 160 keV during the calibration runs. It was estimated from the uncertainty of the magnetic field for the last bending magnet in the beam line. This beam energy uncertainty can be converted to the momentum uncertainty of the scattered electron using Equation 5.4: it was $160 \text{ keV}/c$. Because the central momentum of the Spek-C was set to 195 and 208 MeV/c in the ^{181}Ta target runs, while it was 125 MeV/c in the hypernuclear runs, the momentum uncertainty was scaled by a factor of $133/((195 + 208)/2) = 0.66$. This scale factor was ensured with the magnetic field measurement from the NMR probes in the dipole magnets. Thus the momentum ambiguity for the pion momentum due to the beam energy uncertainty was estimated as $160 \times 0.66 = 110 \text{ keV}/c$.

■ Effects for the angle of Spek-C

The momentum of the scattered electron was changed with the installed angles of Spek-C as shown in Equation 5.4. The angles of Spek-C was ensured with an accuracy of 0.1° , which corresponds to less than $1 \text{ keV}/c$ for the momentum ambiguity thanks to the heavy mass of the ^{181}Ta target in the calibration runs. Therefore, the momentum ambiguity due to the Spek-C angle was negligibly small.

■ Effects for the beam position at the target

The tracking reconstruction from the detector plane to the target position was performed with an assumption of the fixed beam position at the target. If the beam position changes, the reconstructed momentum should be changed, too. During the experiment, about 2.2 mm beam position shift for the non-dispersive direction of Spek-C was observed using the Al_2O_3 screen. Because the beam optics of Spek-C was set to be parallel-to-point for the non-dispersive plane, the reconstructed momentum is not affected by this beam position shift qualitatively. In order to check the effect to the reconstructed momentum qualitatively, the reconstructed position at the target was changed by 2.2 mm. By this way, we confirmed the momentum ambiguity due to the

beam position is $50 \text{ keV}/c$.

■ Effects for the energy loss corrections

The accuracy of the energy loss calculation using the Bethe-Bloch formula is less than 0.1% for the high velocity particle [Zieg99]. Because the mean energy loss in the materials was about 120 keV in the ^{181}Ta calibration runs, the uncertainty from the formula is negligible small. The thickness of the air gap between the target vacuum chamber and the Spek-C vacuum chamber was set to 10 cm, however, this thickness may changes due to dents of the vacuum windows with the pressure difference. The mean energy deposited changes only +6 keV even if the air gap was not 10 cm but 12 cm. Therefore, we concluded the momentum ambiguity due to the energy loss corrections is less than $10 \text{ keV}/c$.

■ Effects for the stability of the magnetic field

The first dipole magnet in Spek-C equips the compensation circuit to keep the NMR readout constant. However, the compensation circuit did not work in the first 2 weeks in the experiment. The readouts from the NMR probes was recorded every ~ 10 minutes. However, because Spek-C has two dipole magnets and these two magnets control each other, momentum correction using the NMR readouts is difficult. Therefore, we estimate the momentum ambiguity from the distribution of the NMR readouts in the first dipole magnet, which is the estimation in worst case. The root-mean-square of the distribution was $\Delta B = 0.10 \text{ mT}$, which corresponds to $\Delta B/B = 0.30\%$. As a result, the momentum ambiguity due to the stability of the magnetic field was estimated with $133 \text{ MeV}/c \times 0.30\% = 40 \text{ keV}/c$.

■ Effects for the momentum linearity

The relative momentum of the $^4_{\Lambda}\text{H}$ peak was $dp = +12\%$, while the calibration points in the relative momentum in Spek-C were $dp = +0$ and $+7\%$. The momentum of the $^4_{\Lambda}\text{H}$ peak is extrapolation point with the calibration momentum. Therefore, only ^{181}Ta data set is not enough to guarantee the linearity.

Therefore, we used the excitation energies of the ^{12}C runs which cover $dp = +4 \sim +14\%$; this dependence is suitable to evaluate the momentum linearity for region of interest. As already shown in Figure 5.10, the excitation energies for the ^{12}C peaks did not have dependence with the relative momentum, that is a good proof to ensure the good momentum linearity. In this thesis, the momentum ambiguity due to the momentum linearity was estimated with $<30 \text{ keV}/c$ from the fluctuation of the ^{12}C peak positions.

In summary, the total systematic uncertainty was obtained with the square-root of sum of squares for each uncertainty. As a result, the systematic uncertainty of the momentum for the

Table 6.3: A summary of systematic uncertainties.

Beam energy in the momentum calibration	110 keV/c
Angles of the pion spectrometer	<10 keV/c
Beam position	50 keV/c
Energy loss corrections	<10 keV/c
Stability of the magnetic field	40 keV/c
Momentum linearity	<30 keV/c
Total	120 keV/c

${}^4_{\Lambda}\text{H}$ peak was 120 keV/c in total as summarized in Table 6.3. This uncertainty was dominated with the uncertainty of the electron beam energy during the calibration runs. The momentum uncertainty can be translate into the uncertainty of the Λ binding energy using a factor of 0.725. Thus, the final systematic uncertainty was obtained with 90 keV/c.

6.4 Discussion

We observed the ${}^4_{\Lambda}\text{H}$ peak at $133 \text{ MeV}/c$ with a peak significance of 7.9σ . The peak width and shape were well consistent with the expected peak. The final peak momentum of ${}^4_{\Lambda}\text{H}$ in this thesis was obtained with:

$$p_{\pi^-} = 132.92 \pm 0.02(\text{stat.}) \pm 0.12(\text{sys.}) \text{ MeV}/c.$$

That is translated into the Λ binding energy as follows:

$$B_{\Lambda} = 2.12 \pm 0.01(\text{stat.}) \pm 0.09(\text{sys.}) \text{ MeV}.$$

This result is the first determination of the Λ binding energy of ${}^4_{\Lambda}\text{H}$ with a high accuracy using the spectroscopic method. Figure 6.10 shows a summary of the measured Λ binding energies for $A=4$ hypernuclear system. The latest world average of the Λ binding energy of ${}^4_{\Lambda}\text{H}$ is $B_{\Lambda} = 2.04 \pm 0.04(\text{stat.}) \text{ MeV}$ from the three body decay events of ${}^4_{\Lambda}\text{H}$ in the emulsion experiments. The other result was $B_{\Lambda} = 2.34 \pm 0.28(\text{stat.}) \text{ MeV}$ reported from decay pion measurement in the $(K_{\text{stop}}^-, \pi^-)$ reaction.

Figure 6.11 shows the latest level schemes of $A=4$ hypernuclei. From the Λ binding energy in this thesis, the binding energy difference in the $A=4$ hypernuclear system becomes $\Delta B_{\Lambda}^4 = 0.27 \pm 0.03(\text{stat.}) \text{ MeV}$, which is 80 keV smaller than the emulsion results, however, it is consistent within the uncertainty. This result still shows the large CSB effect for the ground state in $A=4$ system.

Recently, Gal calculated the Λ binding energies in $A=4$ system using the effective ΛN interaction derived from NSC97 models [Gal15]. In the calculation, the OPE was allowed for the $\Lambda\text{-}\Sigma^0$ mixing, and a spin dependent central interaction was included as the $\Lambda\text{N-}\Sigma\text{N}$ interaction. This theoretical calculation succeeded to represent the large Λ binding energy difference between ${}^4_{\Lambda}\text{H}$ and ${}^4_{\Lambda}\text{He}$ in the ground states ($\sim 0.25 \text{ MeV}$), which was consistent difference with the experimental measurement, whereas it predicted a small Λ binding energy difference in the excited states ($\sim 0.03 \text{ MeV}$).

Very recently, the Λ binding energy difference between the excited state (1^+) and the ground state (0^+) was measured for ${}^4_{\Lambda}\text{He}$ with hypernuclear γ -ray spectroscopy, and 1.406 MeV energy difference was reported [Yama15]. The small CSB effect for the excited state in $A=4$ system $0.03 \pm 0.05(\text{stat.}) \text{ MeV}$ was reported.

As the $A=4$ hypernuclei is simplest iso-multiplet hypernuclei with a baryon many-body system, the numerical technique to describe hypernuclear state accurately are well established.

Jülich group studies the CSB effect of A=4 system qualitatively using the NSC Λ N interaction models [Haid13]. They contained not only the simple baryon-baryon force but also the three baryon force including Σ and other baryons for the short range interaction. They calculated the Λ binding energies of both states in ${}^4_{\Lambda}\text{H}$ with changing the scattering length of Λ N. The calculation can be compared with the experimental data and discussed the reliability of the current baryon-baryon interaction. This kind of the theoretical approach for the very light hypernuclei is very important to clarify the baryon-baryon interaction.

The systematic uncertainty was dominated by the ambiguity of the beam energy. Because this ambiguity is determined by the uncertainty of the magnetic field at the final dipole magnet in the electron beam line, magnetic field measurements with high accuracy is useful to improve the systematic uncertainty. The second main components in the systematic uncertainty are the stability of the magnetic field and the momentum linearity. The stability of the magnetic field can be controlled by the filed compensation circuit with an accuracy of $\Delta p/p < 10^{-4}$, if the circuit dose not fail to work. In the physics experiment, we performed the calibration experiment with ${}^{12}\text{C}$ at only one condition. If the momentum calibrations are performed with much more conditions, the momentum linearity will be checked more accurately. In these ways, it is possible to reduce the systematic uncertainty, and the Λ binding energy can be determined with higher accuracy (\sim a few tenth keV).

6.4.1 Future prospects

The hypernuclear decay pion spectroscopy carried out the Λ binding energy of the ground state of ${}^4_{\Lambda}\text{H}$ with high accuracy. This experiment took a first step of the new hypernuclear mass spectroscopy method, and other hypernuclei might be measured their binding energies in subsequent experiments. In this section, future possibilities of this method will be represent.

■ Λ binding energies of other hypernuclei

The monochromatic pion peaks from other hypernuclear decay can be detected with more yield of the hypernuclear events. In the decay pion measurement using stopped K^- beam, the production rates of hyperfragments were calculated with the AMD calculation [Nara95]. The expected rate of ${}^3_{\Lambda}\text{H} \rightarrow {}^3\text{He} + \pi^-$ was two-third of ${}^4_{\Lambda}\text{H} \rightarrow {}^4\text{He} + \pi^-$ on ${}^{12}\text{C}$ target. Other hypernuclear events such as ${}^7_{\Lambda}\text{He} \rightarrow {}^7\text{Li} + \pi^-$ and ${}^9_{\Lambda}\text{Be} \rightarrow {}^9\text{B} + \pi^-$ were one order of magnitude less than ${}^4_{\Lambda}\text{H} \rightarrow {}^4\text{He} + \pi^-$ [KawaD].

As the other theoretical calculation, the hyperfragment formation probabilities were also calculated with the statistical decay model [Lore11]. The relative hypernuclear yields in the

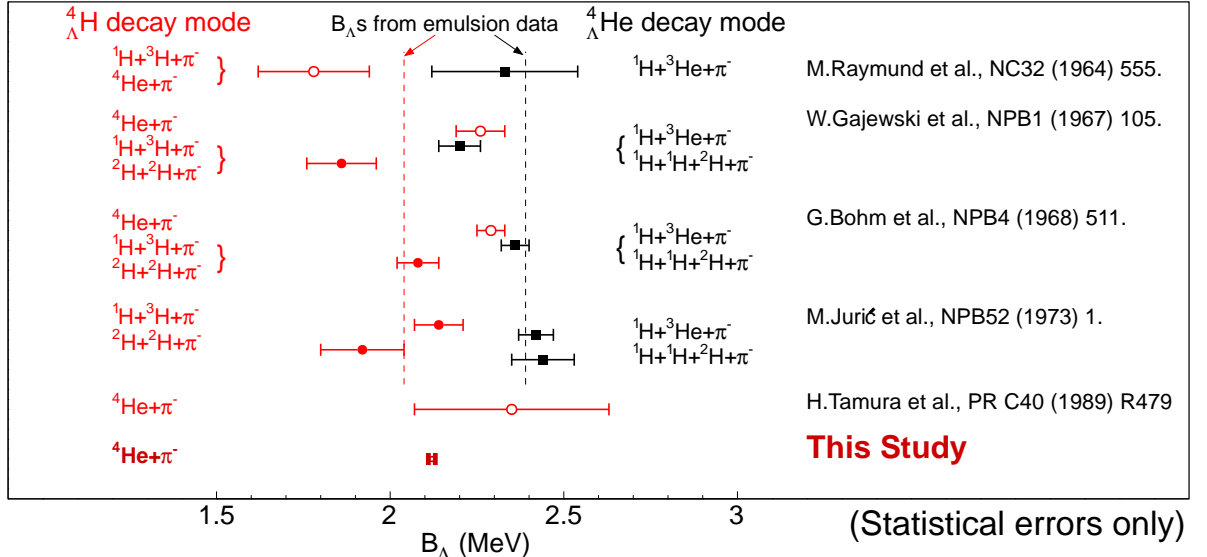


Figure 6.10: A summary of Λ binding energies in $A=4$ hypernuclei. Error bars were described with only statistical uncertainties. The all emulsion results for ${}^4_\Lambda H$ (red) and ${}^4_\Lambda He$ (black) are represented. The world data of the emulsion results are given with dotted lines, the Λ binding energies are $2.04 \pm 0.04(\text{stat.})$ MeV and $2.39 \pm 0.03(\text{stat.})$ MeV for ${}^4_\Lambda H$ and ${}^4_\Lambda He$, respectively. Some Λ binding energies of two body decay events (empty circle) ${}^4_\Lambda H \rightarrow {}^4\text{He} + \pi^-$ were reported, however, they are not included in the world average. The systematic uncertainties of 0.05 MeV in each hypernucleus were reported by Davis *et al.* [Davi05]. The bottom point was given by the present study $B_\Lambda = 2.12 \pm 0.01(\text{stat.}) \pm 0.09(\text{sys.})$ MeV.

electro-photo production were estimated, and monochromatic pion peaks from other hypernuclei, e.g. ${}^7_\Lambda \text{He}$, were expected [Esse13].

This kind of theoretical calculation is very useful to design further experimental setup. At the same time, the measurements of the hyperfragment formation probabilities is useful to test the theoretical models.

On the other hand, from the point of view of the ΛN CSB in $A=4$ hypernuclear system, the absolute Λ binding energy measurement of the ground state of ${}^4_\Lambda \text{He}$ is very important. In the present hypernuclear decay pion spectroscopy, it is difficult to measure the binding energy because the monochromatic pion peak from ${}^4_\Lambda \text{He} \rightarrow {}^4\text{He} + \pi^-$ cannot be observed, ${}^4_\Lambda \text{He}$ goes to more than three-body decay. If the Λ binding energy of ${}^4_\Lambda \text{He}$ is deduced from its decay particles in the counter experiments, precise energy measurements of two γ -rays from ${}^4_\Lambda \text{He} \rightarrow {}^4\text{He} + \pi^0 \rightarrow {}^4\text{He} + 2\gamma$ or a precise momentum measurement of decay pion and proton from stopped ${}^4_\Lambda \text{He} \rightarrow {}^3\text{H} + p + \pi^-$ is necessary: that is experimentally difficult. The emulsion experi-

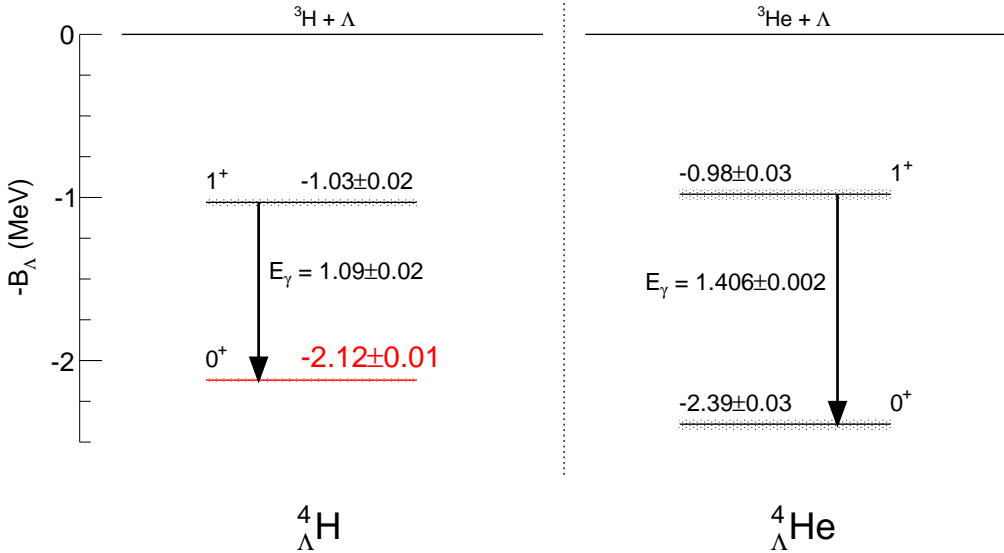


Figure 6.11: Level schemes of $A=4$ hypernuclei. Only statistical errors are shown. The Λ binding energy of the ground state of ${}^4_{\Lambda}\text{H}$ was obtained by this thesis. The binding energy of the mirror hypernucleus ${}^4_{\Lambda}\text{He}$ was reported by the emulsion experiment [Juri73]. The excitation energies were measured with γ -ray spectroscopy [Beje76, Beje79, KawaD, Yama15]. Only the statical uncertainty are represented with meshed area.

ments might be the easiest way to determine the Λ binding energy.

Similarly, the Λ binding energy measurement for ${}^5_{\Lambda}\text{He}$ and ${}^7_{\Lambda}\text{Be}$, which is a isospin pair of the $A=7$ iso-triplet hypernuclei, is impossible in the setup of this thesis. However, the measurements for other isospin pairs of light hypernuclei ($A=6,8$) is possible using this method in principle, through the decay width of π^- mesonic weak decay for p -shell hypernuclei ,e.g. ${}^{12}_{\Lambda}\text{C}$, is about ten times less than that of ${}^4_{\Lambda}\text{H}$.

In order to observe next hypernuclear peak and expand the decay pion spectroscopy, the further experiments with higher signal-to-noise ratio are important.

■ Spin assignment

As already mentioned in Section 1.3.1, the decay ratio of ${}^A_{\Lambda}\text{Z} \rightarrow {}^A_{\Lambda}\text{Z}-1 + \pi^-$ and ${}^A_{\Lambda}\text{Z} \rightarrow {}^A_{\Lambda}\text{Z}-1^* + \pi^-$ is strongly related with the spin state of the hypernucleus because the property of the non-spin-flip weak decay dominance of Λ particle. If several peaks from hypernuclear decay can be observed and a species of parent hypernucleus can be identified, the spin state of this hypernucleus can be confirmed from only the peak position using the similar method in the stopped K^- experiment [Agne09]. The further experiment with higher statistics might be approach it.

■ Decay pion spectroscopy using meson beams

Because of the property of the hypernuclear decay pion spectroscopy, this method can be performed with not only the electro-photo production but also the meson production. On the current beam power, enough hypernuclear yield cannot be achieved using the meson beams because the π^+ beam intensity ($\sim 10^6$ Hz) is much less than e^- beam intensity ($\sim 10^{14}$ Hz) even if the larger cross section of hypernuclear production is taken into account. However, nowadays the high intensity frontier is developed at J-PARC, and a pion beam line with an intensity of $\sim 10^9$ Hz might be constructed. Because the hypernuclear yield is comparable with the electro-photo production, the hypernuclear decay pion spectroscopy can be expand even using the pion beam. An advantage of the spectroscopy using the pion beam is the experiment can be performed with (π^+, K^+) missing mass spectroscopy simultaneously. Therefore, a relation between the fragmentation yield and the hypernuclear continuum state above the Λ separation energy might be understood.

■ Room for Improvement

In order to expand the hypernuclear decay pion spectroscopy, there are mainly three important improvements; yield, background, and accuracy.

yield

In this thesis, 20- μ A electron beam introduced to the target in 2 weeks. After the minor upgrade of the setup, higher beam current might be achieved. We already took about four times more data in 2014. The statistics was increased ~ 4 times with two times higher beam intensity and two times longer beam time; that is a reasonable limit to perform the experiment at MAMI-C in the present setup. If we take data with much more higher statistics, upgrades of the experimental setup are necessary. One idea is an installation of a new K^+ tagger which has larger acceptance. The hypernuclear yield is limited with the solid angle and the momentum acceptance of Kaos. If we can install additional K^+ tagger or replace a new K^+ tagger, the statistics will be increased. The other idea is an identification of hypernuclear event with not K^+ tag but a delayed timing tag from the weak decay. Because the lifetime of the hypernuclear weak decay is ~ 200 ps, the pions from hypernuclear decay can be separated with other pions from decay events of strong interaction using a detector of good time resolution ($\sigma \lesssim 100$ ps). If this kind of new hypernuclear tagging system is established, direct measurements of hypernuclear lifetime is also available.

background

The background on the decay pion spectrum was dominated with pions from quasi-free hy-

perons. In the present experimental setup, this background cannot distinguish with the pion signal from hypernuclei. However, because the quasi-free hyperons are boosted in forward angles on the laboratory frame, almost of them decay and emit pions out of the target, even though a hypernucleus decays and emits the decay pion at the target position. The suppression of the background pions from quasi-free hyperons was suggested by cutting the events coming from outside of the target[Naga13]. In 2014, a background suppressor made by tungsten was installed around the target positon to absorb pions from quasi-free hyperons. We expect about 70% of background pions might be suppressed.

accuracy

In this thesis, the systematic uncertainty for the Λ binding energy of $^4_{\Lambda}\text{H}$ was dominated with the uncertainty of the electron beam energy. If this energy can be measured with higher accuracy, the systematic uncertainty can be reduced. We plan to measure the magnetic field for a final dipole magnet of MAMI-C beam line which is installed around the entrance of A1 experimental hall.

6.5 Summary

A new spectroscopic technique of hypernuclear decay pion spectroscopy was proposed to determine the Λ binding energies of light hypernuclei with an accuracy of 100 keV in total error. Through the comparison between new measurements and the theoretical calculations, the understanding of the ΛN interaction can be significantly progressed. In addition, the new determination of the Λ binding energy for $A=4$ hypernuclear system is very important to understand the origin of the ΛN Charge Symmetry Breaking effect which have been discussed for a long time.

In this thesis, the hypernuclear decay pion spectroscopy was designed so as to observe the decay pion peak from ${}^4_{\Lambda}H$. The expected spectrum was simulated using the expected hypernuclear yield and background which were assumed with the realistic hyperon production cross section. As a result, we found the Λ binding energy of ${}^4_{\Lambda}H$ can be measured with the required using the 125- μm thick 9Be target, 20- μA intense electron beam, and the spectrometers (Kaos, Spek-A, and Spek-C) at MAMI-C.

We performed the pilot experiment to proof the experimental principle in 2011. In this experiment, we confirmed the counting rate per unit beam current in the pion spectrometers was ~ 1 kHz/ μA , that was enough low rate to perform the experiment. On the other hand, because the counting rate at the Kaos detector plane limited the maximum beam current it was necessary to improve the detector setup.

After the pilot experiment, the newly designed lead wall for the e^+ background suppression and the additional Aerogel Cherenkov counter (AC2) for the $\pi^+ - K^+$ separation were constructed and installed. Thanks to these improvements, the counting rate was drastically decreased with a factor of 30 even at 10 times higher beam intensity, we succeeded to take physics data effectively in 2012.

The performance and the stabilities were checked for all detectors. In Kaos, K^+ 's were selected using the particle velocity β , the energy deposit in the scintillation detectors, and the NPEs of the ACs in two ways (threshold cut and likelihood cut) with the supports from the detailed Monte Carlo simulation of Geant4. In the pion spectrometers, π^- 's were selected with the Gas Cherenkov counters (GCs). Through these particle selection, the coincidence peak between K^+ in Kaos and π^- in Spek-C, which corresponds to hyperon or hypernuclear events, was clearly observed on the reconstructed timing at the target. After the π^-, K^+ coincidence events were selected, we observed the decay pion peak from ${}^4_{\Lambda}H \rightarrow {}^4He + \pi^-$ around 133 MeV/c on the momentum spectrum in Spek-C. The peak significance was 7.9σ with the statistical estimation.

The peak was fitted with the *un-binned maximum likelihood* method, the peak position was determined as $p_{\pi^-} = 132.92 \pm 0.02$ MeV/c after the momentum was calibrated with the elastic scattering electron peak of $^{181}\text{Ta}(e, e')^{181}\text{Ta}$. The momentum linearity was also checked with the peak of $^{12}\text{C}(e, e')^{12}\text{C}$. The systematic uncertainties were estimated from the ambiguities of the beam energy, the pion spectrometer's angle, the beam position, the energy loss corrections, the stability of the magnetic field, and the momentum linearity. Finally, we determined the decay pion momentum from ${}^4_\Lambda\text{H}$ as $p_{\pi^-} = 132.92 \pm 0.02(\text{stat.}) \pm 0.12(\text{sys.})$ MeV/c, which corresponds to the Λ binding energy of

$$B_\Lambda = 2.12 \pm 0.01(\text{stat.}) \pm 0.09(\text{sys.}) \text{ MeV.}$$

This B_Λ achieved the highest accuracy in the spectroscopic measurement of the hypernucleus.

This result shows the first observation of hypernucleus by the decay pion spectroscopy for electro-produced hypernuclei, which indicated this new spectroscopic tool is a good method to determine the Λ binding energy of the ground state of light hypernuclei. The obtained B_Λ supports the large CSB effect in A=4 system. From the recent theoretical calculation, a spin dependent central force originated by Λ - Σ^0 mixing effect might be important. In order to clarify the CSB effect, it is important to measure the Λ binding energy of not only the ground state of ${}^4_\Lambda\text{H}$ but also the ground state of ${}^4_\Lambda\text{He}$ and the excited states. In addition, the measurements for other hypernuclear isospin multiplets such as A=7, 10, and 12 system are also important. The Λ binding energy of these system will be approached using the decay pion spectroscopy at MAMI-C and JLab in future.

Acknowledgment

First of all, I would like to express the deepest appreciation to the A1 hypernuclear collaborations and all people who have cooperated with my work. If it had not been for their contributions and supports, I have not been able to finish this work.

I would like to express my deepest appreciation to my supervisor Prof. Dr. Satoshi Nue Nakamura. His careful supports and encouragements are essential to successfully complete the experiment and the analysis. In addition, his advice has stimulated my thinking and opinion. I could successfully finished my thesis thanks to his dedicated education in meetings, seminars, and discussions. I would like to offer my special thanks to late Prof. Dr. Osamu Hashimoto. He opened my eyes to the physics. I learned the style of the physicist from him. I wish that I had reported about the successful completion of this new experiment before his passing away.

I am deeply grateful to Prof. Dr. Hrokazu Tamura. He advised many things about this experiment to me as a pioneer of the decay pion measurement. In addition, I learned about the hypernuclear physics from his passionate seminar. I feel a good fortune that one of the most familiar physicist about the hypernuclear decay pion is in the same laboratory.

I owe my deep gratitude to Prof. Dr. Josef Pochodzalla. He has suggested the hypernuclear decay pion spectroscopy to be performed in MAMI-C, though we intended to carry out it originally at JLab. I have never performed the experiment without his support. In addition, his unique idea such as the lead wall was essential to successfully complete the experiment.

I would like to show my greatest appreciation to Dr. Kyo Tsukada. I have leaned a lot of things from his prominent techniques. I have to learn more, but his advice as a closest faculty were remain in my mind forever. I would like to express my great thanks to Dr. Patrick Achenbach. I appreciate his advices and comprehensive support for not only this work but also lives in Mainz. I was able to have wonderful experiences and quality time with him.

I owe special thanks to Prof. Dr. L. Tang. This work have never been performed without his efforts to propose an experiment in JLab. His passionate action led to successfully complete this work. I also owe my gratitude to Prof. Dr. J. Reinhold. He supported me in the hypernuclear experiment in JLab. What I learned from him about his Cherenkov detector helped me a lot when I made new aerogel Cherenkov counters in Mainz.

My deep application goes to my thesis committee, Prof. Dr. K. Maeda, Prof. Dr. S. N. Nakamura, Prof. Dr. H. Shimizu, Prof. Dr. S. Sasaki, and Prof. Dr. H. Tamura for their generous advices and suggestions in the pre-defense meeting. Advice and comments from the point of view of the theoretician given by Prof. Dr. K. Hagino, Prof. Dr. E. Hiyama, Prof. Dr. T. Motoba, and Dr. A. Ono has been a great help in this work.

My special thanks goes to Dr. R. Bohm, Dr. M. O. Distler, and Mr. J. Gerhard for their technical support in the experiment. It may have caused them trouble for a lot of things, but their kind support reassured me for many times. I would like to deeply express my thanks to Dr. A. Esser, Mr. S. Schulz, and Dr. L. Debenjak, Ms. M. Gómez. They are important colleagues who performed the experiments and discussions as well as friends to share joys when I stayed in Mainz. I also owe my thanks to Dr. C. Ayerbe Gayoso, Dr. A. Sanchez Lorente, Mr. M. Steinen, Mr. S. Bleser, Mr. A. Weber, Mr. P. Gürker for their warm support. I learned many things about not only the physics but also the lifestyle and more from the discussion with them.

I would like to thank Dr. Y. Fujii, Dr. M. Kaneta, Dr. D. Kawama, and Dr. T. Gogami. They let me as an senior researcher in the group. I wish to express my thanks to all staff of Nuclear Physics group, Prof. Dr. T. Kobayashi, Prof. Dr. N. Iwasa, Prof. Dr. T. Koike, Prof. Dr. K. Sekiguchi, Dr. H. Kanda, Dr. M. Ukai, Dr. K. Miwa, Mr. N. Chiga, Ms. N. Kawamura, Ms. M. Shimaya, Ms. A. Yamanouchi, Ms. S. Fukataki, Ms. H. Arihara, and Ms. Y. Wada for their grateful support. I also want to thank all colleagues, Dr. K. Futatsukawa, Dr. A. Matsumura, Dr. K. Shirotori, Dr. K. Hosomi, Dr. B. Beckford, Mr. T. O. Yamamoto, Dr. R. Honda, Ms. C. Kimura, Mr. T. Fujii, and Mr. Y. Yamamoto. My thank also goes to juniors who support my work, Mr. S. Hirose, Mr. K. Manabe, Mr. N. Arai, Mr. D. Uchiyama, Mr. J. Kusaka, Mr. W. Kusaka, Ms. M. Fujita, Mr. Y. Takahashi, Ms. S. Tomita, and Mr. Y. Toyama, .

Last but not least, I would like to express my sincere gratitude to my family for their perpetually support in every aspect.

Appendix A

Amplifier in R877-100

PMT R877-100 (Hamamatsu) of low momentum side in AC1. We made an additional amplifier circuit inside of the PMT as shown in Figure A.1 because its gain was too small in comparison with R1250.

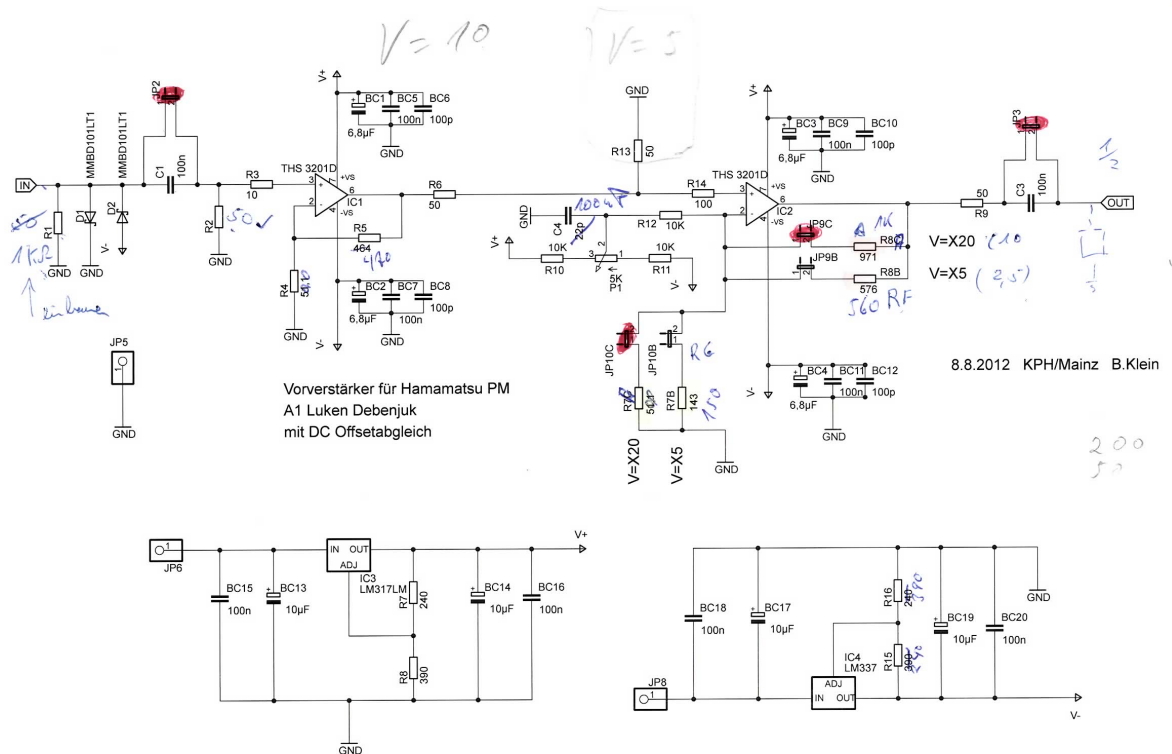


Figure A.1: A circuit diagram of additional amplifier for PMTs in AC1. This was made by B. Klein at KPH/Mainz.

AppendixB

Reflectance

The relative reflectance of AC's reflectors with BaSO₄ was measured using the UV-2101PC spectrometer and the Sample compartment MPC-3100 (Shimadzu). Using these apparatus, the relative reflectance was measured with comparisons of the number of photo electrons from two monochromatic wavelength light. Figure B.1 shows a simple picture to explain the principle of the reflectance measurement.

In the setup for the diffused reflectance measurement, after the reference light introduces from a window, it reflects with BaSO₄ which covered inside of the reflectance box. All reflected light are detected at PMT in the reflectance box. Otherwise, the signal light is introduced from another window. After this light reflects with a sample, e.g. Millipore, the reflected light with mirror reflection go out from the window: it is not detected at PMT, though the reflected light with diffused reflection is detected at the PMT.

In the setup for total reflectance measurement, after the reference light is introduced from a window, it reflects with BaSO₄ and it is detected at the PMT. The signal light from another window reflects with a sample, and all reflected light is detected at PMT.

Before the reflectance measurements with samples, the reflectance were calibrated with BaSO₄. Figure B.2 shows results of the reflectance measurements.

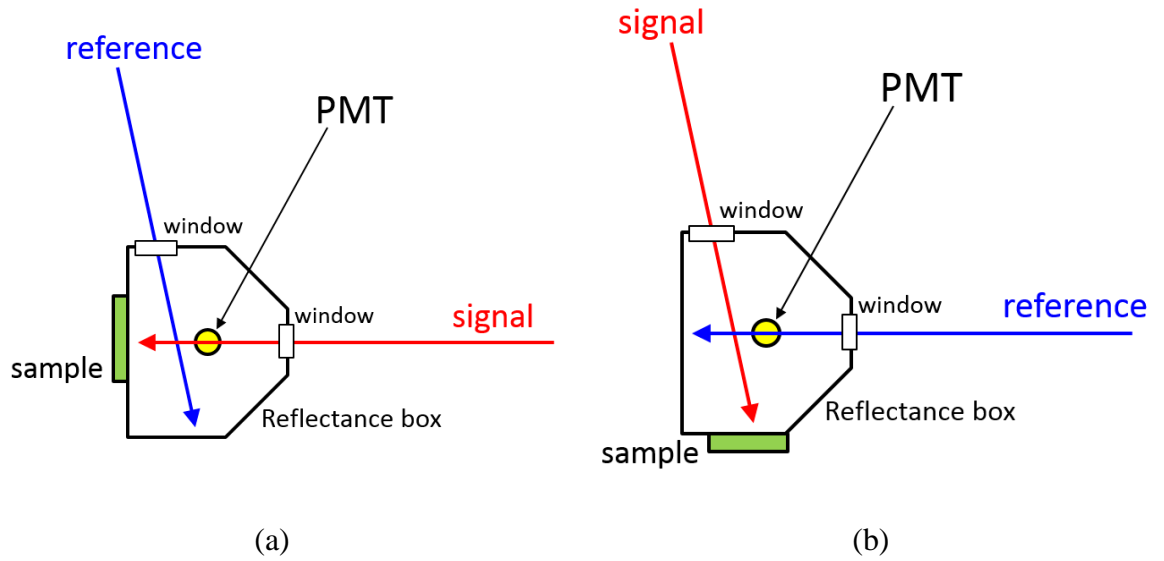


Figure B.1: A simple figure of setup for reflectance measurements. (a) Setup for diffused reflectance measurement. (b) Setup for total reflectance measurement.

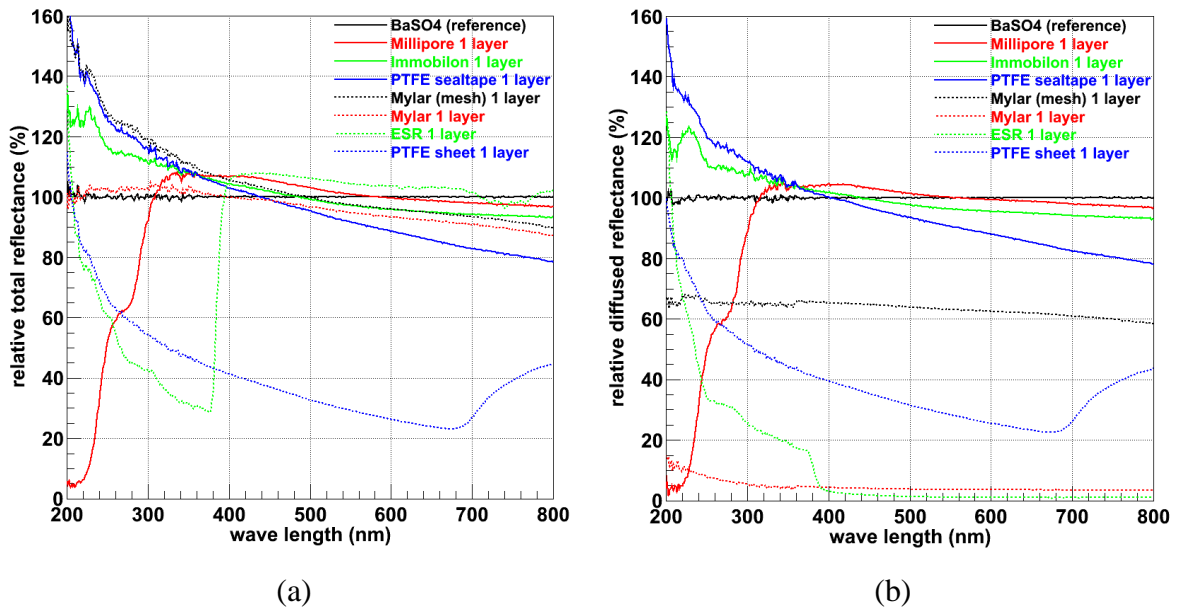


Figure B.2: Reflectance dependences with wavelength in each material. (a) Dependences of total reflectance. (b) Dependences of diffused reflectance.

AppendixC

Momentum spectrum in Spek-A

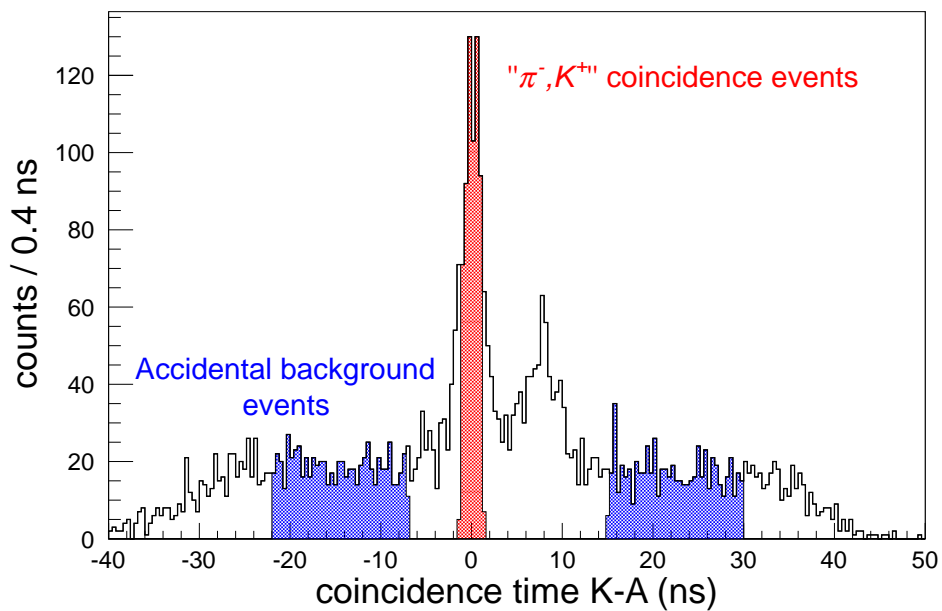


Figure C.1: Coincidence time spectra with tagging K^+ s. Selected " π^-, K^+ " coincidence time windows are filled with a red color for the Spek-A and Kaos coincidence. The width of the time windows are ± 1.25 ns for each coincidence peak. Blue regions are selected to estimate accidental background distribution. The total width of the selected windows are 30 ns for each coincidence spectrum.

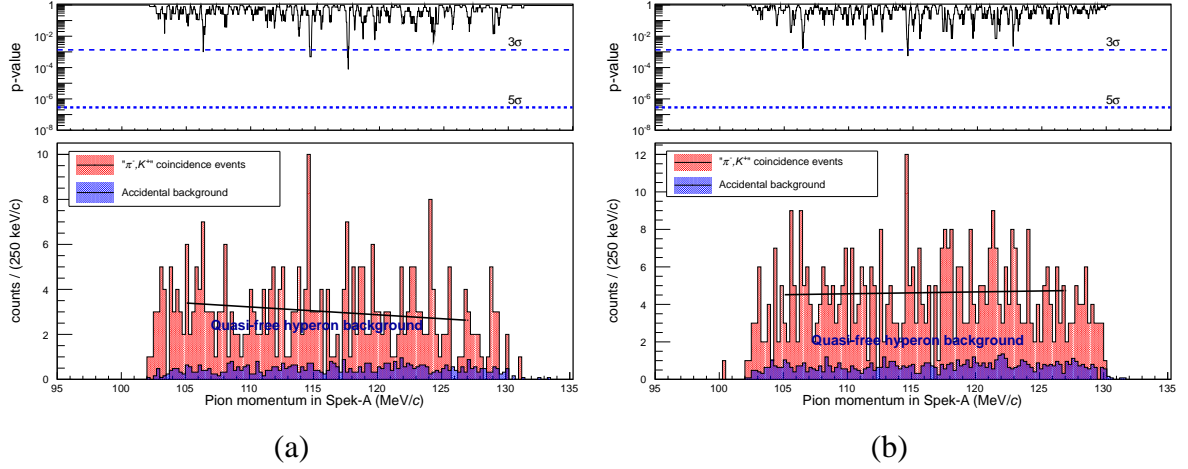


Figure C.2: Pion momentum distributions in Spek-A with (a) the threshold K^+ selection and (b) the likelihood K^+ selection. The momentum distributions in “ π^-, K^+ ” coincidence peaks and those out of peaks (accidental backgrounds) are shown. Lines on the momentum distribution mean fitting results with the linear function. In the top panels, p -values of the peak counts for the background counts are given with lines of the 3σ and 5σ confidence level.

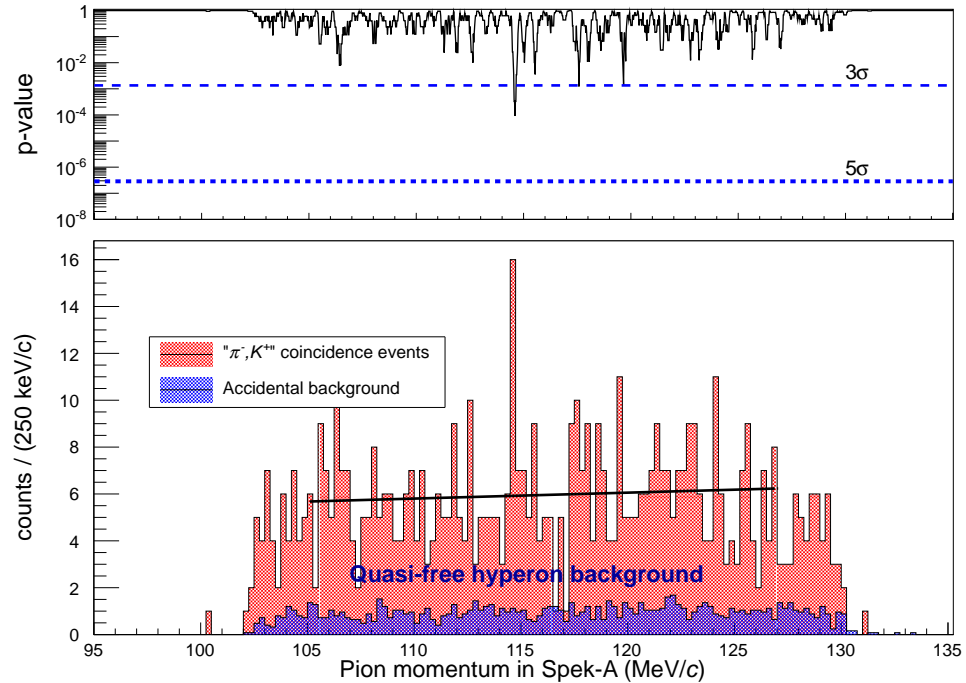


Figure C.3: A pion momentum distribution in Spek-A with the combination K^+ selection with p -values of the peak counts.

AppendixD

Other calibration methods

The calibration method using scattered electrons was introduced in the thesis. In this section, other calibration methods, a momentum calibration using α particle emitter and using primary electron beam, will be mentioned in below.

■ Momentum calibration using α particle emitter

The α particle emitters such as ^{241}Am emit ^4He nucleus with well-known monochromatic momentum. Purchasable α particle emitters are listed in Table D.1 with their α particle energy, momenta and branching ratios. The α particles can be used to calibrate the momentum because they have similar momenta per charge with the pions from hypernuclear decays.

In this method, the emitters are installed instead of the target, and monochromatic momenta of α particles are measured in the pion spectrometer. The momentum calibration is performed by adjusting the measured momenta with the known values. If we measure the α particles from the emitter (1000 Bq) in a spectrometer (20 msr), the rate is 1.5 counts/sec. From the simple statistical estimation for an accuracy of a peak momentum, a precision of the α particle peak in one setting is $\sim 7 \text{ keV}/c$ with 10 minute data taking and $200 \text{ keV}/c$ (rms) momentum resolution. That is enough precision for the calibration.

An advantage of this method is that the calibration is able to be performed in anytime without beam. However, we have to consider the low penetration depth of the α particle. Since the α particles are stopped by air with a thickness of a few cm, or solid materials of 1-mm thick, particle tracking detectors which are filled with a gas such as the drift chamber cannot be used. In addition, a particle tracking detector which can be operated in a vacuum have to be installed at a focal plane position in the pion spectrometer. We need the special detector setup in this way.

Table D.1: Eckert & Ziegler <http://www.ezag.com/>

Radionuclide	α particle energy (MeV)	α momentum per unit charge [(MeV/c)]	Branching ratio (%)
^{148}Gd	3.184	77.033	100
^{237}Np	4.769	94.308	14
	4.774	94.357	18
	4.790	94.512	48
^{239}Pu	5.106	97.581	12
	5.144	97.949	15
	5.157	98.066	73
^{241}Am	5.443	100.753	85
	5.486	101.148	13
^{244}Cm	5.762	103.669	24
	5.805	104.051	76

List of Figures

1.1	Typical examples of hadrons.	3
1.2	A chart of Λ hypernuclei.	4
1.3	Lifetimes of hypernuclei.	6
1.4	Decay widths of light hypernuclear mesonic weak decay.	7
1.5	Typical methods of hypernuclear formation.	7
1.6	Λ recoil momentum dependences on beam momenta in each reaction.	8
1.7	A pion momentum distribution tagged with K^- stopped events in a ${}^9\text{Be}$ target.	11
1.8	Differential cross sections of the hyperon photo productions.	13
1.9	A summary of hypernuclear Λ binding energies for 4-body systems.	18
1.10	A summary of Λ binding energies for $A=7$ iso-triplet hypernuclei.	19
1.11	Λ binding energy differences of the ground states in iso-multiplet hypernuclei as a function of the hypernuclear atomic mass number.	21
2.1	A schematic drawing of the hyperon electro-photo production.	26
2.2	A schematic drawing of the hypernuclear decay pion spectroscopy.	28
2.3	Hypernuclear regions covered on the nuclear chart for ${}^7\text{Li}$, ${}^9\text{Be}$, and ${}^{12}\text{C}$ targets.	31
2.4	A conceptual drawing of a procedure for ${}^4_\Lambda\text{H}$ momentum estimation.	36
2.5	An initial energy distribution of virtual photons and a Fermi momentum distribution of protons in ${}^9\text{Be}$ target.	37
2.6	A differential cross section distribution of $(\gamma + p \rightarrow K^+ + \Lambda)$ reaction.	38
2.7	A simulated momentum distribution of ${}^4_\Lambda\text{H}$ as a function of angles in the laboratory frame.	39
2.8	Results of calculated energy loss distributions as a function of kinetic energies in GEANT4.	41
2.9	Results of stopping range curves in GEANT4.	42
2.10	Stopped time dependences on kinetic energies of ${}^4_\Lambda\text{H}$ and ${}^4_\Lambda\text{He}$ in GEANT4.	43
2.11	Stopping probabilities of ${}^4_\Lambda\text{H}$ and ${}^4_\Lambda\text{He}$ as a function of target thickness.	43
2.12	Energy loss distributions at several absorber thickness.	47

2.13	Root mean squares of energy loss distributions for π^-	48
2.14	An expected accuracy of measured π^- momentum from ${}^4_{\Lambda}\text{H}$ decay.	49
2.15	An expected momentum and angular distribution of quasi-free hyperon backgrounds.	53
2.16	An expected momentum distribution of quasi-free hyperon backgrounds.	54
2.17	Calculated energies of scattered electrons as a function of angles.	56
2.18	An expected spectrum.	57
3.1	MAMI-C floor plan	60
3.2	A photograph of experimental setup in the A1 hall	62
3.3	A top view of the experimental setup in the A1 hall	63
3.4	A schematic drawing of the target and the spectrometer angle	64
3.5	Photographs of the target frame	65
3.6	A schematic drawing of SpekA with beam optics information.	68
3.7	A detector setup of SpekA	69
3.8	A detector setup of Kaos.	72
3.9	A drawing of AC1.	74
3.10	A drawing of AC2.	75
3.11	Total reflectance curves for several reflectors.	76
3.12	A photograph of the experimental setup for J-PARC T44 experiment together with a schematic drawing.	77
3.13	A 2-dimensional TOF distribution in the T44 experiment.	78
3.14	Distributions of the number of photo-electrons and particle survival ratios as a function of the cut threshold in a diffused aerogel Cherenkov counter at T44 experiment.	79
3.15	A photograph of lead walls.	80
3.16	A photograph of the test experiment setup for lead wall.	83
3.17	Particle distribution at lead block position.	84
3.18	Comparisons of lead block effect between experimental data and simulated results.	84
3.19	Configurations of Kaos spectrometer in GEANT4 code for the lead wall simulation.	85
3.20	Dependences of trigger coincidence ratio on the lead wall thickness in GEANT4 simulation.	86
3.21	A simple drawing for an assumption of F_{Recon}	88

3.22	Collected hyperon yield dependences on lead wall thickness.	89
3.23	Figure of merits dependences on lead wall thickness.	89
3.24	An overview of the trigger logic.	92
3.25	A schematic drawing of the grouping circuit.	93
4.1	Differences of detector setup in the Kaos spectrometer	97
4.2	A photograph of tagger counters.	97
4.3	Counting rates of Spek-C in the pilot experiment.	99
4.4	Counting rates of the Kaos triggers in the pilot experiment.	99
4.5	A particle distribution on a particle energy deposited in the scintillation counter and a reconstructed mass square in the Kaos spectrometer.	101
4.6	Coincidence time spectra between Kaos and Spek-C in the pilot experiment. .	101
4.7	A momentum distribution in Spek-C on the pilot experiment in 2011.	102
4.8	Comparisons of counting rates for each paddle in H wall between the pilot experiment in 2011 and the physics run in 2012.	104
4.9	ADC-TOF distributions before and after the time-walk correction.	106
4.10	Time and energy resolutions of each paddle for π^+ s in Kaos.	107
4.11	Run dependences of the particle velocity ($\beta = v/c$) and the energy deposited. .	108
4.12	Number of photo-electrons distributions for π^+ s, K^+ s, and protons in AC2-0 and AC2-4.	110
4.13	Particle survival ratios for NPE cut thresholds in AC1 and AC2 for π^+ s, K^+ s and protons.	110
4.14	Particle survival ratios for NPE cut thresholds in GC for e^- s and π^- s.	111
5.1	A 2-dimensional distribution between the velocity and the energy deposit in the scintillator.	113
5.2	K^+ selections with threshold selection.	114
5.3	K^+ selections with likelihood selection.	115
5.4	Coincidence time spectra between Kaos and Spek-C obtained with the particle selection in Kaos.	115
5.5	Schematic drawings of calibration runs.	117
5.6	Scattered electron angular distribution at target with sieve collimator.	118
5.7	Momentum differences in the calibration data.	122
5.8	A missing mass distribution for carbon target.	124
5.9	Nuclear level structures.	125

5.10	A missing mass dependence on a relative momentum.	127
5.11	A missing mass dependence on a relative momentum with -50 keV beam energy shift.	128
5.12	Energy loss distribution simulated by Geant4.	130
5.13	A simple drawing of multiple scattering effect.	133
5.14	An expected momentum spread with multiple scattering effect.	134
5.15	Momentum differences with angular acceptance cut at run “C1”.	136
5.16	Peak shapes in the calibration runs and expected shapes on decay pion experiment.	142
6.1	Coincidence time spectrum with K^+ tag.	144
6.2	Pion momentum distributions in Spek-C with the threshold K^+ selection and the likelihood K^+ selection.	145
6.3	A pion momentum distribution in Spek-C with the combination K^+ selection.	146
6.4	Λ binding energies of ${}^4_\Lambda H$	147
6.5	Coincidence time spectra in π^+ selection in Kaos, and momentum distribution in Spek-C.	148
6.6	Coincidence time spectra in proton selection in Kaos, and momentum distribution in Spek-C.	149
6.7	The pion momentum distribution with a fitted line in Spek-C.	151
6.8	A distribution of the negative log likelihood as a function of a most provable value of the Landau function.	152
6.9	Results of a peak fitting without parameter limitations.	153
6.10	A summary of Λ binding energies in A=4 hypernuclei.	160
6.11	Level schemes of A=4 hypernuclei.	161
A.1	A circuit diagram of additional amplifier for PMTs in AC1.	168
B.1	A simple figure of setup for reflectance measurements.	170
B.2	Reflectance dependences with wavelength in each material	170
C.1	Coincidence time spectrum with K^+ tag.	171
C.2	Pion momentum distributions in Spek-A with the threshold K^+ selection and the likelihood K^+ selection.	172
C.3	A pion momentum distribution in Spek-A with the combination K^+ selection.	172

List of Tables

1.1	Characteristics of light hyperons.	3
1.2	The experimental result and the theoretical estimations of the charge asymmetric contributions for the binding energy difference between ${}^3\text{H}$ and ${}^3\text{He}$	16
1.3	A summary of measured Λ binding energies in the emulsion experiments for $A=4$ hypernuclei.	18
2.1	A list of expected decay pion momenta.	30
2.2	A list of possible targets.	32
2.3	A Summary of ${}^4_{\Lambda}\text{H}$ yield estimation.	44
3.1	Parameters of MAMI.	59
3.2	A list of targets	66
3.3	Main parameters of SpekA and SpekC.	67
3.4	Main parameters of Kaos.	71
3.5	Coincidence matrix elements in VUPROM2.	94
4.1	Run conditions of the physics run.	105
4.2	Means of NPE distributions for π^+ in each AC segment.	109
5.1	A summary table of calibration runs	117
5.2	Energy loss in each material at calibration experiment.	120
5.3	Results of location parameters with fitting re-parametrized Landau-Gauss function and momentum calibration factors.	123
5.4	A summary table of the excitation energies.	126
5.5	A summary of peak shapes in elastic scattering experiments.	136
5.6	A summary of expected momentum spread due to the matrix ambiguity.	137
5.7	Summary of peak shape assumption	139
5.8	Summary of expected peak shapes on momentum.	141

6.1	A List of the particle masses in the Λ binding energy calculation of $^4_{\Lambda}\text{H}$	147
6.2	A summary of the fitting result for the pion momentum distribution.	154
6.3	A summary of systematic uncertainties.	157
D.1	174	

Bibliography

- [A1Web] <http://www.a1.kph.uni-mainz.de/A1/Welcome.en.html>
- [AcheH] P. Achenbach, Institut für Kernphyik, Johannes Gutenberg-Universität Mainz, Habilitation (2010) .
- [Ache10] P. Achenbach *et al.*, Nucl. Phys A**835** (2010) 313.
- [Agne09] M. Agnello *et al.*, Phys. Lett. B **681** (2009) 139.
- [Agne12a] M. Agnello *et al.*, Nucl. Phys. A**881** (2012) 269.
- [Agne12b] M. Agnello *et al.*, Phys. Rev. Lett. **108** (2012) 042501.
- [Agos03] S. Agostinelli *et al.*, Nucl. Inst. and Meth. A **506** (2003) 250.
- [Akai00] Y. Akaishi *et al.*, Phys. Rev. Lett. **84** (2000) 3539.
- [Akik02] H. Akikawa *et al.*, Phys. Rev. Lett. **88** (2002) 082501.
- [Audi03] G. Audi *et al.*, Nucl. Phys. A **729** (2003) 337.
- [Ajze90] F. Ajzenberg-Selove, Nucl. Phys. A**506** (1990) 1.
- [Beje76] M. Bejedian *et al.*, Phys. Lett. B **62** (1976) 467.
- [Beje79] M. Bejedian *et al.*, Phys. Lett. B **83** (1979) 252.
- [Bert70] D. Bertrand *et al.*, Nucl. Phys. B **16** (1970) 77.
- [BicronWeb] <http://www.crystals.saint-gobain.com/>.
- [Bier80] J. P. Biersack and L. G. Haggmark, Nucl. Inst. and Meth., **174** (1980) 257.
- [Bloc64] M. M. Block *et al.*, Proc. Int. Conf. on Hyperfragments, St. Cergue (1964) CERN report 64/1 p.63.
- [Blom98] K. I. Blomqvist *et al.*, Nucl. Inst. and Meth. A **403** (1998) 263.
- [Bode81] A. Bodek and J. L. Ritchie, Phys. Rev. D **23** (1981) 1070.
- [Bodm85] A. R. Bodmer *et al.*, Phys. Rev. C **31** (1985) 1400.
- [Bohm68] G. Bohm *et al.*, Nucl. Phys. B**4** (1968) 511-526.
- [Bruc78] W. Brückner, *et al.*, Phys. Lett. B**79** (1978) 157.
- [Bran78] R. A. Brandenburg, S. A. Coon, and P. U. Sauer, Nucl. Phys. A **294** (1978) 305.
- [Bran88] R. A. Brandenburg *et al.*, Phys. Rev. C **37** (1988) 781.
- [Cant74] T. Cantwell *et al.*, Nucl. Phys. A**236** (1974) 445-456.
- [Chen08] Q. Chen *et al.*, Phys. Rev. C **77** (2008) 054002.

- [Coon87] S. A. Coon and R. C. Barrett, Phys. Rev. C **36** (1987) 2189.
- [Corthals06] T. Corthals *et al.*, Phys. Rev. C **73** (2006) 045207.
- [Cous08] R. D. Cousins, J. T. Linnemann, and J. Tucker, Nucl. Inst. and Meth. A **595** (2008) 480.
- [Cruz12] L. D. Cruz *et al.*, Phys. Rev. Lett. **108** (2012) 182002.
- [Cusa09] F. Cusanno and G. M. Urciuoli *et al.*, Phys. Rev. Lett. **103** (2009) 202501.
- [Dali59] R. H. Dalitz and L. Liu, Phys. Rev. **116** (1959) 1312.
- [Dali64] R. H. Dalitz and F. von Hippel, Phys. Lett. **10** (1964) 153.
- [Davi54] H. Davies *et al.*, Phys. Rev. **93** (1954) 788.
- [Davi05] D. H. Davis, Nucl. Phys. A **754** (2005) 3c-13c.
- [DebeD] L. Devenjak, University of Ljubljana, Faculty of Mathematics and Physics, Department of Physics, Doctoral thesis (2012).
- [Dey10] B. Dey *et al.*, Phys. Rev. C **82** (2010) 025202.
- [Dulz88] P. Dulzewski *et al.*, Nucl. Phys. A **484** (1988) 520.
- [Dumb83] O. Dumbrajs *et al.*, Nucl. Phys. B **216** (1983) 277.
- [EsseD] A. Esser, Institut für Kernphysik, Johannes Gutenberg-Universität Mainz, Doctoral thesis (2013).
- [Esse13] A. Esser *et al.*, Nucl. Phys. A **914** (2013) 519.
- [Esse15] A. Esser, S. Nagao, F. Schulz, P. Achenbach *et al.*, Phys. Rev. Lett. **114** (2015) 232501.
- [Fese85] H. Fesefeldt, Aachen Report PITHA (1985).
- [Fria70] J. L. Friar, Nucl. Phys. A **156** (1970) 43.
- [Fuji15] Y. Fujii *et al.*, Nucl. Inst. and Meth., to be submitted.
- [G4] <http://geant4.cern.ch/>.
- [Gaje67] W. Gajewski *et al.*, Nucl. Phys. B **1** (1967) 105.
- [Gal09] A. Gal, Nucl. Phys. A **828** (2009) 72.
- [Gal15] A. Gal, Phys. Lett. B **744** (2015) 352.
- [Gibbs72] B. F. Gibson *et al.*, Phys. Rev. C **6** (1972) 741.
- [Glan04] K. -H. Glander *et al.*, Eur. Phys. J. A **19** (2004) 251.
- [GogaD] T. Gogami, Tohoku University, Doctoral thesis (2014) .
- [GoodWeb] <http://www.goodfellow.com/>.
- [Gonz06] D. E. González Trotter *et al.*, Phys. Rev. C **73** (2006) 034001.
- [Haid13] J. Haidenbauer *et al.*, Nucl. Phys. A **915** (2013) 24.
- [Hase96] T. Hasegawa *et al.*, Phys. Rev. C **53** (1996) 1210.
- [Hash06] O. Hashimoto and H. Tamura., Prog. Part. Nucl. Phys. **57** (2006) 564-653.
- [Henl69] E. M. Henley “Isospin in nuclear physics”, Editor D. H. Wilkinson (1969);

- W. E. Ormand and B. A. Brown, Nucl. Phys. A **491** (1989) 1.
- [Hiya01] E. Hiyama *et al.*, Phys. Rev. C **65** (2001) 011301.
- [Hiya09] E. Hiyama *et al.*, Phys. Rev. C **80** (2009) 054321.
- [Hiya12] E. Hiyama *et al.*, Prog. Theor. Phys. **128** (2012) 105.
- [Hotc01] H. Hotchi *et al.*, Phys. Rev. C **64** (2001) 044302.
- [Houk71] T. L. Houk, Phys. Rev. C **3** (1971) 1886; W. Dilg, Phys. Rev. C **11** (1975) 103; L. Koester and W. Nistler, Z. Phys. A **272** (1975) 189; S. Klarsfeld, J. Martorell, and D. W. Sprung, J. Phys. G **10** (1984) 165.
- [Herm76] H. Herminghaus *et al.*, Nucl. Inst. and Meth. **138** (1976) 1.
- [ICRU37] Stopping Powers for Electrons and Positrons, ICRU Report 37 (1984).
- [ICRU49] Stopping Powers and Ranges for Protons and Alpha Particles. ICRU Report 49, (1993).
- [ICRU73] Stopping of Ions Heavier than Helium, Journal of the ICRU Report 73 (2005).
- [Iodi07] M. Iodice *et al.*, Phys. Rev. Lett. **99** (2007) 052501.
- [Juri73] M. Jurić *et al.*, Nucl. Phys. **B52** (1973) 1-30.
- [Kais08] K. H. Kaiser *et al.*, Nucl. Inst. and Meth. A **593** (2008) 159.
- [KawaD] A. Kawachi, University of Tokyo, Doctoral thesis (1997).
- [KMaid] T. Mart *et al.*, <http://portal.kph.uni-mainz.de/MAID//kaon/kaonmaid.html>.
- [Kolb84] K. S. Kölbig and B. Schorr, Comp. Phys. Comm. **32** (1984) 121.
- [LabsphWeb] <http://www.labsphere.com>.
- [Leo] W. R. Leo, *Techniques for Nuclear and Particle Physics Experiments*.
- [Li98] G. Q. Li and R. Machleidt, Phys. Rev. C **58** (1998) 3153.
- [Lore11] A. S. Lorente *et al.*, Phys. Lett. B **697** (2011) 222.
- [Lync91] G. R. Hynch and O. I. Dahl *et al.*, Nucl. Inst. and Meth. B **58** (1991) 6.
- [Mach01] R. Machleidt, Phys. Rev. C **63** (2001) 024001.
- [Mach11] R. Machleidt, D. R. Entem, Phys. Rep. **503** (2011) 1.
- [Mart99] T. Mart and C. Bennhold, Phys. Rev. C **61** (1999) 012201.
- [MatsD] A. Matsumura, Tohoku University, Doctoral thesis (2009).
- [McCr10] M. E. McCracken *et al.*, Phys. Rev. C **81** (2010) 025201.
- [Mill90] G. A. Miller, M. K. Neflens, and I. Slaus, Phys. Rep. **194** (1990) 1.
- [Mill94] G. A. Miller, “Charge Independence and Symmetry of Nuclear Forces” nucl-th/9406023v1.
- [Miur05] Y. Miura *et al.*, Nucl. Phys. A **754** (2005) 75c.
- [Miyo03] T. Miyoshi *et al.*, Phys. Rev. Lett. **90** (2003) 232502.
- [Mizu98] T. Mizutani *et al.*, Phys. Rev. C **58** (1998) 75.

- [Moto94] T. Motoba and K. Itonaga, Prog. Theor. Phys. Suppl. **117** (1994) 477.
- [Naga13] S. Nagao, Proceedings of science, Hadron 2013 (2013).
- [NagaM] S. Nagao, Department of Physics, Graduate School of Science, Tohoku University, Master's thesis (2011).
- [Naka13] S. N. Nakamura *et al.*, Phys. Rev. Lett. **110** (2013) 012502.
- [Naka15] S. N. Nakamura, Talk in 12th International Conference on Hypernuclear and Strange Particle Physics (2015).
- [Nara95] Y. Nara *et al.*, Phys. Lett. B **346** (1995) 217.
- [Nemu02] H. Nemura *et al.*, Phys. Rev. Lett. **89** (2002) 142504.
- [Nogg01] A. Nogga *et al.*, Phys. Rev. Lett. **88** (2001) 172501.
- [Noza90] S. Nozawa and T. -S H Lee, Nucl. Phys. **A513** (1990) 511.
- [NuDat] National Nuclear Data Center, <http://www.nndc.bnl.gov/nudat2/>.
- [Outa98] H. Outa *et al.*, Nucl. Phys. A **639** (1998) 251c.
- [Outa05] H. Outa *et al.*, Nucl. Phys. A **754** (2005) 157c.
- [Over67] O. E. Overseth and R. F. Roth, Phys. Rev. Lett. **19** (1967) 391.
- [Park00] H. Park *et al.*, Phys. Rev. C **61** (2000) 054004.
- [PDG12] J. Beringer *et al.*, Phys. Rev. D **86** (2012) 010001.
- [Pere10] S. A. Pereira *et al.*, Phys. Lett. B **688** (2010) 289.
- [Rapp13] C. Rappold *et al.*, Phys. Rev. C **88** (2013) 041001.
- [Rapp14] C. Rappold *et al.*, Phys. Lett. B **728** (2014) 543.
- [Roch47] G. D. Rochester and C. C. Butler, Nature **160** (1947) 855-857.
- [Saka91] A. Sakaguchi *et al.*, Phys. Rev. C **43** (1991) 73.
- [Sasa04] J. Sasao *et al.*, Phys. Lett. B **579** (2004) 258.
- [Scho84] K. S. Kölbig and B Schorr, Computer Physics Communications 32 (1984) 121.
- [Seng93] P. Senger *et al.*, Nucl. Inst. and Meth. A **327** (1993) 393.
- [Soto00] M. Sotona, Czech. J. Phys. (2000) 50:49-68.
- [Ster84] R. M. Sternheimer, Atomic Data and Nuclear Data Table, **30** (1984) 261.
- [Swar95] J. J. de Swart, C. P. F. Terheggen, and V. G. J. Stoks., “The Low-Energy Neutron-Proton Scattering Parameters and the Deuteron” nucl-th/9509032.
- [Tamu89a] H. Tamura *et al.*, Phys. Rev. C **40** (1989) R479.
- [Tamu89b] H. Tamura *et al.*, Phys. Rev. C **40** (1989) R483.
- [Tamu98] H. Tamura *et al.*, Nucl. Phys. A **639** (1998) 83c.
- [Tamu00] H. Tamura *et al.*, Phys. Rev. Lett. **84** (2000) 5963.
- [Tamu05] H. Tamura *et al.*, Phys. Phys. A **754** (2005) 58c.
- [Tang14] L. Tang *et al.*, Phys. Rev. C **90** (2014) 034320.

- [Tani01] K. Tanida *et al.*, Phys. Rev. Lett. **86** (2001) 1982.
- [Tsai74] Y. S. Tsai , Rev. Mod. Phys. **46** (1974) 815.
- [Ukai04] M. Ukai *et al.*, Phys. Rev. Lett. **93** (2004) 232501.
- [Ukai06] M. Ukai *et al.*, Phys. Rev. C **73** (2006) 012501.
- [Ukai08] M. Ukai *et al.*, Phys. Rev. C **77** (2008) 054315.
- [Wu90] Y. Wu, S. Ishikawa, and T. Sasakawa, Phys. Rev. Lett. **64** (1990) 1875.
- [Wu05] S. C. Wu., Nuclear Data Sheets **106** (2005) 367.
- [Yama15] T. O. Yamamoto *et al.*, arXiv:1508.00376.
- [Yuan06] L. Yuan *et al.*, Phys. Rev. C **73** (2006) 044607.
- [Zieg85] J.F. Ziegler, J.P. Biersack and U. Littmark, “The Stopping and Range of Ions in Matte”, Pergamon Press, 1985.
- [Zieg99] J. F. Ziegler, Rev. Appl. Phys. **85** (1999) 1249.
- [Zieg10] J. F. Ziegler, M. D. Ziegler and J. P. Biersack, Nucl. Inst. and Meth. B **268** (2010) 1818.